Summer 2015

Synthesis and characterization of metal doped titanium dioxide, transition metal phosphides, sulfides and thiophosphates for photocatalysis and energy applications

Nathaniel Coleman Jr.
University of Iowa

SYNTHESIS AND CHARACTERIZATION OF METAL DOPED TITANIUM DIOXIDE, TRANSITION METAL PHOSPHIDES, SULFIDES AND THIOPHOSPHATES FOR PHOTOCATALYSIS AND ENERGY APPLICATIONS

by

Nathaniel Coleman Jr.

A thesis submitted in partial fulfillment
of the requirements for the Doctor of
Philosophy degree in Chemistry
in the Graduate College of
The University of Iowa

August 2015

Thesis Supervisor: Associate Professor Edward G. Gillan

Graduate College
The University of Iowa
Iowa City, Iowa

CERTIFICATE OF APPROVAL

_____

PH.D. THESIS

_____

This is to certify that the Ph.D. thesis of

Nathaniel Coleman Jr.

has been approved by the Examining Committee
for the thesis requirement for the Doctor of Philosophy
degree in Chemistry at the August 2015 graduation.

Thesis Committee: _____
Edward G. Gillan, Thesis Supervisor

_____
Johna Leddy

_____
Sarah C. Larsen

_____
Tori Z. Forbes

_____
David M. Cwiertny

To Mom and Dad

ACKNOWLEDGMENTS

I would first like to thank all of the people that have helped me achieve this milestone. My lord and savior, Jesus Christ is first above all. Without his support and faith encouragements I would have not even been able to get this far. I would like to acknowledge my immediate family next. My loving parents Norma Coleman and Nathaniel Coleman Sr. have supported and pushed me harder than ever throughout my life to never give up, no matter how bleak situations are. My mother has greatly encouraged me to stay faithful in the eyes of the lord for it will bless me throughout my life. My father, a very hardworking individual, provided me with a strong will and effort to accomplish anything placed in my path. Even after the passing of my father, I will never forget his life teachings that have aided me and kept me strong through the tough times. My siblings Neil, Neelan, and Norissa Coleman have always looked up to me as their role model, which has always inspired me to pursue a successful, noteworthy lifestyle.

I would like to thank my very understanding advisor Ed Gillan. He has been an excellent teacher, role model, and advisor throughout my years as a graduate student. I greatly appreciate the experiences of traveling to ACS conferences, the advanced lab skills and techniques, and professional career lessons that he has provided me with. I would like to thank my past and current lab mates Brian Barry, Andrew Zimmerman, Anthony Montoya, Nathan Black, and Matt Lovander.

Lastly, I would like to thank Sharon Robertson for keeping me up to date with due dates and handling paperwork, Janet Kugley for getting me involved with departmental activities, Benj Revis for all of the support working with glass ware, Earlene Erbe,

Shonda Monette, and Brian Morisson for supporting me through my semesters of TA duties.

ABSTRACT

This thesis covers synthetic investigations, characterization, and applications of transition metal doped titanium dioxide materials and transition metal phosphide/sulfide structures. Both areas are useful in heterogeneous catalysis, battery energy storage, and in semiconductor light to energy conversion. Two main synthesis routes have been investigated: 1) rapid solid state metathesis (SSM) of transition metal oxides, phosphides, sulfides, and thiophosphates, and 2) sealed ampoule routes of transition metal phosphides and thiophosphates. SSM reactions tend to yield kinetically controlled multiphase products while sealed ampoule routes gave more thermodynamically favorable single phase materials.

Approximately 10 mol% of many first row transition metals (M = Cr, Mn, Fe, Co, Ni, Cu) were targeted for doping into TiO_2, using MCl_x, and sodium peroxide in SSM reactions, targeting an ideal mixed phase of $M_{0.1}Ti_{0.9}O_2$. X-ray diffraction showed rutile TiO_2 and generally no separate dopant metal phases were seen until subsequent 1000 °C annealing in air. Energy dispersive spectroscopy (EDS), inductively coupled plasma optical emission spectroscopy (ICP-OES), and X-ray photoelectron spectroscopy (XPS) analysis showed slightly lower than the targeted M:Ti ratios; however the manganese sample had more than the ideal 10 mol % of dopant. Diffuse reflectance spectroscopy (DRS) data showed estimated bandgap energies of the doped samples within 1.33-2.55 eV visible range. Magnetic susceptibility showed small paramagnetic responses from all samples that increase upon annealing. Scanning electron microscopy (SEM) showed that the doped SSM-TiO_2 samples were mixtures of aggregates and blocky particles.

The synthesized doped titanias were tested for methylene blue and methyl orange photodegradation under UV and visible light and for H_2 generation from water reduction under UV light. The doped titania samples absorb significant amounts of methylene blue dye in the dark with the manganese doped TiO_2 sample being the most absorbent. Degradation of methylene blue under UV illumination was observed; however, only modest degradation under visible light was observed. The samples performed better than Degussa P25 TiO_2 standard under visible light. The doped titanias did not degrade methyl orange well under UV light and they did not show detectable H_2 generation from water in UV light even with surface platinum additions.

Transition metal phosphide, sulfide and thiophosphate materials were synthesized in two different ways. The metal halides $FeCl_3$, $CoCl_2$, $NiCl_2$, and $CuCl_2$, red phosphorus and elemental sulfur (or P_2S_5) were common to both SSM and ampoule reactions. Both SSM reactions and sealed glass ampoules are solvent-less direct solid state reactions to target FeP_2, CoP_3, NiP_2, CuP_2, FeS_2, CoS_2, NiS_2, CuS, $FePS_3$, $CoPS_3$, $NiPS_3$ and Cu_3PS_4 phases. SSM reactions utilized MCl_x/Li_3N mixtures to produce elemental metals to then react with P/S reagents leading to metal-rich phosphides, sulfur-rich phases or mixes of M-P-S and sulfur rich phases. Phosphorus-rich phases were seldom seen. Ampoule reactions in contrast, produced single phase phosphorus-rich phases and M-P-S products. Sulfide phases were not produced in ampoule systems.

To encourage unique product morphologies, the metal phosphide and thiophosphates were directly synthesized on P25 TiO_2 powders, and pre-made molten fluxes (KCl/LiCl eutectic, tin, or bismuth) to encourage crystal growth of unique structures. M-P products were successfully synthesized in the eutectic and tin fluxes,

except for FeP_2 in the halide eutectic flux. FeP_2 was grown in the tin flux at lower than normal reaction temperatures (500 °C vs 700 °C). Monoclinic NiP_2 was synthesized instead of the cubic phase which was seen in ampoule reactions. M-P-S products were seen in the eutectic flux only, while SnS, M-P, or M –Sn-P products were observed in tin fluxes. All reactions were unsuccessful in bismuth flux. The deposition reactions yielded M-P and M-P-S products on P25 TiO_2 powder. The NiP_2 and CuP_2 products were seen while FeP_2 and CoP_3 were not observed. From these samples, only FeP and CoP was detected on P25 TiO_2. The M-P-S reactions formed the targeted phases on P25 TiO_2 successfully. These deposited materials were tested for their photo-reactivity towards water reduction.

Preliminary tests for UV light induced and electrolytic hydrogen evolution were done using some ampoule synthesized M-P and M-P-S materials. None of the samples showed H_2 generation using UV light, however H_2 was detected from several MP_x and MP_xS_y materials in this thesis under acidic electrochemical conditions at fairly low applied overpotentials of -40 mV to -240 mV.

PUBLIC ABSTRACT

This thesis describes synthetic investigations, characterization, and applications of transition metal doped titanium dioxides (M-TiO_2) and transition metal phosphide/sulfide (M-P/M-S) structures. These materials are useful in heterogeneous catalysis, battery energy storage, and in light to energy conversion. Two main synthesis routes have been investigated: 1) rapid solid state metathesis (SSM) reactions to form transition metal oxides, phosphides, sulfides, and thiophosphates, and 2) evacuated sealed glass tube reactions to grow metal phosphides and thiophosphates (M-P-S).

First row transition metals were doped into the TiO_2 structure using rapid SSM reactions. Several characterization methods were made to identify and quantify amounts of dopant metals. M-TiO_2 samples also tested for organic dye degradation under UV and visible light and for H_2 formation from water under UV light.

The M-P, M-S and M-P-S materials were synthesized using solvent-free rapid SSM reactions and in evacuated, sealed glass tubes. Solid metal halides were heated with red phosphorus, sulfur, or both. Rapid SSM reactions tend to yield multiphase products while sealed ampoule reactions produced single phase materials.

To encourage unique product shapes and crystal growth, the M-P and M-P-S materials were grown on Degussa P25 TiO_2 powder, and in molten fluxes. Preliminary UV photocatalysis and electrochemical hydrogen evolution were done using select ampoule synthesized M-P and M-P-S materials.

TABLE OF CONTENTS

LIST OF TABLES

LIST OF FIGURES

CHAPTER 1

INTRODUCTION TO METAL OXIDE, PHOSPHIDE, SULFIDE AND THIOPHOSPHATE MATERIALS

1.1 Background on materials used in this work

This introductory chapter will set a foundation for the research reported in this dissertation. The focal point is the synthesis of targeted metal oxide, phosphide, sulfide and mixed phosphide-sulfide materials (thiophosphates). The materials are an inspiration from past group work that demonstrated new reaction pathways using rapid solid state synthetic approaches using first row transition metals[1] and unique phosphorus reactions.[2] Modified traditional solid state reactions and growth techniques for binary and tertiary materials were targeted. Characterization techniques used in the research will be explained as well. In this chapter, common solid state synthetic techniques will be discussed and compared to the reactions used in the synthesis of materials that will be discussed in the following chapters.

Transition metal materials are abundant in a wide variety of applications. These elements are reflected in their abundance in the earth's crust as minerals. Metal oxides are common minerals that can be mined, collected, and reacted to produce useful starting materials, such as metal halides and nitrides. Most thermodynamically stable metal oxides are insoluble in water and organic solvents. Often mixtures of hot concentrated oxidizing acids, HF, or aqua regia can dissolve the metal oxides. Metal oxides are also resistant to heat treatment. A list of common first row transition metals and their respective physical properties are listed in Table 1.1. The heats of formation are given along with the melting points of common metal oxides. The oxides listed are all thermodynamically stable, as shown by their relatively large exothermic ΔH_f values. The melting points of the oxides are often very high, which is advantageous for industrial uses.

Table 1.1 Selected common first row transition metal oxides. Respective metal oxidation states, melting points and heats of formation are given for each solid. (D) denotes decomposition upon melting. Data from CRC Handbook of Chemistry and Physics 71st Edition and Thermochemical Data of Elements and Compounds.

Metal Oxide	**Cation Oxidation State**	**Melting Point (°C)**	**ΔH_f (kJ/mol metal)**
TiO_2, Ti_2O_3, TiO	4+, 3+, 2+	1857, 1842, 1750	-945, -761, -543
V_2O_5, VO_2, V_2O_3	5+, 4+, 3+	690, 1545, 1967	-775, -714, -609
CrO_3, CrO_2, Cr_2O_3	6+, 4+, 3+	185(D), 375(D), 2330	-579, -582, -570
MnO_2, MnO, Mn_3O_4	4+, 2+, 2+/3+	535(D), 1810, 1565	-522, -382, -462
FeO, Fe_3O_4, Fe_2O_3	2+, 2+/3+, 3+	1377,1597,1594	-266, -372, -411
CoO, Co_3O_4	2+, 2+/3+	1795, 1805	-238, -302
NiO	2+	1955	-240
Cu_2O, CuO	1+, 2+	1236, 1326	-84, -156
ZnO	2+	1975	-351

Similar to metal oxides, several metal phosphides and sulfides are found in some natural minerals and are extracted by mineralizing acids. Selected metal phosphide and sulfide materials and their physical properties are shown in Tables 1.2 and 1.3. Traditional synthesis methods are also shown in each table and are often high temperature ampoule syntheses. Several metal phosphides and sulfides are black in color and are used in catalysis.

Table 1.2 Selected first row transition metal phosphides. Respective metal oxidation states, heats of formation, and traditional synthesis conditions are given for each compound. The data is from CRC Handbook of Chemistry and Physics 71st Edition, Thermochemical Data of Elements and Compounds, or cited from superscripted references. (NR = not reported)

Metal Phosphide	**Cation Oxidation State**	**Traditional Synthesis Methods**	**ΔH_f (kJ/mol metal)**
TiP	+3	From elements, 850 °C silica tubes, 10 days[3]	-283
VP_4	+2	From elements using I_2 vapor transport, 550 °C in silica tubes[4]	-239[5]
CrP_4	+2	From elements, 900-1200 °C, 15-65 kbar, high pressure anvil press[6]	NR
MnP_4	+2	From elements, 1227-1427 °C, 30-55 kbar high pressure anvil press [7]	NR
FeP	+3	From elements, 900 -1150 °C in silica tubes[8]	-126
CoP_2	+4	From elements using I_2 vapor transport, 600 °C in silica tubes[4]	NR
Ni_2P	+2	From elements, T $\geq$1000 °C silica tubes[9]	-167[5]
Cu_3P	+1	From elements, 500- 1000 C, silica tubes[10]	-129

Table 1.3 Selected first row transition metal sulfides. Respective metal oxidation states, heats of formation, and traditional synthesis conditions are given for each compound. Synthesis methods are for the bold phases. Data from CRC Handbook of Chemistry and Physics 71st Edition, Thermochemical Data of Elements and Compounds, or cited from superscript references.

Metal Sulfide	**Cation Oxidation State**	**Traditional Synthesis Methods (Bolded phases)**	**ΔH_f (kJ/mol metal)**
TiS,**TiS_2**	2+, 4+	From the elements, I_2 vapor transport, 750 - 900 °C, silica tubes, 14 days [11]	-272, -407
MnS, **MnS_2**	2+, 4+	From the elements, 250-700 °C, silica tubes, 30 days[12]	-213, -226
FeS, **FeS_2(p)**	2+, 2+	From the elements, I_2 vapor transport, 620 °C, silica tubes, 5 days[13]	-102, -172
CoS_2, Co_2S_3, **Co_3S_4**	2+, 3+, 2+/3+	From the elements, 700-800°C, silica tubes[14]	-153, -147, -359
NiS, Ni_3S_2	2+, 2+	From the elements, 1000 °C, silica tubes[15]	-134, -203
CuS, **Cu_2S**	2+, 1+	From the elements, sulfur vapor, 550° C, silica tubes[16]	-53, -80

In industry, these materials are used in optics (ZnS), mechanical lubricants (layered MoS_2) fertilizers, pesticides, and semiconducting materials. Some metal phosphides and sulfides are used in the semiconducting field for their tunable lower band gap energies (GaP, InP). A compilation of band gap energies for common metal oxide (M-O), metal phosphide (M-P), and metal sulfide (M-S) materials are shown in Table 1.4. All entries without superscripts are from the same reference source. [17] The band gap energy is an important feature of the electronic structure of compounds. The band gap is the energy between the highest occupied molecular orbital, the top of the valance band (VB) and the lowest un-occupied molecular orbital, the bottom of the conduction band (CB) within a material. Under normal conditions, most electrons are localized in the VB

and can be excited to the higher energy CB upon an applied electrical potential, light, heat, and other forms of energy input.

Table 1.4 Band gap energies (E_g) of metal oxide, phosphide, sulfide and thiophosphate materials at room temperature. Super script numbers are cited references.

Metal	**Oxide (B.G. eV)**	**Phosphides (eV)**	**Sulfides (eV)**
Ti	TiO_2 (R=3.20, A=3.00)	TiP (metallic)[18]	TiS_2 (1.24)
V	V_2O_5 (2.34)	VP(metallic)[19]	VS_4 (1.35)[20]
Cr	Cr_2O_3 (1.62)	CrP(metallic)[19]	Cr_2S_3 (0.90)
Mn	MnO_2 (0.28)	MnP_4 (0.14)[21]	MnS (6.20)
Fe	Fe_2O_3 (2.34)	FeP_2 (0.40)	FeS_2 (1.2)
Co	Co_3O_4 (2.43)[22]	CoP (1.71)[23]	CoS (1.13)[24]
Ni	NiO (3.70)	NiP_2 (0.50)	NiS_2 (0.50)
Cu	Cu_2O (2.02)	CuP_2 (1.4)	Cu_2S (1.84)
Zn	ZnO (3.35)	Zn_3P_2 (1.15)	ZnS (3.87)

1.1.1 Structure and Common Applications of Transition Metal Oxides

First row transition metal oxides for a wide variety of structures under ambient and pressure/reaction related conditions. TiO_2 forms three common phases under ambient conditions. These are anatase, brookite and rutile. Anatase and rutile both adopt tetragonal unit cells while brookite is orthorhombic. Vanadium oxides range in symmetry from trigonal to rock salt cubic structures. Chromium, manganese, iron, and cobalt oxides form spinel and corundum like unit cells. Nickel and copper oxides form cubic and monoclinic structures. Zinc oxide forms the hexagonal wurtzite structure.

Some examples of the crystal structures of first row transition metal oxides are shown in Figure 1.1.

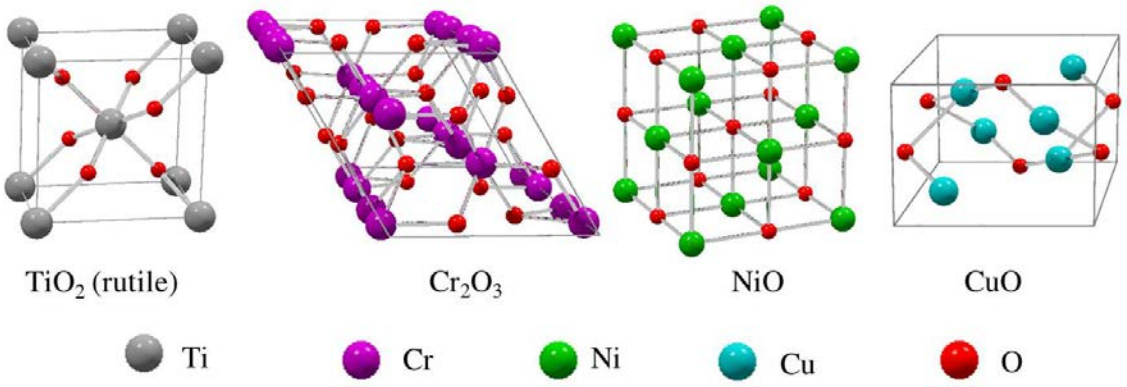

Figure 1.1 Examples of first row transition metal oxides demonstrating different Bravis lattices. TiO_2 in the rutile phase is tetragonal, Cr_2O_3 is rhombohedral, NiO is cubic, and CuO is monoclinic.

Colored metal oxides are used as pigments in ceramics, as glazes and refractory materials utilize the oxides in cements and hard clays for improved structural integrity. The structure of the metal oxides influences the use. For example hematite, Fe_2O_3, is a reddish solid that is used as a red pigment, an abrasive polish, and an additive in cosmetics, while magnetite, Fe_3O_4, is used as a black pigment and in biological studies as nanoparticle magnetic contrasting agents and in catalysis.[25-28] TiO_2 has several uses in both consumer products and industry. It can be found in pigments, papers, and plastics. In research, TiO_2 is a very important photo-catalyst. V_2O_5 is a very commonly used industrial catalyst for H_2SO_4 production, thermal imaging, and in redox batteries. CrO_2 is primarily used in magnetic tape material that is located in CD's and DVD's, while CrO_3 is a very powerful oxidizing agent used in chrome plating and as a stripping reagent.

MnO is used as a green pigment in ceramics and MnO_2 is well known for its use in dry cell batteries. CoO is used as a deep blue pigment in ceramics. NiO is also used as a pigment but also has uses in Ni-Fe batteries. Cu_2O is a red solid used as an anti- fungal agent while CuO is a black solid used in the welding industry or as a black pigment in ceramics. ZnO is used in several consumer products, particularly in the manufacture of rubbers and plastics. The second row transition metal oxides have some interesting properties and uses. The most common oxide, zirconium dioxide (ZrO_2), is used as a ceramic material and has noteworthy use as an O_2 sensing material in O_2 sensors due to oxygen's high mobility through its crystal structure. It is also used as a thermal barrier coating for its high thermal stability

Of the oxides mentioned, TiO_2 is by far the most commonly used oxide in research for its non-toxic nature and wide variety of uses. TiO_2 can be found in practically any white colored consumer and industry product and is used as a sunscreen additive, since TiO_2 absorbs UV light. For this reason, TiO_2 is well known as a useful UV photocatalyst. UV light however, is only a small fraction of light that is emitted from the sun, and because of this, several efforts have been made in research to adjust the usefulness of TiO_2 into the visible light region.

Over the years, there have been several literary reviews demonstrating doping and the effects on improved photo-response in the visible light regions.[29,30] Traditional doping methods involve using small amounts (~1-5 atomic %) of another atom to replace atoms within the TiO_2 structure. The uses of doped TiO_2 are numerous, with organic pollutant degradation and water oxidation/reduction being the leading uses. Using visible light from sunlight is ideal since it emits a majority of visible light wavelengths. Doping methods using metal and non-metal ions aid in facilitating electron movement to higher energy orbitals allowing catalytic reactions to be performed in higher wavelengths within the visible light region.

Nitrogen and carbon doping are examples of anion doping used for shifting the band gap energy of TiO_2 into the visible region. This is done by anionic replacement of a small amount of oxygen atoms with nitrogen, carbon or mixtures of both. Nosaka et. al utilized organic guanidine and urea to dope nitrogen into TiO_2.[31] Sato et. al doped TiO_2 with nitrogen using aqueous ammonia solutions in combination with titanium tetrachloride or titanium tetraisopropoxide hydrolysis ending with calcination.[32] Hydrothermal synthesis of N-doped TiO_2 was done by Cong et al. using organic nitrogen containing compounds.[33]

Carbon has also been doped into TiO_2 to improve its catalytic performance under visible light. Common methods involve mild heating of TiO_2 in the presence of hydrocarbons or volatilizing carbonaceous material in the presence of a titanium precursor, and then growing carbon and TiO_2 together using transport methods. Irie et al. produced carbon doped anatase TiO_2 from mild heating of TiC at 350 °C in air followed by annealing at 600 °C under O_2 atmosphere and showed decomposition of 2-propanol under visible light.[34] Wu et. al. produced carbon doped TiO_2 from chemical vapor deposition synthesis of nanotubes and nanospheres from a $Ti(OC_4H_9)_4$ precursor and tested the material for its capabilities to perform as a visible light photocatalyst by UV-Vis techniques.[35] Ren et. al. synthesized carbon doped TiO_2 using a hydrothermal treatment of amorphous TiO_2 and glucose at 160 °C and tested for rhodamine B dye degradation under visible light.[36] Other anions, such as fluorine, sulfur,[37] and phosphorus have been doped into TiO_2 and are doped in similar fashions to carbon and nitrogen.

Cation doping of metal ions into TiO_2 has been done to promote visible light catalysis. These involve substitutional doping, which replaces Ti^{4+} ions for similar sized metal cations. Interstitial doping can be used, but often requires small ions that can fit within the voids of a crystal lattice (e.g. Li^+). Transition metals are ideal targets due to variations in d-orbital electronic structures which lead to visible colors. Strategies of doping often involve pyrolysis of mixed titanium and transition metal precursors in air,

sol-gel precipitation, and hydrothermal synthesis. Dvoranova et. al. produced Cr, Mn, and Co doped TiO_2 using hydrolysis of $TiCl_3$ or $TiCl_4$ with Cr_2O_3, $CrCl_3$, $MnCl_2$, or $CoCl_2$ followed by heating to 500 or 600 °C under inert or slightly reducing H_2/N_2 atmosphere.[38] The dopants were varied from 0.2-1.0 atomic percent. Nagaveni et. al. utilized a solution combustion method to produce undoped and transition metal doped anatase TiO_2 using $TiO(NO_3)_2$ as the titanium source, glycine, and aqueous dopant precursors of Zr, Ce, V, W, Cu, and Fe. The solutions were heated to dryness at 350 °C and the dopants were varied from 1-10 atomic %.[39] Elaborate materials from combining both non-metals and metals as co-dopants within the TiO_2 structure have also been synthesized.

1.1.2 Structure and Common Applications of Transition Metal Phosphides, Sulfides and Thiophosphates

Phosphorus forms a wide variety of compounds with majority of the elements. The structures of metal phosphides vary depending on the metal. These structures are often complex with unexpected oxidation states. For example, Li_3P is a black solid and consists of Li^+ and P^{3-} anions, while α-Li_3P_7 is a yellow solid that consists of P_7^{3-} cage like anions.[40,41] The transition metal phosphide structures are even more complex. Ni_5P_4 consists of an unusual array of two types of anions: P^{3-} and P_4^{6-} pyramids.[41,42] TiP_2 consists of P^{3-} and infinite P^- chain like anions.[41,43] Transition metal phosphides have some applications in and industry but are rare since they are not naturally common in nature. The most common use is in catalysis. Ni_2P is widely used as a catalyst in hydrodenitrogenation (HDN and hydrodesulfurization[44-46] (HDS) processes. ZnP is used as rodenticide, producing phosphine gas when interacting with HCl.

Similarly with metal phosphides, the sulfides have many compounds for each transition metal. There are a wide variety of titanium and vanadium sulfides for each

oxidation state of the metals. A list of the first row metal sulfides (and phosphides) is shown in Table 1.2. There are several chromium sulfides known which include CrS, Cr_2S_3, and Cr_3S_4. The crystal structures vary from each chromium sulfide. Manganese sulfide, MnS, forms a cubic structure. The most common iron sulfide material is pyrite, FeS_2, and has a cubic unit cell. Cobalt sulfides such as CoS_2 and Co_3S_2 are commonly seen, having pyrite and spinel structures respectively. Nickel forms the NiS trigonal structure mainly. Several copper sulfides are known, such as CuS, Cu_2S, and CuS_2, and are used as semiconductors. ZnS is used as a wide band gap semiconducting material. Zinc sulfide forms the cubic, zinc blend structure under ambient conditions, and hexagonal phase at higher temperatures (~1000 °C). The heavier transition metals form metal sulfides that are often layered, such as MoS_2, and are used as mechanical lubricants. Most sulfide materials are used in catalysis as semiconducting photocatalysts, HDN and HDS catalysts.[47-49]

Ternary metal thiophosphate materials have interesting structures. Example unit cell structures of nickel phosphide, sulfide and thiophosphate are shown in Figure 1.2

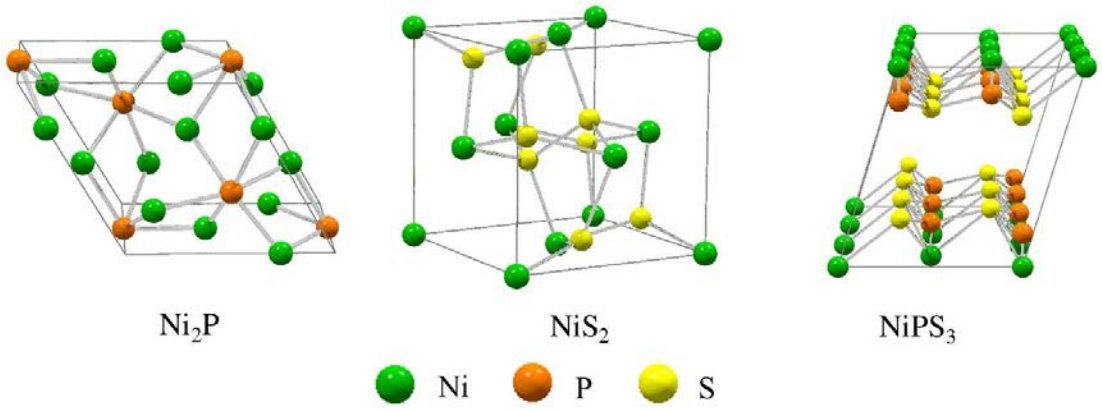

Figure 1.2 Example unit cell structures of nickel phosphide, sulfide and thiophosphate compounds.

Materials with the MPX_3 (X= S, Se) formula form layered structures similar to $CdCl_2$, missing a layer of atoms within the unit cell. The unit cells are either monoclinc or rhombohedral and consist of metal M^{2+} ions and P_2 pairs in octahedral sites, and the chalcogen atom having ccp arrangement of atoms. The empirical formula is similar to MS_2 and can be thought as $[M_{(2/3)}(P_2)_{(1/3)}]S_2$.[50] Another way to think of the structure is two M^{2+} cations shared between $P_2S_6^{4-}$ anions. The lack of atoms occurs every second octahedral site layer between the chalcogen atoms and is a considered a Van der Waals gap in the MPX_3 structures since in one direction, the unit cell is only held together by Van der Waals forces. The sulfur (or selenium) atoms are in direct contact with the gap which is useful for several intercalation chemistries. There are 24 known compounds with MPX_3 structures, where M= Mg, Ca, V, Mn, Fe, Co, Ni, Pd, Zn, Cd, Hg, In, Sn, and Pb. Vandium, cobalt, palladium, and zinc do not form $MPSe_3$ structures.

1.2 Background on Common Synthetic Methods

Depending on the application, materials can be synthesized a variety of ways. The ideal materials needed for catalysis require high purity, good crystallinity, high surface area and very small particle sizes. Solution phase synthesis is traditionally done to achieve this. One advantage of solution phase synthesis is that isolated, uniform, nanoscale materials can be achieved using capping agents[51,52]. Co-precipitation techniques can also be incorporated into this system to produce more exotic doped or composite materials[30,53,54]. To achieve desired phases and to maximize product yields, the reaction speeds are slow and temperatures are often relatively low (T< ~200 °C).

One disadvantage of solution phase synthesis is that the synthesis requires a solvent, which is often not environmentally friendly. Solid state synthesis methods often require no solvent and rely on solid-solid interactions to produce products. Reagents are ground together physically and then heated in either air, inert atmosphere, or under a

desired gas. As seen in Tables 2.3 and 2.4, traditional solid state synthesis methods often require materials to be heated at high temperatures and for long periods of time. This is because the solid to solid diffusion rate is slow compared to similar solution phase reactions.

To help bridge the diffusion gap between solid interactions and solution reactions, the use of fluxes have greatly improved the overall reaction quality in solid state chemistry. Molten metals and metal salts have been used extensively in this aspect of research. Low melting elements such as tin or bismuth are often used due to their low reactivity (if any) towards glass and metal oxide reactor vessels. Alkali metal salts have been used in flux chemistry however they are often reactive towards glass at high temperatures over long periods of time, causing glass to become brittle. Eutectic mixtures of salts and metals have also been used to reduce the required temperature to melt the solids. Eutectics can be formed by physically mixing two or more reagents at appropriate ratios and heating them together to form an even lower melting solid.

Metal halides, carbonates, nitrates, phosphates and sulfates are popular useful materials in this respect. Several examples of flux synthesis exist in literature. Bondioli et al. synthesized CeO powders comparing LiCl/KCl, $NaNO_3/KNO_3$, NaOH/KOH fluxes.[55] Composite SnO_2/TiO_2 materials were synthesized by Naidu et al. using LiCl/KCl eutectic flux.[56] An interesting solid state metathesis reaction utilizing eutectic LiCl/KCl flux chemistry to form $Er_2(CN_2)_3$ from the reaction between $ErCl_3$ and $Li_2(CN_2)$ was done by Poser and Meyer.[57]

Fluxes need to be robust to handle extreme reaction conditions, and thus metals are often used. The low melting points of tin (232 °C), lead (327 °C), bismuth (271 °C), and indium (156 °C) are ideal for reactions that would normally require higher temperatures or long heating times. Gallium is sometimes used for its very low near room temperature melting point (29 °C). Single crystals can be grown from fluxes using vapor/deposition methods. Removal of the crystals can be done by physically pulling

them from the cooled fluxes or by dissolving away the flux in acids. Acid usage may remove desired products or alter morphology, therefore the choice of acids and concentrations need to be considered.

1.2.1 Common Transition Metal Oxide Synthesis Techniques

The metal oxides are widely used for their physical and electronic properties. As mentioned earlier, the synthesis technique is usually driven by the desired products and their functionality. Heating metal powders in air or under O_2 flow is the most straightforward method of synthesizing metal oxides. Other simple growth methods involve hydrolysis of moisture sensitive reagents or pyrolysis of organometallic materials. For example, TiO_2 can be synthesized from the hydrolysis of $TiCl_4$ in the reaction in Equation 1.1, or from high temperature pyrolysis of titanium tetraisopropoxide in Equation 1.2.

$$TiCl_4 + 2\ H_2O \rightarrow TiO_2 + 4\ HCl \quad (1.1)$$

$$Ti(OCH(CH_3)_2)_4 + 18\ O_2 \rightarrow TiO_2 + 12\ CO_2 + 14\ H_2O \quad (1.2)$$

Solution pyrolysis is also a quick and effective technique to produce metal oxides. A mixture of metal nitrates and an organic fuel source heated in air (or inert pyrolysis) will produce metal oxides. For example, transition metal oxide nanostructures were synthesized using pyrolysis of octadecene in the presence of Cr, Mn, Fe, Co, and Ni salts.[58] Spray pyrolysis is an effective technique to produce metal oxides in the form of thin films, and involves heating a very thin layer of a solution of metal reagents and a fuel source.[59] This is particularly useful in the solar cell industry.

Nanoscale structures such as plates,[60,61] hollow tubes,[62,63] rods,[64,65] and spheres[66,67] are desirable especially as catalysts due to their unique structures, uniformity,

and large surface areas. Such materials are usually grown from hydrothermal and solvothermal synthesis due to slow growth times (~12 hours) and low temperatures (T < 300 °C). The materials are isolated using appropriate solvents and drying under vacuum.

1.2.2 Common Metal Phosphide, Sulfide, and Thiophosphate Synthesis Techniques

Metal phosphides, sulfides and thiophosphates can be synthesized in a similar fashion to the metal oxides. The most basic routes are to start with inert heating of the elements in silica tubes. As mentioned before, this process is usually very lengthy and has solid diffusion barrier issues. Solution based routes are usually performed to obtain specific morphological moieties. For example, metal phosphides can be synthesized in a solution of trioctlyphosphine (TOP) and trioctylphosphine oxide (TOPO) with metal salts or organometallic reagents such as $CoCl_2$ or $Fe(CO)_5$. The $Fe(CO)_5$ reaction with TOPO and TOP produces nanowire like FeP structures at 300 °C.[68]

One unique set of reactions will be discussed in the next section, which involves rapid propagation of products which will be further investigated in this thesis.

1.3 Background Information on Targeted Products and Reaction Types in the Proceeding Chapters

1.3.1 Structural Information on Targeted Materials

The targeted M-P products are FeP_2, CoP_3, NiP_2, and CuP_2, and the targeted M-S products are FeS_2, CoS_2, NiS_2, and CuS. M-P-S targeted products are $FePS_3$, $CoPS_3$, $NiPS_3$, and Cu_3PS_4. A listing of M-P and M-S structural details is shown in Table 1.5 and M-P-S structural details are in Table 1.6.

Table 1.5 Targeted M-P and M-S structural information. References are superscripted numbers.

Compound	Unit Cell	Space Group (number)	Lattice Parameters (Å)	Volume ($Å^3$)	Density (g/cm^3)
FeP_2[69]	Orthorhombic	Pnnm (58)	a = 4.97 b = 5.66 c = 2.72	76.60	5.11
CoP_3[70]	Cubic	Im-3 (204)	a = 7.07	457.83	4.41
NiP_2[71]	Cubic	Pa-3 (205)	a = 5.47	163.72	4.90
CuP_2[72]	Monoclinic	P21/c (14)	a = 5.80 b = 4.81 c = 7.53 β =112.70°	193.57	4.31
FeS_2[13]	Cubic	Pa-3 (205)	a = 5.42	159.04	5.01
CoS_2[73]	Cubic	Pa-3 (205)	a = 5.53	168.93	4.84
NiS_2[74]	Cubic	Pa-3 (205)	a = 5.69	183.96	4.44
CuS[75]	Hexagonal	P63/mmc	a = 3.79 c = 16.34	203.47	4.681

Table 1.6 Targeted M-P-S structural information. References are superscripted numbers.

Compound	Unit Cell	Space Group (number)	Lattice Parameters (Å)	Volume (Å^3)
$FePS_3$[76]	Monoclinic	C2/m (12)	a = 5.95 b = 10.30 c = 6.72 β =107.16°	393.43
$CoPS_3$[76]	Monoclinic	C2/m (12)	a = 5.90 b = 10.22 c = 6.66 β =107.17°	383.71
$NiPS_3$[77]	Monoclinic	C2/m (12)	a = 5.81 b = 10.07 c = 6.63 β =106.98°	371.23
Cu_3PS_4[78]	Orthorhombic	Pmn21 (31)	a = 7.28 b = 6.34 c = 6.08	280.43

The unit cell structures of the M-P and M-S products are shown in Figures 1.3 and 1.4 respectively. The bonding in the M-P targeted structures is complicated, and usually involves P-P bonding. FeP_2 has P_2^{4-} dumbbell anions, CoP_3 has P_4^{4-} rings, and NiP_2 (cubic) has infinite P^- chains.[41] CuP_2 has edge sharing puckered-like P_{10}^{5-} rings and Cu-Cu bonding.[79] The bonding in the M-S targeted structures is similar except for CuS. FeS_2, CoS_2, and NiS_2 all exhibit the pyrite structure which consists of fcc metal ions and S_2^{2-} anions.[80] CuS is hexagonal having tetrahedral Cu^{2+} cations and S_2^{2-} anions.

The unit cell structures of the M-P-S products are shown in Figure 1.5. Extended structures are shown as well to illustrate the layering of the MPS_3 materials and to show the differences between the MPS_3 and Cu_3PS_4 structures. As mentioned earlier, the MPS_3 structures contain two divalent metal cations and PS_4^{3-} anions. The Cu_3PS_4

contains three Cu^{+} cations and PS_4^{3-} anions The $FePS_3$ unit cell contains fewer atoms per cell than the $CoPS_3$ and $NiPS_3$.

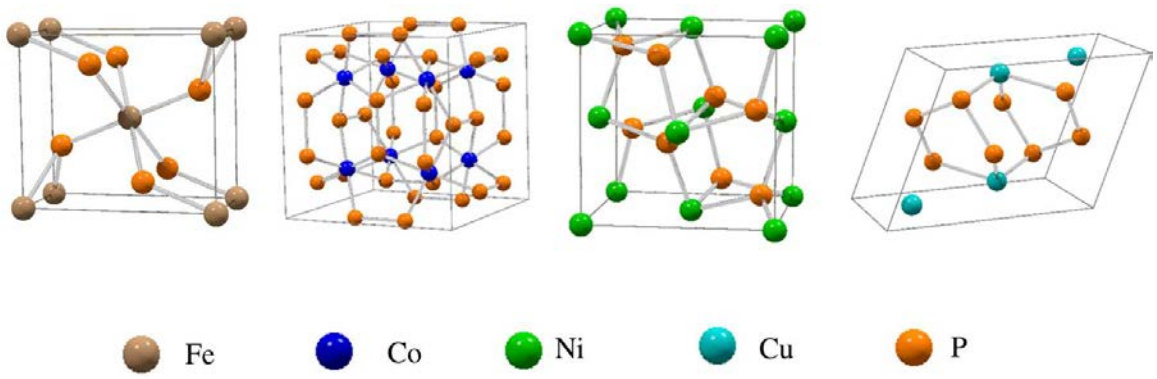

Figure 1.3 Unit cell structures for the targeted products FeP_2, CoP_3, NiP_2 and CuP_2.

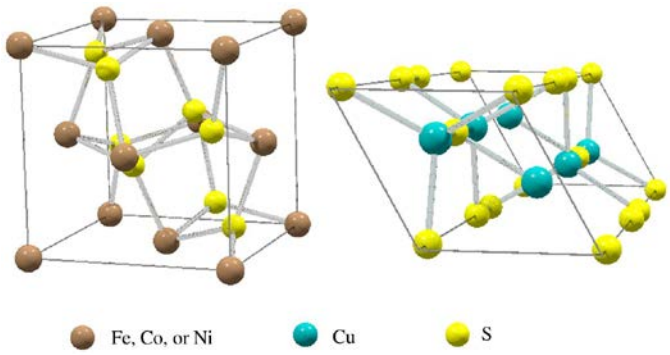

Figure 1.4 Unit cell structures for pyrites (FeS_2, CoS_2, NiS_2) and CuS.

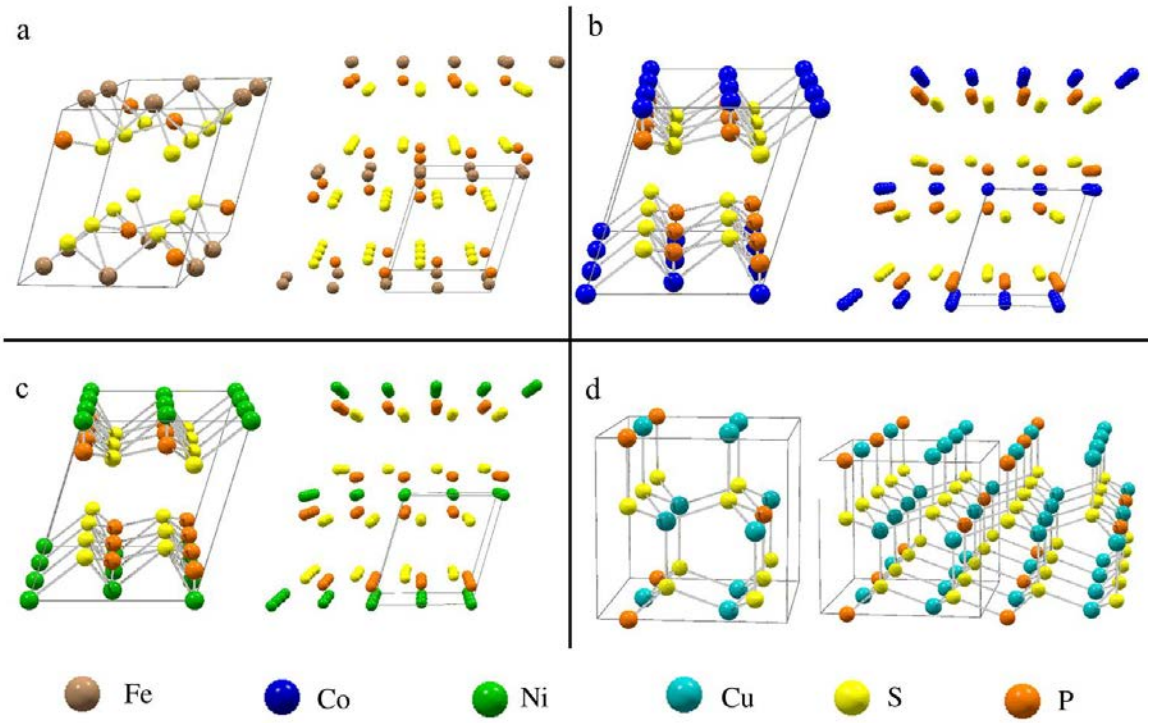

Figure 1.5 Unit cell and extended structures for the targeted products $FePS_3$ (a), $CoPS_3$ (b), $NiPS_3$ (c), Cu_3PS_4 (d). Each extended structure shows 4 unit cells.

1.3.2 Solid state metathesis reactions

Solid state metathesis reactions (SSM) reactions are exchange reactions between two or more reagents. The reactions have the general formula AX +RZ → AZ + RX. SSM reactions performed in this thesis involve reacting metal halides and sodium peroxide (Na_2O_2) to form metal oxides, or the metal halides with lithium nitride (Li_3N), phosphorous or sulfur to produce metal phosphide, sulfide or thiophosphates. The by-products are NaCl, and O_2, or LiCl, and N_2. All of the reagents must be handled in an air free environment. Na_2O_2 and Li_3N react exothermically with moisture. The metal halides will form hydrates in water, therefore changing the reactivity of the compound. The nature of the reactions is very violent, quick, and exothermic. They are triggered by

an energy source at a single point, such as a heated filament, or self-ignite upon grinding. Both triggers cause reactions to propagate, reacting with all reagents in close vicinity. Both types of reactions form very stable salts that are the driving forces of the reaction.[81]

Reactions done in this research were adaptations from work done by R. Kaner and I.P. Parkin. Kaner et al. produced refractory materials such as MoS_2, $MoSe_2$, WS_2, and WSe_2 from the metal halides and Na_2S through SSM techniques.[82] Kaner, Treece, et al. produced AlX, GaX, and InX materials, (X= As, Sb or P) using SSM based techniques.[83] Kaner et. al. also produced several metal borides,[84] nitrides,[85-87] and several oxides.[88,89] The starting reagents are crucial to desired product formation and reduced undesired byproducts such as reduced metals. The violent nature of the reactions gives off enough heat, reaching temperatures T > 1000 °C,[90] which melts some starting reagents and the byproduct salt for a very short period of time, followed by rapid cooling.

Parkin has synthesized several transition metal-main group compounds throughout his research. For example, Parkin et al. synthesized TiC, ZrC, V_8C_7, WC and Mo_2C from the transition metal halides and Al_4C_3 in sealed ampoules at the halide melting points or 450 °C.[91] A composite list of starting materials and respective products for these reactions have been investigated and reviewed in great detail.[81] Since the reactions are quite violent, the reaction vessel needs to be able to withstand the heat and gas expansion.

The SSM reactions in this thesis are a continuation from prior research done in our group.[1] Transition metal doped TiO_2, transition metal phosphides, sulfides, and thiophosphates were targeted. The starting materials are anhydrous metal chlorides $TiCl_3$, $CrCl_3$, $MnCl_2$, $FeCl_3$, $CoCl_2$, $NiCl_2$ and $CuCl_2$, and Na_2O_2 for the doped TiO_2 work. $TiCl_3$ is a dark purple solid that is moisture sensitive and melts/decomposes at 425 °C. $CrCl_3$ is a flaky purple solid that melts at 1152 °C. $MnCl_2$ is a light pink solid that melts at 654 °C. $FeCl_3$ is a shiny black solid that melts at 306 °C and sublimes. $CoCl_2$ is a blue powder when anhydrous and becomes purple when in contact with moisture. It

has a melting point of 735 °C. This compound is commonly used as moisture indicator in Drierite indicating desiccant. $NiCl_2$ is a yellow solid and has a melting point of 1001 °C. $CuCl_2$ is a brown solid and melts at 498 °C. Na_2O_2 is a yellow solid that melts/decomposes at 460 °C. It is used as the oxidant in the SSM reactions.

The starting materials for the M-P, M-S and M-P-S work are $FeCl_3$, $CoCl_2$, $NiCl_2$, $CuCl_2$, Li_3N, red phosphorus, sulfur, and P_2S_5. The M-P, M-S and M-P-S work uses similar starting reagents used in the TiO_2 work. The main differences are the use of red phosphorus, sulfur, P_2S_5, and Li_3N. Red phosphorus adopts a polymeric chain of phosphorus atoms. Red phosphorus is air stable at room temperature. It undergoes a phase change at 416 °C to air reactive white P_4 tetrahedra. Yellow sulfur has several allotropes but is commonly found as S_8 rings. It melts at 115 °C and become gaseous at 444 °C. P_2S_5 is a molecular combination of phosphorus and sulfur that is commonly a dimer, P_4S_{10}. The structure of P_4S_{10} (2-P_2S_5) consists of four fused PS_4 tetrahedra, having one P-S double bond for each tetrahedron. The compound is moisture sensitive and melts at 288 °C. Li_3N is a dark purple solid that melts at 813 °C. It is moisture sensitive and decomposes in water exothermically.

1.3.3 Ampoule reactions

Metal phosphide, sulfide and thiophosphate materials were targeted using sealed evacuated glass ampoules. We have synthesized transition metal phosphides via PCl_3 elimination in our group and the research done in this thesis continues and expands on these topics.[2] These reactions mimic the SSM reactions but differ from the lack of salt formation, therefore Li_3N is not used. The reactions are much slower, heated for several hours with a slow ramp rate in tube furnaces. The products are given enough time to form and crystallize. These reactions are adaptations from prior work on pressed pellets and now the incorporation of sulfur. The starting materials are anhydrous metal chlorides

$FeCl_3$, $CoCl_2$, $NiCl_2$ and $CuCl_2$, red phosphorus, sulfur, and P_2S_5. The properties of the reagents are described in section 1.3.2.

1.4 Background on Characterization Methods Used in the Chapters

1.4.1 Powder X-ray Diffraction (XRD)

X-Ray diffraction techniques are useful for identifying crystalline phases in materials. Powder XRD is used in this study to analyze a large range of randomly shaped crystallites. The diffraction technique utilizes and X-ray source (often copper or molybdenum Kα) and the ability of the X-rays to diffract off of planes of atoms within a crystal lattice. X-rays enter the sample at a certain angle and if the diffraction is constructive, the rays diffract towards the detector at the same angle. Constructive interference produces peaks in XRD pattern while destructive interference does not.

The peak profile and location can give information about the unit cell of the materials analyzed. XRD patterns are plotted 2θ vs intensity. The spacing between the layers can be calculated using the Bragg equation, $n\lambda = 2d\sin\theta$, where $\boldsymbol{\lambda}$ is the x-ray source wavelength, **d** is the spacing between the diffraction planes within the unit cell, and $\boldsymbol{\theta}$ is the angle of diffraction in radians. The general trend with peak position and unit cell size is that smaller unit cells have diffraction peaks at higher 2θ and vice versa. Peak shifting relative to the reference pattern gives information relating to the atoms in the respective planes. Peak shifting to lower diffraction angle indicates larger atoms in the layer and vice versa.

Peak shape gives information about the particle size and crystallinity of the particles. Highly crystalline materials have very intense, narrow, sharp peaks. Nanoscale materials have broad peaks. The average particle sizes can be calculated using the Debye-Scherrer equation $\tau = k\lambda/\beta\cos\theta$. The equation relates the peak broadening to the particle size. In the equation $\boldsymbol{\tau}$ is the average size of crystalline domains, **k** is the shape

factor (dimensionless), λ is the x-ray wavelength, β is the full width half max intensity and θ is the diffraction angle measured in radians.

XRD is useful in this thesis as an effective characterization technique for phase identification and changes from reaction conditions such as atom doping, acid washing, high temperature inert annealing and reagent choice. The process is non-destructive so the sample can be recovered if necessary.

1.4.2 Magnetic Susceptibility

Magnetic susceptibly measurements give information of the magnetic response with respect to an external magnetic field due to the spins of unpaired electrons in a sample. Commonly, magnetic measurements are made on temperature dependent systems. The Evans (Gouy) balance is used in this study is limited to room temperature measurements. Materials that repel the magnetic field (e.g. glass, plastics, and insulators) give diamagnetic signals and require correction once samples are measured. Materials that have a weak attraction to a magnetic field are considered paramagnetic. Ferromagnetic materials are strongly attracted to a magnetic field and need to be "diluted" with a diamagnetic matrix prior to analysis.

The samples are pre-ground powders and are measured in glass tubes. The Evans balance provides the volume and mass susceptibilities along with the magnetic moment. Diamagnetic correction of the elements and glass were taken into consideration. As a precaution, each sample was tested for any magnetic attraction using a neodymium magnet. Ferromagnetic materials may damage the sensitive instrument and were diluted with a diamagnetic solid matrix. NaCl works well since it is diamagnetic, easy to grind with the samples, and can be removed with water if sample recovery was needed. Correction for the mass addition of NaCl was needed to obtain an accurate magnetic susceptibility values.

1.4.3 Fourier Transform Infrared Spectroscopy (FT-IR)

FT-IR measurements analyze the vibration modes of IR active (requiring a dipole moment) bonds in a molecule once exposed to infrared light. The technique is commonly used in organic chemistry to analyze the functional groups within a compound. Materials are either pressed between NaCl salt plates or pressed into a pellet with an IR silent, or negligent, matrix such as KBr. Inorganic compounds are not as straightforward since the often contain metals which are much heavier than the main group elements. The vibrations are low energy showing large broad peaks at low wavenumbers. Depending on the material, FTIR instruments may require manipulation of the optics to measure lower wavenumber peaks.

1.4.4 Energy Dispersive Spectroscopy (EDS) and Scanning Electron Microscopy (SEM)

EDS utilizes X-rays from a sample that has been hit with a beam of electrons to give information on the weight and atomic percent values of the elements in a sample. When a sample is hit with an electron beam, some electrons are reflected back from the sample surface. These are called backscattered electrons. The electron beam also causes core electrons to eject from the sample. These are called secondary electrons. The ejected electrons are replaced with outer shell electrons within the sample, which releases energy in the form of X-rays. Every element has a characteristic X-ray emission which is useful for identifying individual elements by EDS. SEM utilizes ejected secondary electrons, or in the case of porous samples, backscattered electrons. EDS is often coupled with SEM since both techniques use an electron beam and require vacuum.

Samples are loaded onto conductive stubs, either carbon or aluminum typically, with a conductive connection such as carbon tape, carbon paste, or silver paste. The samples also need to be conductive for good imaging and appropriate X-ray signal otherwise they will undergo “charging”, having a build-up of electrons on the surface. If

samples are insulating, coating them with a thin layer conductive coating such as gold-palladium or carbon can be done. Carbon coating is advantageous for both imaging and EDS, since the metallic coating can interfere with EDS results. EDS has some limitations with detecting elements lighter than sodium unless specific windows are utilized in the instrument. Lithium and hydrogen are still not accurately detected by EDS, and some energy lines for elements can overlap.

1.4.5 Diffuse Reflectance Spectroscopy (DRS)

DRS utilizes diffuse reflected light to give information on what wavelengths of light are absorbed by a solid powdered sample. When light hits a sample, light is reflected in all directions. Some light is reflected back immediately, without entering the sample. This is called specular reflection and occurs on a perfectly reflective surface. Some light from the incident beam is absorbed by the sample as well. The complement wavelength of this light is responsible for the colors of materials that we see. There is also some light that enters the sample and undergoes a series of additional reflections and refractions due to the random crystallite grain sizes. Some of this light reflects back out of the sample. This reflected light wavelength is similar to the transmitted light from a sample but at a lower intensity than normal transmitted light. This is due to the “trapped light” being absorbed as it is reflected and refracted within a sample. This reflected light is called diffuse light. The diffuse light is collected by an integrating sphere detector apparatus to increase signal intensity and can give electronic information, such as the band gap, of a material. The band gap of a material is the difference in energy from the collection of molecular orbitals that make up the higher energy conduction band (CB) and the lower energy valence band (VB). The band gap energy is an important feature of semiconductors for use in catalysis.

We utilize DRS by attaching an integrating sphere accessory to our UV-Vis instrument. Solid samples are prepared by first grinding into a fine powder and then embedding the powders into opaque white filter paper. The paper is sandwiched between glass microscope slides to prevent loose solid from entering the DRS accessory. The slides are held up to the accessory at with a 8° wedge, and with a black opaque background to prevent light from escaping the sample. A reference white opaque material is set perpendicular to the sample as well with a 0° wedge. The data that we retrieve is absorbance data and the wavelengths that correspond to the diffuse reflectance give an onset decrease in absorbance (or rise in transmittance).

1.4.6 Residual Gas Analysis (RGA) Mass Spectrometry

The RGA system analyzes gases in a reaction container. The gases are sampled through a small capillary and partitioned off into sampling gas and waste gas. The sample gases are first ionized using a hot filament. The charged ions are then sent through a quadrupole mass spectrometer and the mass to charge ratios (M/Z) are analyzed. The system can also record relative gas pressure versus time for several gases within ~207 amu (or g/mol). The pressures of the gases can be recorded as low as 10^{-8} Torr on our system. We primarily use the RGA in this research for the detection of H_2 gas evolution.

1.5 Background Information on Catalytic Experiments

1.5.1 Organic dye degradation using UV and visible light

Dye degradation is important in the textile industry since several organic dyes are waste byproducts that are sometimes not removed appropriately or are costly to do so. Utilizing inexpensive simple heterogeneous catalysts can help prevent and remove un-managed waste and are of great interest in research. Common dyes that are commonly

used in research are shown in Table 1.5. The dyes are degraded through photo-oxidation or reduction. Solid catalysts are suspended in an aqueous solution of the dyes and then exposed to either UV or visible light. The optical absorbance of the solutions is monitored using a UV-vis spectrometer.

There are several factors that can affect the degradation of dyes in solution. The pH of the solution is one of them. The pH of dye solutions are usually kept at pH= 7 since the degradation process can be enhanced, or tarnished by changes in pH for different dyes. Several studies have shown the influence in pH using TiO_2 based catalysts with methylene blue and methyl orange dyes.[92-94] Photo-oxidation increases with pH > 7 for methylene blue, and pH < 7 for methyl orange. Methylene blue is not stable at pH >10.[92] Also, several dyes such as methyl orange are pH indicator dyes and change color thus changing the λ_{max}.

Table 1.7 Common dyes used in photocatalysis research with respective physical properties. (*) Denotes color from fluorescence. Cited references are superscript numbers.

Organic Dye Molecule	**Chemical Formula**	**Molar Mass (g/mol)**	**Color in Water (pH =7)**	**Wavelength Observed (λ_{max} nm)**
Methylene Blue[95]	$C_{16}H_{18}N_3SCl$	319.68	Blue	660
Methyl Orange[96]	$C_{14}H_{14}N_3NaO_3S$	327.20	Orange	462
Phenol Red[97]	$C_{19}H_{14}O_5S$	354.26	Red-Orange	431
Rhodamine B[98]	$C_{28}H_{31}ClN_2O_3$	478.73	Pink (Orange*)	553
Orange G[95]	$C_{16}H_{10}N_2Na_2O_7S_2$	458.28	Orange	495
Congo Red[95]	$C_{32}H_{22}N_6Na_2O_6S_2$	696.44	Red	510
Alizarin Red S[95,99]	$C_{14}H_7NaO_7S$	342.13	Red	520

The dyes can degrade several ways in solution. The degradation mechanisms are often complex and can vary from the use of different catalysts. Full oxidation of the products is ideal and would consist of small molecules. Monitoring of the decomposition products is not commonly done, however the change in color is. Methylene blue and methyl orange both decolor upon degradation. The structures of methylene blue and methyl orange are shown in Figure 1.6. The de-colorization is most likely due from breaking of the azo group (R-N=N-R′), since the delocalization of electrons is responsible for the vivid coloration of the molecule. Breaking the 6-membered rings in the structures can also cause a loss of color.

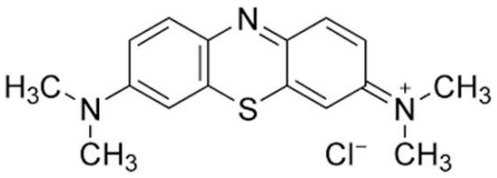

Methylene Blue

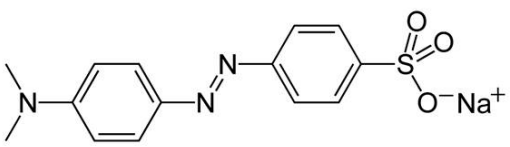

Methyl Orange

Figure 1.6 Molecular structures of methylene blue and methyl orange organic dyes

In our work we utilize TiO_2 based catalysts to degrade methylene blue and methyl orange dyes under UV or visible light and monitor the λ_{max} of the dyes over time relative to a blank dye solution. The light source is a medium pressure mercury vapor lamp. Visible light experiments utilized filtered UV light from colored glass band pass filters which prevent wavelengths less than 420 nm from passing through. For consistency across several different catalysts, we did not analyze multiple pH values in this study.

1.5.2 H_2 Generation from Water Using Light and Electrochemical Methods

Hydrogen generation from water involves performing the reverse of the reaction $H_2 + ½\ O_2 \rightarrow H_2O$ (g) (ΔH_{rxn} = -237 kJ/mol). In 1972, the groundbreaking research from Fujishima and Honda using electro-photochemical methods to split H_2O back into H_2 and O_2 using TiO_2 has led to numerous research pathways.[100] Many researchers have found methods to improve the process utilizing UV and more interestingly, visible light. The overall goal is to utilize H_2 as a potential fuel source. There are obvious dangers with hydrogen gas as a fuel, however finding safe suitable methods to store and controllably release would be ideal and is the next step in current research.

According to several accounts in literature, semiconductor materials must have specific band gap energies in order to split water into H_2 and O_2 and this leads to a large

volume of candidate materials that qualify.[101-103] Essentially, the band gap energy of the semiconductor must contain the redox potential energy difference between the two half reactions of water. The two half reactions and their corresponding redox potentials (at pH = 0) are shown in Equations 1.1 and 1.2.

$$2\ H_2O \rightarrow O_2 + 4\ H^+ + 4\ e^- \qquad \Delta E° = 0.82\ V \qquad (1.1)$$

$$2\ H^+ + 2\ e^- \rightarrow H_2 \qquad \Delta E° = -0.41\ V \qquad (1.2)$$

The difference in redox potential is 1.23 V therefore the band gap energy of material would have to encompass this energy. TiO_2 is among several candidates for this, but it lacks majority of the drawbacks. For example, CdS has a band gap of 2.5 eV and has been used extensively in photocatalysis. The major issue of CdS is photo-corrosion, leaving Cd^{2+} and solid sulfur in solution. Cadmium ions are very toxic to aquatic life. Efforts have been made to help prevent this kind of corrosion.[104]

When light hits a semiconductor surface and is of sufficient energy, it causes electrons in the valence band to become excited, crossing the band gap to the conduction band. When this happens, positively charged holes remain in the valence band. The excited electrons can undergo reduction of water to form H_2 while the holes can undergo oxidation of water to produce O_2. The electron and hole separation is not energetically favorable, and very quick recombination of the two occurs. To help suppress this recombination, the use of electron rich donating molecules, or “hole” scavengers, can be used. Common molecules used are alcohols and amines. Conversely, electron scavengers can be used to supply positively charged holes for O_2 production reactions. A proposed mechanism for water reduction using methanol are shown in Equations 1.3-1.7.[105]

$$TiO_2 + h\nu \rightarrow h^+ + e^- \quad (1.3)$$

$$CH_3OH + H_2O + 6\,\mathbf{h}^+ \rightarrow CO_2 + 6\,H^+ \quad (1.4)$$

$$H_2O \rightarrow H^+ + OH^- \quad (1.5)$$

$$H_2O + \mathbf{h}^+ \rightarrow H^+ + OH^\bullet \quad (1.6)$$

$$2H^+ + 2e\text{-} \rightarrow H_2 \quad (1.7)$$

When UV light hits TiO_2, holes ($\mathbf{h}^+$, VB) and electrons (e^-, CB) are produced. The methanol reacts with water and the photogenerated holes to give H^+. Water also goes through dissociation to generate H^+ and it can react with the holes to produce more H^+. The H^+ can react with donated electrons to yield H_2. Technically, the hydroxyl radical that is also produced in Equation 1.6 could react with the holes to form O_2 and the produced H^+ and electrons could react with O_2 to reform water, however the methanol reaction consumes the necessary H^+ for this reverse reaction, thus the reaction is not likely to occur.[105]

TiO_2 suffers from its large band gap of 3.3 eV for anatase or 3.0 eV for rutile. To aid with the band gap issue, several modifications can be made to help shorten the path of electrons from the valence band to the conduction band. Adding a semiconductor to the surface of TiO_2 that has a smaller band gap than TiO_2 can provide an easier stair step for electrons to move to the conduction band. Another method is to add metals such as Pt, Ag, or Pd to the surface of TiO_2. These metals act as electron siphons to draw out reactive conduction band electrons. Often combinations of surface shuttling of electrons and sacrificial reagents are used in tandem to enhance the proficiency of water splitting reactions.

In our work, we examine our TiO_2 based catalysts with UV light to photoreduce water in the presence of sacrificial hole scavengers. The gas produced is monitored by an RGA system and the relative amounts of H_2 gas pressure are recorded. The H_2 pressure

can be compared to the background argon gas and the relative amounts of moles of gas can be found utilizing the ideal gas law.

1.6 Thesis Chapters Overview

The materials synthesized in the proceeding chapters demonstrate solid state methods to produce metal oxide, phosphide, sulfide and thiophosphate materials. Rapid synthesis of TiO_2 is the focal point in Chapter 2, and doping its rutile structure with other transition metals was done. The goal of doping was to harness the visible light photocatalytic capabilities of TiO_2. The materials were characterized and tested for their catalytic activity towards dye degradation and water reduction. Transition metal phosphide, sulfide, and thiophosphate materials synthesis are the focal points for Chapters 3 and 4. The materials were synthesized by two different methods (solid state metathesis and sealed ampoule) and characterized. Assisted growth synthesis of the transition metal phosphides and thiophosphate materials using fluxes and deposition techniques will be discussed in Chapter 5. The last chapter, Chapter 6, will provide an overall summary of the research done along with future research topics of interest.

CHAPTER 2

SYNTHESIS OF TRANSITION METAL DOPED TiO_2 VIA SOLID-STATE METATHESIS REACTIONS

2.1 Introduction and Background

Titanium dioxide (TiO_2) is an extremely useful material that is used in everyday consumer products, primarily as a white, inert pigment. Some common products include paints, dyes, opacifiers, and cosmetics. TiO_2 is inert to most corrosive environments and is often used as a protective corrosion resistant thin coating. It dissolves in hydrofluoric acid (HF) or hot concentrated sulfuric acid (H_2SO_4) under rapid mixing for several hours.

In the materials community, TiO_2 is mainly known as an effective UV photocatalyst for the photo-oxidation of organic pollutants and photovoltaic absorber for solar cells. TiO_2 exists in nature mainly in composite minerals or as rutile. There are other phases of TiO_2 that are not as thermodynamically favorable as rutile. These are anatase and brookite and some high pressure and temperature phases. The unit cell structures of the different phases of TiO_2 are shown in Figure 2.1. Rutile and anatase have the tetragonal unit cell while brookite has an orthorhombic unit cell. The lattice parameters for anatase are a= b= 3.785 Å, c= 9.514 Å, rutile a= b=4.593 Å, c= 2.959 Å[106,107] and brookite a= 9.184 Å, b=5.447Å, c=5.145 Å[108,109] respectively. Brookite is rarely observed in TiO_2 synthesis.

Under ambient pressure anatase converts to rutile at $T \geq 600°C$.[110] The anatase phase is more photocatalytically active of the three phases. As a reference material, Degussa P25 TiO_2, a mixture of anatase and rutile (~4:1) shows an even better

photocatalytic response than pure anatase alone. P25 TiO_2 has a surface area of ~ 40-50 m^2/g, but can be increased from added supports, or deposition.[111,112] It is one of the leading materials in UV photocatlysis.[113] Reasons behind this enhanced activity have been investigated. The leading explanation is the mixture of particle sizes and surface morphology which may lead to the synergistic effects between mixtures of anatase and rutile phases.[114] P25 TiO_2 works well in UV light situations, yet suffers under visible light conditions due to the lack of energy required to promote electrons to higher energy conduction band orbitals for photoreduction, leaving holes in the valence band for oxidation.

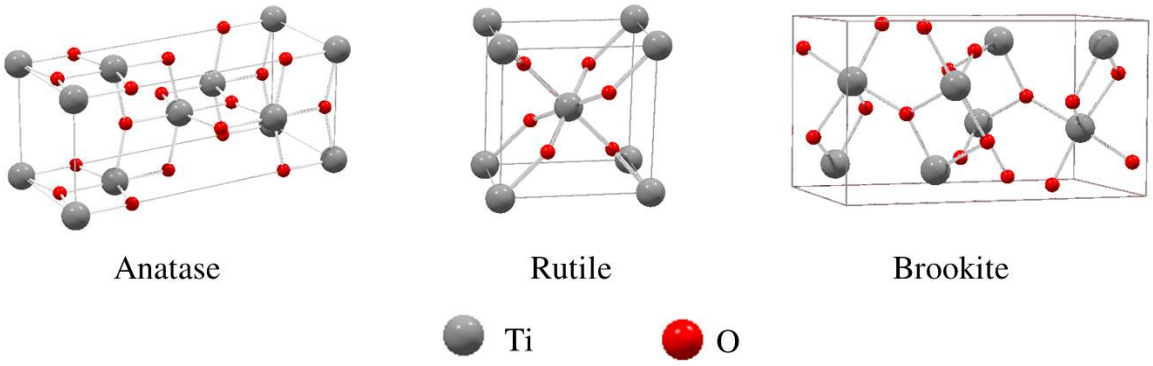

Figure 2.1 Unit cell structures of the three phases of TiO_2.

There is a large volume of research devoted to improving the photocatalytic ability of TiO_2, through modification of its light absorption, making it more feasible to lower energy (visible light) requirements. Approaches include altering the surface of TiO_2 to help facilitate electron flow to the conduction band using precious metals such as silver,[115] platinum,[116,117] gold,[118] and palladium,[119] exotic structural synthesis to expose

active atom planes,[120,121] and co-doping of smaller band gap semiconductors.[122,123] The available literature on doping TiO_2 with either metals or non-metal materials is extensive.[30,124,125]

There are a variety of means for altering the reaction media to aid with TiO_2 catalysis. These techniques are used either alone or in conjunction with catalyst modification. The use of a sacrificial hole scavenger is advantageous in photoreduction reactions and often involve using electron donors such as methanol, ethanol[126] or triethanolamine.

Synthesis of transition metal catalyst materials is done by solution precipitation or solid state reactions. One type of solid state synthesis method adopts the use of rapid exchange based reactions. These are solid state metathesis reactions (SSM) and are effective ways to rapidly produce highly crystalline materials in the solid state. Much SSM work has been done with the transition metals and reactions with main group elements. Early SSM work has shown that $MoCl_5$ and WCl_6 can be reacted with Na_2S to produce layered MoS_2 and WS_2 materials very quickly.[82] Both reactions are highly exothermic and produce crystalline materials. Semiconducting materials such as GaP and GaAs have also been synthesized using SSM techniques by reacting GaI_3 with either Na_3P or Na_3As.[127]

Rapid and exothermic self-propagating SSM methods for the synthesis of inorganic oxide and non-oxide materials have broad flexibility to produce a wide variety of binary solids and more complex structures containing intimately mixed multiple metal and non-metal components. Prior studies have produced solid-solutions such as $Ga_{1-x}Al_xAs$ and $MoS_{1-x}Se_x$ or mixed metal structures such as $LnFeO_3$ and $LnCrO_3$ synthesized

from lanthanide chlorides, $FeCl_3$, $CrCl_3$ and Li_2O.[128] $SrFe_{12}O_{19}$ was synthesized from a self-propagating high temperature reaction between SrO_2, Fe, and Fe_2O_3.[129]

These self-propagating solid state reactions may be initiated by a hot filament or heated in a furnace. Several literary accounts on SSM reactions point out that some of the main advantages of SSM reactions are the quick reaction speed of crystalline materials, the lack of organic solvents needed for synthesis, and moderate control over the wide variety of products that can form depending on the choice of starting materials.[81,90] The byproducts are generally alkali halide salts that can be removed easily with alcohol solvents or water. These reactions propagate rapidly from a heat source and are driven thermodynamically to form products, often in high yield. Doping of these materials can also be proposed using similar metathesis methods and were investigated in this study.

In our previous work, we synthesized rutile phase TiO_2 via a solvothermal route using $TiBr_4$ and Na_2O_2 to obtain anatase TiO_2 nanoparticles with a yields as high as 60%. We have also synthesized TiO_2 by the rapid, exothermically driven, solid state metathesis (SSM) method using $TiCl_3$ and Na_2O_2 to obtain rutile phase TiO_2 (Equation 2.1).[1]

$$TiCl_3 + 1.5\ Na_2O_2 \rightarrow TiO_2 + 3\ NaCl + 0.5\ O_2 \qquad (2.1)$$

Very crystalline materials are synthesized in seconds using this simple and direct exothermic exchange reaction with yields in the 50-60% range. In the current study, we examine more complex variations of this rapid and highly exothermic SSM titania formation reaction to incorporate transition-metal dopants into the TiO_2 structure.

The characterization of doped titania products and their utility in methylene blue and methyl orange dye oxidation photocatalysis and H_2 evolution reactions will be described.

In the current study, we take advantage of the rapid and non-equilibrium exothermic processes of SSM reactions to incorporate moderate amounts (~1-10 atomic %) of a second transition-metal dopant into the rutile TiO_2 structure (generically referred to as M-TiO_2 products). Typically such doping processes use sol-gel or solution precipitation methods followed by thermal processing, which leads to low, thermodynamically formed, metal dopant levels (~1-3 atomic %) in titania.[130] Given the rapid heating/crystallization afforded by SSM reactions, there is potential for kinetically stabilized higher dopant level incorporation, thus we chose to typically "overload" the reaction system with 10% dopant metal. Such additions, should impart visible optical absorption properties to the UV absorbing titania structure, which may enhance its visible light photoreactivity.

2.2 Experimental Section

2.2.1 Starting Materials

All starting materials were used as received: $TiCl_3$ (Aldrich, 99%), $CrCl_3$ (Alfa Aesar, 98%), $MnCl_2$ (Specialty Inorganics, 99.5%), $FeCl_3$ (Alfa Aesar, 98%), $CoCl_2$ (Alfa Aesar, 99.7%), $NiCl_2$ (Alfa Aesar, 99%), $CuCl_2$ (Alfa Aesar, 98%), Na_2O_2 (Sigma Aldrich, 97%), and $H_2PtCl_6 \cdot 6H_2O$ (Strem Chemicals, 99.9%). Distilled deionized water (18 MΩ) and 1 M HCl (Fisher Scientific, diluted) was used for wash processes. Degussa P25 TiO_2 and methylene blue (high purity, Alfa Aesar) or methyl orange (85% dye content, Sigma Aldrich) dyes were used in photocatalysis studies.

2.2.2 Synthesis of Transition Metal Doped Titania

Transition metal doped TiO_2 (M-TiO_2) was synthesized using a modified steel reactor used in our previous work.[1] All solid manipulations were done in a Vacuum Atmospheres argon filled glove box. Typically, 2.00 g of $TiCl_3$ (0.013 mol), 1.65 g (0.0211 mol) Na_2O_2, and ~10 mol % of the dopant metal halides [$CrCl_3$ (0.228g, 0.00144 mol), $MnCl_2$ (0.182 g, 0.00145 mol), $FeCl_3$ (0.236 g, 0.00145 mol), $CoCl_2$ (0.188 g, 0.00145 mol), $NiCl_2$ (0.184 g, 0.00142 mol), or $CuCl_2$ (0.193 g, 0.00144 mol)] were ground together for several minutes using an agate mortar and pestle. The Na_2O_2 is shipped in pellet form and was pre-ground to a fine powder prior to adding to the reagents.

The ground powders were then loaded into a metal crucible and placed into the stainless steel reactor. The reactor was sealed, removed from the box, and then heated resistively through a 0.64 mm nichrome wire using a Variac transformer at ~10-12 % output voltage in the fume hood. The reactor setup is shown in Figure 2.2. The reactions were very violent upon initiation by the nichrome wire. Each reaction gave off varied amounts of gas. Initial experiments used a ceramic Coors crucible insert. The insert often shattered due to the rapid evolution of heat and gas pressure of the reaction. More durable crucible materials were examined, which included alumina, quartz, nickel, and finally stainless steel. The insulating properties of both the ceramic materials and quartz allow for better heat detainment, thus allowing for a more complete reaction. However, the alumina crucible also shattered, and quartz chipped after each experiment. The nickel and stainless steel crucibles lost more heat than the ceramic materials, yet reactions are

successful. Over time, the nickel crucible began to corrode from exposure to very hot materials and was replaced with the stainless steel crucible.

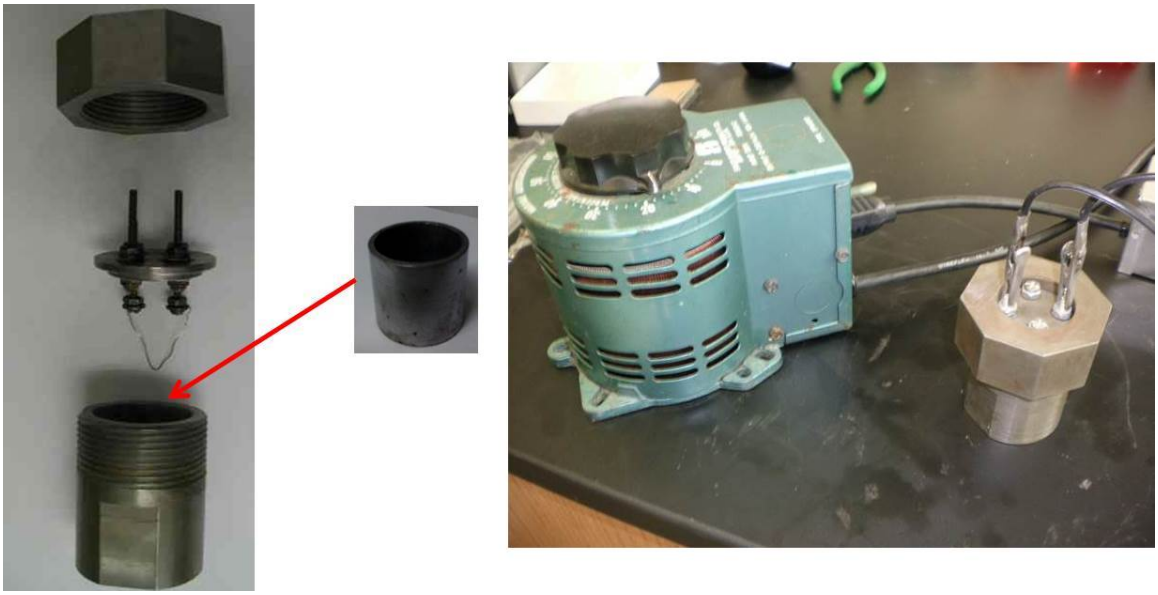

Figure 2.2 SSM reactor layout and ignition assembly using a Variac

The crude SSM products were washed with 1M HCl for 30 minutes at room temperature. This was done to remove soluble impurities, salt, and unreacted starting material. A good indication that a reaction had sodium peroxide remaining was vigorous bubbling upon water or acid addition. It should be noted that most materials yielded an orange-brown supernatant after washing in 1M HCl. The solid materials were separated from the aqueous layer via centrifugation. The samples were rinsed several times in deionized water until the pH of the supernatant became neutral. Samples were air dried at room temperature and stored in glass vials.

2.2.3 Sample Characterization

Phase identification was conducted using a Siemens D-5000 or a Bruker D-8 DaVinci powder X-ray diffraction (XRD) system that analyzed ground powders affixed to glass slides either by vacuum grease or acetone drying. Morphologies and semiquantitative elemental analysis was obtained by scanning electron microscopy (SEM) and energy dispersive spectroscopy (EDS) using a Hitachi S-4800 or S-3400 system. The samples were prepared by first grinding each sample in an agate mortar and pestle for uniform mixing. Next, thin pressed pellets were made using an IR die set in which were pressed gently onto carbon tape on aluminum stubs. The samples were carbon coated due to charging effects. Quantitative analysis by ICP-OE spectrometry (Varian 720-ES) was performed on acid dissolved samples. Approximately 5 mg of each sample was dissolved in an acid mixture of 5 ml of concentrated H_2SO_4 and 1 ml of concentrated HNO_3, which was heated to 385 °C for 1 hour. The cooled solutions were diluted with 5% HNO_3 to the 1 to 100 ppm range depending on the metal concentration. Calibration standard curves were used to determine weight percent content for dopant metals and titanium.

Magnetic susceptibility measurements were performed on solid powders at room temperature using a Johnson-Matthey MSB (Evans) magnetic susceptibility balance. Strongly magnetic samples were diluted in NaCl prior to analysis. Glass tubes were filled with ~15 mm of sample that was packed down to eliminate uneven layering of the sample. Diamagnetic correction of the glass and of the elements was performed. Solid diffuse reflectance UV-vis measurements (DRS) were made with a LabSphere RSA accessory on an HP 8453 UV- vis spectrometer. The powders were physically embedded

onto filter paper supports sandwiched between glass microscope slides and clamped to the reflectance accessory on the UV-Vis instrument with an opaque black backing to prevent light from passing through the sample. Each sample's raw diffuse reflectance (absorbance) data was converted to Kubelka-Munk units and used to estimate absorption energy onsets or band gaps. Typically reported onset data is derived from extrapolation of linear region of absorption rise down to baseline spectral region. Single baselines were used except for the Co- and Mn-TiO_2 data where different baselines better represented onset starting points of different regions. FT-IR spectra were obtained for each sample using KBr pellets in a Nicolet Nexus 760 spectrometer.

Unique to this chapter, X-ray photoelectron spectroscopy (XPS) data were obtained on a Kratos Axis Ultra Imaging spectrometer. XPS provides information on the surface environment and electronic states of the samples. Powders were embedded in indium foil for analysis. Survey spectra were obtained for acid washed samples (nominally 10% M doped TiO_2 samples) and regional area spectra were obtained for Ti2p, O1s, as well as M2p (M = Fe, Mn, Co, Ni, Cu). Data were recorded with a tilt angle of 45° using monochromatic Al K_α radiation. Peak positions are reported relative to the organic C1s peak at 284.5 eV. Semi-quantitative surface compositions and peak deconvolutions were performed using CasaXPS software package (www.casaxps.com) and a Kratos-specific RSF element library. Relative atomic surface compositions were measured from survey scans.

2.2.4 Photo-degradation of Organic Dyes and Water Reduction

Photocatalytic oxidative degradation of methylene blue (MB) and methyl orange (MO) in air was performed using an Ace-Hanovia medium pressure 450 W mercury lamp in a water cooled Pyrex jacket. Approximately 10 mg of the transition metal doped TiO_2 samples were loaded into 20 ml glass vials (pre-washed and dried) with 10 mL of a 3.00 $x10^{-5}$ M MB solution or $6.11x10^{-5}$ M MO solution and a mini stir bar. Visible light experiments were done using three cutoff filters which were placed in a cardboard box frame in that encased the samples.

Water reduction was attempted using an Ace-Hanovia medium pressure 450 W mercury lamp in a water cooled Pyrex jacket as the UV light source. The samples were loaded with ~1% Pt which was photoreduced on the surface. Approximately 10 mg of the Pt coated transition metal doped TiO_2 was added to a 50 mL Schlenck flask with 10 mL of a 50/50 Water/Methanol solution and a stir bar. The flask was purged under argon flow for several minutes. A capillary was attached to the flask and connected to a Stanford Research Systems QMS 300 Series Residual Gas Analyzer (RGA). Under a slow stream of argon, the flask was irradiated with UV light under constant stirring. Atmospheric and H_2 gases were monitored in pressure vs time mode.

2.3 Results and Discussion

The ideal SSM reactions used MCl_2 (Mn, Co, Ni, Cu,) and MCl_3 (Cr, Fe) for doping and are shown in Equations 2.2 and 2.3. In all cases, the SSM reactions were easily initiated in a self-propagating mode using a heated nichrome filament.

$$0.9\ TiCl_3 + 0.1\ MCl_2 + 1.45\ Na_2O_2 \rightarrow M_{0.1}Ti_{0.9}O_2 + 0.45\ O_2 + 2.9\ NaCl \qquad (2.2)$$

$$0.9\ TiCl_3 + 0.1\ MCl_3 + 1.5\ Na_2O_2 \rightarrow M_{0.1}Ti_{0.9}O_2 + 0.5\ O_2 + 3\ NaCl \quad (2.3)$$

The doped titania products after water and acid workup were visibly colored, with colors generally consistent with the dopant metal in an oxide environment. Images of the colored samples are shown in Figure 2.3. An undoped sample was synthesized in the same manner as the doped samples following Equation 2.1. The undoped sample is also shown and Degussa P25 TiO_2 is shown as a reference color for TiO_2.

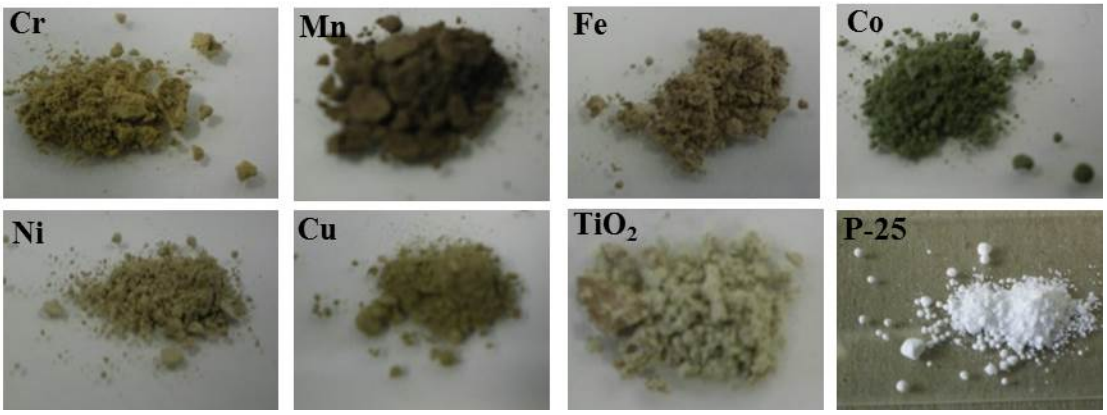

Figure 2.3 Images of acid washed M-TiO_2 samples. The undoped sample is denoted as "TiO_2" and P25 TiO_2 is shown for color comparison of pure TiO_2.

Initial SSM experiments used water to wash the products free of the NaCl byproduct and unreacted starting material, however isolated yields were sometimes over 100% based on pure TiO_2 and XRD data showed the presence of Na-Ti-O phases (e.g., $Na_2Ti_6O_{13}$), consistent with results observed in our earlier SSM TiO_2 work.[1] Acid washing of crude samples was done for ~30 minutes at room temperature to remove $NaTi_xO_y$ impurities. The acid wash solutions, regardless of metal dopant become orange

colored, reminiscent of the colors observed for Ti^{4+} ions in solution bound to peroxo ligands observed in our prior solvothermal $TiBr_4/Na_2O_2$ studies.[131] The percent isolated yields for the acid washed materials (assuming $M_{0.1}Ti_{0.9}O_2$ compositions) were generally in the ~60 - 80% range and are shown in Table 2.1 along with sample colors. The lower yields after acid washing reflect removal of the sodium titanate phases and possibly some dopant leaching.

Table 2.1 SSM synthesized transition metal doped TiO_2 colors and yields

Sample Type (M-TiO_2)	**Product color, percent yield**
Cr-TiO_2	yellow, 71%
Mn-TiO_2	brown, 86%
Fe-TiO_2	light brown, 73%
Co-TiO_2	green, 68%
Ni-TiO_2	grey, 67%
Cu-TiO_2	light brown, 58%

2.3.1 Powder XRD Analysis of Acid Washed and Acid Washed and Annealed M-TiO_2 Samples

The acid washed and acid washed annealed samples were analyzed for crystalline phases using powder XRD. The patterns for the acid washed and acid washed annealed non-doped TiO_2 sample are shown in Figure 2.4. The acid washed sample showed two phases. The most intense phase was tetragonal rutile TiO_2 (PDF #00-021-1276). Very small peaks for a sodium titanate phase were also seen. This phase was $Na_2Ti_6O_{13}$ (PDF

#00-077-9461). There is an unidentified peak at 12°. To improve the crystallinity and to determine if any additional phases could be seen, the sample was annealed in air to 1000 °C and held for several hours and then allowed to cool to room temperature naturally. XRD of the annealed sample showed a greatly pronounced rutile TiO_2 and the only impurity phase was $Na_2Ti_6O_{13}$.

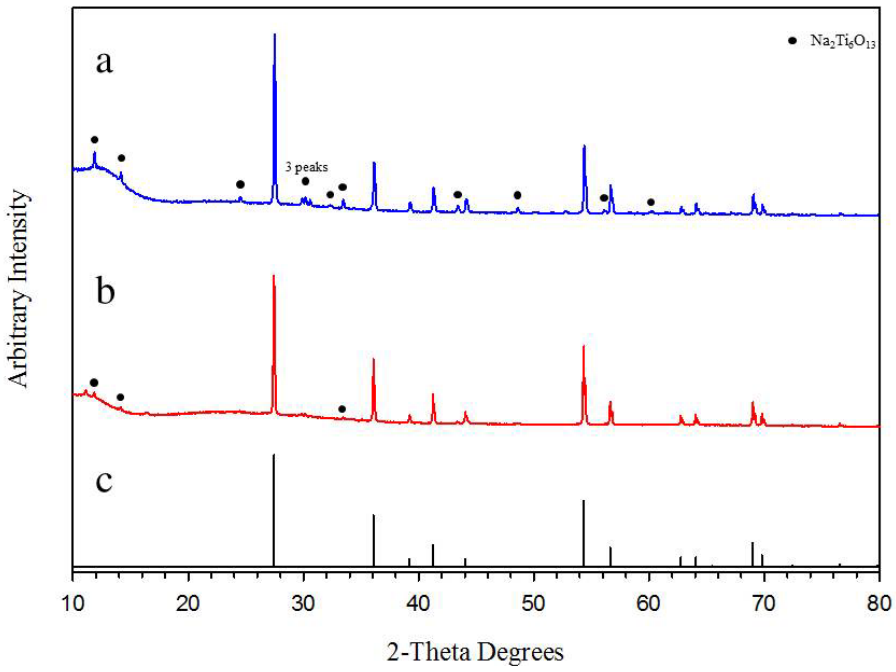

Figure 2.4 Powder X-Ray diffraction patterns of the acid washed annealed SSM undoped TiO_2 sample (a), the undoped TiO_2 acid washed sample (b), and the rutile reference pattern (c).

The patterns for the acid washed M-TiO_2 samples are shown in Figures 2.5 and 2.6. The patterns of the M-TiO_2 acid washed annealed samples are shown in Figures 2.7 and 2.8. The acid washed Cr-TiO_2 sample (Figure 2.5 a) showed clear crystalline peaks for rutile phase TiO_2 (PDF #00-021-1276 along with small peaks for $Na_2Ti_6O_{13}$ (PDF #00-037-0951). There are several small unidentified peaks in the 15-45° range that may

be are another Na_xTiO_y phase. The sample was annealed in air to 1000 °C. XRD of this sample (Figure 2.7 a) showed more pronounced rutile TiO_2 peaks. There are very small crystalline peaks for the phase $Na_2Cr_2Ti_6O_{16}$ (PDF# 00-052-1309) and for the phase $Na_2Ti_9O_{19}$ (PDF# 04-009-6404). An unidentified shoulder peak is present at 28°.

The acid washed Mn-TiO_2 sample (Figure 2.5 b) showed crystalline peaks for rutile phase TiO_2 (PDF #00-021-1276). There are very small crystalline peaks for the phase $Na_2Mn_2Ti_6O_{16}$ (PDF #00-052-1308) (not shown). Small unidentified peaks are present at 19° and 33°. The acid washed sample was annealed in air to 1000 °C directly for 24 hours. XRD was done on the acid washed annealed sample (Figure 2.7 b) and showed sharper rutile TiO_2 (PDF #00-021-1276). There were small peaks for $Na_2Mn_2Ti_6O_{16}$ (PDF #00-052-1308) and Mn_3O_4 (PDF #04-015-2577). There are a few very small unidentified peaks in the ~35- 55° region.

The acid washed Fe-TiO_2 sample (Figure 2.5 c) showed crystalline peaks for rutile phase TiO_2 (PDF # 00-021-1276) There are also very small peaks which could indicate a sodium titanate phase $Na_{0.23}TiO_2$ (PDF #00-022-1404). The annealed acid washed Fe-TiO_2 sample was heated in air at 1000 °C for 24 hours. The XRD pattern of this material (Figure 2.7 c) showed crystalline rutile phase TiO_2 (PDF #00-021-1276), along with the phases $Na_2Ti_9O_{19}$ (PDF # 04-009-6404) and $Na_2Fe_2Ti_6O_{16}$ (PDF #00-052-1307). The rutile peaks are more intense and narrow due to the annealing process. The two sodium phases indicate that there was some sodium impurities in the acid washed material that was either very poorly crystalline or amorphous. Neither of these phases was identified in the acid washed XRD pattern.

The acid washed Co-TiO_2 sample (Figure 2.6 a) showed crystalline peaks for rutile phase TiO_2 (PDF #00-21-1276). There are also crystalline peaks for the phase $CoTiO_3$ (PDF #00-015-0866) and unidentified peaks at 15°and 49°. The sample was annealed in air at 1000 °C for 24hrs. XRD was done on the sample (Figure 2.8 a) and showed rutile TiO_2 with much more pronounced peaks, and $NaTi_{3.5}Co_{0.5}O_8$ (PDF #04-008-9091). This phase has much more intense peaks than TiO_2.

The acid washed Ni-TiO_2 sample (Figure 2.6 b) showed crystalline peaks for the rutile TiO_2 (PDF #00-021-1276). There are crystalline peaks for the phase NiO (PDF #00-047-1049). The sample was annealed in air at 1000 °C for 24 hours. XRD of the acid washed annealed sample was done (Figure 2.8 b) and showed more pronounced rutile TiO_2 and NiO peaks, along with peaks for $Na_{0.23}TiO_2$ (PDF #00-022-1404). There are also peaks for the phase $NiTiO_3$ (PDF #04-012-0745). Rutile TiO_2 has the most intense peaks, and then the sodium titanium oxide and nickel titanate phases have similar intensities at a 1:3 peak ratio with TiO_2.

The acid washed Cu-TiO_2 sample (Figure 2.6 c) showed crystalline peaks for the rutile TiO_2 phase (PDF #00-021-1276) and an unidentified peak at 15°. There are several small peaks which agree with the pattern $Na_2Ti_6O_{13}$ (PDF #00-037-0951), however most are broad and very close to baseline noise. The sample was annealed in air to 1000 °C for 24 hours. XRD was done on the annealed sample (Figure 2.8 c) and showed very intense, much more pronounced rutile TiO_2 peaks. There are two Na-Cu-Ti-O related phases that are present. These are $Na_{0.86}Cu_{0.43}Ti_{3.57}O_8$ (PDF #00-053-0081) and $NaCu_{2.5}Ti_{4.5}O_{12}$ (PDF # 04-013-1447). The intensity of the $Na_{0.86}Cu_{0.43}Ti_{3.57}O_8$ phase is

much lower than rutile TiO_2. The $NaCu_{2.5}Ti_{4.5}O_{12}$ phase is much lower in intensity to either phase and is close to baseline noise.

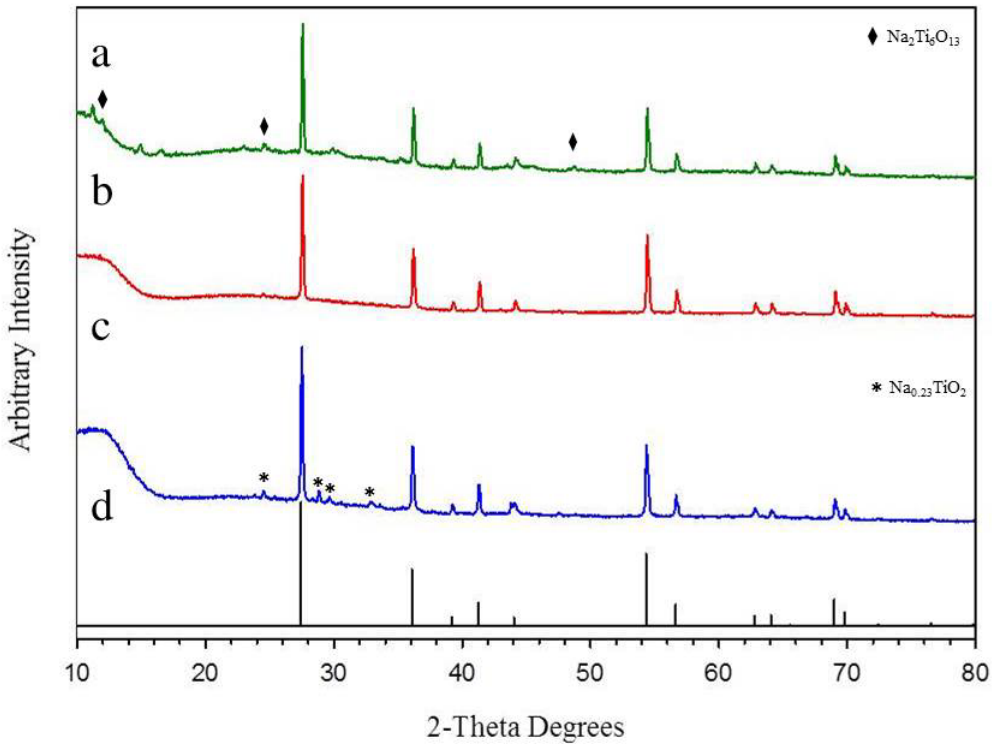

Figure 2.5 Powder X-ray diffraction patterns of the acid washed M-TiO_2 samples are shown with a = Cr-TiO_2, b = Mn-TiO_2, c = Fe-TiO_2, d = reference rutile TiO_2.

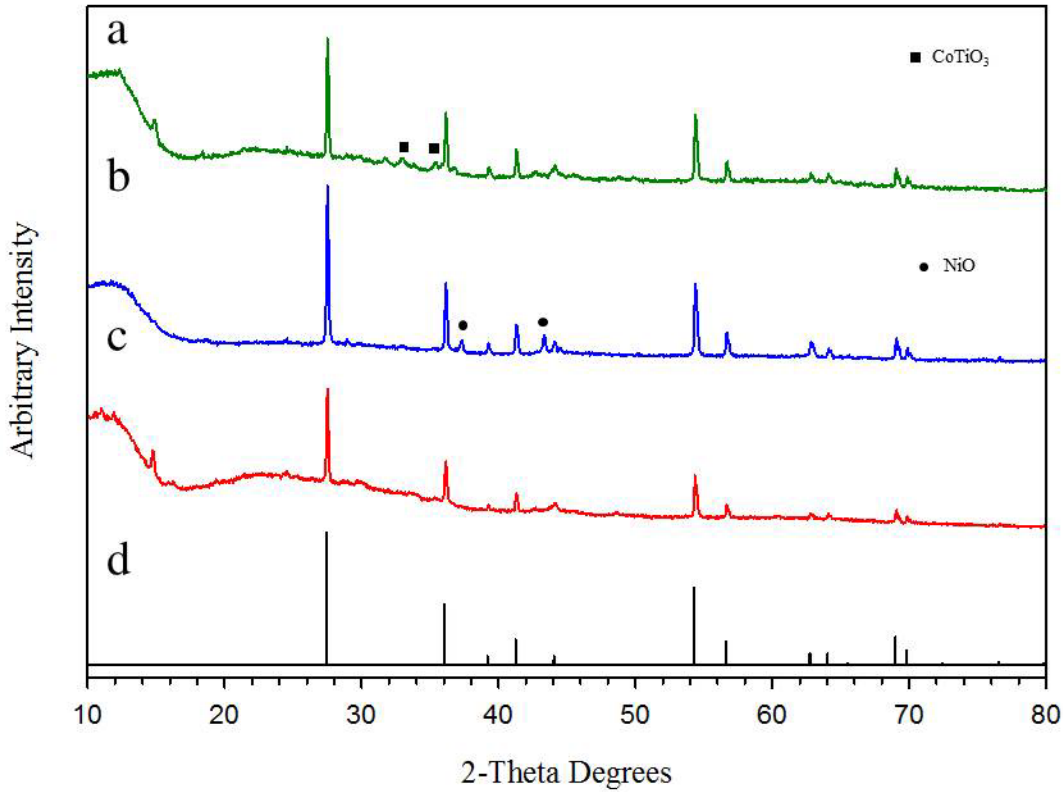

Figure 2.6 Powder X-ray diffraction patterns of the acid washed M-TiO_2 samples are shown with a = Co-TiO_2, b = Ni-TiO_2, c = Cu-TiO_2, d = reference rutile TiO_2.

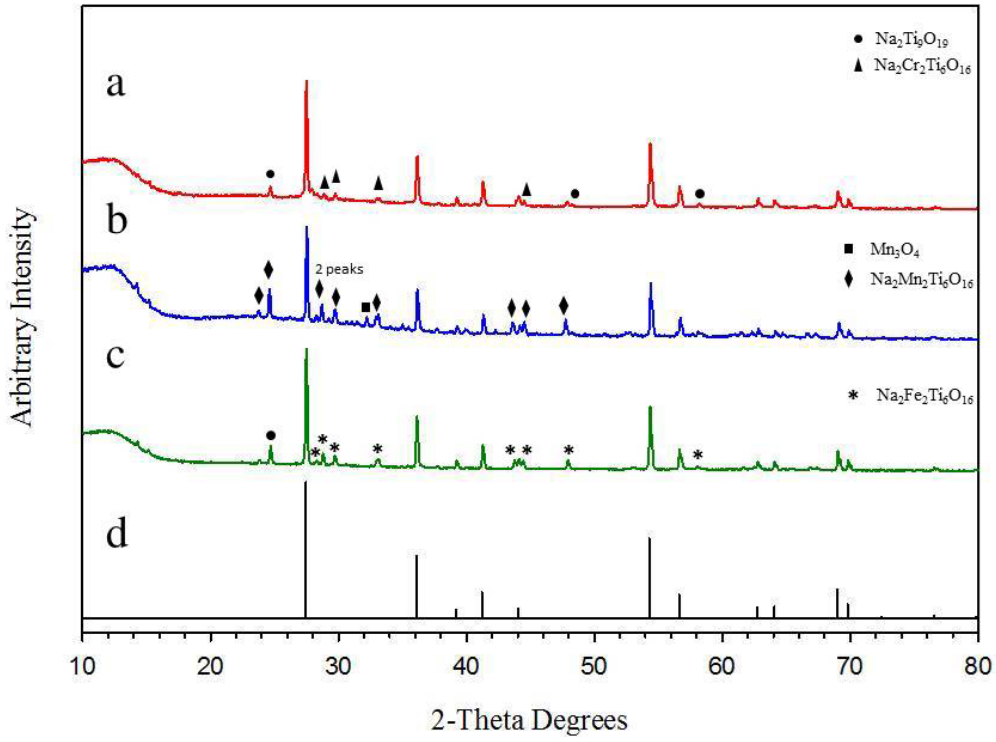

Figure 2.7 Powder X-ray diffraction patterns of the acid washed annealed M-TiO_2 samples are shown with a = Cr-TiO_2, b = Mn-TiO_2, c = Fe-TiO_2, d = reference rutile TiO_2.

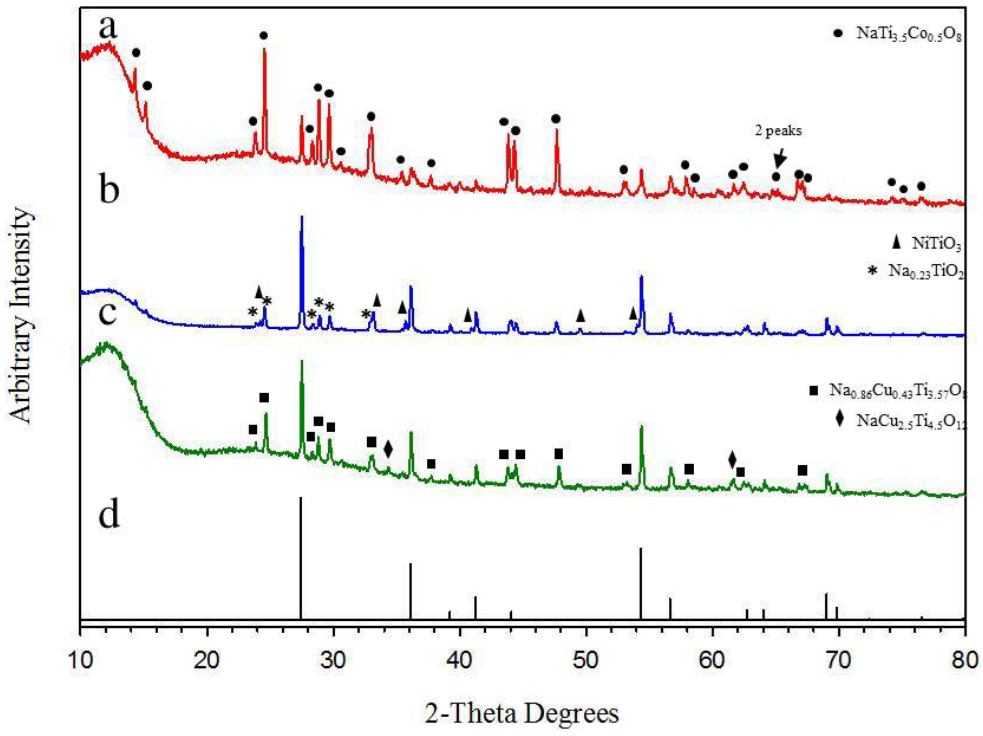

Figure 2.8 Powder X-ray diffraction patterns of the acid washed annealed M-TiO_2 samples are shown with a = Co-TiO_2, b = Ni-TiO_2, c = Cu-TiO_2, d = reference rutile TiO_2.

SSM reactions produced crystalline materials overall, yielding crystalline rutile TiO_2 primarily and some minor impurity Na-Ti-O phases. The nature of the SSM reaction causes rapid product formation and does not allow for prolonged crystallization times at high temperature. Annealed samples generally showed more crystalline rutile TiO_2 peaks and verified the evidence of the dopant metals by showing peaks for mixed phases. Also, sodium mixed phases crystallize upon annealing. It should be noted that the Co-TiO_2 and Ni-TiO_2 samples were the only samples that showed M-TiO_x phases versus Na-M-Ti-O phases.

2.3.2 M-TiO_2 Elemental Analysis (EDS and ICP-OES)

The EDS data was taken on either gently pressed ground sample powders on carbon tape or thinly pre-made sample discs. All of the samples were sputter coated with carbon to reduce charging. EDS measurements were taken over a large 1 mm area and several small flat sampling regions. The data in Table 2.2 are average relative atomic percent values relative to titanium in each sample. As mentioned earlier, the ideal Ti:M molar ratio should be 0.9 : 0.1 (or 1.0 : 0.11) for M = Cr, Mn, Fe, Co, Ni, and Cu. A majority of the samples showed dopant ratios close to the target ratio. The chromium sample had the lowest dopant ratio of 0.037. EDS sampling depth only penetrates the sample a few micrometers thick. As mentioned earlier, the samples were taken in sections over a large area to obtain more quantitative information.

Since EDS data is semi-quantitative, a more quantitative measure of the bulk sample was necessary. ICP gives better quantitative bulk information about the elements in samples compared to EDS data. The ICP data was collected from samples dissolved in hot concentrated, H_2SO_4 and HNO_3, as TiO_2 is insoluble in HNO_3 alone. All samples were compared to the concentrations of elemental standards for each metal. The manganese and cobalt samples are close to the ideal Ti:M ratio having ratios of 1:0.104 and 1:0.102 respectively. All of the other samples have dopant ratios within (~0.40 – 0.70). ICP data shows dopant levels below the expected values which may be due to the leaching of dopants from acid washing and only partial dopant incorporation into TiO_2. Overall, the data is in fair to good agreement with the EDS data and higher EDS values may indicate preferential surface allocation of the dopant.

Table 2.2 XRD, ICP, and EDS data is shown for the acid washed M-TiO_2 samples. TiO_2 is rutile phase. Bolded XRD phases are dominant phases. ICP and EDS data are normalized to titanium content.

Sample Type M-TiO_2	**XRD Phases**	**EDS Ti:M molar ratio**	**ICP Ti:M molar ratio**
Cr-TiO_2	**TiO_2**, $Na_2Ti_6O_{13}$	1.0 : 0.046	1.0 : 0.037
Mn-TiO_2	TiO_2	1.0 : 0.174	1.0 : 0.104
Fe-TiO_2	**TiO_2**, $Na_{0.23}TiO_2$	1.0 : 0.061	1.0 : 0.063
Co-TiO_2	**TiO_2**, $CoTiO_3$	1.0 : 0.115	1.0 : 0.102
Ni-TiO_2	**TiO_2**, NiO, $NiTiO_3$,	1.0 : 0.090	1.0 : 0.042
Cu-TiO_2	**TiO_2**	1.0 : 0.115	1.0 : 0.069

In contrast to typically low ~1% metal dopant levels found in solution methods to metal doped titanias, the ICP results show there is much higher bulk dopant metal content present in these SSM synthesized M-TiO_2 materials. The actual transition-metal dopant range from being very near to the ideal ($M_{0.1}Ti_{0.9}O_2$) Ti:M ratio of 1.0 : 0.11 down to 1.0: 0.05. Given that ICP and EDS data are for acid washed isolated products, it is encouraging that these acid washed SSM reaction products retain significant amounts of dopant metal that may be in a combination of places; doped into the TiO_2 crystal structure, and on the surface.

2.3.3 Magnetic Susceptibility of M-TiO_2 Samples

The magnetic susceptibility of the M-TiO_2 samples was measured at room temperature in glass sample tubes. The magnetic data is shown in Table 2.3 for acid washed samples and in Table 2.4 for acid washed annealed samples. The estimated spin-only magnetic moment was calculated at room temperature from molar susceptibility data. The molar susceptibility data was calculated using the equation $\chi_m = \chi_g$ * (molar mass), removing the TiO_2 χ_m value and then scaled per mol of metal in M-TiO_2 based on ICP data. The χ_g term is the gram susceptibility and was calculated using the equation $\chi_g = \chi_v*(h*\pi r^2/m)$ where χ_v is the volume susceptibility given by the instrument, h is the sample height in the sample tube, r is the tube radius, and m is the mass of the sample. The molar mass is based on the ideal $M_{0.1}Ti_{0.9}O_2$ empirical formula. The magnetic moment was calculated using the equation $\mu_B = 2.83* (\chi_M* T)^{1/2}$ where T is the temperature in Kelvins.

The magnetic susceptibility of the non-doped SSM TiO_2 sample was taken and gave a small paramagnetic molar susceptibility value of 7.20 x10^{-5} cm^3/mol. As a reference, Degussa P25 TiO_2 was measured and gave a negative diamagnetic response as expected. This is because the electronic states in TiO_2 result in a diamagnetic arrangement of electrons as the Ti^{4+} oxidation state has no unpaired pairs of electrons (d^0). After core diamagnetism was accounted for, the P25 TiO_2 sample had a very small paramagnetic response. This may be due to trace impurities. The P25 TiO_2 sample was also annealed and tested for its magnetic susceptibility. Surprisingly, there was a small paramagnetic response from the sample due to minor impurities. The small paramagnetic

response from the SSM TiO_2 sample likely comes from the small amounts of impurities in the material such as a $Na_xTi_yO_z$ phase that may have Ti^{3+} (d^1) content.

Table 2.3 Magnetic susceptibility measurements are shown for the P25 TiO_2, SSM TiO_2, and acid washed M-TiO_2 samples. χ_M values have been corrected for core diamagnetism.

Sample Type	**Mass Magnetic Susceptibility χ_g x 10^{-6} (cm^3/g)**	**Molar Magnetic Susceptibility χ_m x 10^{-3} (cm^3/mol)**	**Magnetic Moment μ_B per mol M (BM)**
TiO_2 (P25)	0.01	0.03	0.27
TiO_2 (SSM)	0.54	7.20	0.41
Cr-TiO_2	6.34	13.6	5.70
Mn-TiO_2	7.55	6.00	3.79
Fe-TiO_2	17.1	23.5	7.48
Co-TiO_2	11.2	9.30	4.72
Ni-TiO_2	7.54	14.8	5.95
Cu-TiO_2	4.20	4.80	3.37

Table 2.4 Magnetic susceptibility measurements are shown for P25 TiO_2, SSM TiO_2, and acid washed M-TiO_2 samples that have been annealed at 1000°C in air for 24 hours. χ_M values have been corrected for core diamagnetism.

Sample Type	**Mass Magnetic Susceptibility χ_g x 10^{-6} (cm^3/g)**	**Molar Magnetic Susceptibility χ_m x 10^{-3} (cm^3/mol)**	**Magnetic Moment μ_B per mol M (BM)**
TiO_2 (P25)	0.057	0.034	0.28
TiO_2 (SSM)	0.384	2.20	2.29
Cr-TiO_2	10.60	23.7	7.52
Mn-TiO_2	27.70	1.61	1.96
Fe-TiO_2	120.00	169	20.08
Co-TiO_2	9.42	7.78	4.31
Ni-TiO_2	19.10	40.0	9.77
Cu-TiO_2	6.92	8.24	4.43

All acid washed M-TiO_2 samples gave small to moderate paramagnetic responses. From the phases identified from XRD, there is no obvious contribution to this paramagnetism. One possibility to this response may be due to amorphous reduced titania species present in the sample. The annealed acid washed M-TiO_2 samples showed an increase in paramagnetic response, except for the Mn and Co-TiO_2 samples, which had a slight decrease. If any reduced titania was present in the acid washed sample, annealing it would fully oxidize the material, causing a drop in the magnetic susceptibility. Also, the formation of paramagnetic or ferromagnetic phases from the dopants may cause an increase in χ_M.

2.3.4 Diffuse Reflectance of M-TiO_2 Samples

The diffuse reflectance data of the acid washed M-TiO_2 samples is shown in Table 2.5. The samples were analyzed for their onset absorptions and peaks in the spectra. Table 2.5 shows the onset absorbance events are denoted with "**o**" and broad absorbance peaks are denoted with "**p**". Onsets were measured by linear line extrapolation. Estimated band gap energies were calculated by observing the onset tangent lines from the plot using the Kubelka-Munk equation shown in Equation 2.4 as a function of energy.

$$F(R) = (1-R)^2/2R \quad (2.4)$$

"R" is the diffuse reflectance of the sample and represents the light which is not absorbed (transmitted and/or reflected) and focused by the integrating sphere part of the accessory. The estimated band gap energies are converted to electron volts (eV) units.

Degussa P25 TiO_2 and un-doped SSM TiO_2 were used as references. P25 TiO_2 is a mix of rutile (20%) and anatase (80%) TiO_2 phases which have band gap energies of 3.0 and 3.2 eV, respectively. Undoped SSM TiO_2 has an estimated band gap energy of 3.00 eV. The lower band gap energy may be due to the additional impurity phases seen in the XRD pattern. The M-TiO_2 samples have smaller estimated absorption energies within 1.35- 2.55 eV. The extrapolation of the raw data and the Kubelka-Munk calculations agree reasonably well. Some of the samples have multiple onsets which could indicate either different absorption processes. Darker colored samples, such as Mn-TiO_2 and Co-TiO_2 have broad absorbance regions over the visible spectra and have onsets near or within the IR region.

Table 2.5 Diffuse reflectance data of acid washed doped titania samples. The onset absorption is denoted with "o" and broad peaks "p". The estimated band gap energies are in extrapolated. Kubelka-Munk calculations for each onset value are tabulated for comparison to extrapolation.

Sample Type	**DRS UV-vis absorbance in nm (type, E in eV)**	**Absorption onsets by Kubelka-Munk analysis (eV)**
TiO_2 (P25)	408 (**o**, 3.04)	3.05
TiO_2 (SSM)	415 (**o**, 2.99)	3.00
Cr-TiO_2	570 (**o**, 2.18), 700 (**p**, 1.77), 800 (**o**, 1.55)	2.15, 1.50
Mn-TiO_2	670 (**o**, 1.85), 710 (**p**, 1.75),920 (**o**, 1.35)	1.80, 1.35
Fe-TiO_2	480 (**o**, 2.59), 490 (**p**, 2.53), 580 (**o**, 2.53)	2.45, 2.10
Co-TiO_2	510 (**o**, 2.43), 580 (**p**, 2.14), 660 (**p**, 1.88), 800 (**o**, 1.55)	2.40, 1.60
Ni-TiO_2	500 (**o**, 2.48), 740 (**p**, 1.68), 810 (**o**, 1.53)	2.55, 1.55
Cu-TiO_2	490 (**o**, 2.53), 740 (**p**, 1.68)	2.55

2.3.5 X-ray photoelectron spectroscopy of M-TiO_2 Samples

The acid-washed metal doped TiO_2 powders with nominal $M_{0.1}Ti_{0.9}O_2$ target compositions were analyzed by XPS to examine relative composition of metals on the powder surface and chemical states of the surface species. Table 2.6 summarizes both survey scan and regional scan data for the metal doped titania powders. In most cases the semiquantitative surface compositions (Ti:M ratios) for the powders is comparable to the bulk analysis results described earlier, with a few notable exceptions. While the bulk and most of the surface analysis results support that the intended Ti:M ratio of 1:0.11 leading to a $M_{0.1}Ti_{0.9}O_2$ product is generally one with less dopant metal than targeted, both the Cr and Mn doped samples have very fairly high surface metal dopant relative to their bulk

compositions. In particular, the Mn-TiO_2 sample has a nearly 1:2 ratio of Mn:Ti on its surface. This result was verified on several different reaction products. The high dopant surface content may have implications in molecular dye adsorption discussed later in this chapter.

Table 2.6 Summary of Analysis of XPS Data on M-TiO_2 Powders

Compound	**Surface Ti:M (rel. molar amt)**	**Ti2p$_{3/2}$ transition (eV)**	**M2p$_{3/2}$ transitions (eV)**
Cr-TiO_2	1 : 0.384	458.3	**576.8**, 579.4
Mn-TiO_2	1 : 0.599	458.0	**641.3, 642.7**
Fe-TiO_2	1: 0.064	458.4	**710.7, 712.7**
Co-TiO_2	1 : 0.109	458.2	**780.1, 782.0**, 784.6, 786.5
Ni-TiO_2	1: 0.100	458.2	**855.3**, 861.4
Cu-TiO_2	1 : 0.089	457.2	**931.4,** 932.8, **933.7**, 939.8, 942.3

The metal dopant's $2p_{3/2}$ peak positions are generally consistent with metal oxidation states found in binary oxides specifically (literature value, eV) Cr^{3+} (576), Fe^{3+} (710.8), Mn^{3+} (643), Co^{2+} (780.6) and Ni^{2+} (855.6), and Cu.[132-141] In the Mn-TiO_2 case, the lower energy shift for the Mn peak suggests that there is some Mn^{2+} species present on the surface. Degussa P25 TiO_2 yields a Ti $2p_{3/2}$ peak at 458.7 eV, and SSM produced TiO_2 without dopant has a peak at 458.5 eV which are very near literature titania values.[132,142] The Ti $2p_{3/2}$ binding energies for metal doped TiO_2 in Table 2.6 are generally close to the pure TiO_2 values, but several are shifted to lower energies that may indicate some reduced Ti^{3+} present on the surface. In examining the O1s peaks,

commercial P25-TiO_2 has one oxygen chemical environment, while all of the M-TiO_2 samples clearly indicate several different oxide environments present on the surface.

2.3.5 Scanning Electron Microscopy of M-TiO_2 Samples

Scanning electron microscope images of the acid washed samples are shown in Figure 2.9. The undoped acid washed SSM TiO_2 sample was examined as well. Acid wash annealed samples were scanned using the same initial preparation techniques except that the samples were used as free powders and coated with a gold-palladium layer for improved image quality.

The undoped acid washed SSM TiO_2 sample showed a mix of large rectangular blocky shard-like structures and aggregates. The shards range from ~2-10 micrometers to several tens of micrometers. Aggregates range greatly from ~1-20 micrometers. The morphology of this sample is useful since all doped samples are mainly TiO_2 and ideally should have some similarities. The Cr-TiO_2 sample also showed a mixture of shard-like structures and smooth spherical structures. The shards range from several hundred nanometers to a tens of micrometers and the spherical shapes are as small as 500 nanometers. There was a small amount of charging still even though the sample was carbon coated.

The Mn-TiO_2 sample consists of a mix of large blocky 20 to 30 micrometer structures mixed in with very small aggregates that are ~ 1-5 micrometers. The small aggregates make up a majority of the sample. The Fe-TiO_2 is mainly populated by smooth spherical structures that are ~1-10 micrometers in size. There are large flat

blocky regions that range from ~5-10 micrometers. There are no rod-like structures visible as seen in the undoped SSM TiO_2 sample.

The Co-TiO_2 also has a mix of majority round spherical structures and some blocky, rectangular structures. The spherical structures range from ~100 - 400 nanometers and the blocky structures range from ~2-10 micrometers. The Ni-TiO_2 also mainly consists of spherical structures. Throughout the sample, there are a few blocky structures that are about ~10-20 micrometers, however ~500- 1000 nm spherical shapes dominate the sample. The Cu-TiO_2 consists of large rectangular blocky structures that are ~5-7 micrometers, and small spherical aggregates that are a few micrometers in size.

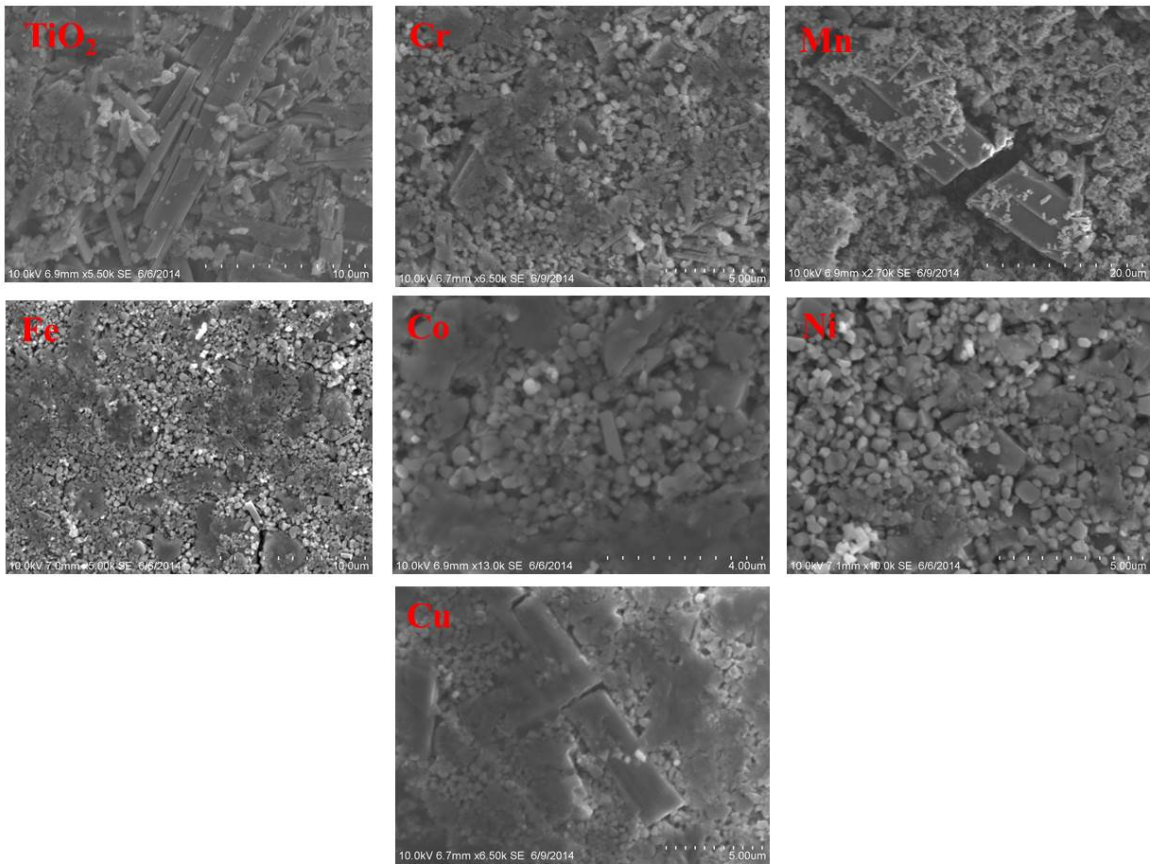

Figure 2.9 SEM images of transition metal doped TiO_2 acid washed samples. Samples were pressed into thin pellets and carbon coated. The non-doped TiO_2 sample is also shown.

The acid washed annealed M-TiO_2 samples were analyzed in a similar fashion as the acid washed samples. The SEM images are shown in Figure 2.10. The annealing process involved heating the acid washed samples to 1000 °C for 24 hours which is expected to promote grain growth and phase separation in the samples. The Cr-TiO_2 showed aggregate smooth blocky structures and smooth spherical structures. These structures range greatly in size from ~500 nanometers to ~7 micrometers for both blocky and sphere-like structures.

The Mn-TiO_2 sample showed large smooth blocky aggregates that range from ~5-20 micrometers. There is an indication of truncated corners on some of the blocks. The Fe-TiO_2 sample consists of smooth blocky structures in the range of several tens of micrometers. There are some smaller aggregates that are a few microns in size. The Co-TiO_2 sample consists of large faceted islands of particles that are ~2-10 micrometers. The islands are as large as ~20-40 micrometers. The Ni-TiO_2 sample consisted of very uniform rectangular prisms which are ~2-10 micrometers, and small spherical particles that are few hundred nanometers to ~2 micrometers. The Cu-TiO_2 sample consists of a mix of large and small shard-like structures. The large shards range from 1-5 micrometers and the small shards range from ~200-500 nm. Overall, in all cases annealing leads to clear particle growth within the ~1-10 micrometer region.

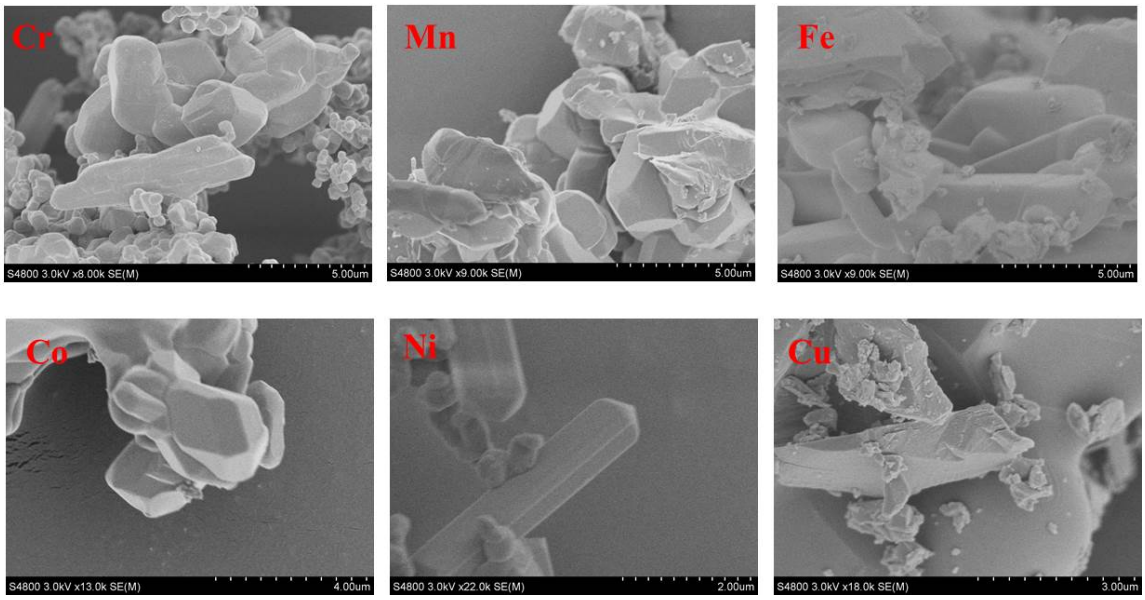

Figure 2.10 SEM images of acid washed M-TiO_2 samples that were annealed in air at 1000 °C.

2.3.6 Photodegradation of Methylene Blue and Methyl Orange Dyes

Photodegradation of methylene blue (MB) and Methyl Orange (MO) dyes were performed using acid washed M-TiO_2 samples. A dye sample with no powder was used as a blank for both dyes. Undoped SSM rutile TiO_2 and Degussa P25 TiO_2 samples were also used for comparison. The sample vials were placed on a large stir plate about 25 cm away from the mercury lamp, all of which were contained in a closed photochemical reactor cabinet shown in Figure 2.11. The samples were allowed to stir in the dark for 30 minutes with the vial caps on to allow surface adsorption and equilibration of the MB or MO dye. With the vial caps off, UV irradiation was in regular intervals of at least 5 minutes in length. Between each interval, the samples were centrifuged and UV-vis measurements were taken on the solution. The analyzed solutions were returned to the original vial and the irradiation was repeated. A similar set of experiments were performed using a 420 nm cut off filter, shown in Figure 2.10, to limit the UV lamp output for visible light photodegradation studies.

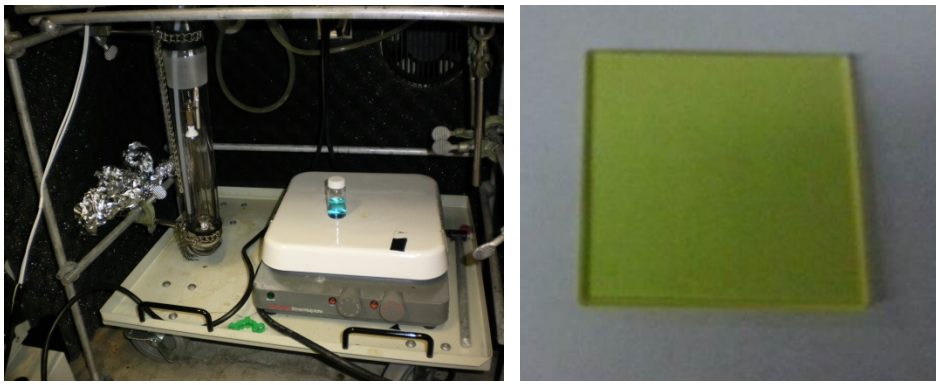

Figure 2.11 Mercury lamp setup for photocatalysis experiments are shown here. The 420 nm cutoff filter used for visible light photocatalysis measurements is shown on the right.

The methylene blue UV experiments were performed over a four-hour period. The images of the samples in methylene blue solutions are shown in Figure 2.12. The solutions after the dark stir are shown along with the solutions after the final data point time of 4 hours. Visual analysis of the samples shows that Mn-TiO_2 sample adsorbs majority of the dye during the dark leaving a faint light blue solution in the vial. The other samples were similar to the dye blank. After the 4 hour irradiation period, majority of the samples were much lighter in color. The blank sample remains visibly unchanged. The P25 TiO_2 sample was colorless. The Mn-TiO_2 sample left a purple colored solution.

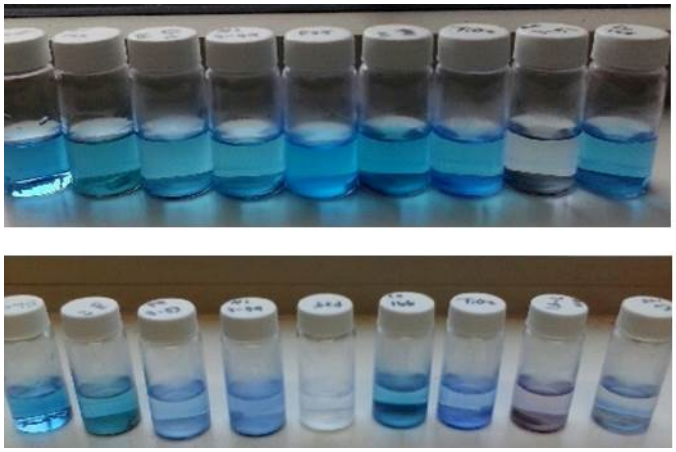

Figure 2.12 Sample vials after dark stir and after UV irradiation of the acid washed M-TiO_2 samples. From left to right: Dye blank, Cr, Fe, Ni, P25 TiO_2, Co, undoped SSM TiO_2, Mn, Cu.

The plotted data of percent remaining dye in solution over time is shown in Figure 2.13. The negative data point is the initial dye solution absorption. The zero mark is the solution absorption after the 30 minute dark stir. All of the samples have some initial dye adsorption. The blank sample does show very slow self-degradation of the MB dye leaving ~80% of the dye in solution. The P25 TiO_2 sample rapidly degrades the MB dye

after 10 minutes to very low levels leaving ~10% of the dye. The Cr-TiO_2 sample removes ~55% of the dye during the dark stir. Little additional dye is removed after the 4 hour UV irradiation period.

The Mn-TiO_2 sample removed ~90% of the dye from solution during the dark stir. Once irradiated, the dye absorption fluctuates minimally, ending with a final percentage of ~9%. The fluctuating absorption values could be due to dye being adsorbed and desorbed from the solid surface during irradiation. The Fe-TiO_2 sample removed ~60% of the dye from the solution after the dark stir. After illumination, the sample gradually degrades the dye to a final percentage of ~10%. The Co-TiO_2 sample removes ~35% of the MB dye from the solution after the dark stir and removes ~80 % of the dye after irradiation.

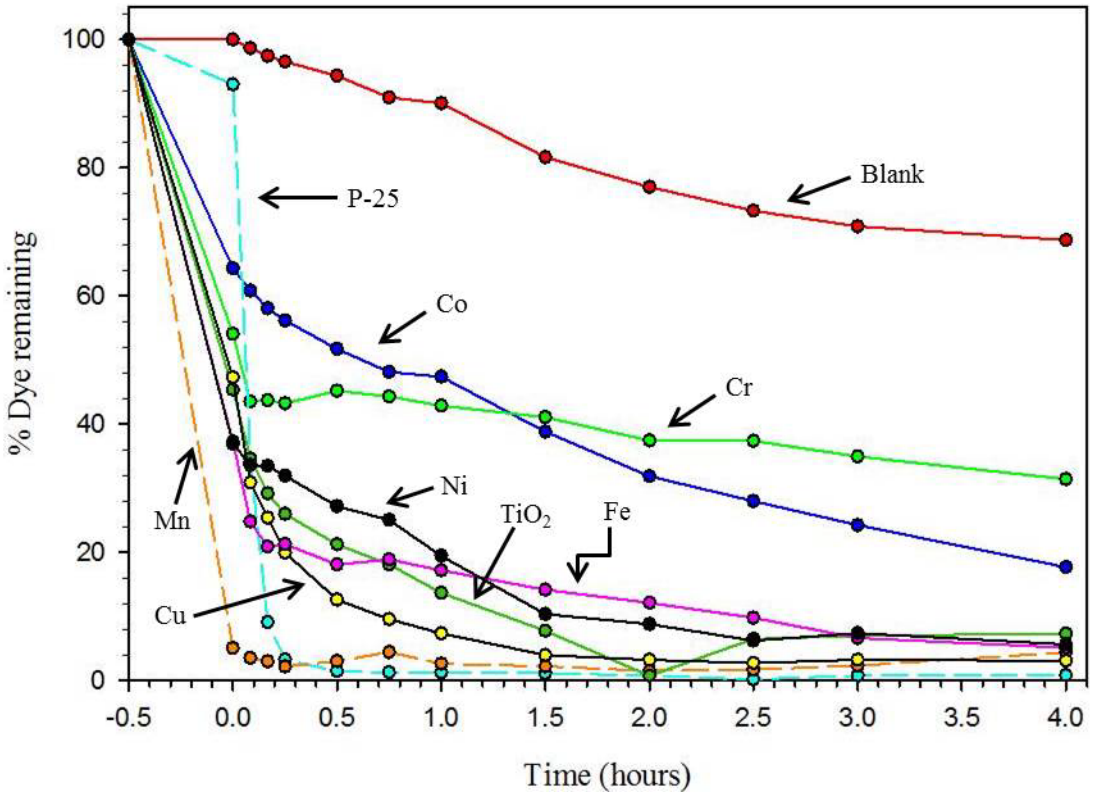

Figure 2.13 Plot of methylene blue degradation over the course of 4 hours using acid washed M-TiO_2 samples under UV light irradiation. The undoped SSM TiO_2 sample is denoted "TiO_2" and P25 TiO_2 is used as the reference TiO_2 catalyst.

The Ni-TiO_2 sample removes ~60 % of the MB dye from the solution after the dark stir. Total dye removal of~90 % is achieved in ~2.5 hours. The Cu-TiO_2 sample removes ~50% of the dye from the solution after dark stirring. After the ~1.5 hour period, the dye is degraded by 95 %.

There is a clear difference between the P25 TiO_2 and the acid washed samples interaction with the dye with and without light. The general trend is that the P25 TiO_2 is poor at adsorbing the dye in the dark but is very efficient at degrading the dye using oxygen and UV light to photo-oxidize the dye. The M-TiO_2 samples seem to adsorb significant amounts of dye in the dark versus P25 TiO_2 and gradually photo-react with the

dye over several hours under UV light irradiation. When methylene blue is fully oxidized, several species remain in the solution and follow Equation 2.5.[99]

$$C_{16}H_{18}N_3S^+ + 51/2\ O_2 \rightarrow 16\ CO_2 + 3\ NO_3^- + SO_4^{2-} + 6\ H^+ + H_2O \qquad (2.5)$$

The precise mechanism is complex since several reactive species, such as hydroxyl radicals or superoxides can be involved in breaking down the dye.

A similar experiment was done using the mercury lamp and 420 nm glass cutoff filters in order to expose the samples to visible light wavelengths only ($\lambda > 420$ nm). The plotted dye absorption data over time is shown in Figure 2.14. An additional P25 TiO_2 sample was annealed (1000 °C, air, 24 hours) to achieve the rutile crystal structure, and was used as a phase comparison to the SSM materials. The dark stir results for each sample were similar to each other, removing ~40-50% of the dye from solution. The annealed P25 TiO_2 sample only removed 10% of the dye from the solution upon dark stirring. P25 TiO_2 removed a bit more dye from the solution compared to the same sample during the UV test. The Mn-TiO_2 sample did not absorb as much dye compared to the UV run, however, only removing ~60% of the dye from the solution after dark stirring. The differences in dark absorption are not dramatically different, which is encouraging for future tests using the same samples.

The annealed P25 TiO_2 sample gradually degrades some dye over the 4 hour filtered UV ($\lambda > 420$ nm) test. The resulting dye removal is ~40% and the P25 TiO_2 sample removed ~70 % of the dye. The Cr-TiO_2 sample had a slight raise in MB absorption at the beginning of the run. This is possibly due to UV-Vis particle scattering

or desorbed dye upon initial irradiation. Over the remainder of the run, the dye degraded linearly, removing 55% of the dye.

The Mn-TiO_2 sample removed ~60% of the dye in solution upon dark stirring. The Mn-TiO_2 sample degrades the dye gradually until an hour of irradiation, and then the degradation slows down considerably. After irradiation 95% of the dye was removed from the solution. The iron sample removed the MB dye from solution better than the manganese sample, removing ~80% of the dye in solution after dark stirring. After about an hour of irradiation, the 90% of the dye was removed, and then the absorption gradually creeps up over time. This may be due to fine particles suspended in solution that did not settle upon separation, thus causing light scattering.

The cobalt sample removed ~50% of the dye in solution after dark stirring. Throughout the run, the dye degraded gradually resulting in 70% dye removal after a 4 hour period. The nickel sample removed ~45% of the dye in solution after dark stirring. The dye degraded gradually over time resulting in ~60% dye removal from the solution. Lastly, the copper sample removed ~50% of the dye from the solution after dark stirring. There was a gradual drop in dye remaining over the 4 hour irradiation period removing ~85% of the dye from the solution.

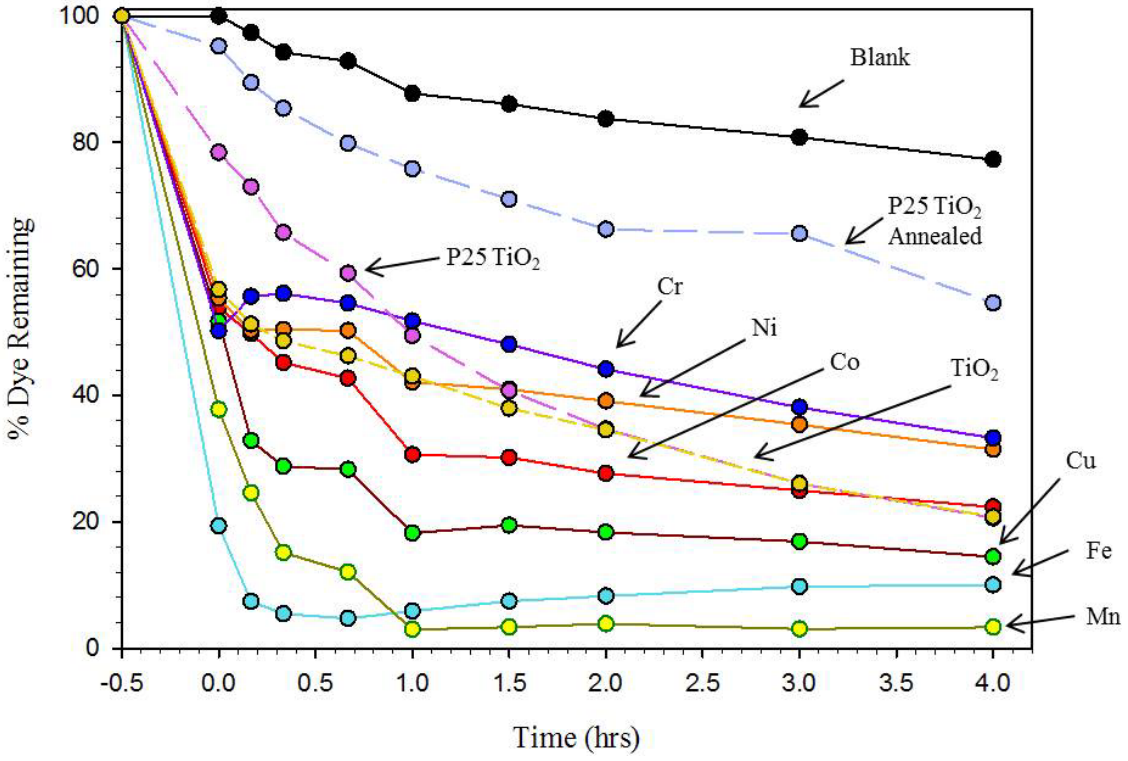

Figure 2.14 Plot of methylene blue degradation over the course of 4 hours using acid washed M-TiO_2 samples under visible light irradiation using 420 nm cutoff filters. The undoped SSM TiO_2 sample is denoted "TiO_2" and P25 TiO_2 is used as the reference TiO_2 catalyst. An annealed version of P25 TiO_2 was used for rutile structure comparison to the other M-TiO_2 samples.

The methyl orange (MO) UV photo-degradation data is shown in Figure 2.15. All of the M-TiO_2 samples did not absorb much dye during the dark stir. The P25 TiO_2 sample, shown in Figure 2.16, had an increase in absorbance due to scattering effects from the fine particle suspension that could not be fully centrifuged. After the allotted UV exposure, the M-TiO_2 samples showed only slight MO dye degradation. The cobalt sample had the best dye removal removing ~20 % of the dye from solution. The latter data points for the other M-TiO_2 samples had a similar fine particle suspension issue seen

with P25 TiO_2 which gave a slight increase in absorbance. The P25 TiO_2 sample degraded a large percent of the dye over the 4 hour period removing more than 98% of the dye from solution and a colorless solution. Because of the dramatic difference between the active P25 TiO_2 sample and the M-TiO_2 samples, the P25 TiO_2 sample is not shown in the same plot but is shown in Figure 2.16. All of the M-TiO_2 samples retained a slightly lighter orange color compared to the dye blank. There was not a visible light MO experiment done using the M-TiO_2 samples due to the very low inactivity from using UV (+ visible) light.

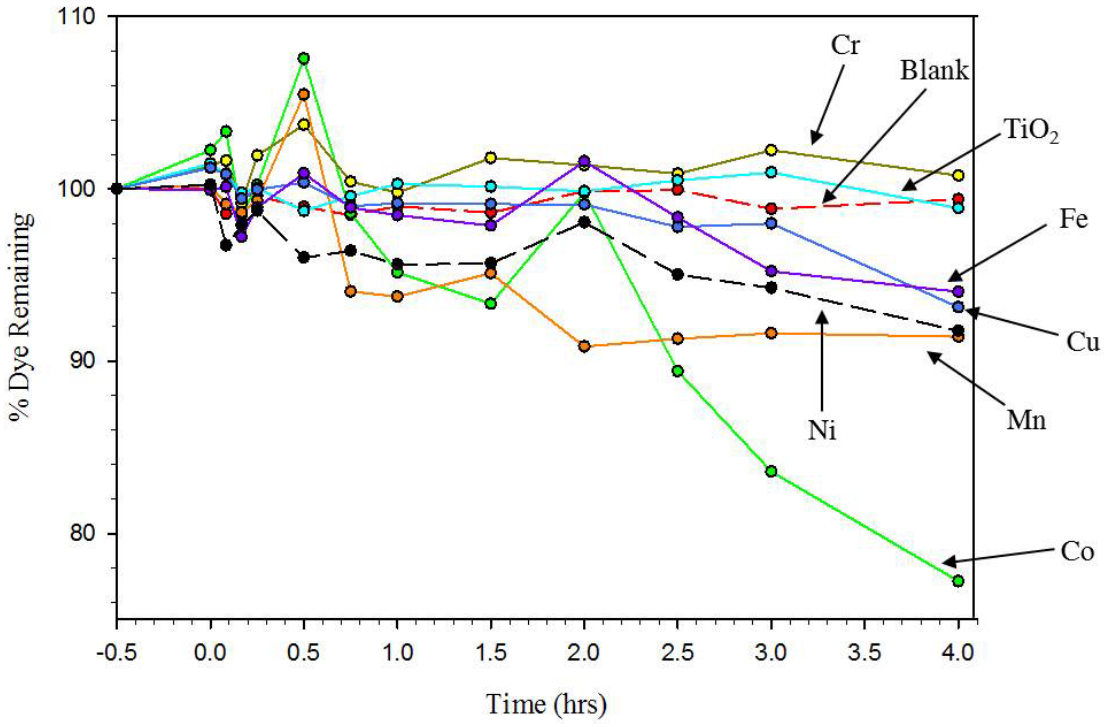

Figure 2.15 Plot of methyl orange degradation over the course of 4 hours using acid washed M-TiO_2 samples under UV light irradiation. The undoped SSM TiO_2 sample is denoted "TiO_2".

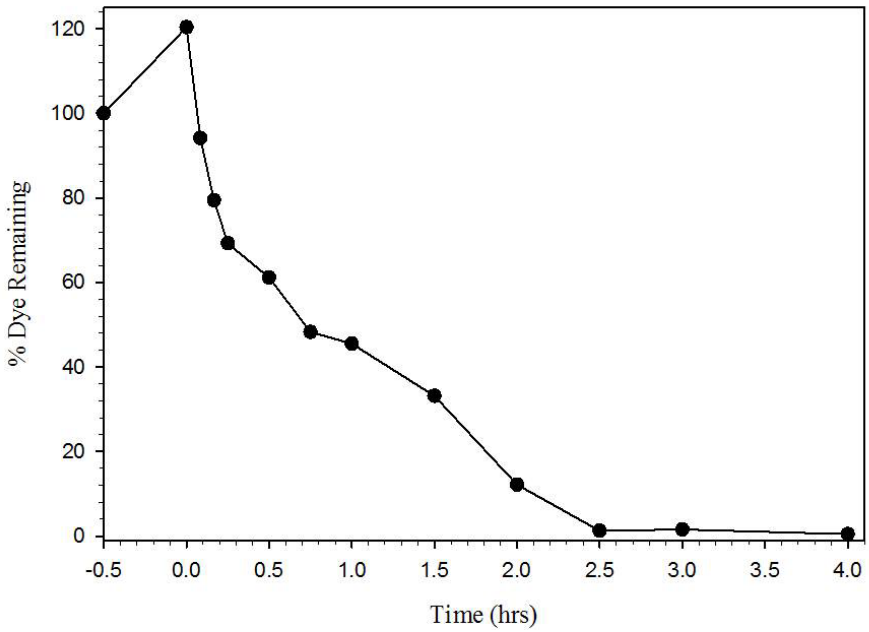

Figure 2.16 Plot of methyl orange degradation over the course of 4 hours using P25 TiO_2 sample under UV light irradiation.

The degradation mechanism of methyl orange in aqueous solutions is complex however, similarly with methylene blue dye, MO can be broken down by multiple reactive species. A study has shown by mass spectroscopy that the dye can break down to smaller sub-units over time.[143] Generally, many literature sources indicate that the degradation is the result of hydroxide or superoxide radicals.[144,145]

2.3.7 H_2 Generation from Water

Water reduction experiments were attempted with acid washed M-TiO_2 samples were done using 1 wt% Pt that was photoreduced onto the surface of samples. Methanol was used as a sacrificial hole scavenger. Each sample was irradiated under UV light for approximately 4 hours. A reference 1 wt% Pt loaded P25 sample was tested as well. The gases that were monitored were Ar, O_2, H_2O, N_2, CO_2, CH_3OH, H_2, and H^1. The H^1

signal is from H_2 ionizing from the filament. We are aware that O_2 and CH_3OH have the same mass (32 g/mol), however if there was a pressure increase from this mass, it would most likely be CH_3OH since our reaction flask did not show air leaks (increase in N_2 pressure).

The M-TiO_2 samples did not show any appreciable amount of H_2 over the 4 hour run time. The reference sample did show a steady stream of H_2. The percent of H_2 pressure relative to argon pressure is shown in the plot in Figure 2.17.

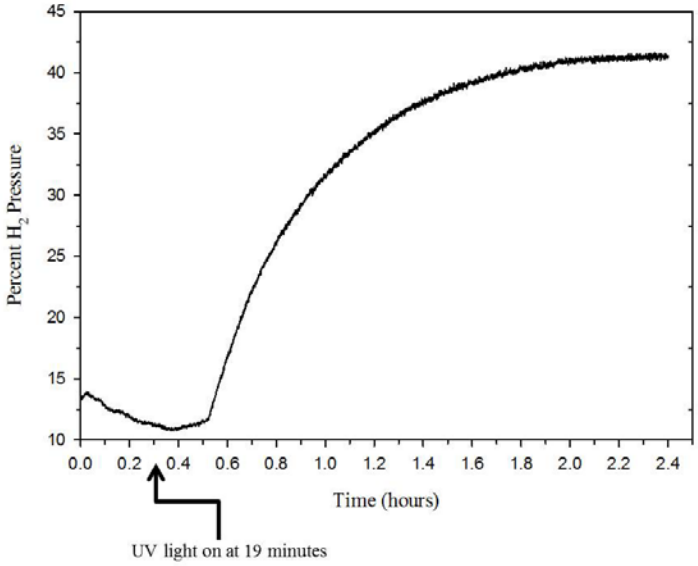

Figure 2.17 H_2 generation over time from the 1wt% Pt loaded P25 TiO_2 reference sample. The percent pressure is relative to the argon background gas.

The RGA system was allowed to equilibrate for several minutes before the UV lamp was turned on. The lamp was turned on after 19 minutes. The system has a small background H_2 signal before each run which may be from water vapor. The H_2 signal plateaus around 42 %, leaving ~58% Ar and trace pressures of all other gas signals.

2.4 Reaction Analysis

SSM reactions are exchange reactions, meaning that the ions between reagents ideally exchange between each other. In the reaction between $TiCl_3$ and Na_2O_2, the targeted solid products seen by XRD are TiO_2 and NaCl. Titanium is oxidized from Ti^{3+} to Ti^{4+}. The reaction is driven by the thermodynamic formation of NaCl (ΔH_f = -411.1 kJ/mol). The reactions proceed from ignition of the combined solids with a resistance heated 22 gauge nichrome wire. Nichrome wire is an alloy of Ni (58%), Cr(16%), and Fe (26%), and sometimes small amounts of silicon depending on the brand. It melts at ~1400 °C. Care has to be taken when using nichrome wire with the metal oxide SSM reactions since the reactions can reach the boiling point of the product salt. NaCl boils at ~1413 °C and is present for a short time as a molten flux, therefore the wire can break if in contact with the hot products. The reactions cool rapidly, however.

The doped reactions behave similarly to the non-doped TiO_2 reaction. Essentially, a small portion of the $TiCl_3$ is substituted for dopant metal halide. The goal of the reaction is to cause "doping" of the rutile lattice with small amounts of another metal cation. The assumption is that the powders are mixed intimately enough to cause this forced defect of other metal ions in the place of Ti^{4+} ions. It was encouraging to see that in the XRD patterns, few or no visibly crystalline dopant oxide peaks, and the synthesized titanias were colored with respect to the dopant metal used.

Doping can occur in several ways. The dopants could be localized on the surface of the rutile crystals. This would explain the color seen of each solid. The dopants could also be located within the crystal structure vacant sites of rutile. The dopants could also replace Ti^{4+} by bonding to oxygen in a similar 6-coordinate fashion to avoid major lattice

parameter changes. Some possible candidates for direct Ti^{4+} replacement and that will bond in a 6-coordinate manner are Cr^{3+} (0.62Å), Mn^{4+} (0.53Å), Fe^{3+} (0.65Å), Co^{3+} (0.61Å), and Ni^{2+} (0.69Å) since Ti^{4+} ionic radii is (0.61 Å).

The targeted mole ratio of Ti:M (M = Cr, Mn, Fe, Co, Ni, Cu) was 9:1 giving an ideal chemical formula of $Ti_{0.9}M_{0.1}O_2$. This assumes that the small amounts of dopant will interact with the rutile structure intimately as opposed to forming separate oxides. Also, the thermodynamic data of the common oxides were shown and discussed in Chapter 1 (Table 1.1). TiO_2 is the most thermodynamically favorable oxide compared to the other first row transition metal dopant oxides with a heat of formation value of ΔH_f = -944.7 kJ/mol and is the major component in the reaction mixture.

The SSM reactions propagate from an initial heat source point producing products. Assuming that all of the reagents are intimately mixed, TiO_2 would form rapidly in the presence of dopant metals. In reality, the powders are dispelled violently throughout the reaction chamber due to gas formation and pressure build up so there is most likely a mixture of products with some local variations in M_xTiO_2. The reagents are not heated for very long periods of time therefore product crystallization time is limited. This may also suppress the formation of separated dopant oxides versus metal ions inside the rutile structure.

2.5 Conclusions

Doped transition metal oxides have been synthesized using a rapid SSM technique in moderate yields. All of the samples were colored, which indicated that the dopant was present within the sample. XRD showed that the rutile phase TiO_2 and some impurity $NaTi_xO_y$ phases are present. Acid washing aided with significant impurity

removal, but ultimately some impurities remaining. Some dopant was lost from acid washing. EDS and ICP showed retention of metal dopants. Annealing studies showed that the metal dopants are still within the rutile structure since crystalline dopant based phases were present. The magnetic data of both the acid washed and acid washed annealed samples allowed us to better understand approximately how the dopant affects the electronic structure of the materials synthesized, with the annealed samples having a higher magnetic response than the acid washed samples alone. The fact the samples show visible light absorption also reinforces the presence of dopant metals. The SEM images of the acid washed samples showed aggregated particles and rods which produced smooth surfaces upon annealing.

The methylene blue dye degradation tests showed that the acid washed samples do have some photo-activity under UV and visible light. P25 TiO_2 out-performs the M-TiO_2 samples under UV light. However, majority of the samples are much better than P25 TiO_2 under filtered UV light using the 420 nm cutoff filters and better than undoped rutile from P25 annealing. Overall in both the UV and visible tests, the sample absorb the dye better in the dark than P25 TiO_2, with M-TiO_2 and Fe-TiO_2 samples having the highest dye removal in the dark.

The platinum loaded undoped and M-TiO_2 samples did not show H_2 generation even after several hours of UV light exposure. This may be due to several factors which include particle size, crystalline phase, and surface area. Improved synthesis methods will need to be investigated to encourage H_2 generation from M-TiO_2 samples. The platinum loaded P25 TiO_2 sample did show H_2 generation over a course of ~2 hours.

The next chapter will incorporate the SSM reaction technique using reactions targeting transition metal phosphide, sulfide, and thiophosphate materials. The goal will be to synthesize materials to obtain targeted phases quickly.

CHAPTER 3
SYNTHESIS OF TRANSITION METAL PHOSPHIDES AND SULFIDES BY SOLID-STATE METATHESIS METHODS

3.1 Introduction and Background

Transition metal phosphides and sulfides have several industrial uses, which have major influences in the semiconductor and catalysis fields. Often these materials are used for corrosion resistance,[146,147] photovoltaics,[148] hydrodenitrogenation (HDN) and hdyrodesulfurization (HDS) catalysts,[45,46] electrochemical catalysts, hydrogen evolution catalysts, mechanical lubricants, battery materials and pesticides. These materials are targeted for their electronic band structures and crystal lattice parameters.

Several materials require synthesis in large quantities. Therefore a cost and time efficient reaction route producing high quality products is beneficial. Wet chemistry methods are often performed to produce specific nanoscale products with unique morphologies. Hydrothermal and solvothermal methods produce uniform nanoscale materials. More exotic synthesis using templates can aid with the formation of unique structures. These techniques often require very specific reagents for desired materials. Solid state routes are good alternatives to solution phase reactions. These types of reactions do not require a solvent in the synthesis, but may need them for post reaction washing.

Traditional solid state syntheses of these materials involve high purity elements, which are often heated to high temperatures for long periods of time under inert conditions. The advantage of using the elements is that there is usually no byproduct materials produced and isolation of products are simple. Also the energy of the reaction is exothermic since the reagents are elements and have a $\Delta H_f = 0$ kJ/mol. For example, the synthesis of CuP_2 from the reaction $Cu + 2P \rightarrow CuP_2$ ($\Delta H_{rxn} = -121$ kJ/mol) should readily form products. However, the reaction requires long heating times at high

temperatures under inert conditions or vacuum. There is also the possibility of multiple phases forming during the allotted heating time. Often, targeted phases are chosen due to thermodynamic properties of the phase. Depending on the reaction, the product yields will vary and characterization by X-ray diffraction techniques can be done.

Changing the starting reagents can aid with product formation. Reagents that form highly stable byproducts can be advantageous for reactions that take very long times to react. The byproducts need to be easily removed from the targeted materials. Materials that can be sublimed away from the desired products are ideal. A simple temperature gradient can be used to cause unwanted materials to condense or deposit on cooler ends of reaction chambers. Salt byproducts are useful since they can be removed by polar solvents such as water or methanol. Care needs to be taken into choosing appropriate solvents that will not damage the targeted metal phosphides or sulfides.

Similar to the synthesis of metal oxide and doped materials mentioned in Chapter 2, transition metal phosphides and sulfides can also be synthesized using solid state metathesis methods. Extensive work by Parkin has shown that transition metal phosphides can be synthesized by using Na_3P and anhydrous metal halides.[149] They were able to produce an array of metal phosphides by heating the reagents in an evacuated ampoule to 550°C for 4 hours or by simply grinding some metal halides and sodium phosphide together under inert atmosphere. These reactions were self-propagating. The driving force behind these reactions was the formation of very stable sodium salts. They reported that the reactions produced metal phosphides, with yields ~ 90%, and a sodium halide salt which was removed by washing with methanol. Results from their powder XRD patterns showed either single or multiple metal phosphide phases.

Parkin et. al. also worked on the synthesis of metal chalcogenide materials using similar techniques compared to their metal phosphide work.[150] They synthesized a range of metal chalcogenides using Na_2X or Na_2S_2 (X = S,Se, Te) and metal halides. The

reagents were reacted in a sealed ampoule at 300 °C for 48 hours. They found that their yields were very high and targeted products were achieved by XRD analysis.

The reactions in this chapter will focus on synthesizing iron, cobalt, nickel, and copper phosphide, sulfide and thiophosphate (M-P-S) materials using SSM techniques. The reactions will involve combining metal chlorides, lithium nitride (Li_3N) as a reducing agent, red phosphorus, elemental sulfur, and phosphorus pentasulfide (P_2S_5) to yield the respective metal phosphide, sulfide or M-P-S material, LiCl and N_2 as byproducts. All of the reactions are exothermic according to Hess's Law calculations. The heats of formation for the respective metal halides and the target products are listed in Table 3.1.

Table 3.1 Heats of formation of starting reagents and target products. Data are from CRC Handbook of Chemistry and Physics 71st Edition, the book Thermochemical Data of Elements and Compounds, or the book Metallurgical Thermochemistry. (ΔH_f Li_3N = -164.56 kJ/mol)

Compound Name	**ΔH_f (kJ/mol M)**
$FeCl_3$	-401
$CoCl_2$	-393
$NiCl_2$	-306
$CuCl_2$	-218
FeP_2	-221
CoP_3	-280
NiP_2	-129
CuP_2	-121
FeS_2	-171
CoS_2	-153
NiS_2	-125
CuS	-53

3.3 Results and Discussion

3.3.1 Synthesis Analysis of M, M-P, and M-S Materials

The SSM reactions targeting the elemental metals involved heating the metal halides with Li_3N. The balanced reactions are the following:

$$FeCl_3 + Li_3N \rightarrow Fe + 3\ LiCl + 0.5\ N_2 \quad (3.1)$$

$$3\ CoCl_2 + 2\ Li_3N \rightarrow 3\ Co + 6\ LiCl + N_2 \quad (3.2)$$

$$3\ NiCl_2 + 2\ Li_3N \rightarrow 3\ Ni + 6\ LiCl + N_2 \quad (3.3)$$

$$3\ CuCl_2 + 2\ Li_3N \rightarrow 3\ Cu + 6\ LiCl + N_2 \quad (3.4)$$

The SSM reactions targeting the products FeP_2, CoP_3, NiP_2, and CuP_2 involved heating the metal halides with Li_3N and red phosphorus. The balanced reactions for each targeted material are the following:

$$FeCl_3 + Li_3N + 2\ P \rightarrow FeP_2 + 3\ LiCl + 0.5\ N_2 \quad (3.5)$$

$$3\ CoCl_2 + 2\ Li_3N + 9\ P \rightarrow 3\ CoP_3 + 6\ LiCl + N_2 \quad (3.6)$$

$$3\ NiCl_2 + 2\ Li_3N + 6\ P \rightarrow 3\ NiP_2 + 6\ LiCl + N_2 \quad (3.7)$$

$$3\ CuCl_2 + 2\ Li_3N + 6\ P \rightarrow 3\ CuP_2 + 6\ LiCl + N_2 \quad (3.8)$$

The SSM reactions targeting the products FeS_2, CoS_2, NiS_2, and CuS involved heating the metal halides with Li_3N and elemental sulfur. The balanced reactions for each targeted material are the following:

$$2\ FeCl_3 + 2\ Li_3N + 4\ S \rightarrow 2\ FeS_2 + 6\ LiCl + N_2 \quad (3.9)$$

$$3\ CoCl_2 + 2\ Li_3N + 6\ S \rightarrow 3\ CoS_2 + 6\ LiCl + N_2 \quad (3.10)$$

$$3\ NiCl_2 + 2\ Li_3N + 6\ S \rightarrow 3\ NiS_2 + 6\ LiCl + N_2 \quad (3.11)$$

$$3\ CuCl_2 + 2\ Li_3N + 3\ S \rightarrow 3\ CuS + 6\ LiCl + N_2 \quad (3.12)$$

The corresponding heats of reaction for ideal products from the above reactions are in Table (3.2). The calculated ΔH_{rxn} indicate that the LiCl production (ΔH_f = -400.9 kJ/mol) creates a very exothermic reaction, even in the case of the elemental metal reactions. The targeted products have slightly exothermic ΔH_f values (see Table 3.1). For the SSM reactions, temperatures typically reach the boiling point of LiCl around ~1380 °C and then rapidly begin to cool in seconds.[86]

The yield calculations for the SSM reactions are challenging due to mixtures of multiple crystalline products from a single reaction and will be determined later. For clarity, the yields can be separated into three categories: (**1)** targeted phase yield (**2)** resultant yield from major phase detected (**3)** mass recovery using the metal and P-S

starting mass. The targeted phase yield is the calculated yield from the balanced reactions assuming that the desired products have formed. After characterization, most reactions show multiple phases which made the actual yield a more complicated estimation that cannot be calculated accurately. The yields appear to vary due to the thermal stability of each targeted product and the starting metal halides. For the metals, Fe, Ni, and Cu have high yields, while Co metal forms a low yield. The wash solutions from the targeted elemental metal reactions consist of a very fine solid suspension and a bulky, denser solid. The solid materials were separated by first removing the dense solid with a magnet (or decanting for the copper case), and then centrifuging the fine solid suspension. The mass recovery compares the initial metal, phosphorus or sulfur reagent mass and the final washed product mass. The copper recovery percentage is greater than 100% due to additional mass uptake from precipitated hydroxides during the methanol washing step.

The yields of the metal phosphides and sulfides vary from 40 to 80 %. The iron phosphide, cobalt phosphide and cobalt sulfide samples have lower yields than the other samples. This could indicate that the initial reactions that form iron and cobalt metal were incomplete and translate to incomplete M+P or M+S reactions. The yields for the targeted products are found in Table 3.2.

Table 3.2 Calculated product yields and ΔH_{rxn} of SSM reactions involving metal halides, Li_3N, red phosphorus and sulfur. The yields are for the "targeted products" based on equations 3.1 -3.12.

Reaction Type (all have Li_3N)	**Target Product**	**Yields for Ideal Products**	**ΔH_{rxn} (kJ/mol of M)**
$FeCl_3$	Fe	80 %	-660.3
$CoCl_2$	Co	40 %	-315.1
$NiCl_2$	Ni	78 %	-401.8
$CuCl_2$	Cu	3 %	-486.6
$FeCl_3$ + P	FeP_2	30 %	-881.2
$CoCl_2$ + P	CoP_3	42 %	-595.4
$NiCl_2$ + P	NiP_2	77 %	-531.5
$CuCl_2$ + P	CuP_2	49 %	-607.6
$FeCl_3$ + S	FeS_2	81 %	-838.5
$CoCl_2$ + S	CoS_2	19 %	-580.3
$NiCl_2$ + S	NiS_2	54 %	-526.7
$CuCl_2$ + S	CuS	71 %	-539.8

3.3.2 Powder X-Ray Diffraction (XRD) and Elemental Analysis of M, M-P, and M-S Products

The XRD patterns of the products from the reaction of the metal halides and Li_3N are shown in Figures 3.1 and 3.2. Figure 3.1 shows the XRD of the product from the reaction of $FeCl_3$ and Li_3N showed crystalline peaks for iron metal (PDF #04-007-9753). The baseline is high in intensity due to the fluorescence background of iron. No other peaks are present in the pattern. XRD on the product from the reaction of $CoCl_2$ and Li_3N revealed peaks for poorly crystalline peaks for cobalt metal (PDF #00-15-0806).

The pattern has a very noisy base line which is due to the fluorescence background of cobalt when using copper radiation. There are no other noticeable peaks in the pattern.

Figure 3.2 shows the XRD of the product from $NiCl_2$ and Li_3N shows crystalline peaks for Ni metal (PDF #00-04-0850) and NiO (PDF #00 47-1049). The XRD pattern for the SSM reaction between $CuCl_2$ and Li_3N is shown in Figure 3.2 and yielded a poorly crystalline Cu metal phase (PDF #00-004-0836) with the most intense peaks corresponding to CuO (PDF #04-007-1375). The presence of the metal oxides in the XRD is most likely due to reactions of the metal nanoparticles with air or methanol during workup.

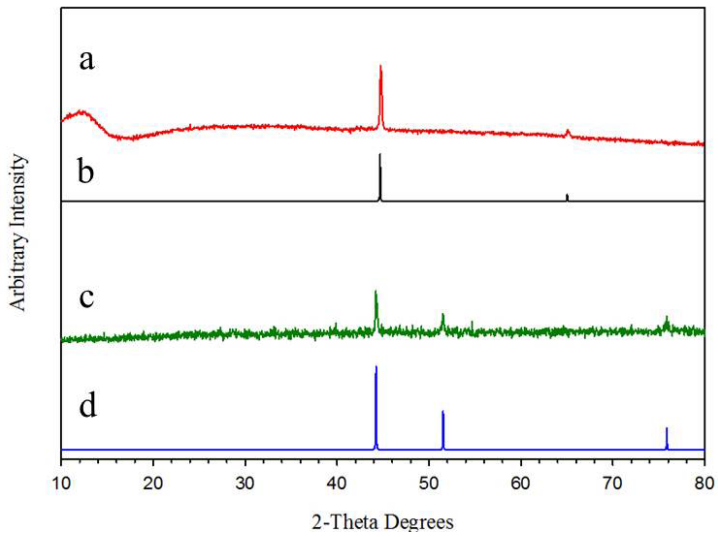

Figure 3.1 Powder XRD patterns of the iron sample (a) and the cobalt sample (c) from the SSM reaction between the metal halides and Li_3N. The reference bcc Fe metal pattern (b) and fcc Co metal pattern (d) are shown below the sample patterns.

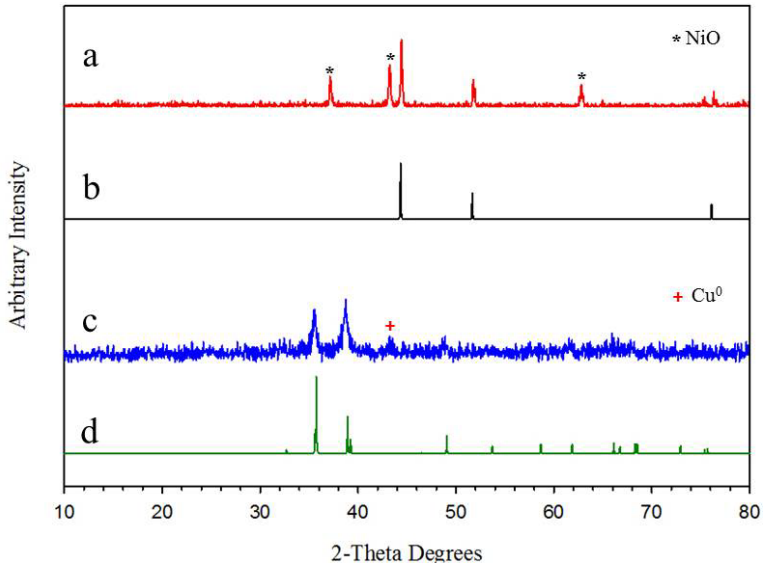

Figure 3.2 Powder XRD patterns of the nickel sample (a) and the copper sample (c) from the SSM reaction between the metal halides and Li_3N. The reference fcc Ni metal pattern (b) and CuO pattern (d) are shown below the sample patterns.

The XRD patterns of the products from the reaction of the metal halides, Li_3N and red phosphorus are shown in Figures 3.4 and 3.5. There were no metal halide or LiCl peaks in any of the samples, which indicated good washing techniques. The XRD pattern of the product from the reaction between iron chloride and red phosphorus, shown in Figure 3.4, showed a crystalline orthorhombic FeP pattern (PDF #03-065-2595). The baseline is high from the fluorescent background of iron. The peaks are small and some are close to the baseline. The targeted FeP_2 phase was not observed. No other phases could be clearly identified from the pattern.

The XRD pattern for the Co-P SSM reaction showed poorly crystalline orthorhombic CoP (PDF #00-29-0497) phase. There were no peaks for the targeted CoP_3 phase. To help improve the crystallinity, the sample was annealed at 500°C for 24 hours in an evacuated Pyrex ampoule. The XRD pattern of the annealed material, In Figure 3.4, only showed slightly improved crystalline peaks for CoP. The Ni-P and Cu-P SSM

reaction XRD patterns are showed in Figure 3.5. The Ni-P sample showed crystalline peaks for the Ni_2P (PDF # 03-065-3544). There were no other recognizable peaks in the pattern. The targeted NiP_2 phase was not present in the pattern.

The XRD pattern for the targeted Cu-P SSM reaction showed poorly crystalline Cu_3P (PDF #00-02-1263). The sample was annealed in an evacuated Pyrex ampoule at 500°C to improve crystallinity. XRD of the annealed sample showed much more pronounced Cu_3P peaks. There are also peaks that match copper metal (PDF# 00-04-0836). The presence of the copper metal peaks could indicate an incomplete reaction.

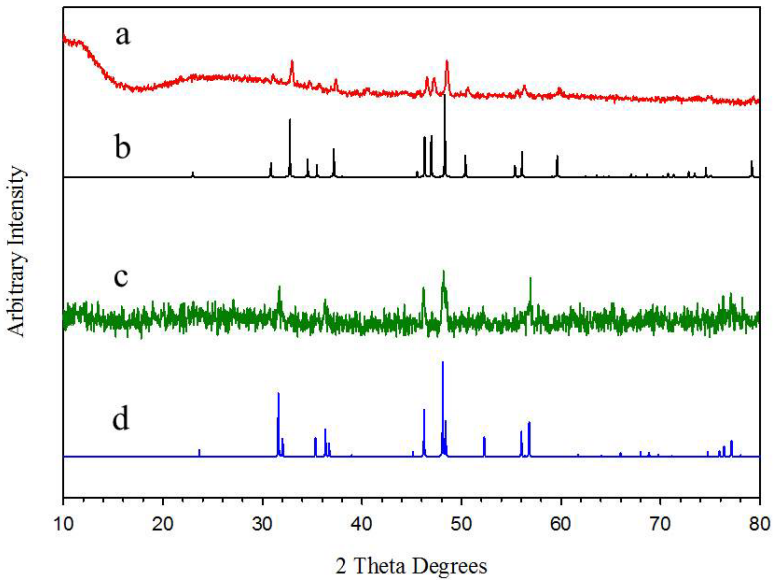

Figure 3.3 Powder XRD patterns of the iron phosphide sample (a) and the cobalt phosphide sample (c) from the SSM reaction between the metal halides, Li_3N and red P. The reference FeP pattern (b) and CoP pattern (d) are shown below the sample patterns.

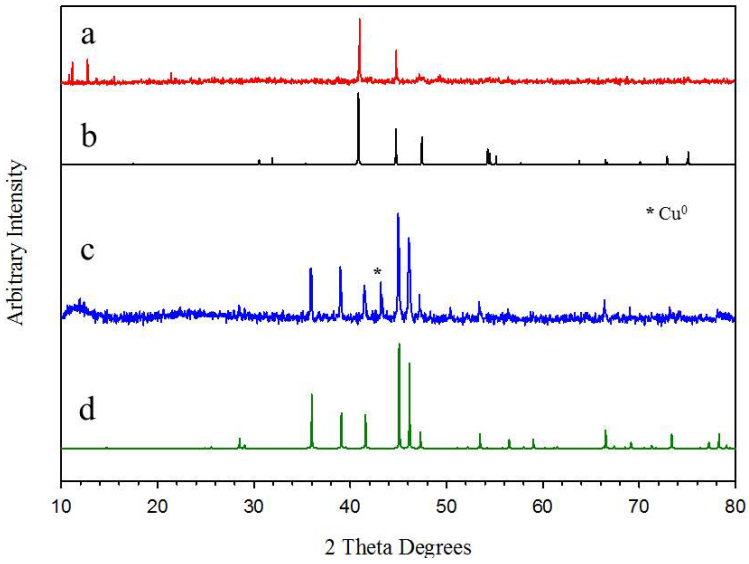

Figure 3.4 Powder XRD patterns of the nickel phosphide sample (a) and the copper phosphide annealed sample (c) from the SSM reaction between the metal halides, Li_3N and red P. The reference Ni_2P pattern (b) and Cu_3P pattern (d) are shown below the sample patterns.

The XRD patterns of the products from the reaction of the metal halides, Li_3N and sulfur are shown in Figures 3.6 and 3.7. The Fe-S sample in Figure 3.6 showed multiple phases with a large noisy baseline due to the iron fluorescence background. The most intense crystalline peaks unexpectedly agree best with an orthorhombic S_8 phase (PDF #01-078-8201). Two other phases present in the pattern are a monoclinic Fe_7S_8 phase (PDF #00-029-0723) and monoclinic $Fe_{11}S_{12}$ phase (PDF #01-029-0723) which are both close to a Fe:S composition of 1:1. No other crystalline peaks can be seen in the pattern.

The XRD pattern (not shown) of the Co-S sample showed poorly crystalline CoS (PDF #04-003-2150). The material was annealed in an evacuated Pyrex ampoule at 500°C for 24 hours to improve crystallinity. The XRD pattern of the annealed sample, shown in Figure 3.6, showed crystalline peaks of the CoS (PDF #04-003-2150). There are also very small crystalline peaks for cubic Co_3S_4 (PDF #04-004-5624). The targeted CoS_2 phase was not observed.

The XRD pattern of the products from the reaction of nickel chloride, Li_3N and sulfur gave a very noisy pattern and is in Figure 3.7. There are indications of peaks for the hexagonal pattern NiS (PDF #01-078-4718). The sample was annealed at 500°C for 24 hours to improve crystallinity. Two phases were present in the XRD pattern. The most intense peaks were for a cubic NiS_2 phase (PDF #04-003-1992). The peaks for hexagonal NiS (PDF #04-002-6886), are much less intense than the NiS_2 phase.

The XRD pattern of the copper sulfide product showed a poorly crystalline material. There are peaks that could indicate a hexagonal CuS phase (PDF #04-004-8687). To help improve the crystallinity of the product, annealing was done at 500°C for 24 hours. XRD of the annealed sample shown in Figure 3.7, gave very crystalline peaks that agreed best with the rhombohedral Cu_9S_5 phase (PDF #00-047-1748). No other peaks were present in the pattern.

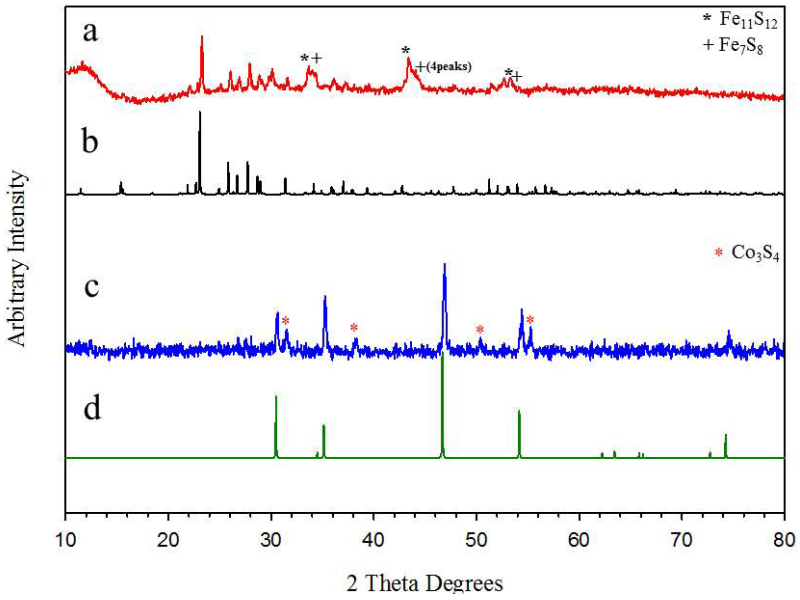

Figure 3.5 Powder XRD patterns of iron sulfide sample (a) and the annealed cobalt sulfide sample (c) from the SSM reaction between the metal halides, Li_3N and sulfur. The reference S_8 pattern (b) and CoS pattern (d) are shown below the sample patterns.

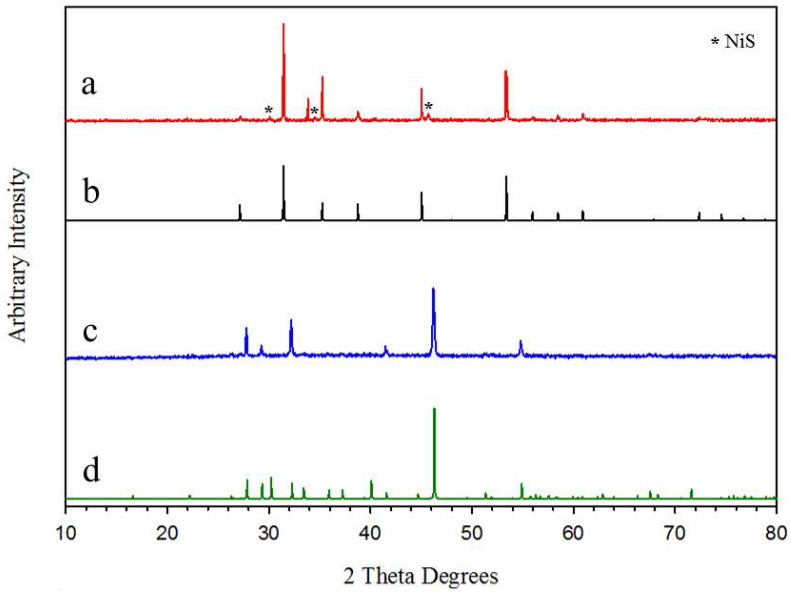

Figure 3.6 Powder XRD patterns of the annealed nickel sulfide sample (a) and the annealed copper sulfide sample (c) from the SSM reaction between the metal halides, Li_3N and sulfur. The reference NiS_2 pattern (b) and Cu_9S_5 pattern (d) are shown below the sample patterns.

The elemental analysis data of the metal, M-P, and M-S samples are in Table 3.3. All of the data were taken from thinly pressed pellets of the materials except for the metal materials. The data compares the atomic percent ratios of the metal content, P(S) and chlorine. All of the phases seen by XRD are also listed. The metal samples have no phosphorus or sulfur. There are very low amounts of residual chlorine in the samples. The atomic ratios agree well with the XRD patterns seen with the metal samples.

The M-P atomic ratios do not agree well with the phases seen by XRD, being more phosphorus rich. This may be due to amorphous phosphorus in the sample. For all M-P materials, the chlorine content was very low. The Fe:P ratio was 1:0.99 which is in good agreement with FeP that was seen by XRD. The chlorine content was ~0.03. The Co-P sample had a Co:P ratio of 1:1.64, having a richness in phosphorus. The XRD phases were CoP and Co_2P with about equal intensity. The average phosphorus content would be 0.75 between the two phases. The Ni-P sample had a Ni:P ratio of 1:1.57

which is rich in phosphorus according to the XRD phase Ni_2P. The chlorine content is the highest of all of the M-P products, giving a value of 0.23. The Cu-P sample had a Cu:P ratio of 1:0.19. This is a bit low in phosphorus content according to the phases seen. The chlorine content was 0.10.

The M-S samples have slightly poor sulfur content with respect to the phases seen in the XRD and the metal content. The Fe-S sample had a Fe:S ratio of 1:0.57 and very low chlorine content. This ratio is close to the phase $Fe_{11}S_8$ seen by XRD. The Co-S sample had a Co:S ratio of 1:0.95. This ratio is close to the major phase CoS seen in the XRD. The chlorine content was very low. The Ni-S sample had a Ni:S ratio of 1:0.72 which is a poor in sulfur compared to the XRD phases NiS and NiS_2. The chlorine content was very low. The Cu-S sample had a Cu:S ratio of 1:0.37 which is sulfur deficient compared to the Cu_9S_5 phase seen in the XRD pattern. The chlorine content was the highest of the M-S materials, with a normalized atomic ratio value of 0.27.

Table 3.3 EDS data for the metal, M-P, and M-S samples are given. Bolded phases are the major phases. The column on the far right represents the atomic ratios of either phosphorus or sulfur, and residual chlorine with respect to the metal for each sample.

Sample Type	Targeted Phase	XRD Phases	M : P(S) : Cl
Fe	Fe	Fe	1 : 0 : 0.03
Co	Co	Co	1 : 0 : 0.02
Ni	Ni	**Ni**, NiO	1 : 0 : 0.04
Cu	Cu	Cu, **CuO**	1 : 0 : <0.01
Fe-P	FeP_2	FeP	1 : 0.99 : 0.06
Co-P	CoP_3	CoP, Co_2P	1 : 1.64 : 0.07
Ni-P	NiP_2	Ni_2P	1 : 1.57 : 0.23
Cu-P	CuP_2	**Cu_3P**, Cu	1 : 0.19 : 0.10
Fe-S	FeS_2	$Fe_{11}S_8$, Fe_7S_8	1 : 0.57 : 0.04
Co-S	Co_2S_3	**CoS**, Co_3S_4	1 : 0.95 : 0.01
Ni-S	NiS_2	**NiS_2**, NiS	1 : 0.72 : 0.07
Cu-S	CuS	Cu_9S_5	1 : 0.37 : 0.27

3.3.3 SEM Analysis of M, M-P, and M-S Products

Scanning electron microscope images of SSM products targeting elemental metals, M-P and M-S products were collected. The SEM images of the metal products from the reaction between the metal halides and Li_3N are located in Figure 3.8. The images show a mixture of aggregated sub-micrometer sized particles for the iron, cobalt, and nickel samples. The iron sample consists of large aggregate smooth particles about 2-3 microns in length. The cobalt sample consists of random aggregate particles that are several microns long. The nickel sample also consists of aggregate particles. There are some plate-like structures mixed into the aggregates. The plate structures range from 2-5 microns in length. The copper sample showed a mixture of uniform rectangular prisms

and spheres. These particles range from 80-150 microns. Closer inspection of the particles showed smaller microstructures within the larger spheres and rectangular prisms.

The SEM images of the M-P products are located in Figure 3.9. The iron sample shows a mixture of small and large aggregate particles throughout the sample measuring several microns in length. The cobalt sample showed a mixture of small aggregate particles and large blocky or shard-like structures ranging from a few microns to several tens of microns. The cobalt sample consists of small rough edged particles that are several microns. The copper sample consists of large blocky structures with small aggregate particles covering them. The blocky structures have an average size of ~300 microns.

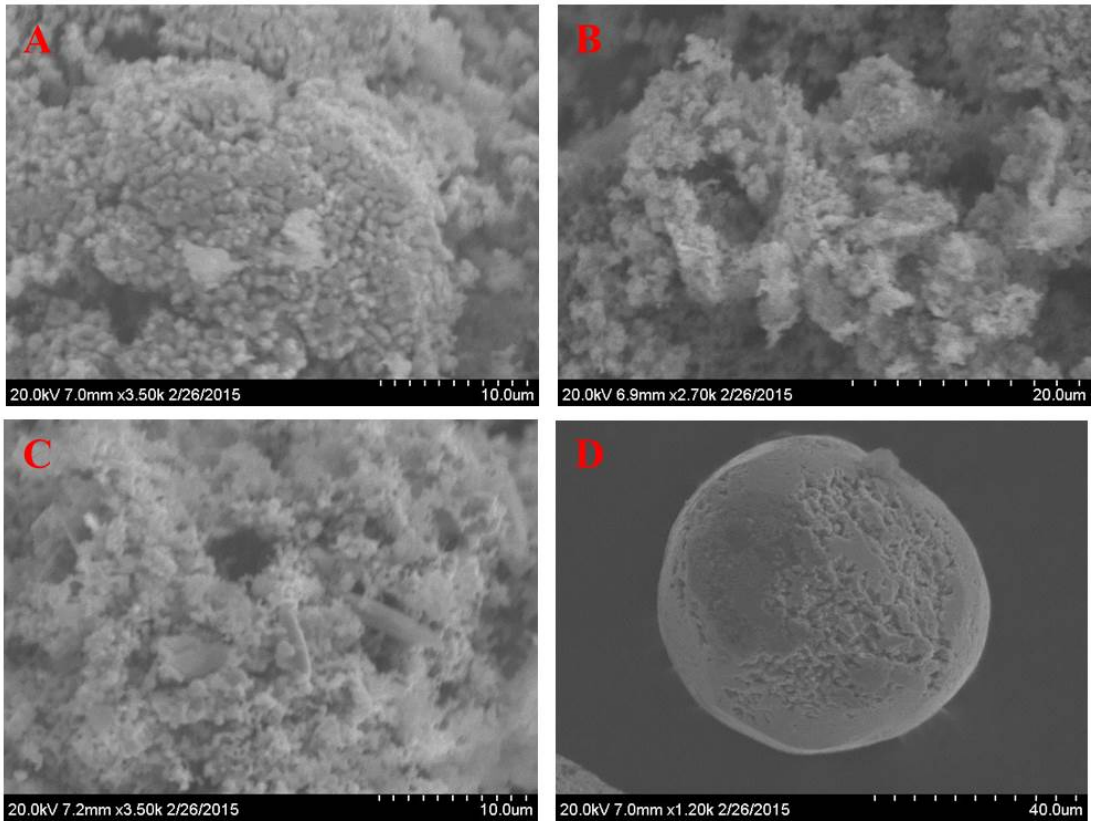

Figure 3.7 SEM images of SSM metal products from the reactions of metal halides and Li_3N. A = Fe, B = Co, C = Ni, D = Cu

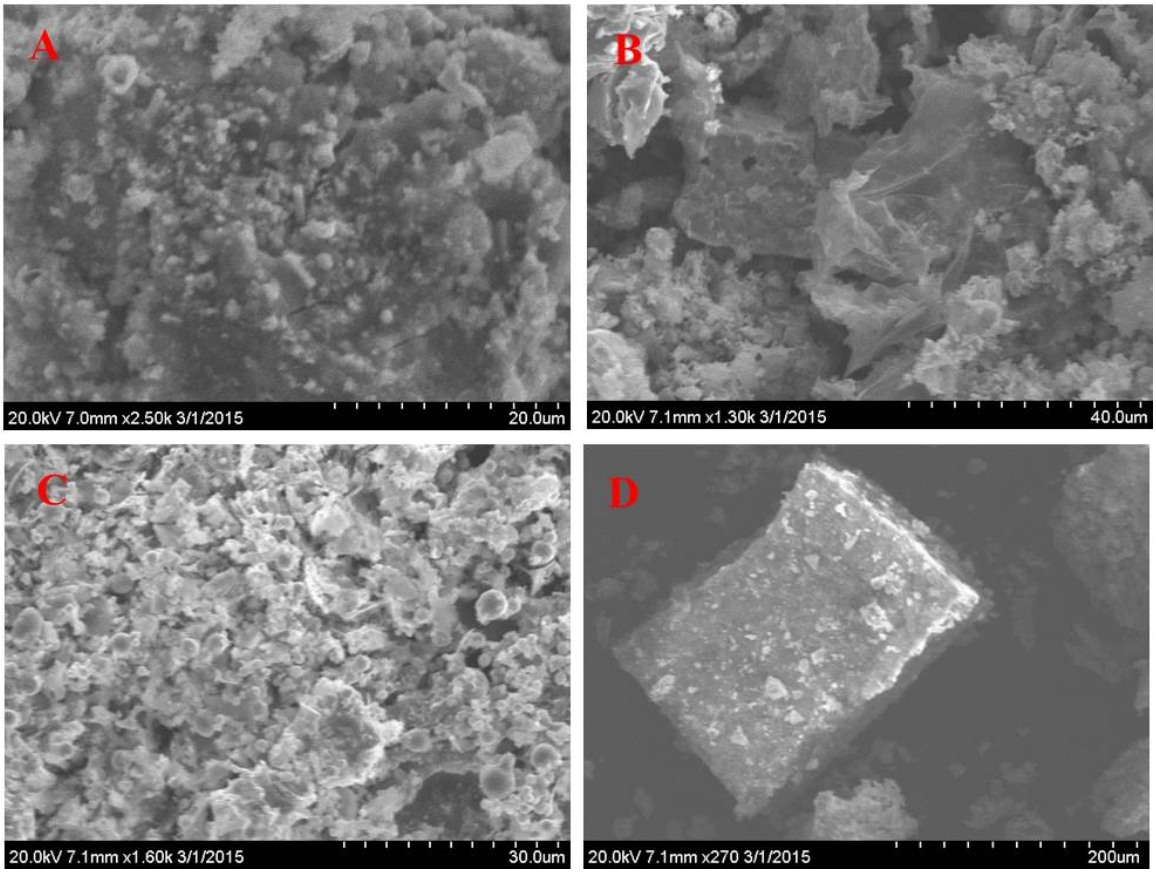

Figure 3.8 SEM images of SSM metal phosphide products from the reactions of metal halides, Li_3N, and red phosphorus. A = Fe, B = Co, C = Ni, D = Cu

The SEM images for the M-S products are located in Figure 3.10. The iron sample showed a mixture of aggregate particles and flat blocky shapes. These particles have a range of sizes, with some particles reaching sizes of ~40 microns. The cobalt sample consists of sub-micron particles that form aggregates with a variety of sizes ranging from a couple of microns to a few tens of microns. The nickel sample consists of a mixture of small aggregate particles, ranging from a few micrometers, and large blocky structures measuring up to ~25 microns in length. The copper sample also contains a

mixture of aggregate particles and larger structures that are covered with small particles of a few microns in length.

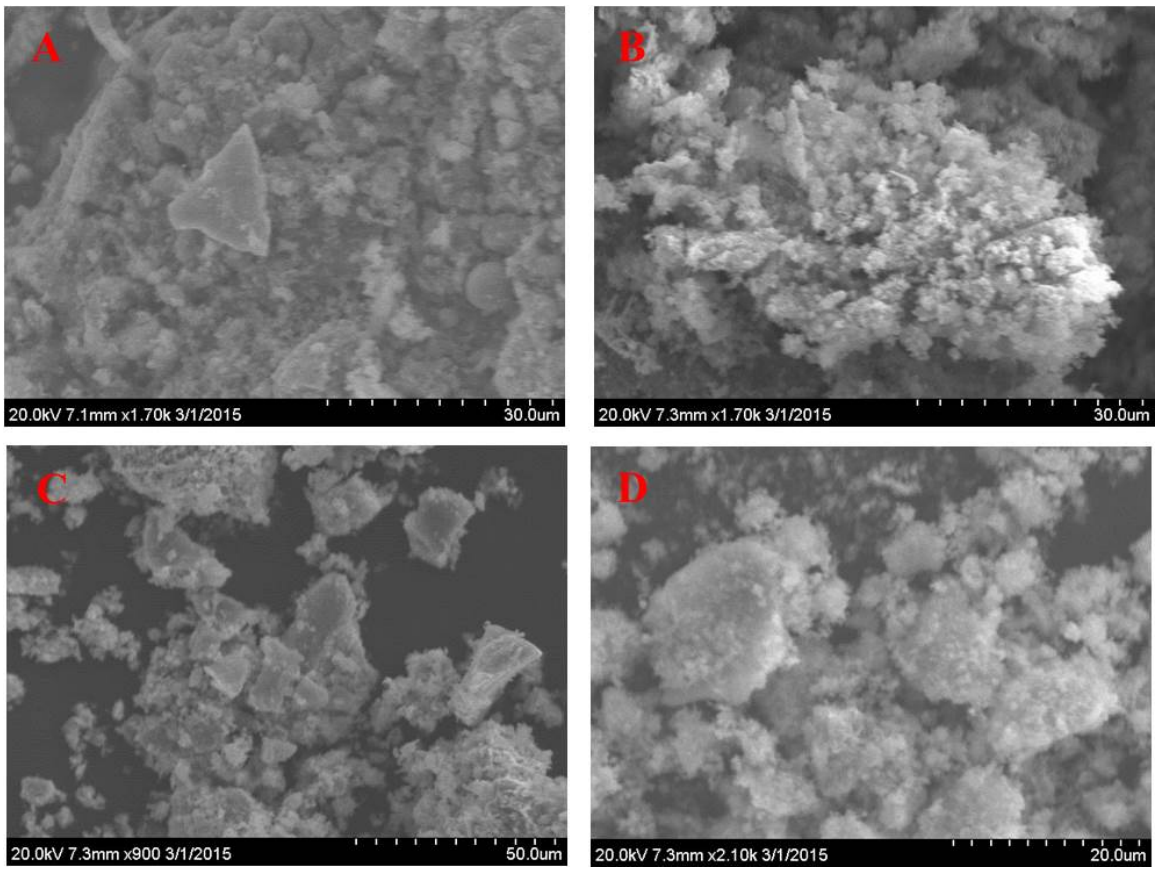

Figure 3.9 SEM images of SSM metal sulfide products from the reactions of metal halides, Li_3N, and elemental sulfur. A = Fe, B = Co, C = Ni, D = Cu

The M-P and M-S materials behave differently in terms of reactivity. This is due to the nature of sulfur and phosphorus at high temperatures. The phosphorus goes through a structural change to white phosphorus P_4 tetrahedra, and a molecular gas phase change at ~416 °C. The gaseous phase change can be troublesome in terms of producing products. This is not the case for sulfur, since it only undergoes a phase change from a

solid to a molten liquid ~289°C. The solid-molten liquid interaction of materials can produce interesting products if the both the phosphorus and sulfur reactions are combined. The reactions were combined and initial experiments were conducted to target each of the M-P and M-S products from the reactions mentioned in section 3.3.1. These products were not seen, but interesting M-P-S phases was observed.

3.3.4 Characterization Results of M-P-S Materials

The synthesis of metal thiophosphate materials brings in new challenges compared to the metal phosphide reactions. These reactions incorporate elemental sulfur or P_2S_5 into the reaction $MCl_2 + Li_3N$ (M= Fe, Co, Ni, Cu). Adding another reagent further complicates the reaction. Elemental sulfur is not as volatile as red phosphorus. P_2S_5 is also not as volatile as red phosphorus and behaves more like elemental sulfur when heated. Once the reaction chamber reaches ~ 289 °C, P_2S_5 and sulfur will become molten, viscous liquids and red phosphorus will remain a solid.

The cobalt and nickel balanced reactions have the general form (M = Co, Ni):

$$3\ MCl_2 + 2\ Li_3N + 3\ P + 9\ S \rightarrow 3\ MPS_3 + 6\ LiCl + N_2 \quad (3.13)$$

$$3\ MCl_2 + 2\ Li_3N + 1.5\ P_2S_5 + 1.5\ S \rightarrow 3\ MPS_3 + 6\ LiCl + N_2 \quad (3.14)$$

The iron and copper balanced reactions have different stoichiometry. The following balanced equations are listed:

$$2\ FeCl_3 + 2\ Li_3N + 2\ P + 6S \rightarrow 2\ FePS_3 + 6\ LiCl + N_2 \quad (3.15)$$

$$2\ FeCl_3 + 2\ Li_3N + P_2S_5 + S \rightarrow 2\ FePS_3 + 6\ LiCl + N_2 \quad (3.16)$$

$$3\ CuCl_2 + 2\ Li_3N + P + 4\ S \rightarrow Cu_3PS_4 + 6\ LiCl + N_2 \quad (3.17)$$

$$6\ CuCl_2 + 4\ Li_3N + P_2S_5 + 3\ S \rightarrow 2\ Cu_3PS_4 + 12\ LiCl + 2\ N_2 \quad (3.18)$$

As seen with the previous reactions, the nature of the SSM reactions are very violent, displacing materials all over the interior of the reactor, and being very exothermic.

The ideal yields of these M-P-S reactions are located in Table 3.3. The targeted yields were calculated assuming that the respective targeted products were isolated. As noted earlier, the yields are approximations as powder XRD identified multiple phases, which complicates an accurate yield calculation. P_2S_5 was used as a molecular comparison to the reactions using phosphorus and elemental sulfur individually. The goal was to start with a material that had pre-formed P-S bonds and then to react them with the metal formed from the reaction between metal halides and Li_3N. The iron, nickel, and cobalt samples have similar yields between their (P+S) and (P_2S_5 + S) reactions. The cobalt reaction with (P+S) has a higher yield than the (P_2S_5 + S) reaction. This may be due to the nature of how the initial reaction with cobalt chloride and Li_3N responds to the addition of two reagents that are not as volatile as red phosphorus. The mass recovery is very similar to the ideal product yield in all cases except for the copper reactions.

Table 3.4 The calculated target product yields of SSM reactions involving metal halides, P_2S_5 and elemental sulfur are shown.

Reaction Type (all have Li_3N)	**Target Product**	**Yields of Ideal Products**
$FeCl_3 + P + S$	$FePS_3$	25 %
$FeCl_3 + P_2S_5 + S$	$FePS_3$	27 %
$CoCl_2 + P + S$	$CoPS_3$	37 %
$CoCl_2 + P_2S_5 + S$	$CoPS_3$	13 %
$NiCl_2 + P + S$	$NiPS_3$	26 %
$NiCl_2 + P_2S_5 + S$	$NiPS_3$	21 %
$CuCl_2 + P + S$	Cu_3PS_4	62 %
$CuCl_2 + P_2S_5 + S$	Cu_3PS_4	60 %

3.3.5 Powder X-Ray Diffraction of M-P-S Materials from (P + S) reactions

The XRD patterns of the products from the reaction of the metal halides, Li_3N, red phosphorus and sulfur were analyzed for crystalline phases. These patterns are shown in Figures 3.11 and 3.12. The MPS_3 known structures consist of M^{2+} cations (M = Fe, Co, Ni) and $P_2S_6^{4-}$ anions bound in a layered fashion with the sulfur atoms weakly bonding together vacant layers. The missing layer is a cation layer and can be seen in the XRD by the presence of the (001) peak at 13°. The copper reaction does not produce a layered material, but an orthorhombic Cu_3PS_4 phase product. This structure is composed of Cu^+ cation and PS_4^{3-} anions. Structural representations of Cu_3PS_4 and $CoPS_3$ are shown in Figure 3.10. The $FePS_3$ and $NiPS_3$ unit cells are identical to the $CoPS_3$ unit cell. The missing layer of atoms can be seen in the unit cell with sulfur atoms aligned towards the gap. The orthorhombic Cu_3PS_4 unit cell has no such gap.

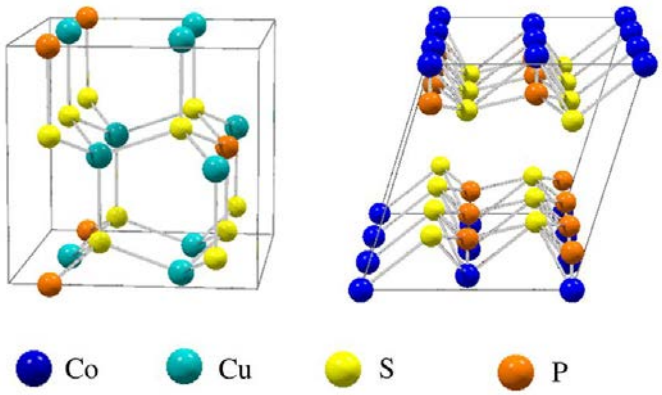

Figure 3.10 Unit cell representations of Cu_3PS_4 (left) and $CoPS_3$ (right).

The XRD of the iron thiophosphate (Fe-P-S) sample, shown in Figure 3.11, showed two phases. The most intense phase was the targeted monoclinic $FePS_3$ (PDF #04-005-1516) and the second phase present was hexagonal FeS (PDF #04-009-7914). The $FePS_3$ to FeS peak intensity ratio was ~ 3:1. There were no iron phosphide phases present. In the previous section, the iron sulfide reaction yield (~80%) was much higher than the iron phosphide yield (~30%). This could also indicate that nanoscale iron has a stronger affinity to bind to sulfur than phosphorus and give some reasoning behind why FeS is present in the sample.

The XRD of the cobalt thiophosphate sample shown in Figure 3.11 also showed two phases. The most intense peaks are from hexagonal $Co_{0.88}S$ (PDF #04-003-3441). Monoclinic $CoPS_3$ (PDF #01-078-0498) was barely detectable by its (001) peak at 13°. The baseline is quite high due to the cobalt fluorescent background. The peak ratios of the two patterns $Co_{0.88}S$ and $CoPS_3$ is ~ 8:1.

The XRD pattern of the $NiPS_3$ targeted material are shown in Figure 3.12 and also showed multiple phases. The most intense peaks were from hexagonal NiS (PDF #04-002-6886). There were two other low intensity phases identified as monoclinic $NiPS_3$

(PDF #00-033-0952) and hexagonal Ni_2P (PDF #04-003-1863). The intensity ratio of NiS to ($NiPS_3$: Ni_2P) is approximately 8:1.

The XRD pattern of the Cu_3PS_4 targeted material shown in Figure 3.12 also showed multiple phases. The most intense phase was cubic Cu_7PS_6 (PDF #00-033-0483). There are peaks for the orthorhombic phase Cu_3PS_4 (PDF #04-007-4285) with similar intensity to the Cu_7PS_6 phase. Unidentified peaks are present near 16°, 25°, 26°, and 37°.

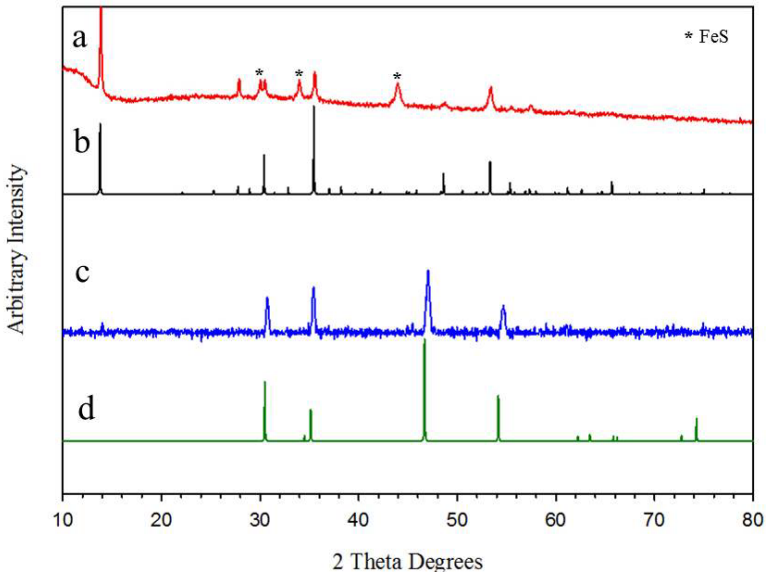

Figure 3.11 Powder XRD patterns of the Fe-P-S sample (a) and the Co-P-S sample (c) from the SSM reaction between the metal halides, Li_3N, red P and sulfur. The reference $FePS_3$ pattern (b) and $Co_{0.88}S$ pattern (d) are shown below the sample patterns.

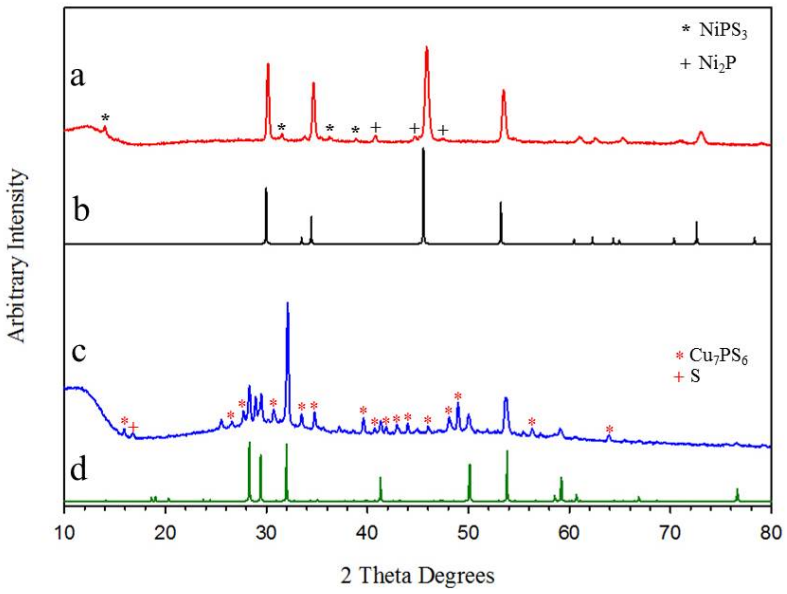

Figure 3.12 Powder XRD patterns of the nickel thiophosphate sample (a) and the copper thiophosphate sample (c) from the SSM reaction between the metal halides, Li_3N, red P and sulfur. The reference NiS pattern (b) and the reference pattern for Cu_3PS_4 (d) are shown below the respective sample patterns.

The M-P-S reactions using red phosphorous and elemental sulfur overall prefer M-S materials over M-P and M-P-S materials. The metal reduction by Li_3N, followed by the addition of phosphorus and sulfur produces the M-S materials most likely due to the intimate contact of molten liquid sulfur with the reactive metal nanoparticles versus gaseous molecular phosphorus. Even when the phosphorous content is high, no M-P phases were detected. The major XRD phases support this observation. The iron sample was the only sample that had a major MPS_3 phase of $FePS_3$. Also FeS was present, and not FeP_x phases were present.

The trend of low phosphorus content is consistent with previous experiments. This was seen in the reactions that targeted the phosphorus rich phases, yet yielded metal rich phases (ex. Co_2P, Ni_2P, Cu_3P). Also, the trend of sulfur rich phase preferences was seen in the M-S reactions. The next section will discuss the characterization from the attempted reactions which use P_2S_5, a reagent that has pre-bonded phosphorus to sulfur. This should aid with reducing phosphorus loss due to vaporization.

3.3.6 Powder X-Ray Diffraction of M-P-S Materials: P_2S_5 + S Reactions

The XRD pattern of the $FePS_3$ targeted products from the reaction of the metal halides, Li_3N, P_2S_5 and sulfur showed several phases. The XRD pattern for this reaction is shown in Figure 3.13. The most intense phase was monoclinic $FePS_3$ (PDF #04-005-1516). The second phase was hexagonal $Fe_{0.875}S$ (PDF #04-006-4096). There is also a very small unknown shoulder peak at 43°.

The XRD pattern of the $CoPS_3$ targeted product from the reaction of $CoCl_2$, Li_3N, P_2S_5, and sulfur showed multiple phases and is shown in Figure 3.13. The most intense phase was hexagonal CoS (PDF #03-065-3418) followed by the cubic phase $CoP_{0.5}S_{1.5}$ (PDF #04-007-4518). There are no peaks that indicate $CoPS_3$. The base line is very high and noisy due to the cobalt fluorescent background.

The XRD pattern of the $NiPS_3$ targeted phase from the reaction of $NiCl_2$, Li_3N, P_2S_5, and sulfur showed multiple phases and is shown in Figure 3.14. The most intense phase is NiS (PDF #04-003-2151). The next most intense phase was $NiPS_3$ (PDF #04-04-0373). Two other phases of equal intensity are $NiCl_2$ (PDF #00-022-0765) and Ni_2P (PDF #04-001-9848). There is an unknown shoulder peak at 31°. The presence of $NiCl_2$ is unexpected due to the high solubility of $NiCl_2$ in methanol and the phase identification is based on a single diffraction peak.

The XRD pattern of the Cu_3PS_4 product from the reaction of $CuCl_2$, Li_3N, P_2S_5, and sulfur showed multiple phases. The main phase that was present was elemental sulfur (PDF #01-076-0183). This pattern is not shown. There were peaks for orthorhombic Cu_3PS_4 (PDF #04-007-4285). The presence and intensity of crystalline sulfur indicates that the reaction may have not gone very far towards completion. The sample was annealed in an evacuated Pyrex ampoule for 24 hours at 500°C. The Cu_3PS_4 phase is much more intense and all of the other unknown peaks are not present. The annealed pattern is shown in Figure 3.14. The sulfur peaks are not present in the annealed pattern, however a few small unidentified peaks are present between ~35-55°.

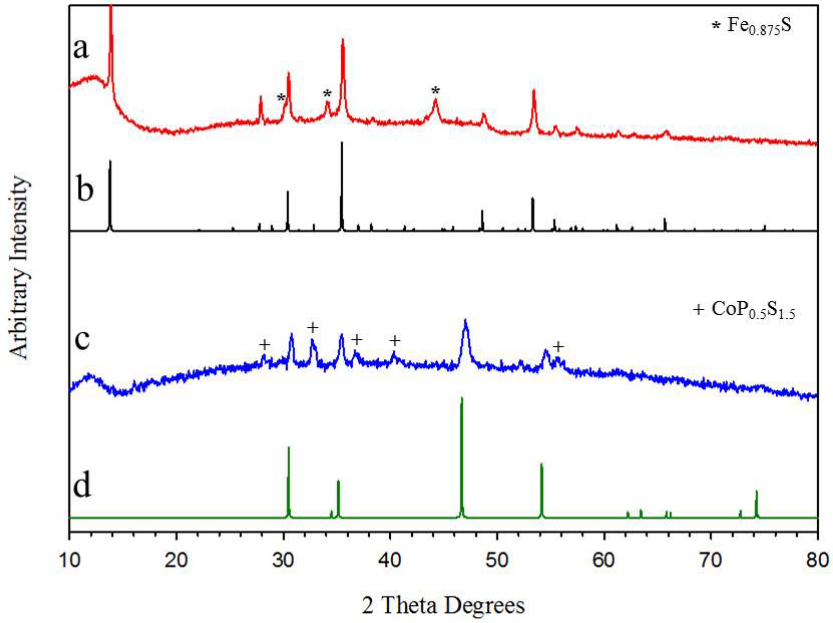

Figure 3.13 Powder XRD patterns of the Fe-P-S sample (a) and the Co-P-S thiophosphate sample (c) from the SSM reaction between the metal halides, Li_3N, P_2S_5 and sulfur. The reference $FePS_3$ pattern (b) and CoS pattern (d) are shown below the sample patterns.

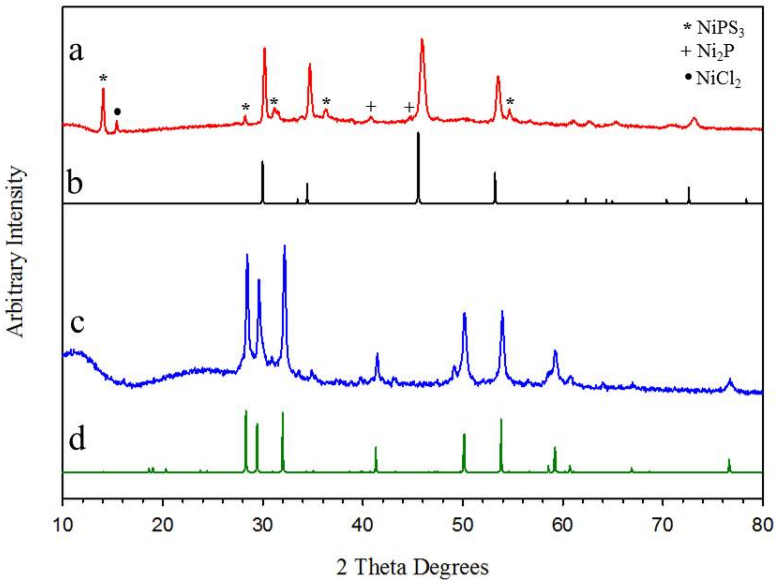

Figure 3.14 Powder XRD patterns of the Ni-P-S sample (a) and the annealed Cu-P-S sample (c) from the SSM reaction between the metal halides, Li_3N, P_2S_5 and sulfur. The reference NiS pattern (b) and the reference pattern for Cu_3PS_4 (d) are shown below the respective sample patterns.

3.3.9 Elemental Analysis of M-P-S Products

The EDS data for the M-P-S materials synthesized from the metal halides, (P + S), and Li_3N is shown in Table 3.5. The samples were either flat regions of free powders or pressed pellets. The XRD data showing all phases was added to help understand the atomic ratio data. All of the samples show very low chlorine content which demonstrates good washing techniques. A general trend in all of the samples is that the phosphorus atomic ratios were relatively low. The ideal M:P:S ratios for the iron, cobalt, and nickel samples should be 1:1:3 and the copper ratio should be 1:0.33:1:33 according to the targeted phases. The nickel sample has the closest ideal phosphorus ratio.

The iron (P+S) sample has an atomic ratio that more closely resembles the FeS phases seen in the sample, however this phase is not the major phase seen by XRD. The cobalt (P+S) sample atomic ratios most likely resembles the $Co_{0.88}S$ phase which is the

most intense phase seen in the XRD data. The nickel (P+S) sample also has relative atomic ratios closer to a 1:1 NiS phase. The copper (P+S) sample gives an atomic ratio that matches the Cu_7PS_6 phase shown in the XRD. The (P_2S_5 + S) versions have higher sulfur content than the (P+S) and are close to the atomic ratios of the dominant phases seen by XRD, except for the nickel case, which is remarkably low.

The EDS data gives information over the regions selected and only a few microns deep within the sample. The data can be compared to the XRD data in terms of the crystalline phases seen. If any amorphous material is in the sample, XRD will not be able to detect this. EDS will show elemental signals for given elements in the sample if they are amorphous or crystalline. Since the samples have several mixed phases, the atomic ratios will vary from the ideal targeted phases.

Table 3.5 EDS and XRD data on the M-P-S materials. The XRD phases are in order of intensity from left to right with the bolded phase as the most intense phase. Atomic ratios lower than the detection limit of the instrument is denoted with < 0.01.

Sample Type	Targeted Phase	XRD Phases	M : P: S : Cl
Fe, P + S	$FePS_3$	**$FePS_3$**, FeS	1 : 0.42 : 0.96 : < 0.01
Co, P + S	$CoPS_3$	**$Co_{0.88}S$**, $CoPS_3$	1 : 0.16 : 0.95 : < 0.01
Ni, P + S	$NiPS_3$	**NiS**, $NiPS_3$, Ni_2P	1 : 0.63 : 0.72 : 0.14
Cu, P + S	Cu_3PS_4	**Cu_7PS_6**, Cu_3PS_4	1 : 0.22 : 0.83 : 0.04
Fe, P_2S_5 + S	$FePS_3$	**$FePS_3$**, $Fe_{0.875}S$	1: 0.43 : 1.53 : < 0.01
Co, P_2S_5 + S	$CoPS_3$	**CoS**, $CoP_{0.5}S_{1.5}$	1: 0.28 : 1.08 : < 0.01
Ni, P_2S_5 + S	$NiPS_3$	**NiS**, $NiPS_3$, Ni_2P, $NiCl_2$	1: 0.07 : 0.24 : < 0.01
Cu, P_2S_5 + S	Cu_3PS_4	**Cu_3PS_4**	1: 0.24 : 0.89 : 0.017

3.3.10 SEM Analysis of M-P-S Products

The SEM images of the M-P-S materials synthesized from (P +S) are shown in Figure 3.15. All of the samples show aggregate particles of various sizes. The iron sample had more fused particles than any of the other samples with particles ranging from ~3-15 microns. The cobalt sample showed large shard like particles with some defined edges. The sizes of these particles range from a few microns to ~ 10 microns. The nickel sample consisted of shard-like chunks which ranged from ~10-50 microns. The copper sample consisted of a mixture of aggregate shard-like shapes. These shapes range from a few microns to several tens of microns in length.

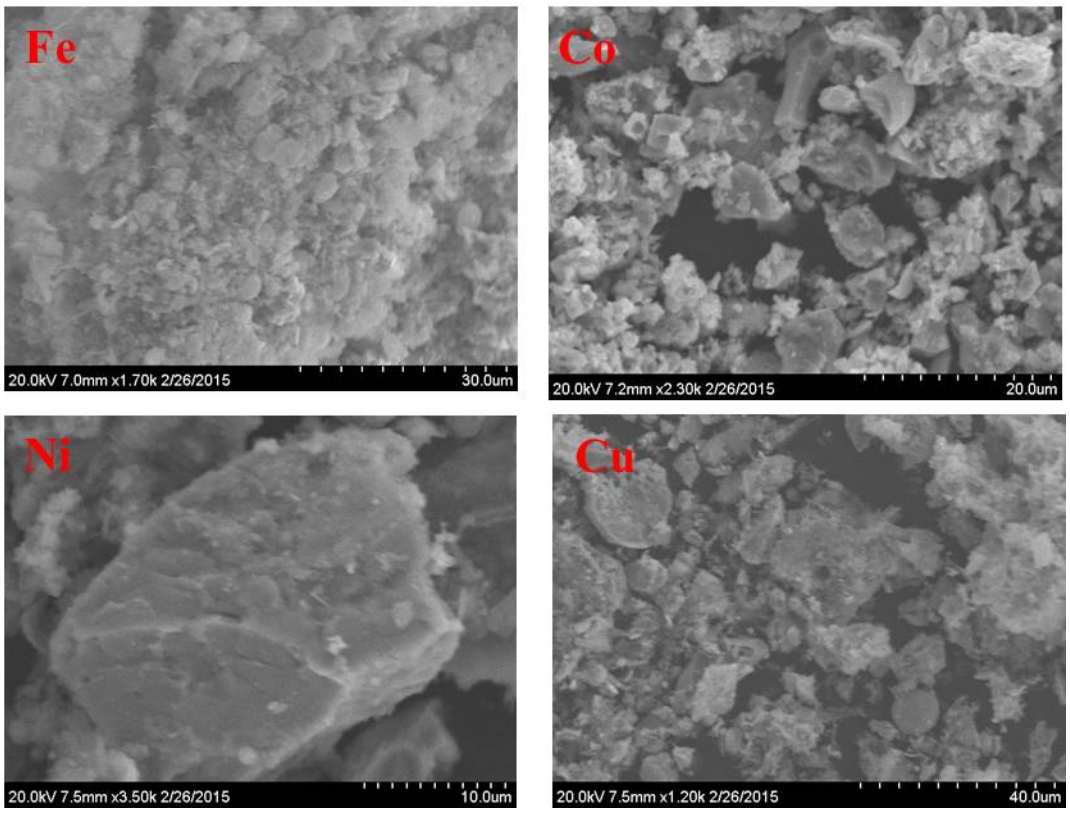

Figure 3.15 The SEM images of M-P-S materials from the SSM reactions of the metal halides, Li_3N and P + S are shown. Samples were free powders pressed into carbon tape and did not have a conductive coating.

The SEM images of the M-P-S materials synthesized from the metal halides, Li_3N and (P_2S_5 +S) are shown in Figure 3.16. All samples consist of fused aggregates. The iron sample has a mix of aggregates and shard-like shapes. These morphologies range in size from a few microns to ~15 microns. The cobalt sample shows some blocky structures mixed in with aggregates. The shapes range from a few microns to ~10 microns. The nickel sample consists of islands of fused aggregates. The aggregates range in size from 2-10 microns. The islands are several tens of microns. The copper sample has interesting morphology. There is a mix of fused blocky and round smooth shapes. The blocky structures range in size from ~2-5 microns with longer growth in one direction. The round shapes range from ~1-10 microns.

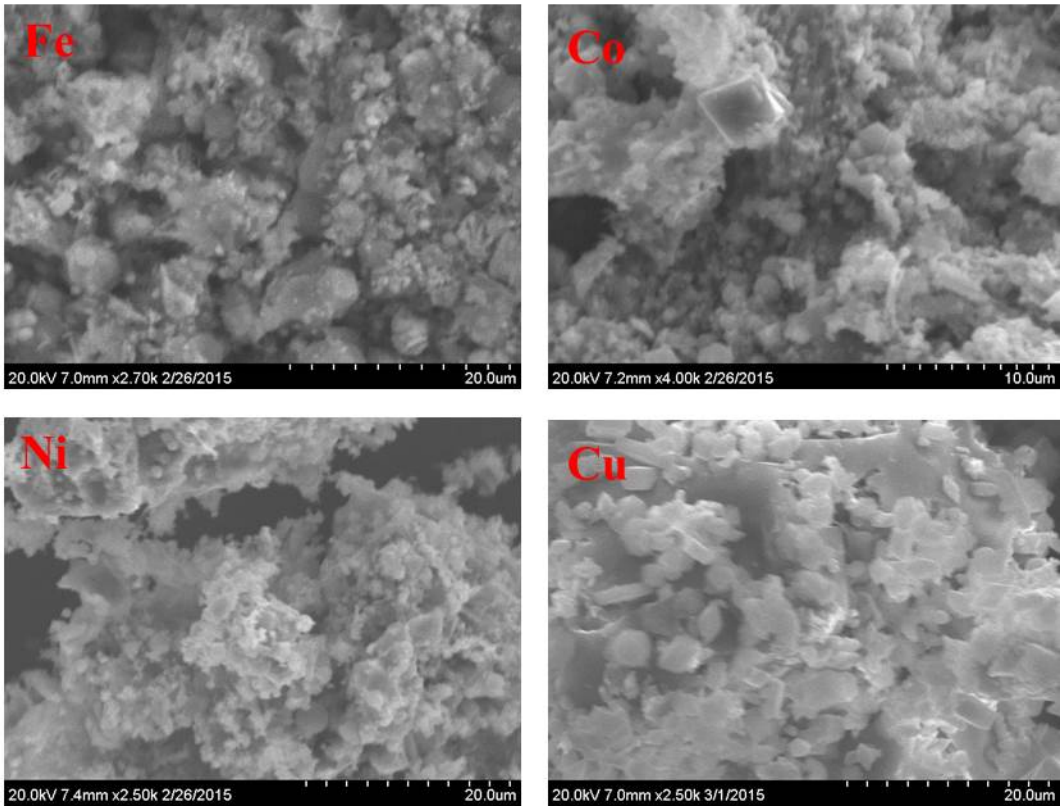

Figure 3.16 SEM images of M-P-S materials from the SSM reactions of the metal halides, Li_3N and P_2S_5 + S

3.4 Reaction Mechanism Analysis

SSM reactions in the bomb reactor occur rapidly in a quick cooled, molten LiCl product flux, which can yield metastable materials and unusual phases. The metal halide reactions with Li_3N produced nanoscale metals, some of which have air reactivity over time. The reasoning behind why the metals are present is that the metal nitrides that may form will rapidly decompose due to extreme temperatures. The synthesis of Ni_3N for example, is also targeted in SSM experiments. This reaction is exothermic and has the following balanced reaction: $3\ NiCl_2 + Li_3N \rightarrow Ni_3N + 6\ LiCl + N_2\ \Delta H_{rxn} = -456$ kJ/mol Ni. While Ni_3N may form, the reaction temperature is dependent on the boiling point of the LiCl salt, which is ~ 1380 °C. Ni_3N decomposes in an inert atmosphere to Ni metal and N_2 gas at ~ 300 °C. The material will not survive in the hot molten flux of LiCl, leaving Ni metal and any unreacted starting material behind. Similarly, this also occurs to iron, cobalt, and copper nitrides. This makes sense since the respective metals were seen in the XRD patterns for each SSM reaction of the metal halides and Li_3N alone.

The complexity of the SSM reaction mechanism increases with the addition of red phosphorus. Red phosphorus sublimes at ~ 416 °C to white phosphorus under inert atmosphere. Since the nature of the reaction will reach at least 1380 °C for a short time, the red phosphorus becomes a very reactive molecular gas. The white phosphorus allotrope reacts with the nanoscale metal from the reaction between halides and Li_3N. At this point, there is a competition for product formation between the metal particles and M-P materials. The vaporization of phosphorus also limits the formation of phosphorus rich phases, hence the metal rich phases seen in the XRD patterns. Since these reactions occur very rapidly, the thermodynamics of the reaction are difficult to interpret or control.

The SSM reactions propagate, heating neighboring solids to produce products. In order for metal phosphides to form, the metal halide, red phosphorus and Li_3N need to be in intimate contact with each other. If phosphorus is not around, the elemental metal will

form instead. It is assumed that the powders are homogeneous from grinding prior to heating, but mixing is limited to grinding with a mortar and pestle and the lack of solvent. In addition to this, the red phosphorus sublimes, leaving the vicinity of the other solid reagents and then re-depositing quickly due to cooling. The enthalpy of formation between the elemental metals and metal phosphides favors the metal phosphides as seen in Table 3.2. However, elemental metal is seen in some of the XRD patterns, thus indicating incomplete (M + P) reactions.

The addition of sulfur causes the reactions to behave differently. The SSM reactions between the metal halides, sulfur and Li_3N produce M-S products and no elemental metal byproduct. This may be due to how sulfur behaves at high temperatures. Sulfur melts at ~115 °C and begins to boil at ~444 °C. Upon phase transformation from solid to liquid, sulfur will become a very viscous dark red liquid. Further heating will cause vaporization. The liquid form of sulfur would be in better intimate contact with the metal particles formed from the reactions between the metal halides and Li_3N than phosphorus vapor, and becomes more reactive, thus producing M-S products. The M-S reactions also have ΔH_{rxn} that are more exothermic than the elemental metal reactions and will produce M-S phases if the reagents are in contact for sufficient amounts of time.

Adding both red phosphorus and sulfur to the SSM reactions consisting of metal halides and Li_3N brings in a more complex reaction scheme. From the characterization, it has been seen that M-S and M-P-S materials form. There are no metal or M-P phases present in the XRD patterns. These products make sense according to the previous reaction mechanism theories. The heats of formation between the M-P and M-S materials are similar with the phosphides being more favorable in most cases, but not dramatically different. Both M-S and M-P energies are more favorable than the elemental metals. The presence of M-S material is seen due to the flux like behavior of sulfur. The lack of the M-P material is most likely due to the fact that the M-P-S materials are more stable and that some of the phosphorus sublimes out of the mixture.

The sulfur flux seems to be able to keep some phosphorus intimately mixed in and thus the M-P-S materials form.

This idea also leads into the possibility of a stepwise reaction mechanism of the metals reacting with the elemental sulfur first and then reacting with phosphorus vapor. Another possibility is that the available phosphorus could also form PCl_3, a by-product seen in ampoule reactions in our previous work. PCl_3 is a liquid at room temperature and would vaporize upon exposure to air. If this is the case, the metal sulfides and metal rich phases would be more prevalent.

The reactions with P_2S_5 simplify the reaction mechanism by having pre-formed P-S bonds. P_2S_5 melts at ~288 °C and boils at ~514 °C. The behavior of this solid is similar to elemental sulfur containing a phosphorus component that does not sublime out. The reactions involving P_2S_5 produced mainly M-P-S materials and some M-S materials. Note that additional elemental sulfur was added to balance the reactions. This may contribute to additional M-S formation. However, according to the XRD patterns, the major phases were the M-P-S materials, except for the nickel reaction that had NiS as the major phase.

3.5 Conclusions

The SSM reactions between the metal halides, Li_3N, red phosphorus and sulfur yielded a variety of phases. The general reaction mechanism involves the initial formation of reactive metal nanoparticles that react with phosphorus and sulfur, with a preference to form metal rich or sulfur containing phases. The use of P_2S_5 tends to form M-P-S phases better than using the elements individually. The target phase yields for the reactions vary from each reaction. The yields that are noticeably low indicate that the initial reaction of $MCl_x \rightarrow M$ is not very successful.

The EDS data varied with the metal to P(S) content compared to the phases seen in the XRD. The metal reactions showed very low to no chlorine content which indicates

good overall metal halide reaction with the other reagents and effective washing techniques. The M-P reactions had phosphorus rich atomic ratios relative to the metal while the M-S reactions were slightly poor in sulfur content. The M-P-S reactions had low phosphorus content but high sulfur content, as seen from the M-S phases seen in the XRD data. The SEM data overall showed aggregates of varying sizes depending on the reaction.

To help improve targeted phases, the reactions can be done in sealed ampoules. The next chapter will utilize previous research on metal phosphides and expand the work with metal sulfide materials. The goal is to simplify the SSM reactions to reduce byproduct formation and to improve overall yield and product purity.

CHAPTER 4
SYNTHESIS OF TRANSITION METAL PHOSPHIDES AND THIOPHOSPHATES USING SEALED AMPOULE REACTIONS

4.1 Background Info on Transition Metal Phosphides and Thiophosphates: Synthesis and Structure

Ampoule synthesis is one method used in solid state chemistry to conduct reactions in a sealed, inert or evacuated atmosphere. The closed environment allows a direct interaction between solid reagents. Glass tubes are chosen initially for their inertness and affordability. Common low temperature ($T < 600$ °C) ampoule synthesis is done in Pyrex glass ampoules. Higher temperature reactions can be done using silica ($T \sim 1100$ °C) or metal ampoules. Care has to be taken for reactions within sealed tubes, since pressure build up from gas evolution can explode glass tubes. It is advised to pre-calculate the maximum possible pressure (~5-10 atm) before performing reactions that evolve gas.

The previous chapter involved the synthesis of transition metal phosphide, sulfide and M-P-S materials using a rapid solid state metathesis approach. This process produced materials in modest yields very quickly. One major disadvantage was that the reactions produced multiple phosphide or sulfide phase materials which made product analysis and characterization challenging. This chapter will focus on a more direct approach to synthesize single phase materials using glass ampoule heating. These reactions are advantageous since there is one targeted volatile byproduct, PCl_3, which can be eliminated by temperature gradients. The reactions involve reacting metal chlorides

with elemental red phosphorus, yellow sulfur, and P_2S_5 to target different M-P, M-S, and M-P-S phases. Initial work using MCl_x and red or white phosphorus was described in our previous work using pressed pellets.[2] The current studies show that the use of pellets is generally not required.

Since these reactions will be done in sealed ampoules, pressure must be taken into account. The SSM reactions in Chapter 3 rapidly produced N_2 gas as a byproduct, but the reactor vented gas easily. The ampoule reactions in this chapter do not use Li_3N as a reagent, so N_2 gas is not an issue. There is a volatility issue with phosphorus once the temperature reaches ~416 °C where it vaporizes into a P_4 species. The main volatiles in sealed ampoules should be phosphorus, PCl_3, and possibly sulfur chloride species. The pressure was calculated for the estimated ampoule volume and was ~4 atm of pressure for all reactions assuming complete reactions.

There is an extensive list of metal phosphide, sulfide, and M-P-S phases that could form from the ampoule reactions. These materials are commonly synthesized from solution phase methods[151] or from the elements in the solid state and are often targeted for their uses as semiconductors, in lithium ion batteries,[152,153] fuel cells, and hydrodenitrogenation and hydrodesulfurization (HDN/HDS) catalysis.[154,155-157] Some of the common metal phosphide phases for each metal are: for iron- Fe_2P, FeP, FeP_2, FeP_4, for cobalt- Co_2P, CoP, CoP_2, CoP_3, CoP_4, for nickel Ni_8P_3, Ni_5P_2, Ni_5P_4, Ni_3P, $Ni_{12}P_5$, Ni_2P, NiP, NiP_2, NiP_3, for copper- Cu_3P, Cu_2P_7, CuP, CuP_2. Similarly, there are several metal sulfide phases and some of the common phases for each metal are: for iron Fe_7S_8, Fe_3S_4, Fe_3S, Fe_2S_3, FeS, FeS_2, for cobalt, Co_9S_8, Co_3S_4, CoS, CoS_2, for nickel, $Ni_{17}S_{18}$,

Ni_7S_6, Ni_6S_5, Ni_3S_4, Ni_3S_2, NiS, NiS_2, and for copper, $Cu_{31}S_{16}$, Cu_9S_5, Cu_7S_4, Cu_2S, CuS, CuS_2.

At normal to low pressures and at moderate temperatures ($T \leq 500$ °C), metal rich phases are typically observed. Compounds can be synthesized in a manner of ways such as solvothermal/hydrothermal synthesis,[158,159] reduction of phosphate or sulfate materials, or by ampoule heating using solid state metathesis reactions. Chalcogen rich phases, such as NiP_2, are traditionally synthesized at high temperatures and pressure from the elements.[160] The solids are pressed together in an anvil press coupled with a thermocouple type of detector to record the temperature. Pressures and temperatures are on the order of 65 bars and 1200 °C.[160]

Mixed phases of phosphorus and sulfur compounds can also form. These materials are used for their semiconducting properties[161] and improved magnetic[162,163] and electrical properties,[164,165] battery applications from intercalation of ions and molecules within the layered MPS_3 family of materials. The commonly observed phases observed for the respective metals are: for iron $Fe_3P_2S_8$, FePS, $FePS_3$, for cobalt Co_3PS_6, Co_2PS_3, CoPS, $CoPS_3$, for nickel $Ni_3P_2S_8$, Ni_3PS_6, NiPS, $NiPS_3$, and for copper, Cu_3PS_4, $CuPS_2$.

The heats of formation of the reagents and targeted products are identical to the products in Table 3.1 in Chapter 3. Since the Li_3N/LiCl reagent/product pair is not present here, the overall reactions in this chapter are not as exothermic as the SSM reactions. The reactions and their thermochemistry will be described in the following sections. Briefly, the reactions involve MCl_x (M = Fe, Co, Ni, Cu) and (P + S) or (P_2S_5 + P) in sealed ampoules. The products were isolated by transporting PCl_3 to the opposite

end of the ampoule using a temperature gradient. The targeted products were chosen either by their thermo-chemical stability or phases seen in previous research. Prior research suggests target phosphorus rich phases as metal rich targets yield phosphorus rich and MCl_x reagents. Reactions conditions such as temperature, time, and pressure could form non-traditional phases.

4.2 Experimental Section

4.2.1 Starting Materials

Transition metal phosphides (M-P) and thiophosphates (M-P-S) were synthesized using sealed Pyrex ampoules. Metal sulfide (M-S) synthesis was also attempted, but was not successful. This will be discussed in detail in the later sections. Medium or heavy walled glass tubes (I.D. ~ 9 mm, O.D. ~13 mm) in combination with small reagent masses, were used to prevent any explosions. Explosion containment using pavement bricks on the exit sides of clam-shell tube furnaces was implemented as well. The starting reagents and their respective purities are the following: $FeCl_3$ (Alfa Aesar, 98%), $CoCl_2$ (Alfa Aesar, 99.7%), $NiCl_2$ (Alfa Aesar, 99%), $CuCl_2$ (Alfa Aesar, 98%), red phosphorus (Aldrich, 99%), sulfur (Alfa Aesar, 99.5%), P_2S_5 (Sigma Aldrich, 99%), methanol (Fisher Scientific, 99.9%), acetonitrile (Fisher Scientific, 99.9%), and ammonium hydroxide ((Fisher Scientific, 14.8 M) that were used as wash solvents in some cases.

4.2.2 Synthesis of M-P and M-S Materials

Transition metal phosphides were synthesized in sealed ampoules using metal halides and red phosphorus. We have synthesized some of these materials in a recent publication in pellet form. The materials produced in our current work were synthesized in the free powder form with similar reactivity and yields. Typically 0.500 g of the metal halides $NiCl_2$ (3.86 mmol), $CuCl_2$ (3.72 mmol), $CoCl_2$ (3.85 mmol) and $FeCl_3$ (3.08 mmol) were reacted with stoichiometric amounts of red phosphorus which were designed to yield the respective metal phosphide and PCl_3 byproduct (volatile liquid at room temperature). The starting materials were ground together in an argon filled glove box with an agate mortar and pestle and then loaded in either a Pyrex or quartz medium wall thickness (~9 mm O.D.) glass tube using a custom made glass funnel. The tube was then attached to a Cajon compression fitting with a Teflon valve attached. The valve was closed and the setup was removed from the glove box. The tube was evacuated on a Schlenk line by opening the valve of the connector slowly to vacuum, and after ~ 15 minutes of evacuation, the ampoule was flame sealed under dynamic vacuum. All reactions minus the iron reaction were heated in a horizontal Linberg Blue M-clamshell tube furnace to 500 °C with a ramp rate of 100 °C per hour (max temperature of 500 °C achieved in 5 hours). The iron reaction used a quartz tube and was heated to 700 °C with a ramp rate of 100 °C per hour. All reactions were heated for approximately 18-24 hours at the reaction temperature.

After heating, the end of the tube without solid was pulled out of the furnace slowly, and allowed to cool down to room temperature. During that time, a colorless liquid condensed at the cold end. When no further liquid condensed, the furnace was

turned off and the entire tube was allowed to cool down to room temperature. Once completely cooled, the tube was opened in air in the hood by making a scratch at the center of the ampoule with a tungsten carbide knife and then snapped open carefully in air. A small amount of smoking occurred on the liquid end. No smoking was seen from the solid. The solid was allowed to sit in air for several minutes, weighed and then stored in a glass vial in the argon filled glove box.

The metal sulfide synthetic attempts involved similar reactions of metal halides $FeCl_3$, $CoCl_2$, $NiCl_2$, or $CuCl_2$, with elemental sulfur in sealed, evacuated Pyrex ampoules. The reaction conditions were identical to the metal phosphide reactions. The reactions were heated to 500 °C at a ramp rate of 100 °C per hour, and then held at 500 °C for approximately 18-24 hrs. After heating, the end of the ampoule without solid was pulled out of the furnace, allowing any liquid to condense. Typically yellow liquid transports were observed. The tubes were opened in the same fashion as mentioned earlier once cooled to room temperature and the solid was collected and stored in the glovebox.

4.2.3 Synthesis of M-P-S Materials

Transition metal thiophosphates were synthesized using a similar synthesis description for the transition metal phosphides. The reactions were done using two different sources of phosphorous and sulfur: elemental red phosphorus + sulfur, and red phosphorus + P_2S_5, a molecularly mixed version of the elements. Initial experiments involved targeting specific individual metal phosphides and sulfides (e.g. FeP_2 and FeS_2). The targeted mixed phases were not observed versus other products. More information on these experiments will be discussed in the following sections. Later experiments

involved targeting a thermodynamically stable family of layered MPS_3 materials. The copper reactions targeted Cu_3PS_4 since copper does not form a MPS_3 phase.

For the M-P-S reactions using the elemental P/S reagents, stoichiometric amounts of the metal halides $FeCl_3$, $CoCl_2$, $CuCl_2$, or $NiCl_2$, red phosphorus, and sulfur were all ground together using an agate mortar and pestle in the argon filled glove box. The powders were loaded into a Pyrex tube, evacuated, and sealed under vacuum. All reactions were heated to 500 °C, with a ramp rate of 100 °C/hr, and held at 500 °C for ~18-24 hours. The ampoules were cooled in a similar fashion as with the previous reactions, however, in addition to a colorless liquid transporting, in some cases a yellowish-white solid would transport as well. The samples were stored in glass vials in the argon filled glove box.

4.2.4 Sample Characterization

Powder X-ray diffraction (XRD) was done using either a Siemens D5000 or a Bruker D8 Advance DaVinci Diffractometer. All materials were scanned using nickel filtered Cu K-α X-ray irradiation, 40kV and 40mA energy output, with a 2-theta angle range from 10 to 80 degrees 2θ. The step size was 0.05 degrees and the slit widths of the X-ray source and detector were 1.00 mm and 5.90 mm respectively. The samples were prepared for analysis by first grinding them down to fine powders using a mortar and pestle. The samples were mounted onto pre-cut glass microscope slides, affixed by air drying in an acetone slurry or by using a very thin layer of vacuum grease. M-S isolated "products" were prepared with a vacuum grease matrix since the acetone slurry method dissolved them. All samples were pressed down flat before examination. The

morphology and elemental analysis of the samples was investigated using scanning electron microscopy (SEM) and energy dispersive spectroscopy (EDS) on a Hitachi S3400 (thermionic) or S4800 (field emission) system. Samples were prepared by pressing pre-ground samples onto carbon tape on aluminum stubs. The samples were not coated with conductive coatings. EDS sample stubs were prepared in a similar fashion but with thin pellets made from a KBr hand press. The magnetic susceptibility was measured using a Johnson-Matthey magnetic susceptibility balance. This was done by grinding the products using a mortar and pestle and then loading them into the sample tube. The products were tested for their magnetic attraction at room temperature. Diamagnetic corrections ion were performed on the data. Optical measurements were performed using a solid state UV-Vis LabSphere RSA attachment on an HP 8453 UV-Vis spectrometer at room temperature. Sample preparations were done by embedding the material into a pre-cut piece of filter paper and then clamped between two glass microscope slides. The samples were tested or their diffuse reflectance. The absorption data was converted to Kubelka-Munk units and the approximate energy band gap and onsets were determined. The vibrational properties of the metal thiophosphate materials were analyzed in KBr pellets using a Nicolet Nexus 760 FT-IR spectrometer.

4.4 Results and Discussion

4.4.1 Synthesis and Analysis of M-P and M-S Materials

Figure 4.1 shows an example M-P (also M-S) ampoule reaction schematic. As noted in the figure, the metal halides and red phosphorus (or sulfur) are loaded into one end of the Pyrex (or silica) tube and slowly heated. When the temperature reaches ~416

°C, red phosphorus undergoes a structural change to white phosphorus and begins to volatilize as molecular tetrahedral P_4.

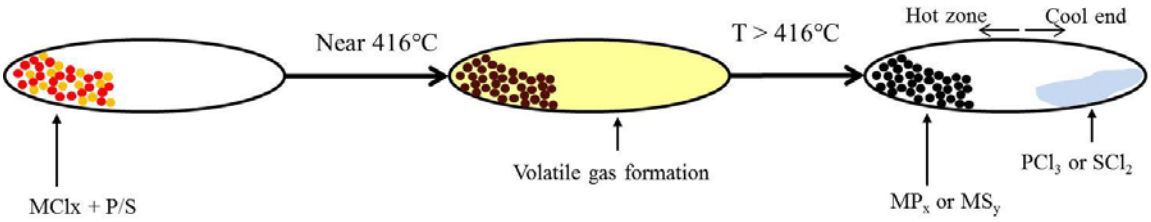

Figure 4.1 Schematic of ampoule M-P (or M-S) synthesis

Over time as the temperature increases to 500 °C, the formation of the M-P product and gaseous PCl_3 develop, which has been analyzed in our previous research. Also, MCl_x begins to darken at ~250 °C. The PCl_3 can be removed by pulling the ampoule end without solid out of the hot zone of the tube furnace. By doing so, PCl_3 transports and condenses as a colorless liquid. The M-S reactions have a similar reaction procedure with postulated SCl_2 formation instead of PCl_3. SCl_2 is a reddish liquid and should transport similarly to PCl_3. Unlike phosphorus, sulfur goes through a molten liquid phase first before evaporation at ~444 °C.

The following balanced reactions were used for the metal phosphides to target phosphorus rich phases detected by our earlier work:[2]

$$3\ MCl_2 + 8\ P \rightarrow 3\ MP_2 + 2\ PCl_3\ (M= Ni, Cu) \quad (4.1)$$

$$3\ CoCl_2 + 11\ P \rightarrow 3\ CoP_3 + 2\ PCl_3 \quad (4.2)$$

$$FeCl_3 + 3\ P \rightarrow FeP_2 + PCl_3 \quad (4.3)$$

The ampoule reactions targeting M-P and M-S materials yielded dark or black solids after heating at 500 °C. The M-P reactions also yielded a colorless liquid PCl_3 transport. Care has to be taken when opening the ampoule due to possible pressure build-up of PCl_3. Also, when opened the ampoule is angled towards the liquid to prevent mixing of the dark solid and the PCl_3.

The attempted metal sulfide reactions which were similar to M-P reactions targeting S-rich phases were carried out using the following balanced reactions:

$$2\ FeCl_3 + 7\ S \rightarrow 2\ FeS_2 + 3\ SCl_2 \quad (4.4)$$

$$2\ CoCl_2 + 5\ S \rightarrow Co_2S_3 + 2\ SCl_2 \quad (4.5)$$

$$NiCl_2 + 3\ S \rightarrow NiS_2 + SCl_2 \quad (4.6)$$

$$CuCl_2 + 2\ S \rightarrow CuS + SCl_2 \quad (4.7)$$

The ampoule reactions produced a yellow liquid transport that solidified to a yellowish white solid near room temperature. The targeted SCl_2 byproduct should be a red liquid at room temperature. The presence of the yellow liquid could indicate that S_2Cl_2 forms. The heats of formation of SCl_2 and S_2Cl_2 are -40 kJ/mol and -58 kJ/mol, respectively. Once the ampoule was opened, the solid products resembled darker versions of the metal halides. Longer air exposure of these solids caused a color change that resembled hydrated metal halides, which suggests very little M-S formation. Also, taking the recovered solids and adding them to methanol dissolves the solid, yielding similar colors to those of the metal halides dissolved in methanol.

From characterization of these M-S materials, it was seen that little or no metal sulfide products were formed. Solid analysis of the transported material from one of the M-S reactions showed small presence of S_2Cl_2 in a sulfur matrix. The product yields and heat of reactions for the M-P and M-S samples are shown in Table 4.1. The metal phosphides produced at 500 °C, minus the iron reaction, have relatively high yields around ~90%. The higher temperature 700 °C iron reaction has a lower yield of 54%. The sulfide reactions yield no products because the starting reagents were detected using characterization techniques and the thermochemical data explains why the MCl_x + S reactions fail. The ΔH_{rxn} for all of the metal phosphide products are exothermic while in contrast, the sulfide reactions all have endothermic ΔH_{rxn} values.

Table 4.1 Sealed ampoule targeted products with yields (washed yields). N.R. indicates no reaction and N/A indicates no wash step required.

Reaction	**Target Product**	**ΔH_{rxn} (kJ/mol)**	**Yields Based on Target Products**
$FeCl_3 + P$	FeP_2	-113	117% (54 %)
$CoCl_2 + P$	CoP_3	-83	87 % (N/A)
$NiCl_2 + P$	NiP_2	-19	91 % (89 %)
$CuCl_2 + P$	CuP_2	-95	93 % (90 %)
$FeCl_3 + S$	FeS_2	+189	**N.R.**
$CoCl_2 + S$	Co_2S_3	+296	**N.R.**
$NiCl_2 + S$	NiS_2	+158	**N.R.**
$CuCl_2 + S$	CuS	+145	**N.R.**

The XRD results for of the M-S reactions are shown in Table 4.2. These patterns all correspond to starting metal halides and were darker versions of the halides, for example, anhydrous $CoCl_2$ is light blue and the recovered product for the copper reaction was a darker light blue. The iron case showed peaks for monoclinic $FeCl_2(H_2O)_2$ (PDF #04-012-4995) and $FeCl_2 \cdot 4H_2O$ (PDF #00-016-0123). The cobalt sample showed very poorly crystalline peaks for the monoclinic $CoCl_2\ (H_2O)_6$ (PDF #04-002-3173) and $CoCl_2 \cdot 6\ H_2O$ (PDF #00-029-0466). The nickel sample showed very crystalline peaks for the rhombohedral $NiCl_2$ (PDF #00-022-0765). The copper XRD pattern showed crystalline peaks for cubic CuCl (PDF #00-006-0344) and peaks for the orthorhombic $CuCl_2(H_2O)_2$ (PDF #04-009-5606). The XRD data demonstrate that the MCl_x + S reactions are unsuccessful in directly producing MS_x products, which is consistent with the expectations from the thermochemical data in Table 4.1.

Table 4.2 Crystalline phases seen in powder XRD patterns from the sealed ampoule reactions of metal halides and elemental sulfur. Bolded phases are dominant phases.

Reaction	Phase(s) Observed by Powder XRD
$FeCl_3$ + S	**$FeCl_2(H_2O)_2$**, $FeCl_2 \cdot 4\ H_2O$
$CoCl_2$ + S	$CoCl_2 \cdot 6\ H_2O$
$NiCl_2$ + S	$NiCl_2$
$CuCl_2$ + S	**CuCl**, $CuCl_2(H_2O)_2$

4.4.2 Powder XRD and Energy Dispersive Spectroscopy (EDS) of M-P Materials

Powder X-ray diffraction of the M-P materials synthesized from the metal halides and red phosphorus was done to analyze crystalline phases. The XRD pattern from the ampoule reaction between $FeCl_3$ and red phosphorus showed is shown in Figure 4.2. The major phase present was the orthorhombic FeP_2 (PDF #04-003-1993). The second minor phase that was present was monoclinic $FeCl_2(H_2O)_4$ (PDF #04-010-9787). There was also minor tetragonal SiO_2 (PDF #00-039-1425) seen in the XRD pattern. The presence of crystalline SiO_2 is the result of devitrification of the glass reaction tube perhaps by the $FeCl_3$. The presence of $FeCl_2$ suggests that the reaction was not complete. Also, some reduction of the $FeCl_3$ has taken place since $FeCl_2$ was seen. The hydrate is most likely due to exposure of the halide to air. Washing of this sample was done in methanol to remove the $FeCl_2(H_2O)_4$. The remaining product was FeP_2 and SiO_2. The XRD pattern of the methanol washed sample is shown in Figure 4.2.

The XRD pattern for the cobalt phosphide sample from the reaction of $CoCl_2$ and red phosphorus is shown in Figure 4.3. Cubic CoP_3 (PDF #04-004-4318) was seen and

no other peaks were present. Peaks for cobalt chloride were not present. This was a good indication of a reaction nearly complete and therefore no washing step was performed. In addition to this, there was the presence of PCl_3 liquid in the ampoule cool end, and the product yield was 87% as seen in Table 4.1.

The XRD pattern for the nickel phosphide sample from the reaction of $NiCl_2$ and red phosphorus is shown in Figure 4.4. The pattern showed predominately highly crystalline, cubic NiP_2 (PDF #04-003-2351). There are very small peaks that represent monoclinic $Ni(PO_3)_2$ (PDF #00-028-0708) and $Ni_3(PO_4)_2$ (PDF #00-035-0987). The presence of this phase could indicate that the anhydrous metal halide reagent may have had some waters of hydration prior to reacting with red phosphorus. Another possible reasoning may be the exposure of the NiP_2 material to moist air. The sample was washed in concentrated ammonium hydroxide (NH_4OH) for 24 hours at room temperature to remove the phosphate phases. The washed pattern, showing only cubic NiP_2, is shown in Figure 4.4.

The XRD of the copper phosphide sample is shown in Figure 4.5. The pattern showed two phases. The first most intense phase was monoclinic CuP_2 (PDF #01-076-1190). There were also peaks for the cubic CuCl (PDF #04-007-3885). The relative peak intensities of these two patterns are approximately 5:1 CuP_2:CuCl. The presence of CuCl indicates that the reaction either did not go to completion or some of the CuP_2 may react with PCl_3 on extended contact. The sample was washed in 100% acetonitrile at room temperature for 24 hours to remove CuCl. The washed pattern, showing only CuP_2, is shown in Figure 4.5.

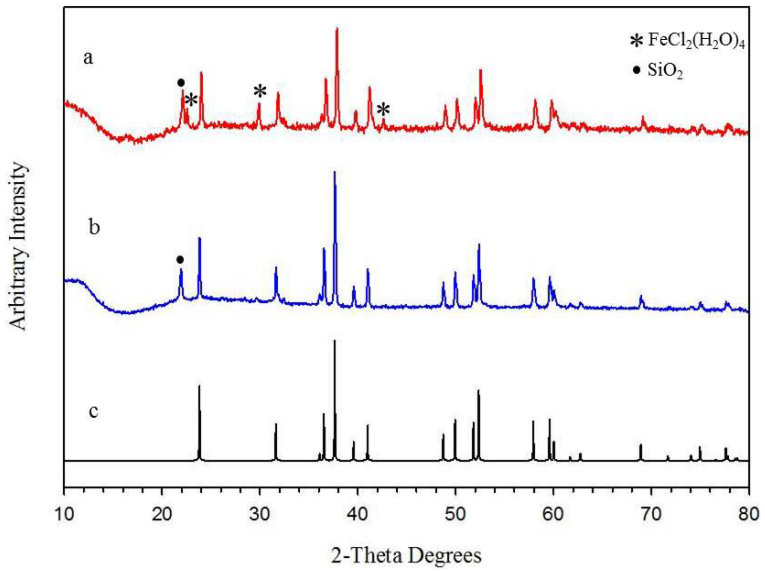

Figure 4.2 Powder XRD patterns of the as synthesized iron phosphide (a) methanol washed version (b), and the reference FeP_2 pattern (c).

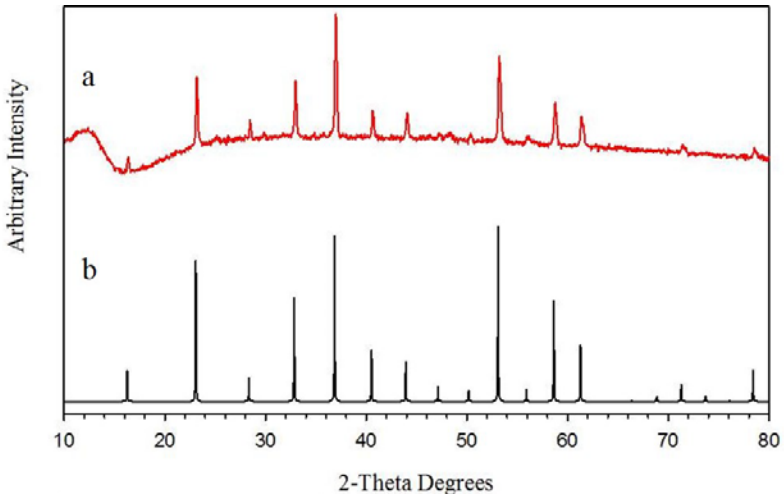

Figure 4.3 Powder XRD patterns of the cobalt phosphide sample (a) and the reference pattern CoP_3 (b).

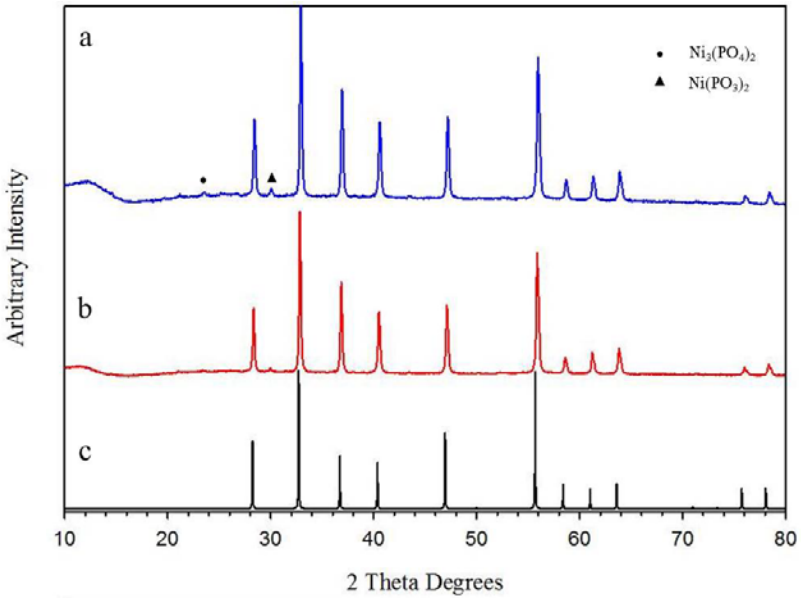

Figure 4.4 Powder XRD patterns for the following: (a) the as-synthesized nickel phosphide sample, (b) the NH_4OH washed nickel phosphide sample, and (c) the reference NiP_2 cubic pattern.

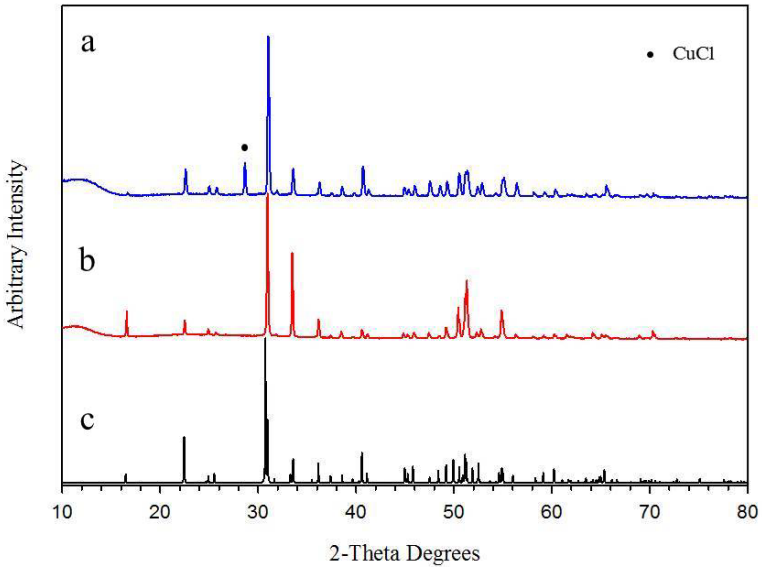

Figure 4.5 Powder XRD patterns for the following: (a) the as-synthesized copper phosphide sample, (b) the acetonitrile washed copper phosphide sample, and (c) the reference CuP_2 pattern.

The EDS of the M-P products are located in Table 4.3. The M-P all samples showed close to the ideal M:P ratios of 1:2 or 1:3 for the CoP_3 case, having some excess phosphorus content. The ratios were consistent with the phases seen by XRD. The unwashed FeP_2 and CuP_2 samples showed lower than expected M:P ratios however. This may be due to low phosphorus content on the surface. Both $FeCl_3$ and $CoCl_2$ have low melting points (306 °C and 498 °C respectively) and would melt or in the iron case, sublime at the reaction temperature of 500 °C. This could result in any unreacted halide to reside on the surface M-P products, thus giving rise to higher chlorine content. The washed versions of these two samples had a much better M:P ratio close to the ideal values. The unwashed and washed FeP_2 samples did show appreciable amounts of silicon which made sense since SiO_2 peaks were seen in XRD patterns. Also the FeP_2 was still P-rich which indicates that amorphous phosphorus may be present. In all samples, minus the unwashed samples, the chlorine content was extremely low and at the detection limit of the instrument.

Table 4.3 EDS atomic percent values relative to the metal content and the observed XRD phases of the M-P products are shown. Bolded phases are dominant phases. The (w) denotes a washed sample.

Reaction	**Targeted Phase**	**Yields Based on Target Phase**	**XRD Phases**	**M : P : Cl**
$FeCl_3$ + P	FeP_2	117 %	**FeP_2**, $FeCl_2(H_2O)_4$, SiO_2	1 : 1.88 : 0.38
$FeCl_3$ + P (w)	FeP_2	54 %	**FeP_2**, SiO_2	1 : 2.32 : <0.01
$CoCl_2$ + P	CoP_3	87 %	CoP_3	1 : 3.72 : <0.01
$NiCl_2$ + P	NiP_2	91 %	**NiP_2**, $Ni(PO_3)_2$, $Ni_3(PO_4)_2$	1 : 2.37 : <0.01
$NiCl_2$ + P (w)	NiP_2	89 %	NiP_2	1 : 2.26 : <0.01
$CuCl_2$ + P	CuP_2	93 %	**CuP_2**, CuCl	1 : 0.84 : 0.10
$CuCl_2$ + P (w)	CuP_2	90 %	CuP_2	1 : 2.03 : <0.01

4.4.3 SEM Images of M-P Materials

Scanning electron microscope images were taken for the M-P products and are shown in Figure 4.4. All of the samples were free powders that were pressed lightly onto carbon tape which were mounted on aluminum stubs. The letter-number combination (ex. A1, A2) is the same sample that has been zoomed in for analysis of smaller structures.

The FeP_2 sample consists of a mixture of aggregates that consist of large groups of fused plate-like shapes. These plates are ~3-5 microns long and appear loosely packed in the larger aggregate structure. The CoP_3 sample consists of large ~100-300 micrometer shard-like blocky structures coated by smaller ~10-20 micrometer aggregated particles. The NiP_2 sample consists of a mixture of small ~3-5 micrometer particles and large blocks that range in size from ~10-60 micrometers. The CuP_2 sample consists of

uniform groups of fused faceted plates. The large plates range from ~30-50 micrometers in length. The plate-like blocks have much longer lengths along two dimensions than the thickness. The thickness of most structures is ~10 micrometers. Of all of the M-P samples, the copper phosphide sample had a very shiny visible luster which may be due to the large CuP_2 crystalline aggregates.

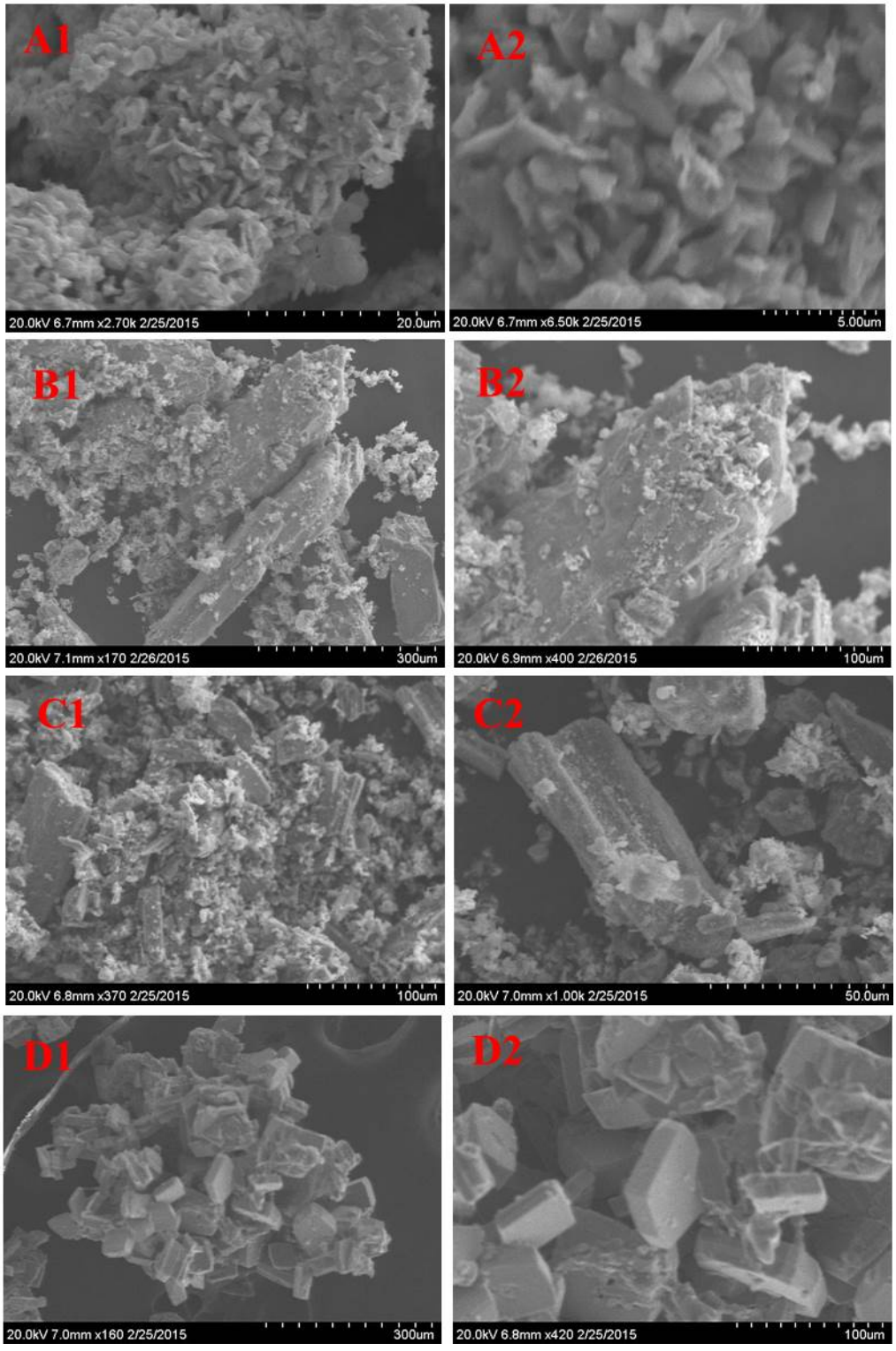

Figure 4.6 SEM images of M-P products (A = Fe, B = Co, C = Ni, D = Cu). Zoomed in versions in the right column are denoted with the number 2.

4.4.4 Magnetic Susceptibility of M-P Materials

The M-P materials were analyzed for their room temperature (298 K) magnetic susceptibility. The molar magnetic susceptibility (χ_m), the magnetic moment and the spin only magnetic moment (μ_B) values were calculated using the equations:

$$\chi_m = \chi_g * (MW) \quad (4.8)$$

$$\mu_B = 2.83(\chi_m * T)^{1/2} \quad (4.9)$$

$$\mu_B = (n(n+2))^{1/2} \quad (4.10)$$

χ_g is the gram susceptibility given by the instrument, MW is the molecular weight of the MP_x product, T is the temperature in Kelvins and n is the number of unpaired d-electrons. The samples were corrected for their core diamagnetism and for the glass sample holder (SiO_2 χ_M -19.5 x 10^{-6} cm^3/mol CRC value). Tabulated data for the samples are shown in Table 4.4. Literature values for each compound are -1.63 x 10^{-6} emu/mol FeP_2,[166] -14.0 x 10^{-6} emu/mol CoP_3,[167] -19.0 x 10^{-6} emu/mol NiP_2 and -44.0 x 10^{-6} emu/mol CuP_2.[79] The literature susceptibility values were converted from the given units of emu/g to cm^3/mol by using the relationship of 1emu/g = 4π x 10^{-3} m^3/kg and then using the molar masses of each MP_x.

All samples were washed, except the cobalt sample, and had relatively low paramagnetic responses. The Fe-P sample showed silica peaks by XRD, which is diamagnetic. The average EDS data was used to obtain an approximate amount of silica in order to perform additional diamagnetic correction. The Co-P sample had the highest paramagnetic response of all of the M-P samples. The Cu-P sample had a small diamagnetic response after the diamagnetic correction was applied. The literature values of the MP_x materials are all diamagnetic. Our samples show small paramagnetic responses most likely due to small amounts of paramagnetic ions, such as Fe^{3+} (d^5), Co^{2+} (d^7), or Ni^{3+} (d^7) , that were not detected in the phases seen by XRD. Traces of Cu^+ (d^9) could be present in the CuP_2 sample which would reduce the diamagnetic response.

Table 4.4 Magnetic data values for washed M-P samples are shown. The spin only cases assume diamagnetic d-orbital arrangements for diamagnetic literature values. χ_M units are cm^3/mol. LS =low spin, O_h = octahedral d-orbital splitting, SP= square planar d-orbital splitting.

Reaction	**Products**	**Spin Only M^{n+}, d^y**	**Literature Value χ_M (x 10^{-4})**	**Exp. χ_M (x 10^{-4})**	**Exp. μ_B (BM)**
$FeCl_3$ + P	FeP_2	Fe^{2+}, d^6 (O_h, LS)	-2.04	2.97	0.84
$CoCl_2$ + P	CoP_3	Co^{3+}, d^6 (O_h, LS)	-1.76	5.19	1.11
$NiCl_2$ + P	NiP_2	Ni^{2+}, d^8(SP)	-2.39	2.10	0.71
$CuCl_2$ + P	CuP_2	Cu^+, d^{10}	-5.53	-0.16	Diamag.

4.4.5 Synthesis and Characterization of M-P-S Products

The thermodynamically favorable M-P ampoule reactions described above propagated by PCl_3 elimination and yielded major phase products of FeP_2, CoP_3, NiP_2, and CuP_2 while analogous M-S reactions fail. The current section combines M-P and M-S reactions using both phosphorus and sulfur to obtain M-P-S materials. Similarly, a second set of reactions were done using P_2S_5 and phosphorus for comparison of the reagents used, targeting the same products. Initial experiments were done targeting individual mixtures of both M-P and M-S products however the separate phosphide and sulfide products were not seen in XRD patterns. Often mixtures of M-P and M-P-S materials were observed. Except for NiS_2 seen in the Ni-P-S reaction, M-S phases were otherwise not detected. In contrast to Chapter 3 SSM reactions targeting MP_x and MS_y mixtures, the products targeted in this section were $FePS_3$, $CoPS_3$, $NiPS_3$ and Cu_3PS_4 since these were the key phases seen repeatedly in our early ampoule experiments. The copper targeted product is different since the $CuPS_3$ phase is not stable and was not observed in initial reactions. The M-P-S reactions were balanced accordingly using MCl_2 or MCl_3:

$$3\ MCl_2 + 5\ P + 9\ S \rightarrow 3\ NiPS_3 + 2\ PCl_3\ (M = Ni, or\ Co) \quad (4.11)$$

$$FeCl_3 + 2\ P + 3\ S \rightarrow FePS_3 + PCl_3 \quad (4.12)$$

$$3\ CuCl_2 + 3\ P + 4\ S \rightarrow Cu_3PS_4 + 2\ PCl_3 \quad (4.13)$$

Similarly to the SSM reactions described in Chapter 3, reactions using the pre-bonded phosphorus and sulfur atoms in P_2S_5 have slightly different balanced reactions. Additional phosphorus was needed to balance the equations. The reactions follow the general equations:

$$3\ MCl_2 + 1.8\ P_2S_5 + 1.4\ P \rightarrow 3\ MPS_3 + 2\ PCl_3\ (M = Ni, Co) \quad (4.14)$$

$$FeCl_3 + 0.6\ P_2S_5 + 0.8\ P \rightarrow FePS_3 + PCl_3 \quad (4.15)$$

$$3\ CuCl_2 + 0.8\ P_2S_5 + 1.4\ P \rightarrow Cu_3PS_4 + 2\ PCl_3 \quad (4.16)$$

For both P + S and P_2S_5 + P sets of experiments, the iron, cobalt, and nickel materials yielded black solids while the copper reactions yielded green solids. The product yields for samples range from the 60 - 90 % and are shown in Table 4.5. In general, the P + S samples have slightly lower yields than the P_2S_5 + P reactions. The iron case is the exception here, having roughly 93% yield for the P + S version and the copper reaction using P + S has over 100% yield. This is probably due to some transported solid material that was collected from the ampoule in addition to the crystalline product. Generally, product separation from the byproducts is simple since the PCl_3 condenses on the opposite, cold end of the ampoule. However, in some cases, the addition of sulfur results in yellow or brown solids transport in addition to PCl_3.

Some of these solids may not have completely transported from the product, thus providing additional mass.

Table 4.5 Product yields from the ampoule reactions targeting M-P-S materials

Reaction	Target Product	Yields Based on Targeted Products
$FeCl_3 + P + S$	$FePS_3$	93 %
$FeCl_3 + P_2S_5 + P$	$FePS_3$	84 %
$CoCl_2 + P + S$	$CoPS_3$	62 %
$CoCl_2 + P_2S_5 + P$	$CoPS_3$	79 %
$NiCl_2 + P + S$	$NiPS_3$	63 %
$NiCl_2 + P_2S_5 + P$	$NiPS_3$	87 %
$CuCl_2 + P + S$	Cu_3PS_4	103 %
$CuCl_2 + P_2S_5 + P$	Cu_3PS_4	94 %

4.4.6 Powder X-Ray Diffraction (XRD) and Energy Dispersive Spectroscopy (EDS) of M-P-S Products

The powder XRD patterns of the metal thiophosphate materials synthesized from the metal halides, red phosphorus, and sulfur are shown in Figures 4.7 and 4.8. The XRD pattern of the iron thiophosphate product showed crystalline monoclinic phase $FePS_3$ (PDF #00-033-0672). There is one very small unidentified peak near the baseline at 30°. The iron fluorescence background was less of an issue in this sample as compared to other iron containing samples.

The XRD pattern of the cobalt thiophosphate sample showed two crystalline phases. Each phase has approximately the same relative intensity. The monoclinic phase

$CoPS_3$ (PDF #01- 078-0498) is present along with the cubic phase $CoP_{0.5}S_{1.5}$ (PDF #04-007-4518). The baseline of the pattern is high due to the fluorescence background from cobalt. The nickel thiophosphate sample XRD pattern also showed two phases. The most intense phase was monoclinic $NiPS_3$ (PDF #01-078-0499). There are very small peaks for a secondary cubic phase NiS_2 (PDF #04-003-4307). The relative intensity ratio of $NiPS_3$ and NiS_2 are approximately 4:1. The XRD pattern for the copper thiophosphate sample showed only highly crystalline peaks for the orthorhombic Cu_3PS_4 phase (PDF #04-004-0447).

The XRD patterns of the products synthesized from the metal halides, P_2S_5 and red phosphorus are shown in Figures 4.9 and 4.10. The reaction conditions are identical to the P + S subset of reactions. The iron thiophosphate sample showed single phase monoclinic $FePS_3$ (PDF #00-033-0672). The cobalt thiophosphate sample showed single phase monoclinic $CoPS_3$ (PDF #01-078-0498). The nickel thiophosphate sample showed peaks for monoclinic $NiPS_3$ (PDF #01-078-0499). There is a small peak at 16° which could indicate $NiCl_2$, however no other $NiCl_2$ peaks are present. The copper thiophosphate sample showed single phase orthorhombic Cu_3PS_4 (PDF #04-004-0447).

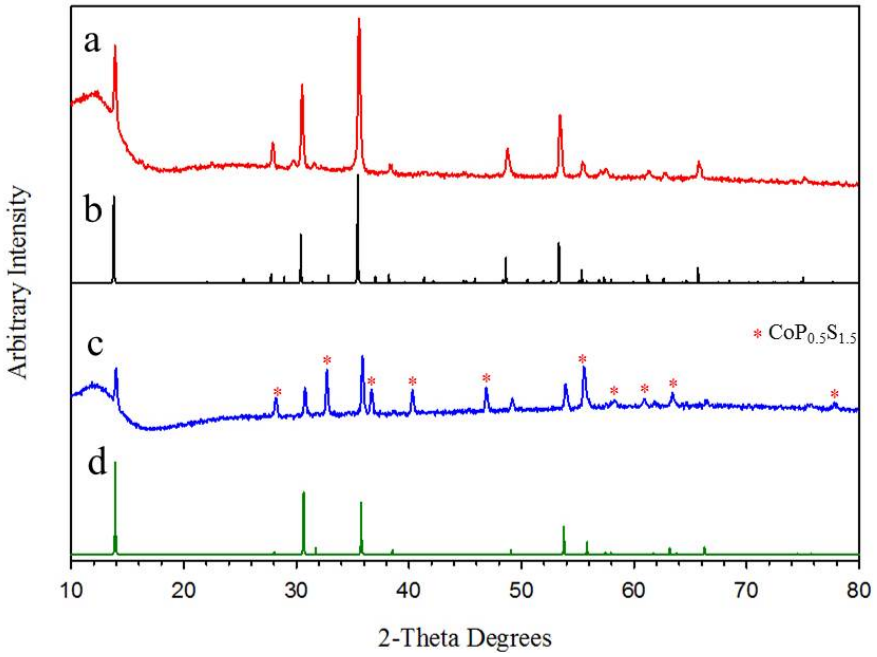

Figure 4.7 Powder XRD patterns of the iron thiophosphate (a) and cobalt thiophosphate (c) samples from the sealed ampoule reaction of the metal halides and P + S. The respective reference patterns of $FePS_3$ (b) and $CoPS_3$ (d) are located below the sample patterns.

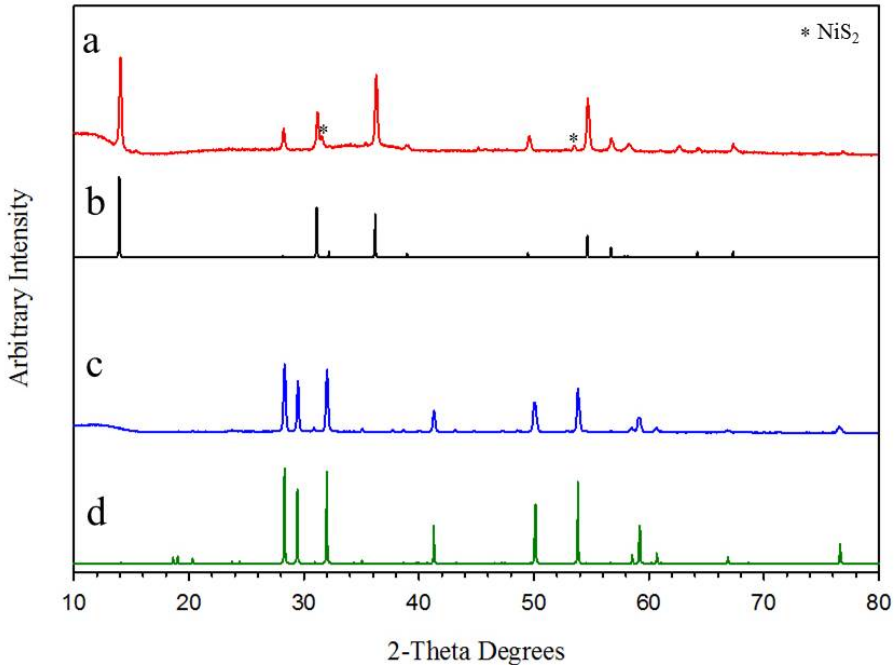

Figure 4.8 Powder XRD patterns of the nickel thiophosphate (a) and copper thiophosphate (c) samples from the sealed ampoule reaction of the metal halides and P + S. The respective reference patterns of $NiPS_3$ (b) and Cu_3PS_4 (d) are located below the sample patterns.

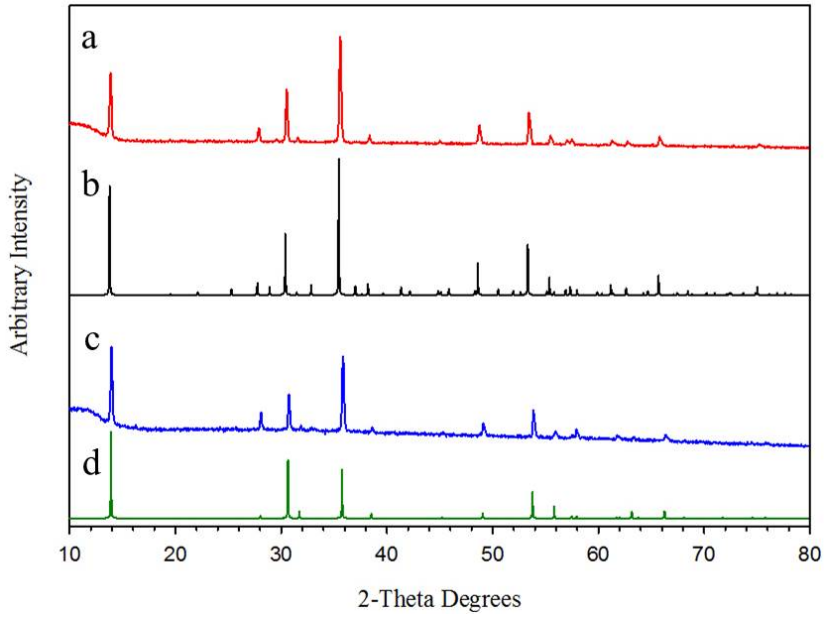

Figure 4.9 Powder XRD patterns of the iron thiophosphate (a) and cobalt thiophosphate (c) samples from the sealed ampoule reaction of the metal halides and P_2S_5 + P. The respective reference patterns of $FePS_3$ (b) and $CoPS_3$ (d) are located below the sample patterns.

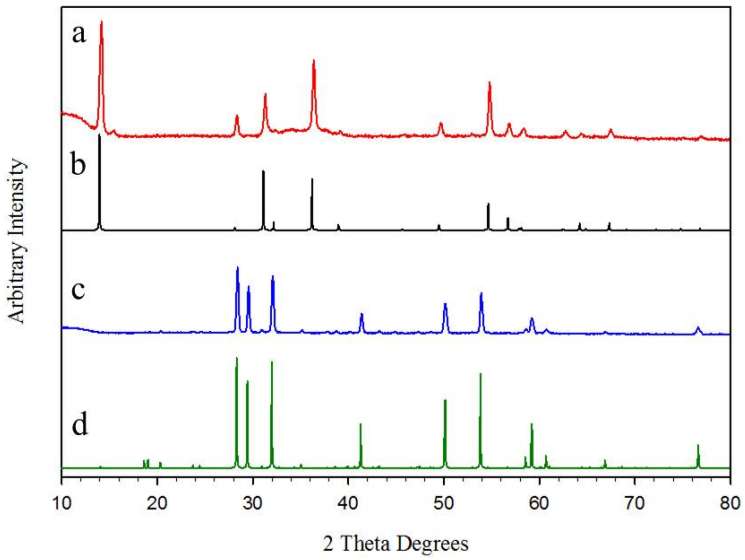

Figure 4.10 Powder XRD patterns of the nickel thiophosphate (a) and copper thiophosphate (c) samples from the sealed ampoule reaction of the metal halides and P_2S_5 + P. The respective reference patterns of $NiPS_3$ (b) and Cu_3PS_4 (d) are located below the sample patterns.

The EDS data for the M-P and the M-P-S is shown Table 4.6. The table shows the relative atomic ratios between the metal, phosphorus and sulfur content. For all samples, the chlorine content was quite low or near the detection limits of the instrument which indicates effective reactions. All samples had high phosphorus content which deviated from the ideal M:P ratio of 1:3 for Fe, Co and $NiPS_3$, and 1:0.33 for Cu_3PS_4. The M:S ratio was also higher than expected, with the Fe (P+S) sample having the closest to the ideal M:S ratio of 1:3.04. The S/P ratio for all samples however was lower than the ideal. From these ratios, this indicates that the samples are phosphorus-rich.

Table 4.6 EDS data for the M-P-S products. The data represents the relative atomic percent values scaled to the metal content. Bold phases are major phases in multiphase systems.

Reaction	Targeted Phase	XRD Phases	M : P : S : Cl	S/P
$FeCl_3 + P + S$	$FePS_3$	$FePS_3$	1 : 1.29 : 3.04 : 0.08	2.35
$CoCl_2 + P + S$	$CoPS_3$	$CoPS_3$, $CoP_{0.5}S_{1.5}$	1 : 1.95 : 4.52 : < 0.01	2.32
$NiCl_2 + P + S$	$NiPS_3$	**$NiPS_3$**, NiS_2	1 : 1.34 : 3.34 : 0.02	2.49
$CuCl_2 + P + S$	Cu_3PS_4	Cu_3PS_4	1 : 0.46 : 1.25 : < 0.01	2.70
$FeCl_3 + P_2S_5 + P$	$FePS_3$	$FePS_3$	1 : 1.36 : 3.24 : < 0.01	2.37
$CoCl_2 + P_2S_5 + P$	$CoPS_3$	$CoPS_3$	1 : 1.97 : 5.13 : < 0.01	2.60
$NiCl_2 + P_2S_5 + P$	$NiPS_3$	**$NiPS_3$**, NiS_2	1 : 1.24 : 3.20 : < 0.01	2.58
$CuCl_2 + P_2S_5 + P$	Cu_3PS_4	Cu_3PS_4	1 : 0.40 : 1.20 : < 0.01	3.01

4.4.7 SEM images of M-P-S Materials

The SEM images of the M-P-S products from the reactions of the metal halides and (P + S) are shown in Figure 4.11. The Fe-P-S sample showed several faceted hexagonal plate-like structures. These structures range from 3-5 micrometers across and are roughly 1 micrometer thick. The Co-P-S sample showed large blocky structures which ranged from 50-300 micrometers. The zoomed in version showed a network of fused octahedral and blocky structures which are several hundred nanometers in size. The Ni-P-S sample showed large aggregates of fused particles which range from single micrometers to several tens of micrometers. Similarly, the Cu-P-S sample showed aggregates, however more defined blocky structures are mixed in. The blocky structures range from a few micrometers to several tens of micrometers.

The SEM images of the M-P-S products from the reactions of the metal halides and (P_2S_5 + P) are shown in Figure 4.12. The Fe-P-S sample showed flat plate like fused structures mixed in with aggregate particles. The plates range from ~ 3-15 micrometers. The plate thickness is a few micrometers. The aggregates are a few micrometers in size. The Co-P-S sample showed fused blocky structures with defined edges that range from ~3-5 micrometers. The Ni-P-S sample showed aggregates of particles and plates that were few micrometers to tens of micrometers in size. The Cu-P-S sample showed a mixture of large blocky structures and small aggregates. The large blocky structures range from ~ 10-20 micrometers. The aggregates range from ~ 1-5 micrometers.

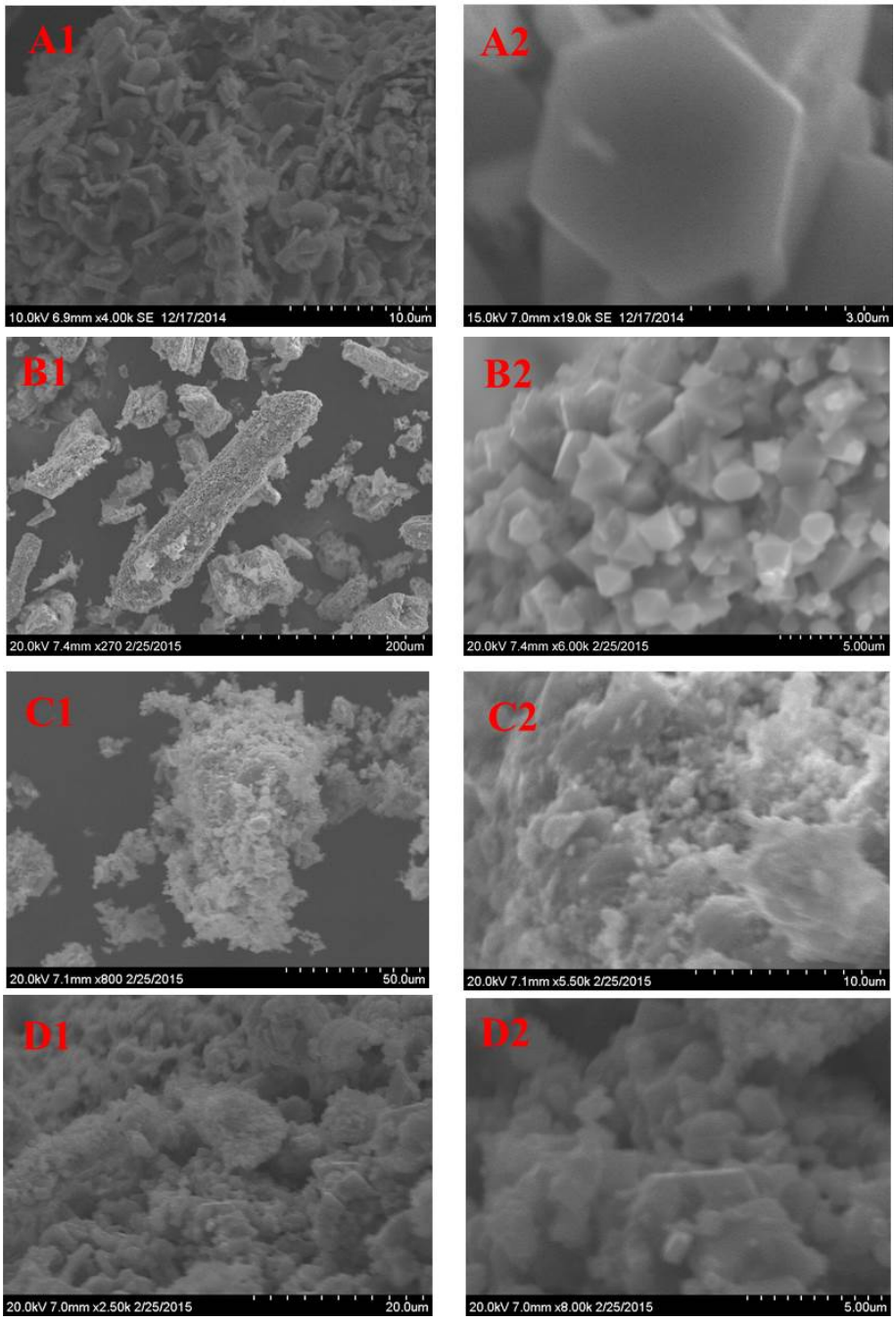

Figure 4.11 SEM images of M-P-S materials from using the metal halides and (P+S). A = Fe, B = Co, C = Ni, D = Cu. Zoomed in versions are denoted with a number 2.

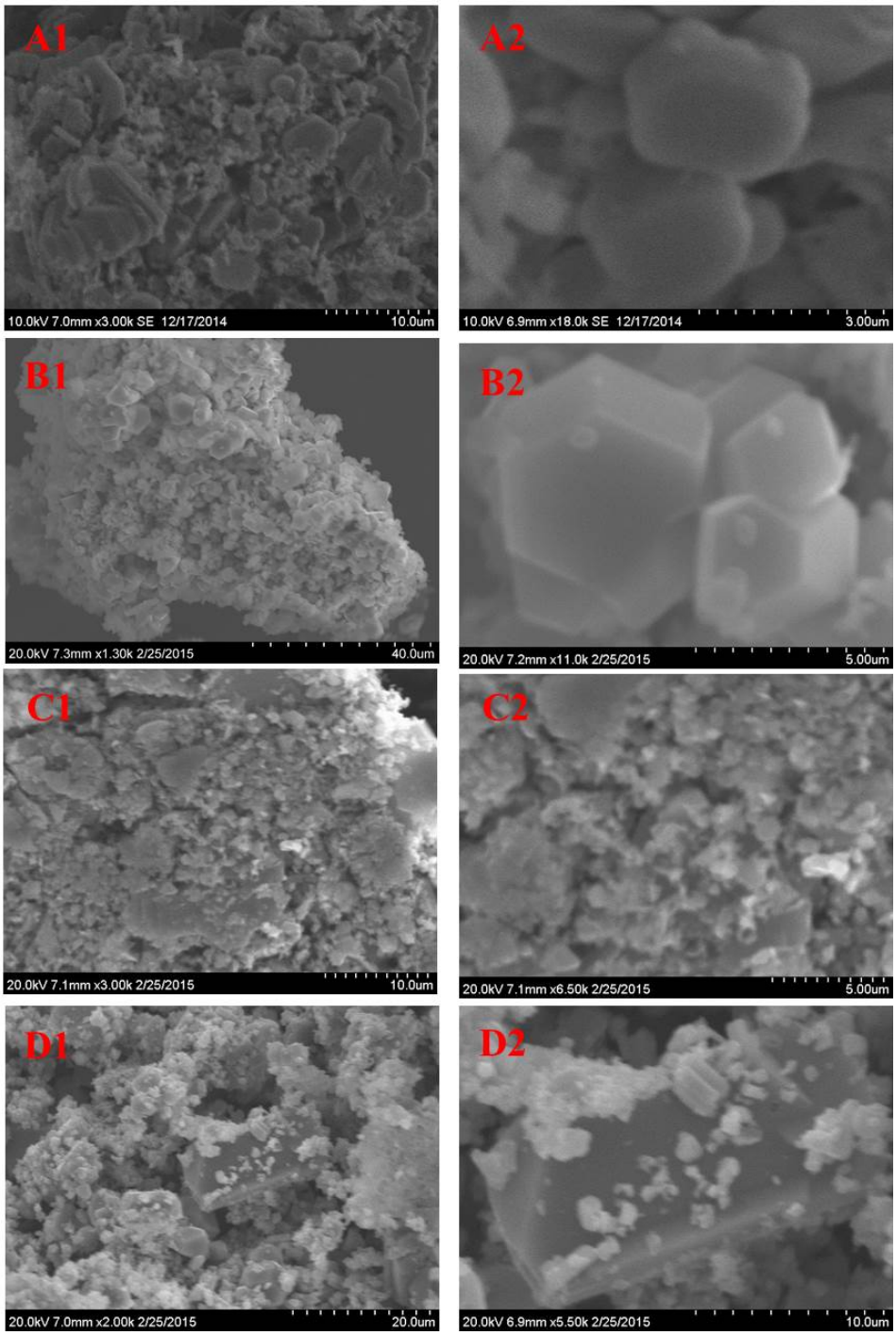

Figure 4.12 SEM images of M-P-S materials from the reaction of the metal halides, and (P_2S_5+ P). A = Fe, B = Co, C = Ni, D = Cu. Zoomed in versions are denoted with a number 2.

4.4.8 Magnetic Susceptibility of M-P-S Materials

The M-P-S materials were analyzed for their room temperature magnetic susceptibility. Ideally, the MPS_3 samples should consist structurally of 2 M^{2+} cations and $(P_2S_6)^{4-}$ anions per formula unit. The Cu_3PS_4 structure consists of 3 Cu^+ and PS_4^{3-} ions per formula unit. The magnetic measurements of the M-P-S materials are shown in Table 4.7 and the data was calculated using Equations 4.8-4.10. The Fe-P-S samples in both the (P + S) and (P_2S_5 + P) reactions had the highest magnetic susceptibility values from all of the samples. The magnetic moment of the (P + S) iron sample is close to a spin only case for a Fe^{2+} d^6 high spin value of 4.90 Bohr Magnetons (BM) while the (P_2S_5 + P) sample is slightly higher. The single phase $CoPS_3$ sample from (P_2S_5 + P) had values close to a Co^{2+} d^7 spin only value of 3.87 BM. The mixed phase $CoPS_3/CoP_{0.5}S_{1.5}$ sample was lower.

The Ni-P-S samples had similar values and both were lower than the ideal Ni^{2+} case (2.83 BM). This is most likely due to the presence of NiS_2. The Cu-P-S samples also had similar low magnetic moment values, which is nearly diamagnetic. The copper samples were ideally (Cu^+, d^{10}) diamagnetic. Once diamagnetic corrections were made, the samples had very weakly paramagnetic responses which were lower than any of the other samples. This could indicate that there are small amounts of paramagnetic impurities that are below the detection of XRD giving paramagnetic responses.

Table 4.7 Magnetic data values for washed M-P-S samples are shown. The spin only cases assume octahedral high spin M^{2+} or M^{+} according to literature values for MPS_3 materials. χ_M units are cm^3/mol. ([a]Cited reference for $MPS_3\mu_{eff}$.)

Reaction	**Products**	**M^{n+}, d^n, spin μ_B (BM)**	**Exp. χ_M ($\times 10^{-3}$)**	**Literature Values μ_{eff} (BM)[168a]**	**Exp. μ_B (BM)**
$FeCl_3 + P + S$	$FePS_3$	Fe^{2+}, d^6, 4.90	10.3	4.94	4.98
$CoCl_2 + P + S$	$CoPS_3$, $CoP_{0.5}S_{1.5}$	Co^{2+}, d^7, 3.87	3.34	4.93	2.87
$NiCl_2 + P + S$	**$NiPS_3$**, NiS_2	Ni^{2+}, d^8, 2.83	1.79	3.90	2.10
$CuCl_2 + P + S$	Cu_3PS_4	Cu^{+}, d^{10}, 0.00	-0.076	Diamag.	0.46
$FeCl_3 + P_2S_5 + P$	$FePS_3$	Fe^{2+}, d^6, 4.90	11.7	4.94	5.28
$CoCl_2 + P_2S_5 + P$	$CoPS_3$	Co^{2+}, d^7, 3.87	5.87	4.93	3.02
$NiCl_2 + P_2S_5 + P$	**$NiPS_3$**, NiS_2	Ni^{2+}, d^8, 2.83	2.00	3.90	2.23
$CuCl_2 + P_2S_5 + P$	Cu_3PS_4	Cu^{+}, d^{10}, 0.00	-0.020	Diamag.	0.48

4.4.9 Fourier Transform Infrared Spectroscopy (FT-IR) and Diffuse Reflectance Spectroscopy (DRS) of M-P-S Products

The MPS_3 (M = Fe, Co, Ni) and Cu_3PS_4 samples synthesized from MCl_x and (P+S) were analyzed for their P-S bond vibrations. A stack-plot of select IR spectra is shown in Figure 4.13. All of the samples had a very strong vibration around 570 cm^{-1} which is characteristic of the PS_3 asymmetric stretching frequency.[169] The presence of a broad peak ~3400 cm^{-1} is seen from using a KBr matrix. The Fe-P-S sample has a very intense peak at 572 cm^{-1} and has two small unidentified peaks at ~1300 cm^{-1} and ~1100 cm^{-1} that could arise from absorbed organics. The Co-P-S sample has a very intense peak

at 580 cm^{-1}. The Ni-P-S sample has an intense peak at 572 cm^{-1}. The Cu-P-S sample had an intense peak at 500 cm^{-1} which is lower than all other samples. This is most likely due to the structural differences between the MPS_3 materials and Cu_3PS_4. The IR data for the samples synthesized from MCl_x and P_2S_5 + P showed similar results.

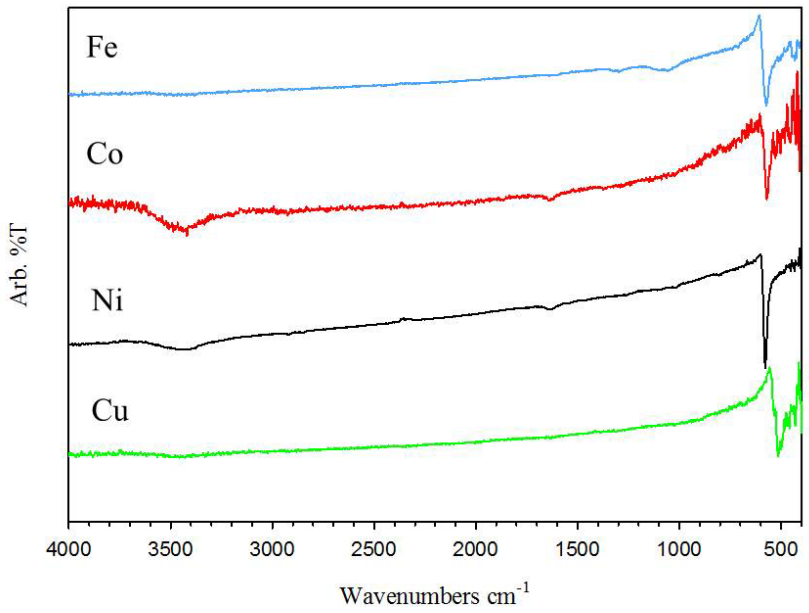

Figure 4.13 Selected IR data for M-P-S samples synthesized from MCl_x and (P +S).

The diffuse reflectance data of the M-P-S materials are shown in Table 4.8. All samples except for Cu_3PS_4, were shiny and black. Because of this, these samples had very broad absorptions across the visible light region and do not have onset drops in absorbance until the far edge of the visible region or into the IR region. The DRS accessory and the UV-Vis spectrometer used for these measurements is limited to accurately recording absorption events beyond 1000 nm. The absorption onsets in this region for select samples were also not strong. The rough estimates of band gaps were calculated using the Kubelka-Munk (KM) function:

$$F(R) = (1-R)^2/ 2R \quad (4.17)$$

where R is the diffuse reflectance of the sample which is derived from the percent transmittance. Extrapolation of the onset absorption events from a plot of the KM function versus energy in electron volts gives rise to estimated band gap energies of the samples. All of the black solids have similar, very small band gaps which indicates that the material behaves more metallic like. The Fe-P-S samples and the Ni-P-S sample synthesized using (P_2S_5 + P) have two absorption onsets. This could be related to the electronic states of the material. The Cu_3PS_4 samples have slightly higher band gaps and have absorption drops at ~ 530 nm (green light) which corresponds to the approximate brownish-green color of the material.

Table 4.8 DRS data from the M-P-S samples. Bold phases are the dominant phases seen by XRD. Samples with multiple onset drops are separated by a semicolon and the major absorption event is in bold.

Reaction	**Products**	**Onset Abs. (nm)**	**Est. Band Gap (eV)**	**Literature Band Gap (eV)**
$FeCl_3$ + P + S	$FePS_3$	760	1.63	1.50[170]
$CoCl_2$ + P + S	**$CoPS_3$, $CoP_{0.5}S_{1.5}$**	940	1.32	1.40[171,172]
$NiCl_2$ + P + S	**$NiPS_3$**, NiS_2	915	1.36	1.60[170]
$CuCl_2$ + P + S	Cu_3PS_4	520	2.38	2.36[161]
$FeCl_3$ + P_2S_5 + P	$FePS_3$	780	1.59	1.50[170]
$CoCl_2$ + P_2S_5 + P	$CoPS_3$	745	1.66	1.40[171,172]
$NiCl_2$ + P_2S_5 + P	**$NiPS_3$**, NiS_2	740	1.68	1.60[170]
$CuCl_2$ + P_2S_5 + P	Cu_3PS_4	525	2.36	2.36[161]

4.5 Reaction Analysis

The M-P and M-P-S materials were synthesized from the metal halides and elemental red phosphorus (and sulfur) at 500 °C. The halides are stable at the reaction temperature, remaining solids until much higher temperatures. $CuCl_2$ does begin to melt at 498 °C however but no visible "melt" was seen during the reaction. Darkening of the halides roughly begins around ~275-300 °C which could indicate initial small reactions with red phosphorus. As the temperature rises, two main events are occurring: 1) breaking of M-Cl and P-P bonds and formation of M-P and P-Cl bonds, 2) rearrangement of polymeric red phosphorus to tetrahedral P_4 with an increased reaction rate with MCl_x. The phase transition of red phosphorus to white at ~416 °C initiates a dramatic color change in the solids, often being very dark brown or black. The reaction temperature was set to 500 °C (or 700 °C for FeP_2) with a 18-24 hour hold to ensure a complete reaction and maximum crystal growth since the diffusion rate of solid-solid interactions are very slow.

The byproduct is PCl_3, and its vapors in the tube are generally colorless. Undesirable byproduct, or unreacted starting halides were seen in some samples and required appropriate washing to remove them. The iron sample, which was heated to 700 °C, showed silica peaks in the XRD which is the result of halide attack on the glass tube. Iron (II) chloride was also present which indicated that a reduction of the $FeCl_3$ took place. The reduction may be the result of prolonged exposure to PCl_3 at high temperature. Phosphorus in the PCl_3 structure does have a lone pair of electrons that could assist with reducing the $FeCl_3$, and the temperature elevation may perpetuate this process. The reaction had little byproduct liquid and the liquid did not behave like PCl_3

(smoking and volatile in air) which supports the idea of secondary reactions that could form air stable products such as $POCl_3$.

The Co-P reaction produced CoP_3 according to XRD without any detectable undesirable byproducts. The melting point of $CoCl_2$ is 735 °C therefore it is stable at the reaction temperature. The nickel sample produced mainly NiP_2 and small amounts of nickel phosphate. The presence of the phosphate is most likely the result of poorly dried starting materials. The anhydrous $NiCl_2$ was used as received, being shipped and stored under argon without any prior drying and the nickel phosphate phases were not seen in previous experiments. Low levels of H_2O could have produced MPO_x side products though. The red phosphorus was dried under vacuum at ~200 °C for 30 minutes prior to cooling and storage under argon in the glove box for future use in all reactions. An alternative explanation could be that the tube was opened in air when the solids were not completely cooled to room temperature.

The Cu-P reaction behaved ideally, forming PCl_3 and CuP_2 in high yield. The CuP_2 sample had a notably shiny luster and produced uniform cubic blocks. This may be due to the fact that $CuCl_2$ begins to melt very close to 500 °C and reacts more intimately with phosphorus. There were peaks in the XRD that showed CuCl however. Similar to the iron reaction, the reduction could be the result of PCl_3 interaction with the halide. The product morphology did not change after removal of CuCl with acetonitrile.

The M-S reactions were all unsuccessful due to the starting metal halide reagents present in the XRD patterns. The ΔH_{rxn} for all of the reactions (Table 4.1) are all endothermic which helps explains this. Also, from physical observation of the reaction, the “products” did not resemble M-S products which are black solids. At 500 °C, sulfur

will become gaseous, $FeCl_3$ will sublime and $CuCl_2$ will begin to melt. $NiCl_2$ and $CoCl_2$ will remain solids since their melting points are 1001 °C and 735 °C respectively and will not be as reactive with sulfur. Overall, none of the reactions were very reactive. The transported material resembled sulfur, since it was yellow in color. Analysis of one of the by-product yellow solids did show signs of S_8 and S_2Cl_2. The presence of S_2Cl_2 indicates that there was a very small reaction with the metal halides, but the reaction is not favorable towards M-S formation.

The M-P-S materials were synthesized from the metal halides and (P+S) or (P_2S_5 +P). The reaction conditions were similar to the M-P reactions, giving off a liquid by-product, but also a yellow or brownish solid. The solids could be transported sulfur. The reactions proceed to form M-P-S materials with some NiS_2 forming in both nickel cases. This is unexpected since the M-S reactions were all unsuccessful. One can speculate that the MCl_x and (P+S) reactions proceed by forming the metal phosphides first and then sulfur can react with the phosphide materials. Another possibility is that phosphorus and sulfur can react together to form a reactive P_xS_y species, and then further react with MCl_x to form products. Perhaps these two reaction pathways occur simultaneously. It is worth noting that P_2S_5 and other P_xS_y products are known to be formed from heating phosphorus and sulfur.

The MCl_x and (P_2S_5 + P) reactions most likely behave similarly to the (P+S) versions since the physical properties of P_2S_5 and S are similar, with P_2S_5 being much more reactive however. The melting and boiling points of P_2S_5 are 288 °C and 514 °C respectively, therefore at the maximum reaction temperature of 500 °C, P_2S_5 would be a liquid. At this point P_2S_5 would be very reactive and in concentrated liquid contact with

MCl_x. The additional red phosphorus would be gaseous P_4. Likewise with the (P+S) reactions, either the P_2S_5 or P_4 can react with the MCl_x, and most likely both reactions occur simultaneously.

4.6 Conclusions

Transition metal phosphides and thiophosphates were synthesized successfully via sealed ampoule techniques. The reactions were driven by producing PCl_3 which was easily removed by a temperature gradient. The reactions containing sulfur or P_2S_5 have PCl_3 transport and a yellowish solid. All solids, except for the Cu_3PS_4 product, were black. Some M-P products contained small amounts of soluble secondary phases. The reaction heating time may be a variable that may improve initial product purity. All reactions were done using stoichiometric amounts of reagents. Adding a small excess of phosphorus could encourage any unreacted metal halide to fully react; however the risk is that in M-P-S reactions, this could cause metal phosphide phases to form in addition to the M-P-S phases.

Since single phases can be targeted from both the M-P and M-P-S reactions, one can think of ways to modify the morphology or structures of samples. The next chapter will utilize the results from the M-P and M-P-S reactions and use flux growth environments to encourage interesting morphologies.

CHAPTER 5

SYNTHESIS OF M-P AND M-P-S MATERIALS USING DEPOSITION AND FLUX GROWTH TECHNIQUES

5.1 Introduction and Background

Flux growth is a useful technique for obtaining unique structures, single crystals, and materials that are often difficult to obtain using conventional solid state techniques. In solid state chemistry, reactions are limited to the diffusion rate of reagents to form products by overcoming solid-solid surface interactions. This is very low, often requiring several grinding and heating sessions. Addition of relatively low melting fluxes helps facilitate the interaction between solids to form products.

Common fluxes (or solvents) used in solid state synthesis are low melting metals such as indium (156 °C), tin (232 °C), lead (327 °C), and bismuth (271 °C). Depending on the reaction and products desired, metals need to be chosen for their inertness, or in certain cases, their reactivity. Fluxes also need to able to be separated from the products easily and not reactive towards the reaction vessel. Several metal carbonates, halides, nitrates, and other salts can also be used as fluxes. The melting points of these salts vary, therefore reactions must be chosen carefully. For example, alkali metal salts (and their respective melting points) such as Na_2CO_3 (851 °C), NaCl (801 °C), or $NaNO_3$ (308 °C) are a few compounds used in flux synthesis. Caution also must be taken when using materials that can decompose upon heating, such as nitrates, since these compounds can decompose and release NO_x based gases.

Inorganic molten salt fluxes are chosen for similar reasons as the metal fluxes. The main difference between metals and molten salt fluxes is that the molten salts are ionic, showing more polar dissolution behavior. The issue with using salt fluxes is often their high melting temperatures. Several reactions require low temperatures for ideal product formation and stability. One approach to avoiding high reaction temperatures is

to use eutectic mixtures of salts. This consists of mixing two or more salts in specific ratios according to phase diagrams to achieve a lower melting temperature than the individual salts.

Metal phosphides have been synthesized using metal fluxes in the literature. Work by Wold et al. have reported that single crystals of CuP_2, NiP_2 and RhP_3 can be synthesized in tin fluxes by using stoichiometric amounts of the elements and 85% tin, heating to 1150 °C for 12-15 hrs.[79] Jeitschko et al. synthesized ternary and binary skutterudite type materials including CoP_3 and NiP_3 using tin fluxes.[173]

In this chapter, two sets of growth techniques for M-P and M-P-S materials are described as follows: flux assisted growth synthesis and their deposition onto P25 TiO_2 (~80 % anatase, ~20 % rutile) powders. M-P and M-P-S materials were synthesized using both salt eutectic and metal fluxes. The eutectic flux chosen was KCl and LiCl. The melting point of KCl and LiCl are 770 °C and 605 °C respectively. When these salts are mixed in a 55:45 KCl:LiCl ratio, a solid solution is formed with a melting point range within 348-361 °C.[174] The solid flux is relatively unreactive towards Pyrex and is separated from the products with methanol and water. Tin and bismuth metal fluxes were also used for flux growth comparison. The surface growth onto TiO_2 was done by depositing one reagent onto the TiO_2 surface and then performing an ampoule exchange reaction seen in Chapter 4. The goals behind the growth techniques are to obtain targeted M-P and M-P-S materials with interesting morphologies that are altered by each flux and to improve photocatalytic activity of TiO_2 using M-P and M-P-S materials grown on its surface.

5.2 Experimental Section

5.2.1 Starting Materials

Transition metal phosphides (M-P) and thiophosphates (M-P-S) were synthesized using a eutectic salt flux, tin flux, bismuth flux or deposited directly on P25 TiO_2 in Pyrex or silica ampoules. The starting reagents and wash solvents with their respective purities are the following: $FeCl_3$ (Alfa Aesar, 98%), $CoCl_2$ (Alfa Aesar, 99.7%), $NiCl_2$ (Alfa Aesar, 99%), $CuCl_2$ (Alfa Aesar, 98%), red phosphorus (Aldrich, 99%), sulfur (Alfa Aesar, 99.5%), P25 TiO_2 (Degussa Corp.), LiCl (Aldrich 99%), KCl (Aldrich, 99%), mossy tin metal, bismuth metal chips (Cerac, 99.9%), methanol (Fisher Scientific, 99.9%), distilled deionized water (18 MΩ) 6 M HCl (Fisher Scientific, diluted) and 7 M HNO_3 (Fisher Scientific, diluted).

5.2.2 Synthesis of M-P and M-P-S Materials Using a KCl-LiCl Eutectic Flux

A pre-made KCl-LiCl eutectic flux was prepared by combining dried KCl and LiCl in a 55:45 mass ratio into a large (O.D. 2.5 cm, I.D. 2.2 cm) Pyrex tube connected to a Cajon compression fitting with a valve in the glove box. The tube was removed from the glove box and evacuated on the Schlenk line. The salts were melted with an oxygen/methane gas torch under vacuum and then allowed to re-solidify and cool to room temperature. The cooled tube was re-introduced into the glove box and the solid was broken into small pieces using a hammer and aluminum foil. The pieces were then ground to a fine powder using a large ceramic mortar and pestle and stored in the glovebox.

The synthesis of the transition metal phosphides and thiophosphates using KCl-LiCl salt flux were done using 0.25 g of the metal halides $FeCl_3$ (0.00154 mol), $CoCl_2$ (0.00193 mol), $NiCl_2$ (0.00193 mol), or $CuCl_2$ (0.00186 mol) and stoichiometric amounts of red phosphorus, and sulfur for M-P-S materials. The pre-made ground salt flux was added in three fold excess to the total mass of the reagents and all reagents were ground together using an agate mortar and pestle in the argon filled glove box.

The solids were loaded into either a Pyrex or quartz tube using a custom made glass funnel. The tube was connected to Cajon compression fitting with a valve. With the valve closed, the tube assembly was removed from the box, attached to a Schlenk line, evacuated, and then sealed under vacuum. The tube was placed in the tube furnace at a slight angle to keep liquid flux at one end, and heated to 500 °C with a ramp rate of 1.67 °C/min (~100 °C/ hr) and held at 500 °C for ~18 hours.

The ampoules were allowed to cool by first pulling the end of the tube without solid out of the tube furnace to allow transported byproducts to condense. The entire tube was allowed to cool to room temperature after no additional byproduct condenses. Once cooled, the ampoules were opened carefully in air in the fume hood. The solids were difficult to remove without the use of hot solvent. The KCl-LiCl flux based reactions required hot methanol coupled with sonication first to remove the solids from the tube. Once all solids were removed from the tube, they were loaded into a beaker with ~100 mL of methanol. Vigorous magnetic stirring was done for about 10 minutes. The solids were isolated using centrifugation. Room temperature deionized water was used as a second wash for 10 minutes to remove KCl. After washing twice in DI water, the solids

were re-suspended in small amounts of DI water and dried in air at room temperature. All materials were stored in the glove box.

5.2.3 Synthesis of M-P and M-P-S Materials Using Metal Fluxes

The synthesis of the transition metal phosphides and thiophosphates using tin or bismuth metal fluxes were done using 0.25 g of the metal halides $FeCl_3$ (0.00154 mol), $CoCl_2$ (0.00193 mol), $NiCl_2$ (0.00193 mol), or $CuCl_2$ (0.00186 mol) and stoichiometric amounts of red phosphorus, and sulfur for M-P-S materials. The metal halide, and phosphorus or sulfur was added to a Pyrex tube using a custom made glass funnel. The Pyrex tube was pre-loaded with tin or bismuth metal, which had up to a fifteen fold mass excess to the total mass of the reagents. The tube was tapped gently to push the metal halide, phosphorus or sulfur between the metal chunks.

The tube was connected to a Cajon compression fitting with a valve. With the valve closed, the tube was removed from the box, attached to a Schlenk line, evacuated, and then sealed under vacuum. The tube was placed in the tube furnace at a slight angle to keep liquid flux at one end, and heated to 500 °C with a ramp rate of 1.67 °C/min (~100°C/hr) and held at 500 °C for ~18 hours.

The ampoules were allowed to cool by first pulling the end of the tube without solid out of the tube furnace to allow transported byproducts to condense. The entire tube was allowed to cool after no additional byproduct condenses. Little to no transported liquid was seen for the M-P and M-P-S samples and the transported liquid did not smoke in air. Once cooled to room temperature, the ampoules were opened carefully in air in the fume hood. The products were isolated from the tin flux using ~150 mL of warm

(~80 °C) 6 M HCl, and for the bismuth flux, ~150 mL warm 7 M HNO_3 was used stirring constantly in both cases. Dissolving the fluxes often take long periods of time even in highly corrosive environments. The tin flux samples usually required several hours to dissolve the metal, while bismuth flux samples took only slightly shorter times to dissolve. The resulting aqueous supernatant for the tin samples were all colorless, however the bismuth samples often had a greenish color. Also, bismuth samples evolved brown NO_2 gas. The samples were removed from the acid solutions once all evidence of gas production from bubbling ceased. The samples were rinsed several times in DI water until the pH of the wash solution was neutral. The samples were dried in air at room temperature and then stored in glass vials in the glove box.

5.2.4 Synthesis of M-P and M-P-S Materials on P25 TiO_2

Transition metal phosphides and thiophosphate materials were deposited on P25 TiO_2 using solvent evaporation and drying of metal halide precursors and then reacting them with P (or S) in sealed ampoules. Typically, 0.25 g of the metal halides, $FeCl_3$ (0.00154 mol), $CoCl_2$ (0.00193mol), $NiCl_2$ (0.00193 mol), or $CuCl_2$ (0.00186 mol), were added to a 100 mL Schlenk flask with 0.25 g of pre-dried P25 TiO_2 and a stir bar in the argon filled glove box. A rubber septum was added to the flask and the stopcock was closed. The flask was removed from the glove box and attached to a Schlenk line in which approximately 50 ml of degassed methanol was added via cannula transfer technique. The flask was allowed to stir for several minutes and then was placed in a warm water bath. The rubber septum was replaced with a glass stopper and a liquid nitrogen cold trap was added to the Schlenk line. The flask was evacuated until all of the

methanol was removed by the trap. The flask was allowed to dry in the warm water bath for an additional 30 minutes under vacuum. Once dry, the flask was closed and returned to the glove box. The solids were removed and added to a mortar along with an appropriate amount of red phosphorus, plus sulfur for the M-P-S materials, and then ground together intimately.

The combined solids were loaded into a Pyrex or quartz ampoule using a custom made glass funnel and a Cajon compression fitting was attached. The valve on the fitting was closed, and the tube was brought out of the glove box. The tube was placed on a Schlenk line, evacuated, and sealed under vacuum using an oxygen/methane torch. The sealed ampoule was placed into a tube furnace and heated to 500 °C, or 700 °C for the iron reaction, with a ramp rate of 1.67 °C/min (100 °C/hour). Once the maximum reaction temperature was achieved, the reaction was allowed to heat for ~18 hours. When the heating program was finished, the ampoule end without solid was carefully pulled out of the tube furnace and allowed to cool to room temperature to allow any transportation of volatile byproducts to occur. Once no additional byproduct transported and condensed, the entire ampoule was allowed to cool to room temperature and then opened carefully in the hood in air. The solids were weighed and then stored in the glove box for future characterization.

5.2.5 Sample Characterization

Powder X-Ray Diffraction (XRD) was done using either a Siemens D-5000 or a Bruker D-8 Advance DaVinci Diffractometer. All materials were scanned using nickel filtered Cu K-α X-ray irradiation, 40 kV and 40 mA energy output, with a 2-theta angle

range from 10 to 80 degrees. The step size was 0.05 degrees and the slit widths of the X-ray source and detector were 1.00 mm and 5.90 mm, respectively. The samples were prepared for analysis by first grinding them down to fine powders using a mortar and pestle. The samples were mounted onto pre-cut glass microscope slides, affixed by air drying in an acetone slurry or by using a very thin layer of vacuum grease. All samples were pressed down flat before examination. The morphology and elemental analysis of the samples was investigated using scanning electron microscopy (SEM) and energy dispersive spectroscopy (EDS) on a Hitachi S-3400 (thermionic) or S-4800 (field emission) system. Samples were prepared by making thinly pressed pellets using a KBr hand press.

5.3 Results and Discussion

5.3.1 Analysis of M-P and M-P-S Materials Using KCl-LiCl Eutectic Salt Flux

The balanced reactions for the KCl-LiCl eutectic salt flux reactions are the same as the reactions seen in Chapter 4, where MP_2, MP_3, MPS_3 or Cu_3PS_4 are stoichiometrically targeted with PCl_3 byproduct formation. The only adjustment is the addition of the premade flux, which was in 3x mass excess with respect to the starting MCl_x and P(S) reagents. The colors and yields of the M-P and M-P-S products are shown in Table 5.1. The M-P reactions all produced colorless liquid by-product which smoked in air, indicating the presence of PCl_3. Likewise, the M-P-S reactions produced familiar byproducts, which were a colorless liquid and brownish yellow solid transport. The Fe-P reaction at 500 °C was not successful however, which was verified from characterization techniques. Also, when removing the flux with methanol and water, the Fe-P reaction's solution was orange, leaving hardly any solid product, indicating that

$FeCl_3$ was present. All other reactions had low to moderate yields between 2% - 68%. The Ni-P and Co-P samples were lighter colored (dark gray) than the pure black colored versions in Chapter 4. The Cu-P sample was matte dark gray and not shiny black as seen in Chapter 4. The M-P-S samples all had familiar colors. The only change was that there was a visible luster in the Ni-P-S and Cu-P-S samples. The yields were calculated based on the targeted M-P and M-P-S products seen in Chapter 4. Samples that had low yields also had colored methanol wash solutions indicating incomplete reactions and dissolved metal ions.

Powder XRD stackplots of the M-P products are shown in Figure 5.1 and key results are summarized in Table 5.1. The Fe-P sample is not shown due to an amorphous pattern. The Fe-P sample was resynthesized and gave the same result. It was seen in Chapter 4 that the Fe-P ampoule reaction required higher heating to 700 °C, therefore the failed reaction is not too surprising. A higher temperature Fe-P reaction was not attempted since the salt fluxes will attack silica tubes. The Co-P sample showed only cubic CoP_3 (PDF# 04-004-4318). The Ni-P sample showed only cubic NiP_2 (PDF# 04-003-2351). The Cu-P sample was interesting, showing two phases. The major phase was monoclinic CuP_2 (PDF# 01-076-1190) and the secondary phase was triclinic Cu_2P_{20} (PDF# 01-077-5934). The unusual Cu_2P_{20} phase has been synthesized in the literature by Nilges et al.[175] The reaction conditions involved using red phosphorus, CuI and Cu_3P heated to 547 °C for one week. The resulting material produced Cu_2P_{20} needle shaped crystals embedded in red solid.

Table 5.1 Characterization results for M-P and M-P-S materials synthesized in a KCl-LiCl flux at 500 °C. Bolded XRD phases are dominant phases. All EDS data was scaled according to the respective metal.

Reaction	**Target Product**	**Color**	**Yields Based on Target**	**XRD phases**	**M : P : S : Cl**
$FeCl_3$ + P	FeP_2	dark brown	2 %	amorph.	(no iron present)
$CoCl_2$ + P	CoP_3	dark gray	44 %	CoP_3	1 : 4.52 : 0 : 0.05
$NiCl_2$ + P	NiP_2	dark gray	68 %	NiP_2	1 : 2.50 : 0 : <0.01
$CuCl_2$ + P	CuP_2	dark brown	8 %	**CuP_2**, Cu_2P_{20}	1 : 3.63 : 0 : 0.13
$FeCl_3$ + P + S	$FePS_3$	dark brown	9 %	$FePS_3$	1 : 1.24 : 2.34 : <0.01
$CoCl_2$ + P + S	$CoPS_3$	black	2 %	$CoP_{0.5}S_{1.5}$	1 : 0.79 : 2.86 : <0.01
$NiCl_2$ + P + S	$NiPS_3$	shiny black	35 %	**$NiPS_3$**, NiS_2	1 : 1.26 : 3.37 : <0.01
$CuCl_2$ + P + S	Cu_3PS_4	shiny yellow-green	63 %	Cu_3PS_4	1 : 0.35 : 1.19 : 0.02

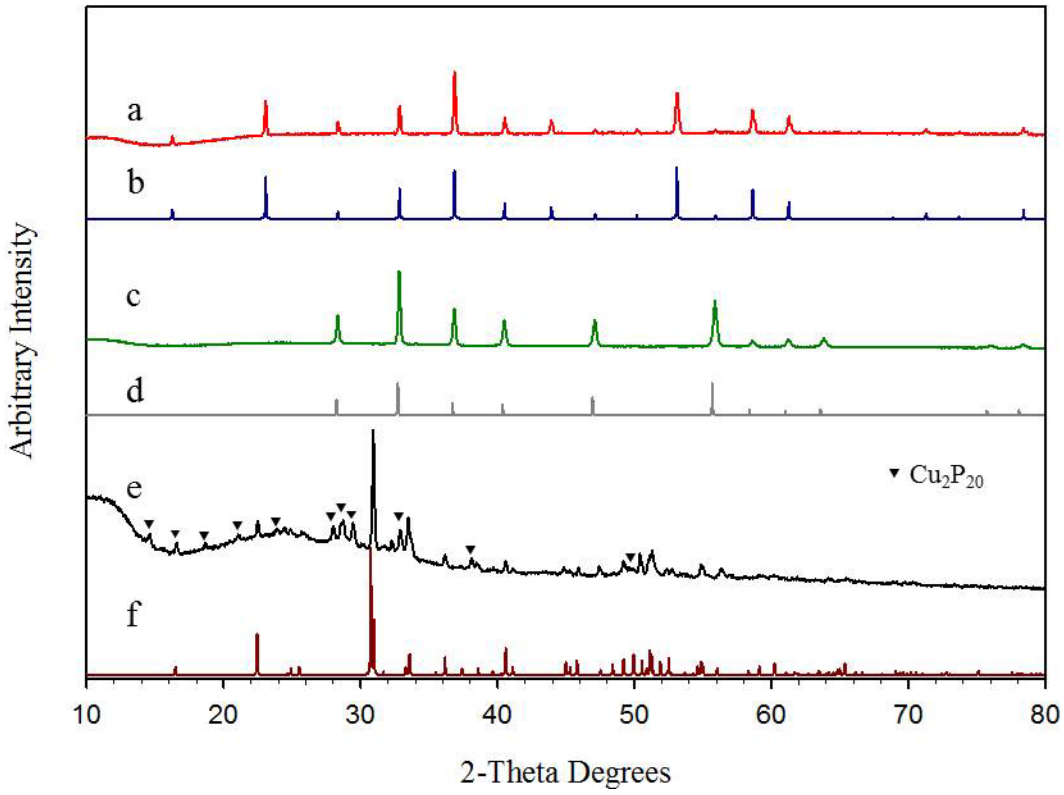

Figure 5.1 XRD stackplot of the M-P products synthesized from KCl-LiCl eutectic salt flux. The respective patterns are: (a) Co-P sample (b) reference CoP_3, (c) Ni-P sample, (d) reference cubic NiP_2, (e) Cu-P sample, and (f) reference CuP_2.

Powder XRD plots of the M-P-S products are shown in Figures 5.2 and 5.3. The Fe-P-S sample showed monoclinic $FePS_3$ (PDF# 04-005-1516). The baseline is high due to the fluorescence background from iron and there is a small unidentified peak at 24°. The only pattern that remotely comes close to matching is the pattern for S_8. This does not make much sense because any unreacted sulfur would have transported away. The Co-P-S sample also has a fluorescence background and showed peaks similar to $CoP_{0.5}S_{1.5}$ (PDF# 04-007-4518). This is the first time that this phase has been seen alone without the $CoPS_3$ phase. $CoP_{0.5}S_{1.5}$ was first seen in the ampoule reaction between $CoCl_2$ + P + S in Chapter 4. It adopts the pyrite structure and can be envisioned as a

CoS_2 phase, which also has the pyrite structure, with phosphorus substituting some of the sulfur atoms, yielding an empirical formula of $Co(P_xS_{1-x})_2$ where x = 0.25. The sample pattern is shifted to the left of the $CoP_{0.5}S_{1.5}$ pattern and shifted to the right of the CoS_2 pyrite pattern (not shown). This indicates that there is most likely a solid solution between these two phases. The flexibility of substituting phosphorus for sulfur within the CoS_2 structure has been investigated by Nahigian et al.[176]

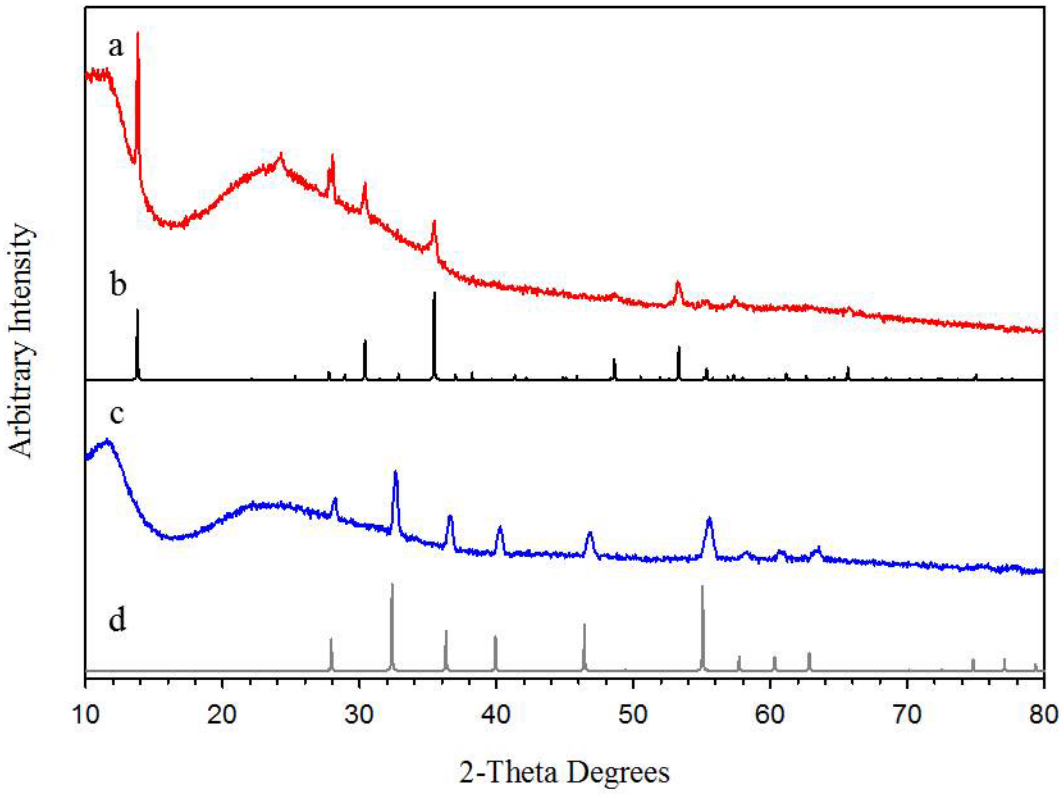

Figure 5.2 XRD stackplot of the M-P-S products synthesized from KCl-LiCl eutectic salt flux. The respective letters are for each pattern: (a) Fe-P-S sample, (b) reference $FePS_3$, (c) Co-P-S sample, and (d) reference $CoP_{0.5}S_{1.5}$.

The Ni-P-S sample (Figure 5.3) showed monoclinic $NiPS_3$ (PDF# 00-033-0952) and very small peaks for cubic pyrite NiS_2 (PDF# 04-003-1992). The (001) peak at 14° which represents the interlayer Van der Waals gap (001 peak) is much more intense in this sample than any of the other MPS_3 synthesized materials. The Cu-P-S sample pattern is also shown in Figure 5.3. This sample showed single phase orthorhombic Cu_3PS_4 (PDF# 04-007-4285).

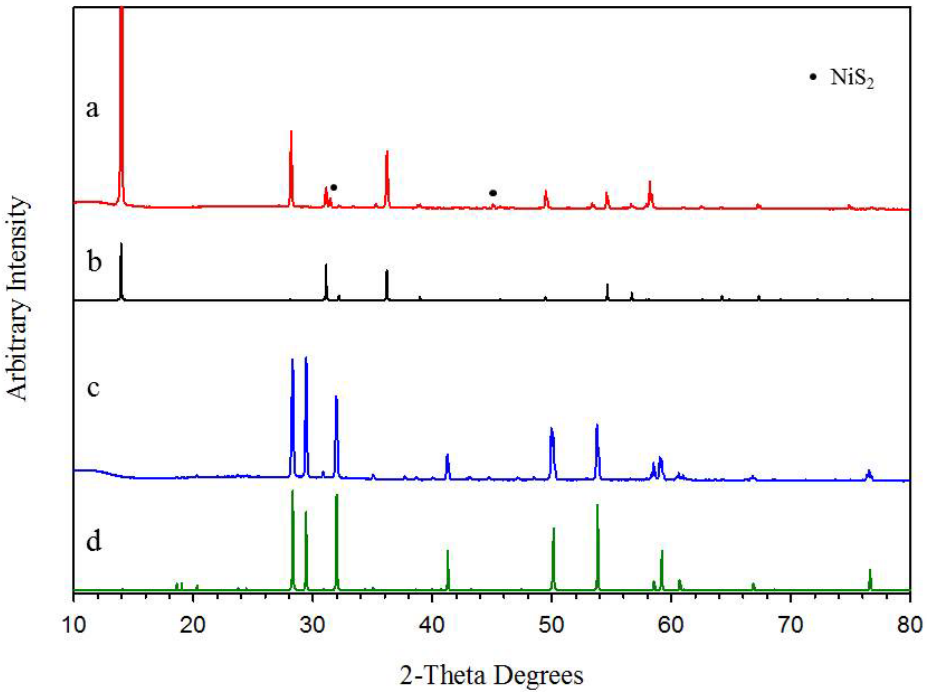

Figure 5.3 XRD stackplot of the M-P-S products synthesized from KCl-LiCl eutectic salt flux. The respective letters are for each pattern: (a) Ni-P-S sample, (b) reference $NiPS_3$, (c) Cu-P-S sample, and (d) modified reference Cu_3PS_4.

The energy dispersive spectroscopy data (EDS) for the M-P and M-P-S samples are shown in Table 5.1. The data represents atomic percents of each element relative to the metal content. For example, for the targeted MP_2 samples, the ideal P/M atomic percent ratio should be 2. For the MPS_3 samples the ideal P/M ratio should be 1 and the

ideal S/M ratio should be 3. For Cu_3PS_4 the ideal ratios are 0.33 for P/M and 1.33 for S/M.

The Fe-P sample was amorphous, which was seen by XRD. The EDS data showed no iron signal. The only elements present were silicon, oxygen, and chlorine. This makes sense since presumably, all of the $FeCl_3$ was washed away during the methanol and water washes. The silicon is present probably from the attack of the metal halides on pyrex. The M-P samples generally showed higher than ideal phosphorus content, very small amounts of residual chlorine. Very little to no oxygen signal and no potassium signal (not tabulated) was seen for the samples.

The M-P-S samples had a slight excess in phosphorus content compared to the major phases seen by XRD. The sulfur content for the iron and copper samples were slightly lower than expected. The nickel and cobalt samples also had an excess in sulfur content. All of the samples had chlorine contents that were near or below detection levels of the instrument. The oxygen content was also negligible, within uncertainties of EDS analysis of light elements.

The SEM images for the M-P materials grown from KCl-LiCl salt flux are shown in Figure 5.4. The Fe-P sample is not shown due to unsuccessful product formation. The Co-P sample showed several large fused shard-like aggregates. The large pieces ranged from ~20-40 micrometers. Closer inspection of the large aggregates showed clusters for fused smaller shards that were approximately ~2-10 micrometers in size. The nickel sample showed similar results, consisting of more blocky clusters of shards which ranged from sub-micrometer to several tens of micrometers in size. The Cu-P sample showed an interesting morphology. The sample consisted of fused blocky structures surrounded in clumps of needle-like clusters. The blocky structures varied in size from about ~5-10 micrometers. The needles vary greatly in length across the sample region, ranging from single micrometers to ~40 micrometers. The needle thickness is ~ 500 nanometers. The

needles may be Cu_2P_{20} as such morphology was previously observed for Cu_2P_{20} by Nilges as well.[3]

The SEM images for the M-P-S materials grown from KCl-LiCl salt flux are shown in Figure 5.5. The Fe-P-S sample showed aggregates of small rounded spherical structures which ranged from single micrometers to approximately 10 micrometers. The Co-P-S sample also showed spherical structures that were more defined and mixed in with some blocky structures. The spheres ranged from a few hundred nanometers to ~ 1-2 micrometers. The blocky structures were ~7-10 micrometers. The Ni-P-S sample formed large fused plate-like structures. The plates ranged from ~20-30 micrometers across. The plate thickness was ~3-4 micrometers. The Cu-P-S sample formed large islands of small fused blocky structures that ranged from ~700 nanometers to ~3 micrometers. The bulky islands varied greatly, often being in the several tens of micrometers.

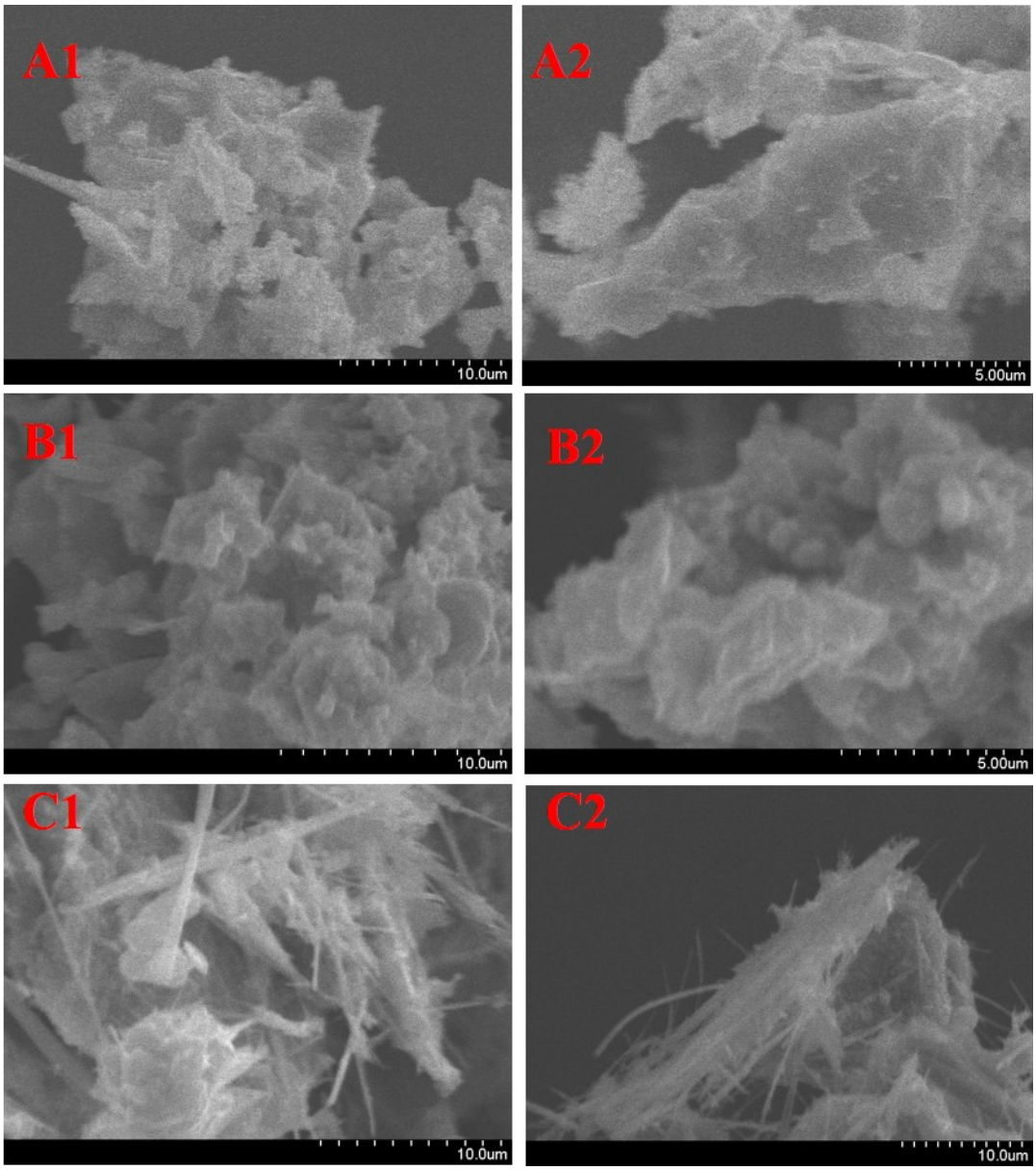

Figure 5.4 SEM images of the M-P products synthesized using the KCl-LiCl flux. A = Co, B = Ni, C = Cu. Numbered images represent either a zoomed in image or area of interest.

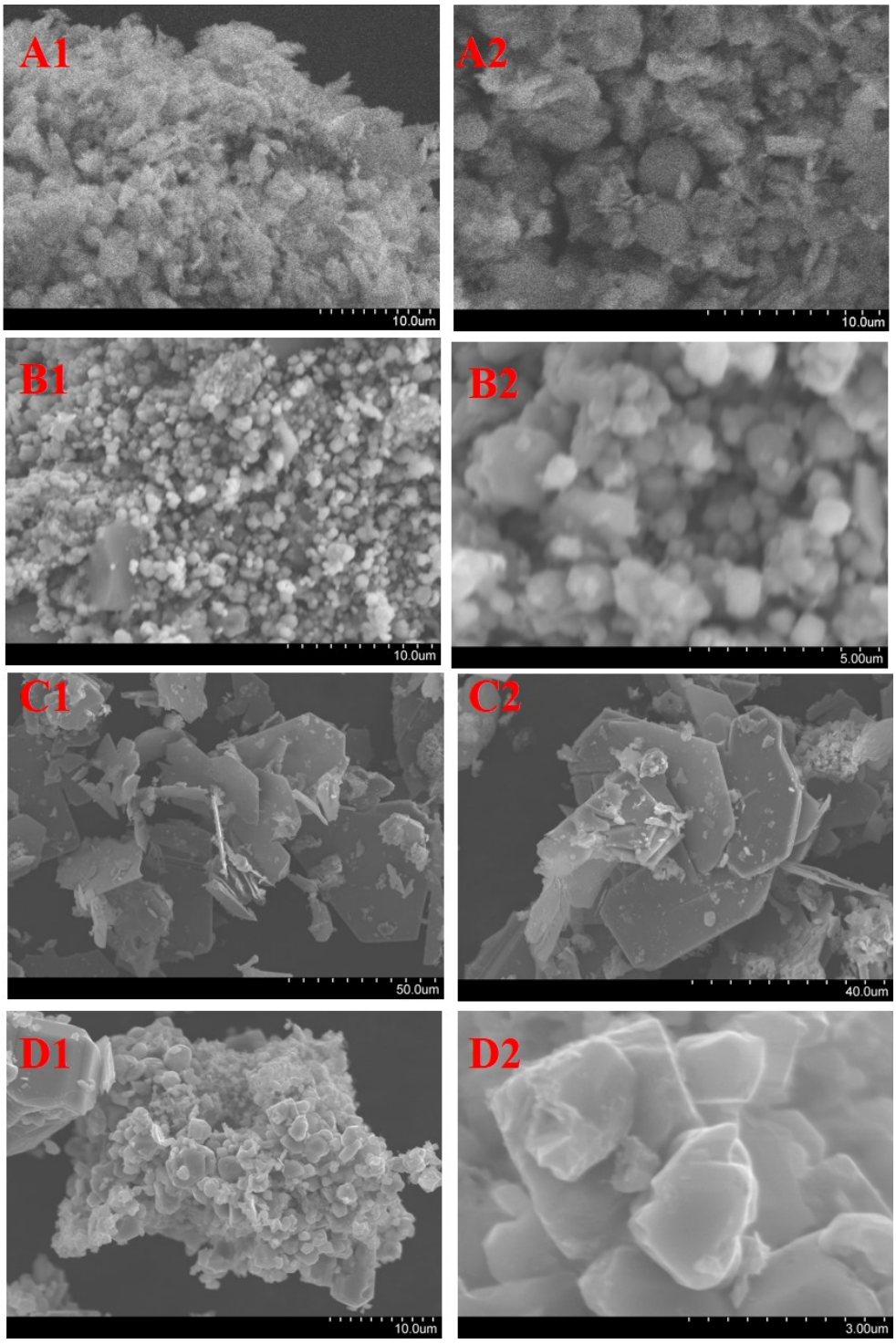

Figure 5.5 SEM images of the M-P-S products synthesized using the KCl-LiCl flux. A = Fe, B = Co, C = Ni, D = Cu. Numbered images represent either a zoomed in image or area of interest.

From analyzing the SEM images and the product phases, the growth of the particles can begin to be rationalized. Reactions are often better facilitated in a liquid phase than solid phase interactions. Melting the KCl-LiCl flux yields a colorless liquid that rapidly solidifies to a very hard solid solution if not heated above ~353 °C. The ionic KCl-LiCl flux is not very viscous when melted but becomes very sluggish when it dissolves the metal halides. Crystal growth seemed to be limited to the phosphorus diffusion into the molten flux. The metal halides dissolve into the ionic flux rapidly, changing color in the flux while red phosphorus tends to sit on the surface interface of the flux. Phosphorus does start to change its phase around the melting temperature of the flux, so more gaseous P_4 units are present than polymeric red phosphorus. In order to form products, the P_4 gas has to be in contact with the metal halide surface. It is difficult to determine how well P_4 gas diffuses through the molten slurry of flux and metal halide. However over time, black (or greenish-yellow for Cu_3PS_4) colored products can be clearly seen throughout the flux which resembles veins as the reaction cools down.

In order to aid with the diffusion of phosphorus into the flux, three different reaction attempts were made. The first method involved grinding the metal halides together with red phosphorus and then grinding them together with the premade flux. The mixed solids were then heated to 500 °C. The second method involved adding the metal halides to the pre-made flux and allowing them to dissolve into the flux. The flux color changes when then metal halides are dissolved into it, (e.g. deep blue/green for $NiCl_2$) and becomes various lighter shades of the anhydrous MCl_x when cooled. Red phosphorus was then added on top of this cooled mixture and then heated to the maximum reaction temperature of 500 °C. The third method was to replicate the same steps in the second method but to grind the flux/metal halide mix and then grind it with the red phosphorus before heating the entire mixture to 500 °C.

Product formations from each of these steps were similar however. Regardless of how intimate phosphorus was to the metal halides, there was always a very visible

separation of the flux/metal halide mix and red phosphorus. One possible explanation is understanding how the compounds are bonded. Both the flux and the metal halides are ionic, having the chlorine atoms donating electrons to the metal orbitals, which explain why the metal halides dissolve into the flux rapidly. However the phosphorus is more covalent in nature, sharing electrons between p-orbitals in both the polymeric and P_4 states. The differences in bonding help explain why there is a visible separation between the reagents that could limit growth and explain low yields for some reactions.

5.3.2 Analysis of M-P and M-P-S Materials using Metal Fluxes

The balanced equations used for the metal flux reactions were identical to the M-P and M-P-S (using red P and S) in Chapter 4. The yields and colors of the samples are shown in Table 5.2. Only data on the tin flux samples are shown since the bismuth flux samples were not very successful. As mentioned earlier, all of the bismuth samples gave a greenish color in the aqueous layer when removing the flux with HNO_3. After the washing step, these reactions gave little to no sample powders.

Majority of the tin flux samples had a visible luster to them. From a physical observation, all of the M-P and M-P-S samples, minus the Cu-P-S sample, showed similar product colors seen in Chapter 4. The Cu-P-S sample was expected to yield a greenish-yellow powder, but produced a black solid instead. The yields were moderate to good ranging from 30-80% across all samples.

The powder XRD stackplots for the M-P products grown in a tin flux are shown in Figures 5.6 and 5.7. The Fe-P sample showed three phases. The major peaks in the pattern represent orthorhombic FeP_2 (PDF# 04-003-1993). This is a very promising result since the tin flux promotes the formation of FeP_2 at a lower temperature (500 °C)

than what was seen in Chapter 4. There were also peaks for FeP (PDF #03-065-2595) and for SnP_3 (PDF #04-007-1068). The presence of a tin phase indicates that the flux is reactive towards red phosphorus. The Co-P sample showed two phases. The major phase was cubic CoP_3 (PDF #04-004-4318). There were peaks for CoP (PDF #04-004-3080). Three unidentified peaks were present at 27°, 45°, and 54°. The Ni-P sample showed two main phases. The major phase was monoclinic NiP_2 (PDF #04-007-3963) and the minor phase was cubic NiP_2 (PDF #04-003-2351). This is the first time that we have observed the $NiCl_2$ + P reaction produce the thermodynamic monoclinic NiP_2 product. The Cu-P sample showed two major phases. The major phase was monoclinic CuP_2 (PDF #01-076-1190) and the minor phase was Cu_4SnP_{10} (PDF #04-010-1052).

Table 5.2 Characterization results for M-P and M-P-S materials synthesized in a tin flux.

Reaction	**Target Product**	**Color**	**Yields Based on Target Product**	**XRD phases**	**M : P : S : Cl**
$FeCl_3$ + P	FeP_2	dark gray	58 %	**FeP_2**, FeP, SnP_3	1 : 1.99 : 0 : <0.01
$CoCl_2$ + P	CoP_3	shiny black	81 %	**CoP_3**, CoP	1 : 2.47 : 0 : <0.01
$NiCl_2$ + P	NiP_2	shiny black	61 %	NiP_2 (**mon.**,cub.)	1 : 2.53 : 0 : <0.01
$CuCl_2$ + P	CuP_2	black	30 %	**CuP_2**, Cu_4SnP_{10}	1 : 2.24 : 0 : <0.01
$FeCl_3$ + P + S	$FePS_3$	black	29 %	**FeP**, FeP_2	1 : 1.14 : 0.02 : <0.01
$CoCl_2$ + P + S	$CoPS_3$	black	37 %	**CoP_3**, CoP, CoP_2	1 : 1.93 : 0.01 : <0.01
$NiCl_2$ + P + S	$NiPS_3$	shiny gray	40 %	**NiP_2**, **Ni_2SnP**	1 : 1.29 : <0.01 : <0.01
$CuCl_2$ + P + S	Cu_3PS_4	dark gray	33 %	**CuP_2**, Cu_4SnP_{10},	1 : 1.82 : <0.01 : <0.01

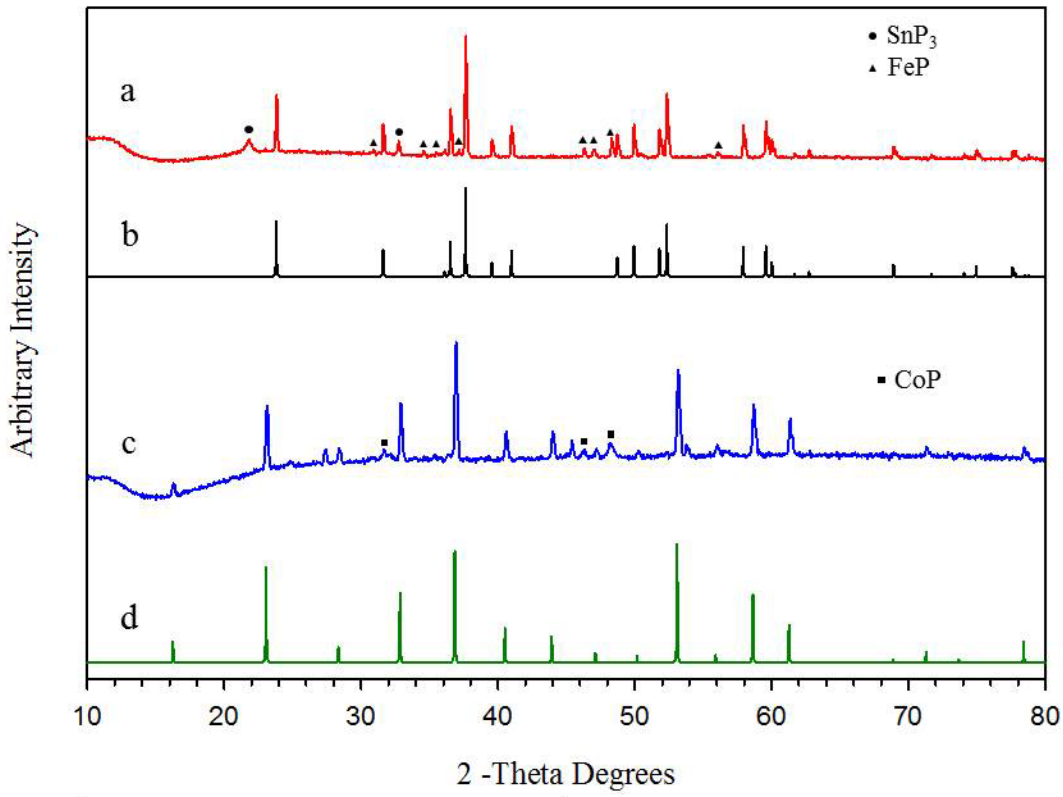

Figure 5.6 XRD stackplot of the M-P products synthesized from tin flux. The respective letters are for each pattern: (a) Fe-P sample, (b) reference FeP_2, (c) Co-P sample, (d) reference CoP_3.

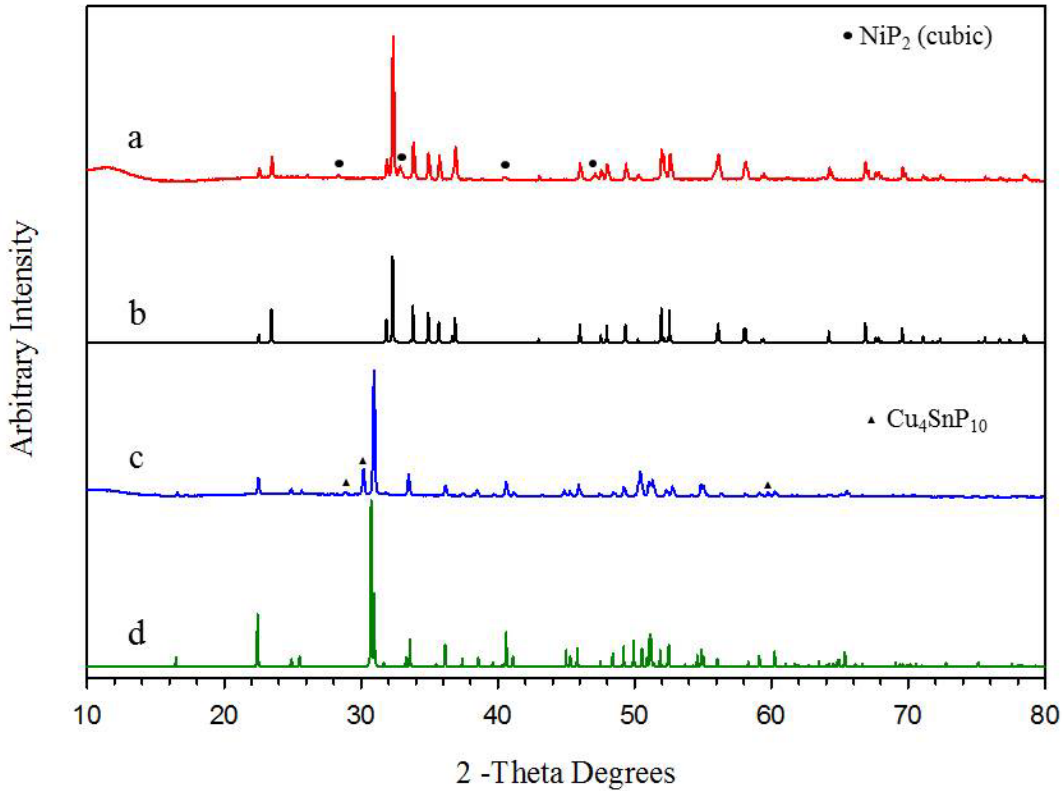

Figure 5.7 XRD stackplot of the M-P products synthesized from tin flux. The respective letters are for each pattern: (a) Ni-P sample, (b) reference monoclinic NiP_2, (c) Cu-P sample, (d) reference CuP_2.

The powder XRD stackplots for the M-P-S products are shown in Figures 5.8 and 5.9. The general yet unexpected trend that was seen in all of the samples was that no M-P-S phases were seen for any of the samples. The Fe-P-S sample showed two phases; FeP (PDF # 03-065-2595) and FeP_2 (PDF # 04-003-1993). The FeP peaks are much broader than the FeP_2 peaks, and are shifted slightly to lower 2-theta values. The FeP_2 peaks are sharp and centered. The Co-P-S sample showed a mixture of cobalt phosphide phases. These phases were CoP_3 (PDF # 04-004-4318), CoP (PDF # 04-004-3080) and CoP_2 (PDF #04-003-4573). There is an unidentified peak at 33.5°. The Ni-P-S sample showed two main phases. The phases monoclinic NiP_2 (PDF # 04-007-3963) and Ni_2SnP

(PDF # 04-010-2577) were present and in equal intensity. The Cu-P-S sample showed two phases. The major phase was monoclinic CuP_2 (PDF # 01-076-1190), and the minor phase was Cu_4SnP_{10} (PDF # 04-010-1053).

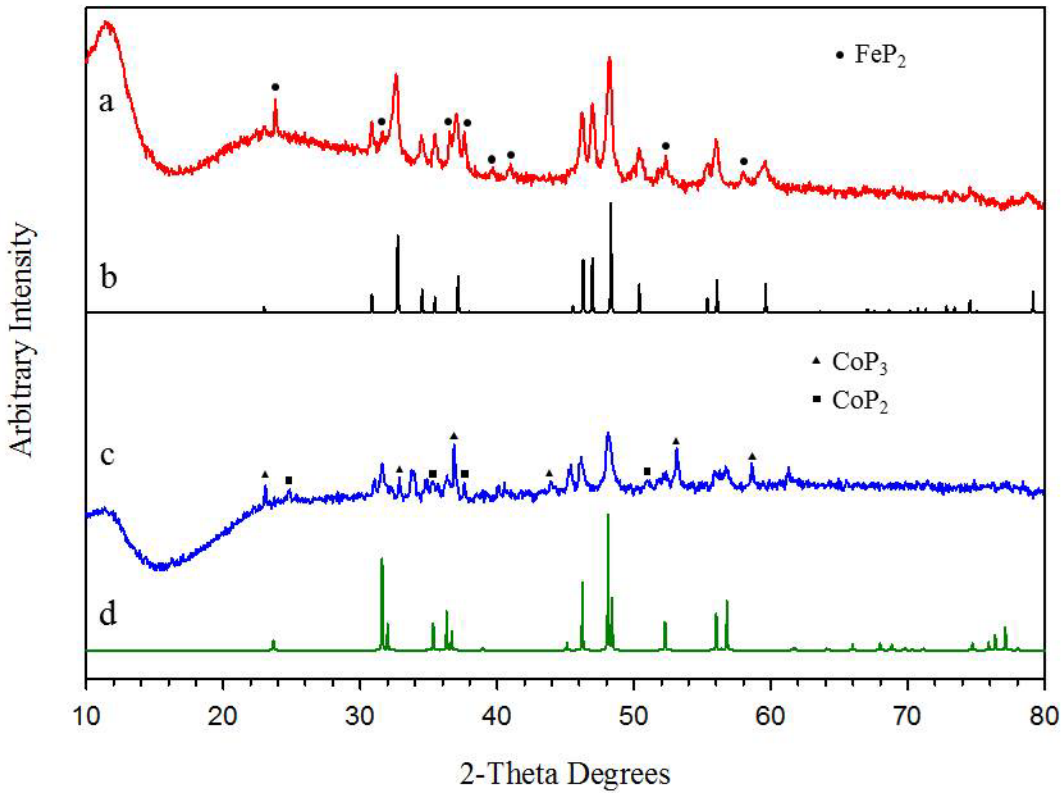

Figure 5.8 XRD stackplot of the M-P-S products synthesized from tin flux. The respective letters are for each pattern: (a) Fe-P-S sample, (b) reference FeP, (c) Co-P-S sample, (d) reference CoP.

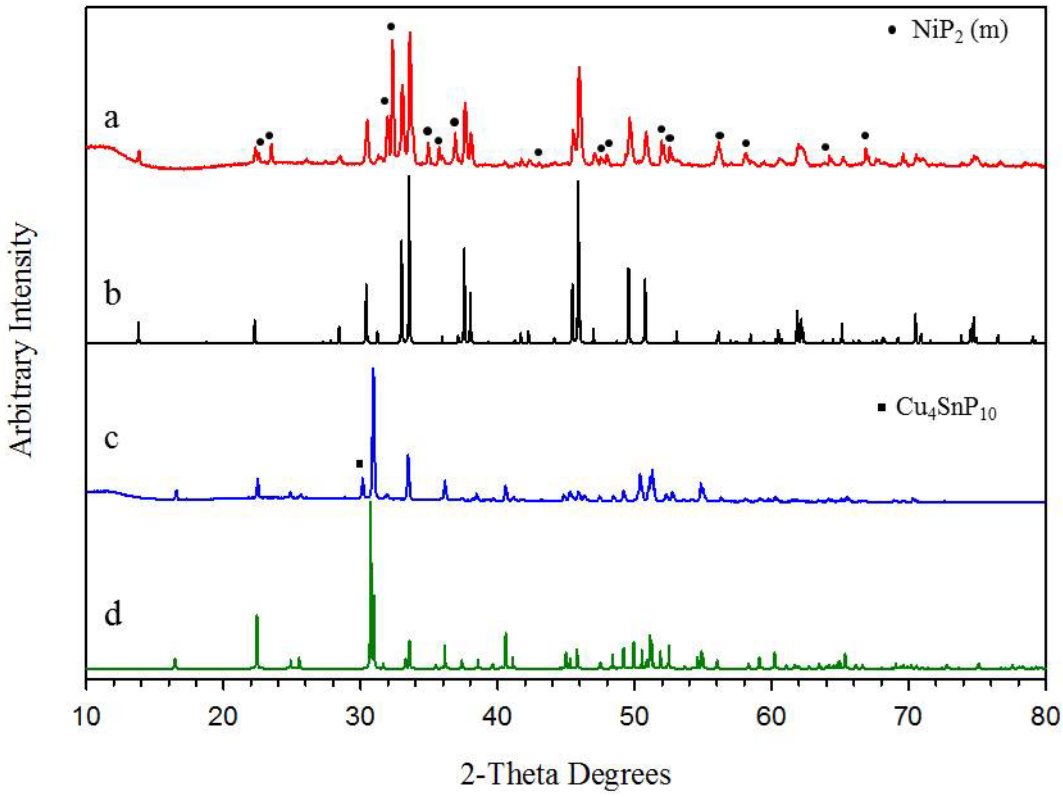

Figure 5.9 XRD stackplot of the M-P-S products synthesized from tin flux. The respective letters are for each pattern: (a) Ni-P-S sample, (b) reference Ni_2SnP, (c) Cu-P-S sample, (d) reference CuP_2.

The EDS data for the M-P and M-P-S samples synthesized in a tin flux are shown in Table 5.2. The M-P samples were generally near the desire phosphorus content or in slight excess. For all cases the chlorine content was below detection limits of the instrument. In the Fe-P, Cu-P, Ni-P-S, and Cu-P-S samples, very small tin atomic percent was detected. All other samples had no detectable tin. The M-P-S samples all had phosphorus content close to the XRD phases seen with most sample being in slight excess. Also, all samples had sulfur content that was at the detection limits of the instrument. The Ni-P-S sample's phosphorus content seemed to be an average between the major phases seen by XRD.

The SEM images for the M-P materials grown from tin flux are shown in Figure 5.10. The Fe-P sample showed uniform small smooth blocky structures. The blocks range from ~500 nm to 6 micrometers. The Co-P sample showed aggregates of fused round particles. Individual particle regions are within ~1-5 micrometers across. The Ni-P sample showed a mixture of shard-like structures and small blocky particles. The shards vary in size anywhere from a few micrometers to several tens of micrometers. The small particles range from ~400 nanometers to single micrometers. The Cu-P sample consists of large ~20-30 micrometer shard-like constructs that are comprised of smaller ~5-10 micrometer shards.

The SEM images for the M-P-S materials grown from tin flux are shown in Figure 5.11. The Fe-P-S sample consists of shard-like structures that range from ~5-20 micrometers. The Co-P-S sample is comprised of very small aggregate particles that are several hundred nanometers to a few micrometers in size. The Ni-P-S sample consists of large blocky structures that are ~5-10 micrometers long. The Cu-P-S sample is a mixture of aggregate particles, blocks and long plate-like structures. The aggregates are within sub-micrometer sizes, the blocks are ~15 micrometers in length, and the plates are ~40-60 micrometers long. The plate growth seems to represent a single, somewhat hexagonal plate growing in one direction.

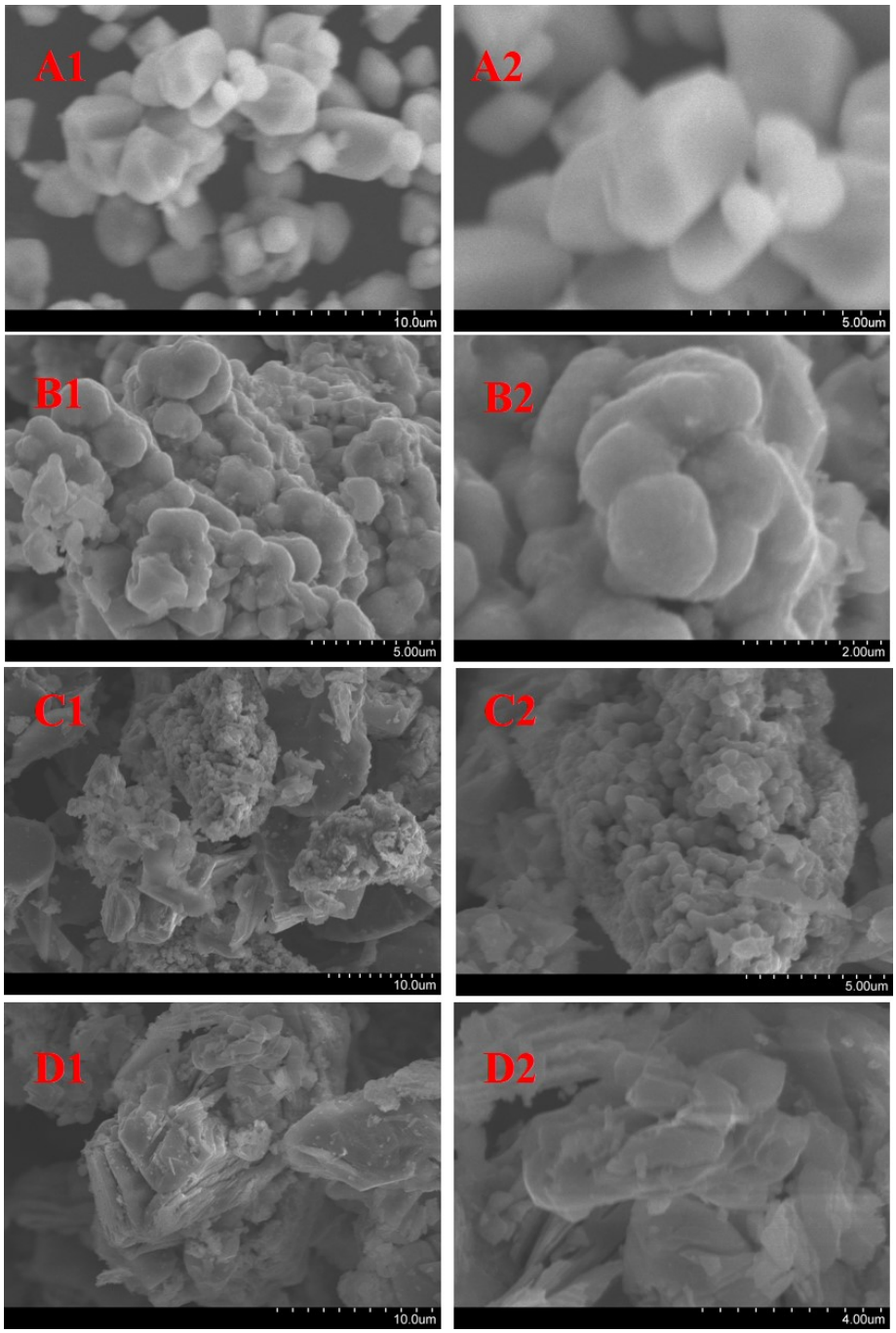

Figure 5.10 SEM images of the M-P products synthesized using tin flux. A = Fe, B = Co, C = Ni, D = Cu. Numbered images represent either a zoomed in image or a different area of interest.

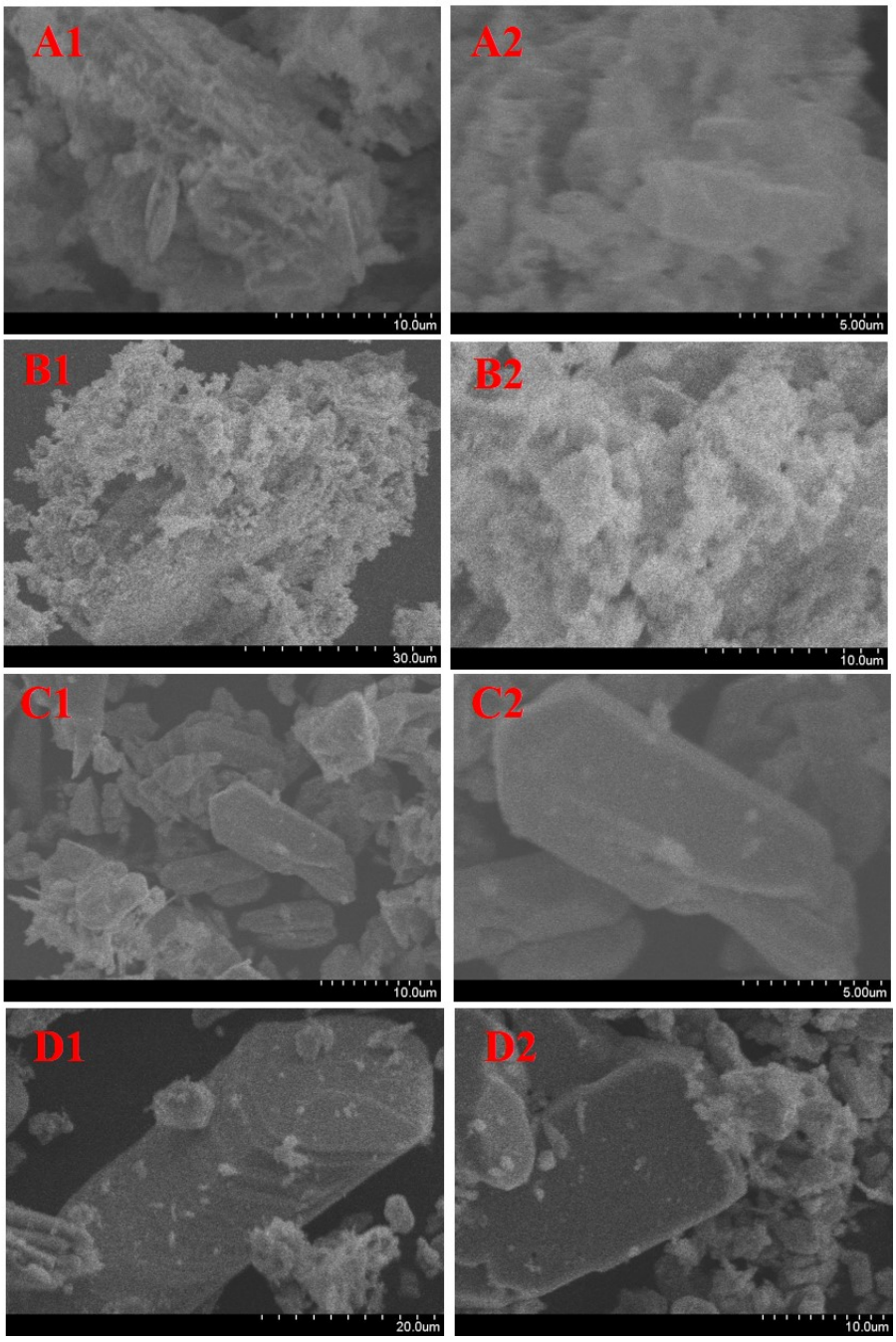

Figure 5.11 SEM images of the M-P-S products synthesized using tin flux. A = Fe, B = Co, C = Ni, D = Cu. Numbered images represent either a zoomed in image or a different area of interest.

Crystal growth in a tin flux produces a variety of morphological changes to M-P and M-P-S materials. The molten metal engulfs the solids reagents and can dissolve elements such as phosphorus better than ionic fluxes. The flux can also force close contact of reagents and provide a uniform heating environment. Also, the density of liquid tin is ~7 g/cm^3 thus applying pressure around the solids. This is denser than the KCl-LiCl flux. This may explain the compactness of The Fe-P and Co-P materials. Cooling the flux slowly can aid in improved crystal formation as well.

5.3.3 Analysis of M-P and M-P-S Materials Deposited on P25 TiO_2

M-P and M-P-S materials were synthesized on P25 TiO_2 via evaporating methanol from a mixture of the metal halides and P25 TiO_2. This resulted in metal halides being deposited on the surface of P25 TiO_2. The precursor composite material was reacted with phosphorus (and sulfur) in sealed ampoules. After heating to 500 °C, the anatase and rutile phases of TiO_2 were still seen. The reactions are similar to the ampoule reactions from Chapter 4 and the targeted products were the same. The TiO_2 is used as a growth surface for the M-P and M-P-S materials in hope to encourage interesting surface particle morphologies, and to utilize the products in UV photocatalysis (see Chapter 3 for TiO_2 photocatalysis details) or photo-electrochemical catalysis. The products are colored, being lighter versions of the pure M-P or M-P-S materials, with some samples having a shiny luster.

The product color and yields are shown in Table 5.3. The yields are calculated from the mass of the M-P or M-P-S material only, minus the presumably unreactive TiO_2. The M-P samples were black or gray and the yields were modest at ~30-45 % except for the Ni-P sample, which had a yield close to ~80 %. The M-P-S samples were similar in

color except for the Cu-P-S sample which had the characteristic olive green color seen for Cu_3PS_4 in Chapter 4. The yields were ~40-68 % however the Ni-P-S sample had a much smaller yield of 13 %. This is surprising as the XRD show that both NiP_2 and $NiPS_3$ are produced by this synthesis method.

The powder XRD patterns of the M-P samples deposited on TiO_2 are shown in Figure 5.12. All of the powder XRD patterns for the deposition reactions showed both anatase and rutile phase TiO_2. The Fe-P sample showed only small signs of a possible FeP phase (PDF# 03-065-2595). This is not surprising since a higher reaction temperature reaction is needed to obtain the targeted FeP_2 phase. The Co-P sample showed orthorhombic CoP (PDF# 03-065-2593) and no peaks for CoP_3. The Ni-P sample showed peaks for cubic NiP_2 (PDF# 04-003-2351). Another nickel phosphide phase was also seen. This was Ni_5P_4 (PDF# 04-014-7901) and was much less intense than NiP_2. The Cu-P sample showed two main copper phosphide phases. The major copper phosphide phase was monoclinic CuP_2 (PDF# 01-076-1190). The phase Cu_2P_7 (PDF# 00-047-1566) was seen as a minor phase. There were very small peaks that indicate the presence of CuCl (PDF# 04-007-3885).

The powder XRD stackplotted patterns for the M-P-S materials grown on TiO_2 are shown in Figure 5.13. Again, each sample showed both anatase and rutile phases of TiO_2. The Fe-P-S sample showed monoclinic $FePS_3$ (PDF# 04-005-1516). The Co-P-S sample showed the cubic pyrite structure phase of $CoP_{0.5}S_{1.5}$ (PDF# 04-007-4518). Similarly seen in the previous sections, this phase and CoS_2 are off set on opposite sides of the pattern, suggesting a solid solution between these two phases. The Ni-P-S sample showed monoclinic $NiPS_3$ (PDF# 00-033-0952). Lastly, the Cu-P-S sample showed

orthorhombic Cu_3PS_4 (PDF# 04-007-4285).

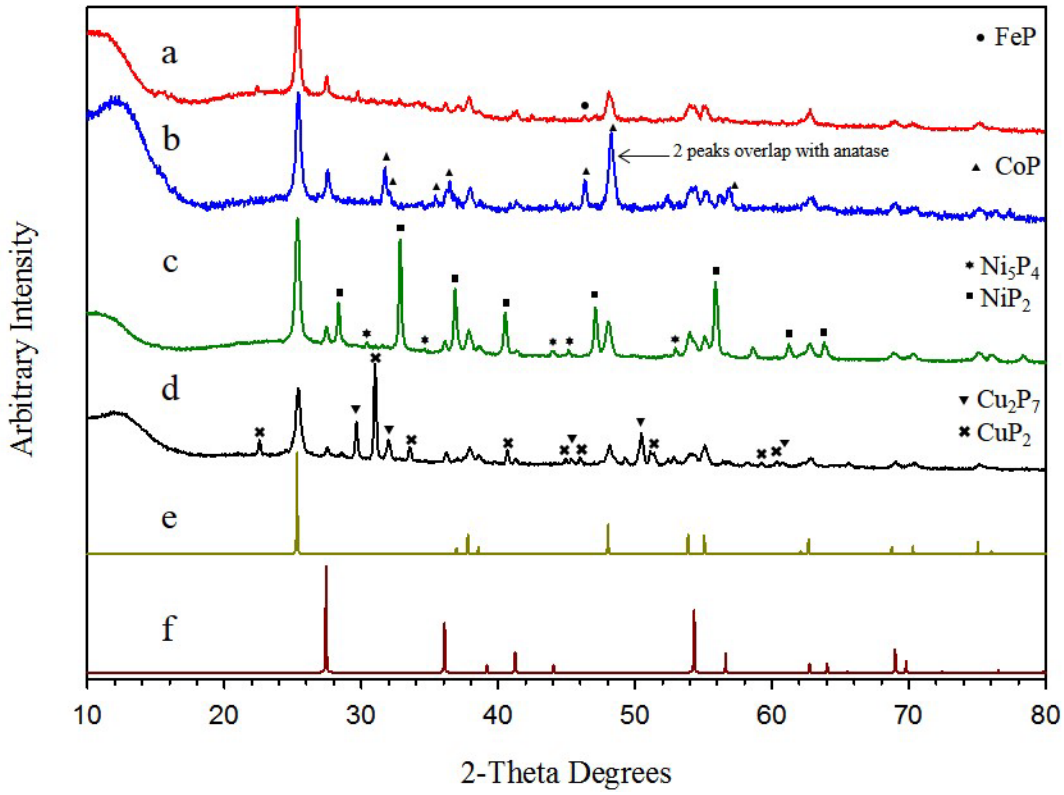

Figure 5.12 XRD stackplot of the M-P products deposited on the TiO_2 surface. The respective patterns are: (a) Fe-P sample, (b) Co-P sample, (c) Ni-P sample, (d) Cu-P sample, (e) reference anatase TiO_2, (f) reference rutile TiO_2.

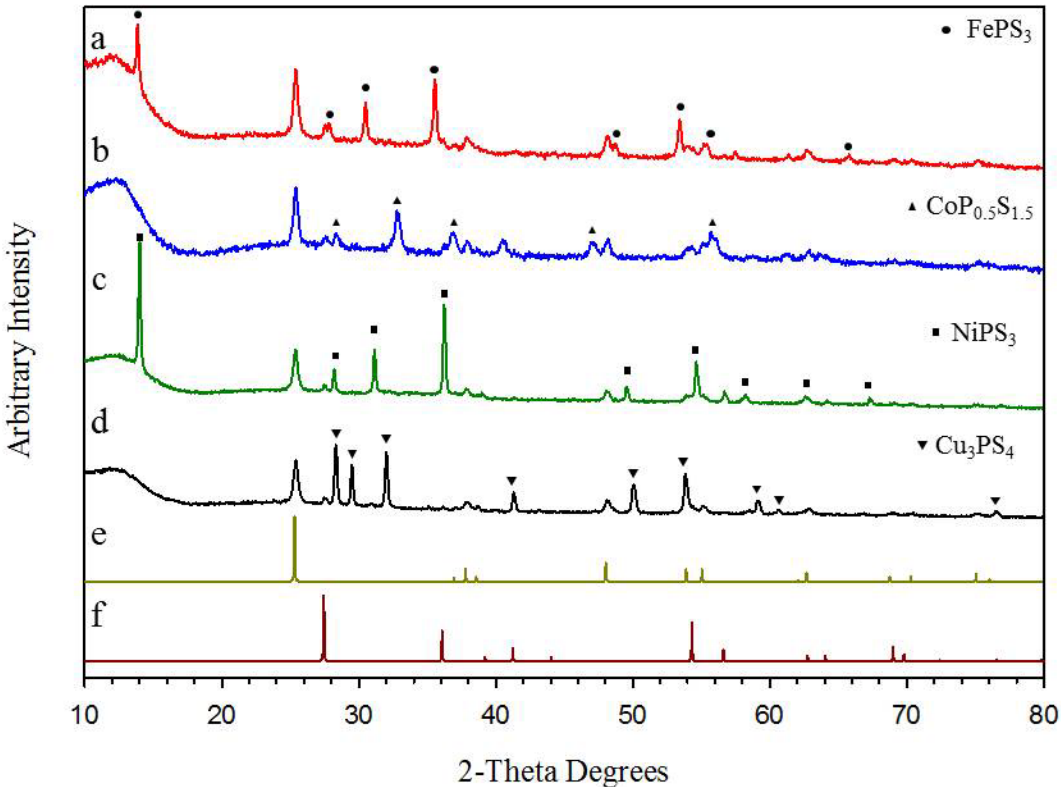

Figure 5.13 XRD stackplot of the M-P-S products deposited on the TiO_2 surface. The respective patterns are: (a) Fe-P-S sample, (b) Co-P-S sample, (c) Ni-P-S sample, (d) Cu-P-S sample, (e) reference anatase TiO_2, (f) reference rutile TiO_2.

The elemental analysis data for the M-P and M-P-S samples deposited on TiO_2 is also shown in Table 5.3. All data was scaled according to the iron, cobalt, nickel, or copper content. Each sample had relative phosphorus content that was close to the phase compositions seen by XRD. The Fe-P sample had a large excess in phosphorus however, which did not reflect the crystalline phases seen in XRD. The Cu-P sample had an average phosphorus content for the two copper phosphide phases seen in XRD. The chlorine content was relatively low for all samples. The iron sample had the highest chlorine content most likely due to incomplete reaction of $FeCl_3$.

The M-P-S samples all were phosphorus rich and all except for the Co-P-S sample were slightly sulfur poor. The chlorine content was very low and in the Co-P-S and Cu-P-S sample.

Table 5.3 The product color and yields of the M-P and M-P-S materials deposited on TiO_2. Bolded XRD phases are major phases. All EDS data was scaled according to Fe, Co, Ni or Cu content.

Reaction	**Target Product**	**Color**	**Yields Based on Target**	**XRD Phases**	**M : P : S : Cl**
$FeCl_3$ + P	FeP_2	dark gray	43 %	**TiO_2**, FeP	1 : 4.05 : 0 : 0.44
$CoCl_2$ + P	CoP_3	dark gray	31 %	**TiO_2**, CoP	1 : 2.69 : 0 : 0.26
$NiCl_2$ + P	NiP_2	black	94 %	**TiO_2**, NiP_2, Ni_5P_4	1 : 1.67 : 0 : 0.05
$CuCl_2$ + P	CuP_2	light gray	43 %	**CuP_2**, TiO_2, Cu_2P_7, CuCl	1 : 2.73 : 0 : 0.08
$FeCl_3$ + P + S	$FePS_3$	black	68 %	**$FePS_3$**, TiO_2	1 : 1.19 : 2.20 : 0.15
$CoCl_2$ + P + S	$CoPS_3$	shiny black	43 %	**TiO_2**, $CoP_{0.5}S_{1.5}$	1 : 1.97: 1.76 : 0.04
$NiCl_2$ + P + S	$NiPS_3$	shiny dark gray	13 %	**$NiPS_3$**, TiO_2	1 : 1.51 : 2.93 : 0.21
$CuCl_2$ + P + S	Cu_3PS_4	olive green	60 %	**Cu_3PS_4**, TiO_2	1 : 0.57 : 0.97 : <0.01

The SEM images of the M-P deposited materials on Degussa TiO_2 are shown in Figure 5.14. The Fe-P, Co-P and Ni-P samples all have similar shapes which consists of large aggregates. These particles range from 5-20 micrometers. The Ni-P sample has very small needle looking nano structures covering the large particles. The Cu-P sample

consists of fused blocky structures that seem to grow outwards from a core aggregate. The blocky structures are large and are ~10-30 micrometers in size.

The SEM images of the M-P-S deposited materials on TiO_2 are shown in Figure 5.15. The Fe-P-S sample consists of round plate like structures that appear to be emerging from very small aggregate particles. The plates range from ~2-10 micrometers across. The plate thickness varies with the plate size. Larger plates have ~1-2 micrometer plate thickness while sub-micrometer plates have thickness of ~300-500 nanometers. The Co-P-S sample consists of very small aggregates which are only a few micrometers in size. Closer examination shows nanoscale aggregates on the surface of the larger particles. The Ni-P-S sample shows a mixture of blocky structures, plates and aggregate particles. The blocky structures are ~ 5-10 micrometers long. The plates are quite thin, being ~ 2-5 micrometers long and ~400-500 nanometers thick. The aggregates are ~300-500 nanometers. The Cu-P-S sample showed thin rectangular prism emerging from very small aggregate particles. The prisms are ~3-10 micrometers long and ~300-500 nanometers across. The aggregates are ~300-500 nanometers.

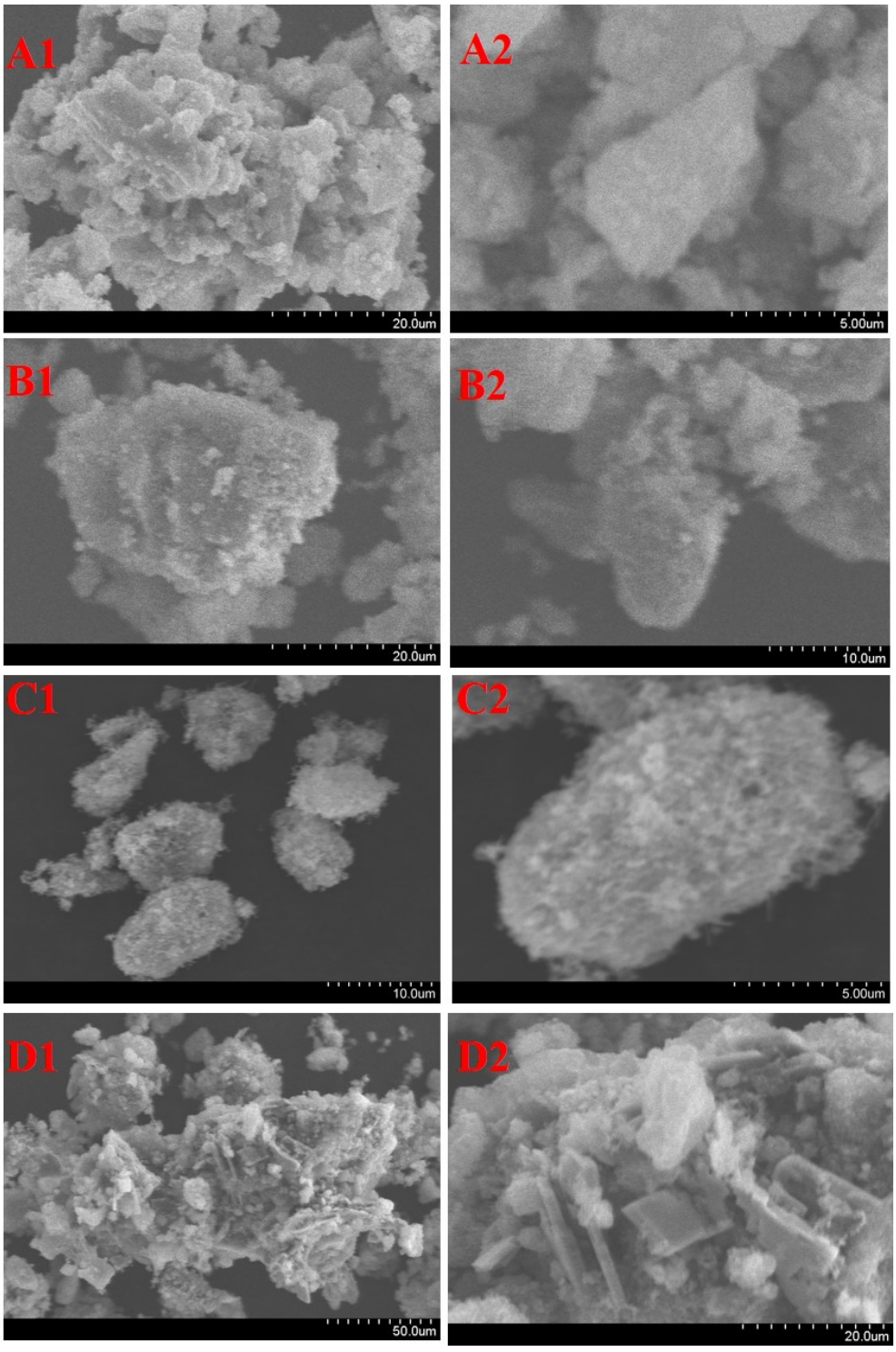

Figure 5.14 SEM images of the M-P products deposited on TiO_2. A = Fe, B = Co, C = Ni, D = Cu. Numbered images represent either a zoomed in image or a different area of interest.

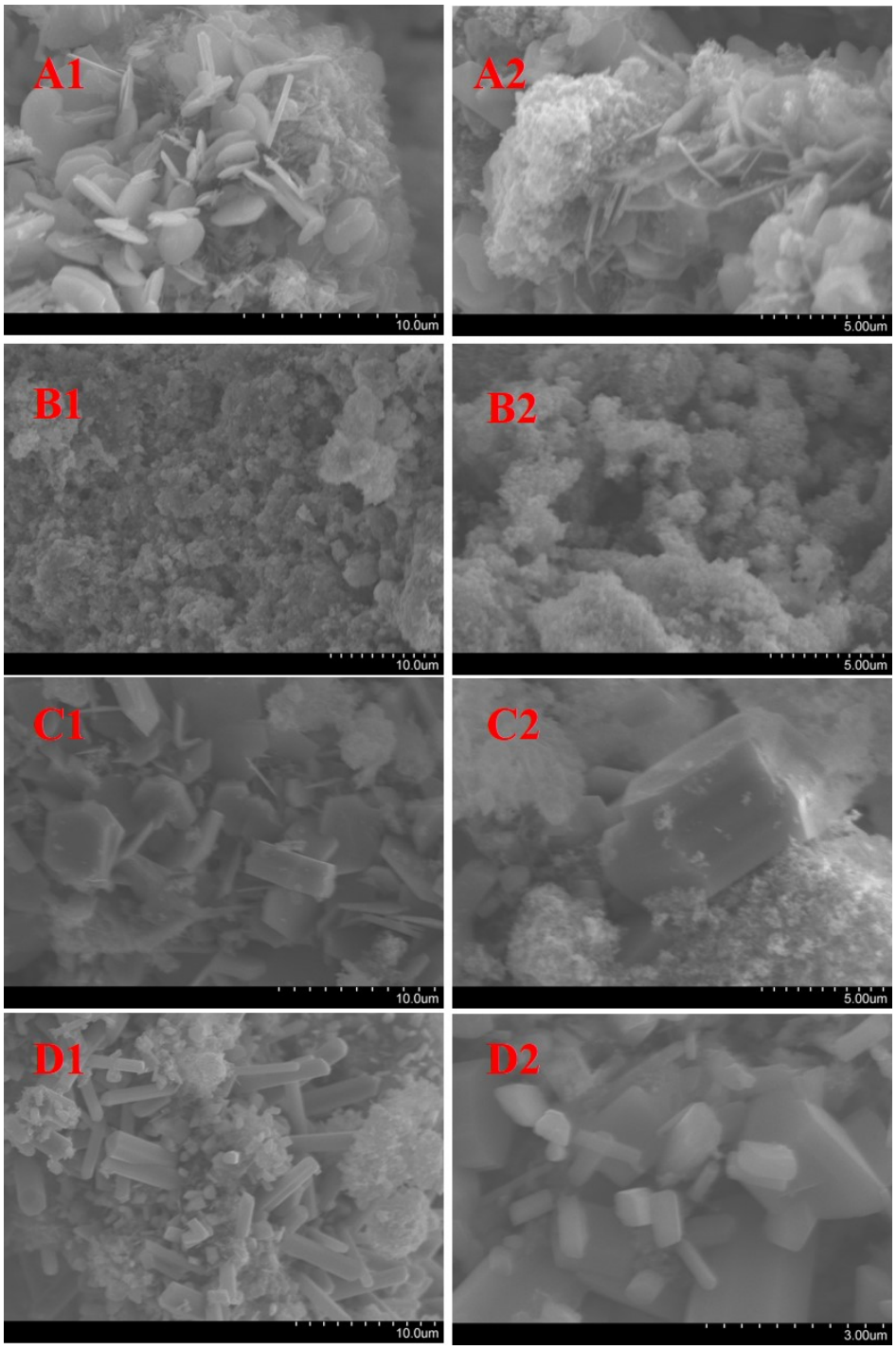

Figure 5.15 SEM images of the M-P-S products deposited on TiO_2. A = Fe, B = Co, C = Ni, D = Cu. Numbered images represent either a zoomed in image or a different area of interest.

Growth of the M-P and M-P-S crystals on TiO_2 seems generally successful but does vary by the targeted product. TiO_2 acts as a growth support for products and is not presumed to react with the metal halide or phosphorus. The anatase and rutile phases are preserved after heating to 500 °C and are generally maintained. In addition to this, there were no phosphate or sulfate materials present in the XRD patterns. The methanol evaporation technique allows the metal halide to adhere to the surface of titania, providing a growth point for the M-P and M-P-S materials. The ampoule reactions behave similarly to those in Chapter 4, with red phosphorus volatizing into P_4 gas and reacting with the surface of the metal halides. Since lower phosphorus content phases are observed, it may be feasible that surface Ti-O groups or water in methanol may react with gaseous P_4 prior to M-P formation. Excess phosphorus may promote targeted phases FeP_2, CoP_3, and CuP_2 on TiO_2.

5.5 Conclusions

The materials synthesized in the fluxes were partially successful and showed changes in the morphology for both the M-P and M-P-S materials. The challenge with using fluxes is finding the optimal reaction conditions according to the desired phases, yield, and morphology. The yields suffered for some of the reactions most likely due to the addition of excess flux, the stability of MCl_x species in the flux, or other variables include the reaction temperature and reaction longevity. Each reaction would need to be optimized by adjusting several of these variables.

The KCl-LiCl eutectic salt flux reactions showed interesting morphologies changes compared to Chapter 4 solids. The M-P samples in Chapter 4 were blocky aggregates of various sizes. The most noteworthy sample was CuP_2 which made uniform cubic blocks. The KCl-LiCl flux produced more fused smooth shapes and in the copper phosphide case, a mixture of smooth shapes covered in needles. It should be noted that

the KCl-LiCl flux reactions produced single phases minus the copper case. The iron case was unsuccessful most likely due to low reaction temperature using the current flux. The M-P-S reactions produced similar products seen in Chapter 4. The morphologies were also different, often being more granular in shape. The Ni-P sample had the most dramatic change, going from fused aggregates to large plates.

The tin flux reactions gave very crystalline materials with good yields and showed interesting morphologies. The M-P products all became more granular and smooth compared to their blocky counterparts in Chapter 4. The M-P-S products became more fused blocks or aggregates. It should be noted that no actual M-P-S samples were seen when using the tin flux. This was probably due to the high reactivity of tin with sulfur. Powder XRD was done on some samples (that could be physically removed from the flux) before washing in HCl. The patterns showed predominately SnS. SnS is very soluble in HCl and therefore was washed away during the removal of the tin flux. This left only M-P and M-Sn-P phases after washing. The corrosive extraction environment may also alter the yield of the products. However, preliminary tests with exposing Chapter 4 materials to the same corrosive environments showed no change in the M-P samples.

The bismuth reactions seemed to fail as evidence by the colored wash solutions and very low yields. Removal of the bismuth flux was a challenge since HNO_3 was needed. Hot concentrated HCl was attempted, but the flux only darkened or took extremely long periods of time to begin to dissolve. The use of HNO_3 could have been detrimental to the products formed. Preliminary tests with materials synthesized in Chapter 4 were exposed to the same corrosive conditions to test for any product solubility. There were no obvious changes in color or phase by XRD. Perhaps the presence of bismuth alters the overall reaction negatively. One theory is that bismuth does have an affinity for halides. Perhaps the bismuth reduces the metal halides by removal of chlorine, leaving only the metals to react with phosphorus (and sulfur)

causing the reaction to become more thermodynamically unfavorable. Also, preliminary XRD of unwashed materials showed $BiCl_3$ in some samples, which supports this theory.

The M-P and M-P-S deposition reactions on P25 TiO_2 produced mainly desired materials. The Fe-P and Co-P samples however, did not yield the targeted FeP_2 and CoP_3 products respectively. The XRD patterns showed highly crystalline peaks for both anatase and rutile even after being heated to 500 °C.

CHAPTER 6

CONCLUSIONS AND FUTURE OUTLOOK

6.1 Solid State Metathesis Synthesis

The following chapter will review all of the conclusions obtained from the chapters in this thesis. Also, the challenges behind the work performed will be discussed along with future insights into the research. The goal is to lay a path for new innovative routes to improved synthesis techniques and applications with the materials from this thesis and beyond.

6.1.1 Metal oxide materials

Transition metal oxide materials were synthesized using SSM techniques from stoichiometric amounts of metal halides and Na_2O_2. The reactions produced colored TiO_2 materials with respect to the metal dopant used in moderate yields. Acid washing of the sample improved the purity of the materials. Interestingly, crystalline dopant phases were not seen, yet atomic ratios of the dopant to Ti were promising. Annealing also re-enforces the fact that the dopant metals are indeed in the TiO_2 sample since the dopant began to show phases in XRD patterns. So far, all reactions have used stoichiometric amounts of dopants to target a specific chemical formula. The addition of dopants to achieve a 50:50 dopant to Ti ratio has been tried in some experiments and still no dopant phases have been seen. Dopant amounts higher than this begin to show oxide phases along with rutile TiO_2.

Work to improve the synthesis of solid state reactions can be investigated by attempting to isolate single phases. The challenge of SSM reactions was that multiple phases were seen by characterization techniques. Single phases can be isolated by using non-reactive matrixes to suppress the violent behavior of the reaction. Adding NaCl or

LiCl for example can suppress reagents from expelling from the reaction container. The amount of salt is critical. Too much salt will greatly reduce the propagation rate of SSM reactions, thus reducing the yield. Uniform heating of the materials, such as in a sealed autoclave or pressure reactor, would be required to propagate the reactions.

The location of the dopant is questionable still, and needs to be investigated. The sheer color of the samples can indicate surface concentration of the dopant metals. Surface analysis of the samples can help determine dopant locale. EDS data gives insight to approximate dopant location since it is a surface analysis technique. XPS analysis is a more sensitive surface technique which also gave the electronic environment of the dopant. Ultimately, a laser ablation addition to XPS can give information of the amounts of dopant from various sample depths.

Future work with SSM oxide reactions can involve targeting oxynitride materials. Early work on a GaN:ZnO solid solution synthesis was attempted. Literature has shown that this solid solution shows catalytic activity for water splitting under visible light.[177,178] The reaction involved combining stoichiometric amounts of $GaCl_3$, $ZnCl_2$, Li_3N, and Na_2O_2 into the bomb reactor. This reaction is extremely reactive when physically mixed, causing auto ignition in the glovebox. The materials were analyzed by XRD and showed $ZnGa_2O_4$. The reaction most likely became too hot for nitrides to form. Perhaps adding salt to this mixture such as NaCl will suppress the reactivity. Preliminary work with synthesizing ZnO has also been done and doping of the hexagonal wutrzite structure with transition metals was done in a similar fashion as with the TiO_2 work.

6.1.2 Metal phosphide, sulfide and thiophosphate materials

Transition metal materials were synthesized in moderate yields. Each type of reaction produced mixed phases of either metal rich phosphides, metal sulfides, and layered MPS_3 (M= Fe, Co,Ni) or orthorhombic Cu_3PS_4. When phosphorus and sulfur are mixed, either M-P-S products or metal sulfides are formed. This was due to phosphorus volatilizing out of the reaction mixture. To help suppress this, using a matrix such as LiCl, can help slow the reaction speed and keep materials within the reaction container. LiCl will act as a flux and can also help isolate single phase materials. Since SSM reactions can reach very high temperatures, M-P materials may have formed and decomposed. Some M-P and M-P-S materials will decompose beyond 600 °C.

Stoichiometric amounts of materials were used to target the M-P and M-P-S phases. Excess amounts of red phosphors could encourage M-P phases to form. However, the risk of excess red phosphorus is the fire hazard of unreacted white phosphorus in air. The choice of starting reagents may also be altered to better target desired phases. Compounds such as Na_3P, Na_2S, Li_3P, or Li_2S can be used instead of Li_3N to target M-P and M-S products respectively. Therefore the reactions using the halides for NiP_2 for example would be $3\ NiCl_2 + 2\ Na_3P + 4\ P \rightarrow 3\ NiP_2 + 6\ NaCl$ ΔH_{rxn} = -1670.76 kJ/mol which is exothermic. NaCl can be washed away with water.

6.2 Ampoule synthesis

6.2.2 Metal phosphide materials

Ampoule reactions produced single phase materials much better than SSM reactions, mainly due to the longer reaction time and simpler reactions. For some of the ampoule reactions, metal halide was present in the sample according to XRD or EDS.

Longer times may give more pure products. The reaction temperatures may be increased as well, however most MP_x, and M-P-S materials will begin to decompose above ~600 °C. Also, all ampoule reactions used stoichiometric amounts of materials. Excess phosphorus, sulfur or P_2S_5 may drive reactions to produce desired products. Care has to be taken since the danger with excess P and S content is the increase in possible volatiles.

The M-P ampoule reactions yielded materials in good yield over a relatively short reaction time. The FeP_2 reaction suffered which is most likely due to the short reaction time. Also the FeP_2 product showed silica which may be due to the reactive nature of $FeCl_3$. A similar reaction with $FeCl_2$ was done and still silica was seen from XRD. The halides may need to be contained in alumina vessels within silica tubes to prevent reactions with silica.

Some metal halide was seen in the FeP_2, and CuP_2 samples which indicate an incomplete reaction or a lack of reagent materials. To remedy this, much longer reaction times over several days or the use of excess phosphorus can be used. Excess phosphorus would ensure that all of the metal halide will be reacted, but again the volatility danger is present.

Some future work with metal phosphide ampoule synthesis can involve targeting the synthesis of other useful phosphides such as GaP, InP for their semiconducting properties, WP_2 for its water splitting capabilities,[179] or mixed metal phosphides. Some early work on Gap and InP synthesis was attempted using $GaCl_3$, $Ga(C_5H_8O_2)_3$, InP_3, or $In(C_5H_8O_2)_3$ ($C_5H_8O_2$ = acetylacetonate or acac) and red phosphorus in sealed ampoules at 500 °C. The reactions were not very successful yielding starting reagents, or black powders which were a mixture of carbonaceous material and starting reagents. Adjustments to these reactions will need to be done which may include changing the starting material or increasing the heating temperature and time, or carefully choosing reactions that are more energetically downhill.

6.2.3 Metal sulfide materials

Metal sulfide material synthesis was not successful in sealed ampoules. This is most likely due to the endothermic nature of the reactions. It is promising though that the byproduct of one experiment showed signals for S_2Cl_2 from GC-MS analysis. Most of the reactions produce a yellow liquid (solid when cooled) transport, which is most likely S_2Cl_2 and S_8. The reactions are just not energetically favorable. In the case of endothermic reactions, applying more energy to the reaction will push the reaction back to reagents. Increasing the reaction temperature and time could improve reactivity between different precursors. Using a more reactive form of sulfur or a sulfur containing salt such as Na_2S, can be used to encourage M-S product formation. Na_2S would form NaCl as a byproduct and can be removed easily. The reaction would be identical to an SSM reaction. Performing a reaction with CS_2 is doable, but dangerous due to volatility of the CS_2. CS_2 will dissolve sulfur which can be advantageous for reacting with metal halides.

6.2.4 Metal thiophosphate materials

Metal thiophosphate materials produced layered monoclinic $FePS_3$, $NiPS_3$, $CoPS_3$, and orthorhombic Cu_3PS_4. Stoichiometric amounts of starting reagents of P + S or P_2S_5 +P gave similar products. The P + S versions had small metal halide signals. To improve this either a slight excess in P and S can be used. The P_2S_5 versions gave more crystalline materials and low to no chlorine content. The P_2S_5 reactions did yield solid transports which could have indicated incomplete reactions.

Reactions with multiple metals can be attempted for a mixed layered $M_xM'_{1-x}PS_3$ phase. A reaction targeting a $Co_{0.5}Ni_{0.5}PS_3$ material was attempted, but multiple phases were seen in the XRD, including $NiPS_3$, $CoP_{0.5}S_{1.5}$, and $CoPS_3$. There are other MPS_3 compounds that can be synthesized as well. The leading MPS_3 compound seen in

literature is $MnPS_3$ for its intercalation chemistry of molecules that improve its physical properties.[180] Synthesizing this compound was attempted from the reaction $3\ MnCl_2 + 5\ P + 9\ S \rightarrow 3\ MnPS_3 + 2\ PCl_3$ in a sealed Pyrex ampoule at 500 °C for 1 day. The reaction yielded a mix of a gray and green solid. Powder XRD showed small peaks for $MnPS_3$ but major peaks of $MnCl_2$ hydrate, indicating a poor reaction. This reaction can be modified by using a longer reaction time, using a different manganese reagent, or perhaps using a flux.

Intercalation within the MPS_3 structures usually involve cationic molecules since the sulfur atoms (δ^- charges) are directed towards the Van der Waals gaps in the MPS_3 structures. Salts such as LiCl, NaCl, KCl, NH_4Cl and organometallic materials such as cobalticenium[181] would be useful for nonlinear optics, battery materials, changes in magnetic properties, and have been investigated in research.[182] The process usually involves reacting MPS_3 materials with n-butyl lithium for Li^+ intercalation,[183] ion exchange soaks in saturated salt solutions for Li^+, Na^+,K^+, NH_4^+ intercalation,[184] and heating in organic solutions with cobalticene.[185] Intercalation of organic molecules is of high interests within the $MnPS_3$ structure and could be used in biological applications. Such techniques have been investigated in the literature.[180]

Pyridine and bipyridine like structures have been exclusively used in research as an intercalant within MPS_3 compounds.[186-188] Intercalation of these molecules involves soaking or heating the MPS_3 materials in pyridine under inert atmosphere for long periods of time.[188] Pyridine intercalation has shown to also improve the physical properties of the MPS_3 materials such as Attempts to intercalate pyridine into some of the materials synthesized in Chapter 4 were made. The reactions involved heating $NiPS_3$, $FePS_3$, or $CoPS_3$ in refluxing pyridine or acidified pyridine for several days. Changes in the XRD peaks were not seen however. The materials will most likely require IR or NMR to determine if pyridine is in fact intercalated.

Extending the MPS_3 systems into $MPSe_3$ systems is of great interest as a next path in our group. Substituting selenium for sulfur can yield useful semiconducting materials such as $FePSe_3$ which has a band gap of 1.3 eV.[170] Some experiments have been attempted using elemental selenium and heating to 500 °C for 1 day to target $MPSe_3$. $CoPSe_3$ was attempted using $CoCl_2$, red phosphorus, and selenium, but it was unsuccessful yielding $CoSe_2$ and $CoCl_2$. $NiPSe_3$ was also attempted using $NiCl_2$, red phosphorus and selenium. The reaction produced a mix of $NiPSe_3$ and $NiSe_2$. These preliminary reactions could lead to future synthesis of other $MPSe_3$ materials. A final summary of both the SSM and ampoule based reactions of the M-P, M-S and M-P-S materials are shown in Figure 6.1.

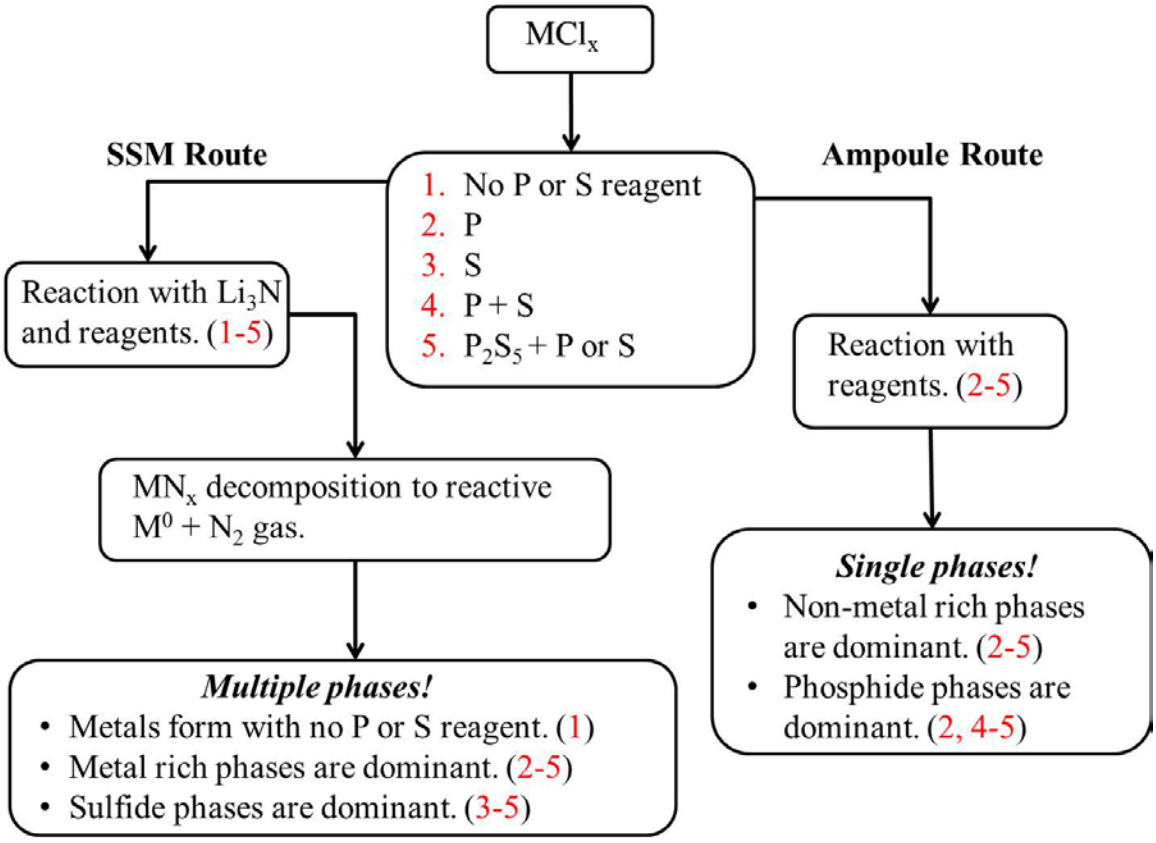

Figure 6.1 Reaction pathways for MP, MS and MPS materials.

6.3 Flux and Deposition Synthesis

6.3.2 M-P and M-P-S from eutectic salt fluxes

The M-P and M-P-S materials produced desired products in low to moderate yields. The yield may be improved by modifying the flux amount. Initial experiments were done using equal amounts of starting reagents and flux. This yielded undesired products and starting material. A large amount of flux was used (30x excess) to test product formation. This reaction showed essentially no product. The 15x excess amount of flux reactions were a middle ground point that gave reasonable yields of products.

Fine tuning of these experiments can be performed to optimize the phase and yield of products.

The LiCl/KCl premixed flux is hard to prepare since it forms a very hard solid after cooling. Improvements to remove the solid are to use liquid N_2 to cause cracking of the salt solid solution, or to cool the hot liquid flux over a flat surface for easy removal. Some experiments using a NaCl/KCl flux were attempted. The premade flux was much easier to make than the LiCl/KCl flux. These reactions were done in silica tubes since the eutectic melting point of the flux is 650 °C. The challenge with these reactions was that the alkali salts attack silica in molten form over long periods of time. Monoclinic NiP_2 was synthesized using the NaCl/KCl salt flux (8x excess) with 27% yield. SEM of the materials showed rhombohedral shapes. Other M-P and M-P-S materials can be attempted, but they may decompose if left in the hot flux for too long.

6.2.3 M-P and M-P-S from metal fluxes

The M-P and M-P-S materials were synthesized in varied yields. The tin fluxes reactions produced M-P products with low to moderate yields and interesting morphologies. It was inspiring to see that FeP_2 forms in the tin flux at 500 °C instead of 700 °C, interesting uniform truncated cube-like structures, and with no silica peaks in the XRD. This was the goal of using the tin flux. The M-P-S material was not seen since SnS forms and was washed away with the flux in concentrated warm HCl. Only M-P and MPSn phases were present. Improvements with the tin flux would involve optimizing the flux amount and reaction times for better yields.

The bismuth flux reactions had very poor yields. This is most likely due to the nature of bismuth with metal chlorides. Another choice in metal starting reagent may produce better reactions in bismuth fluxes. Also, the harsh oxidizing washing conditions

in HNO_3 may have dissolved or decomposed products. HCl appears to only slightly work by only darkening the flux. Alternate separation techniques need to be investigated.

There are other metals that can be used as fluxes. Lead is a low melting metal that has been used as a flux and as a eutectic with bismuth. Indium and gallium can be used as well. The overall concern is separating the fluxes from the products. Each one of these metals is soluble in acids. HCl works well with the M-P products since they are still present after removing the tin flux. Finding the optimal flux amount of each flux for the desired products is ideal.

6.2.4 M-P and M-P-S Deposition on P25 TiO_2

The M-P deposition on P25 TiO_2 did produce metal phosphides while preserving anatase and rutile in the appropriate ratios however, the Ni-P and Cu-P reactions were the only reactions that produced the target NiP_2 and CuP_2 products. The Fe-P reaction was expected to not form FeP_2 since we have only synthesized the phase at 700 °C or using the tin flux at 500 °C. The Co-P reaction was surprising to not form CoP_3 since it was seen at 500 °C in Chapter 4. The P25-TiO_2 may inhibit product formation just by being a physical barrier. The M-P-S products formed crystalline targeted phases in good yields. It was encouraging to see that no secondary phases formed with the mixes of phosphorus and sulfur (or oxygen) as well since some NiS_2 is sometimes seen in the Ni-P-S reactions.

Some future experiments that could be done with deposition experiments could involve deposition of different amounts of products on P25 TiO_2. Estimated amounts of M-P and M-P-S material that was deposited on the surface on P25 TiO_2 ranged from 15-30%, which in a co-catalyst standpoint is very high. Perhaps much smaller amounts of M-P and M-P-S can be targeted. The amount of P25 TiO_2 may need to be adjusted as well since it may inhibit product formation.

6.4 Catalysis Conclusions

6.4.1 Organic molecule degradation

Methylene blue and methyl orange photooxadation reactions were performed using UV or filtered UV light. The transition metal doped TiO_2 samples showed moderate degradation of methylene blue under both UV and visible light, and much better degradation than un-doped TiO_2, but are still out matched by P25 TiO_2 under UV. The doped samples out-perform P25 under visible light however. The particle size and surface areas of the SSM products is no match for P25 TiO_2 unfortunately. Even though quick reaction times do not allow for elaborate crystalline growth, the particles are large compared to P25 TiO_2. Also, only rutile TiO_2 is formed P25 TiO_2 has the advantage of having an effective band gap range from anatase and rutile (3.0-3.3 eV), ~50m^2/g surface area, and a 3:1 mixture of anatase to rutile. The transition metal doped TiO_2 samples are good at adsorbing the dye in the dark however, particularly the Mn-TiO_2 sample. The dye was "removed" by this sample very effectively, just not by photooxidation. One theory is that the surface oxygen atoms in the rutile structure (and doped structures) bind the methylene blue dye effectively.

The transition metal doped TiO_2 samples showed very little activity towards methyl orange photooxidation or physical adsorption, and again are out performed by P25 TiO_2. Methyl orange is an anionic azo dye while methylene blue is a cationic dye with no azo group. The dye may not bind to the surface of the doped samples effectively. It would be ideal to synthesize doped TiO_2 samples that had an average 3:1 anatase to rutile ratio and have high surface areas. By doing this, the samples most likely will be more comparable to P25 TiO_2 for dye degradation. The SSM reactions will need to propagate slower or have a structure modifying agent added to the reagents.

6.4.2 Water oxidation and reduction

Water photoreduction was examined with ~1 wt% Pt deposited materials using methanol as a sacrificial hole scavenger. The transition metal doped TiO_2 samples showed no H_2 production over several hours. The standard reference material was platinum coated P25 TiO_2 which showed a steady increase in H_2 production over several hours. Also, ~5 wt% Pd on P25 $TiO_2$was tested and showed similar results. Tests were done with rutile only P25 TiO_2 (annealed to 1000 °C), and anatase TiO_2, both in which were ~1% platinum coated. Neither sample showed H_2 generation over several hours. This verifies that the particle size and mixes of phases are crucial to water reduction reactions. Also, platinum coated M-P-S and M-P-S on P25 TiO_2 were also tested for water reduction and showed no H_2 generation.

There are several criteria that a material must be met in order to generate H_2 from water. The material must have a band gap energy of at least 1.23 eV, which is the difference in energy between the redox potentials of the oxidation and reduction of water. Smaller band gaps less than 2.30 eV may require an electrical bias voltage or another reagent to induce the reduction. The material must also have a small particle size and high surface area. The sample must be crystalline and lack defects. Detailed explanation of these factors are located throughout the literature.[189]

6.4.3 Electrochemical Water Reduction

Early electrochemical tests were performed on M-P and M-P-S materials. The experiments were done through collaboration with the Leddy Group at The University of Iowa Department of Chemistry. Each test was performed by Matt Lovander. Onset potential values for the hydrogen evolution reaction (HER) was determined for each sample and compared to commercial standard materials. The samples were imbedded

into a custom made carbon wax electrode which is shown in Figure 6.1. The samples that were tested were NiP_2 (cubic), $FePS_3$, $CoPS_3$, $NiPS_3$ and commercial Ni_2P (Aldrich, 98%). The reference material tested was 10% Pt on carbon black (E-Tek) and the blank was carbon wax (graphite powder, Aldrich and parafin wax, Aldrich).

Figure 6.2 Carbon wax electrodes

Each sample was tested in a three-electrode cell with a 0.50 M H_2SO_4 solution at room temperature under continuous stirring. N_2 gas was used as a purge. All runs were done using a Bioanalytical Systems 100b Potentiostat. The data was collected at a 5mV/s scan rate. The HER onset potentials are shown from the current density vs potential plots (Polarization Curves) in Figure 6.2. The NiP_2 sample has the smallest HER onset of -40 mV and is followed by $CoPS_3$ (-60 mV), Ni_2P (-100 mV), $NiPS_3$ (-175 mV), and lastly $FePS_3$ (-240 mV). The reference 10 % Pt on C has an HER onset of +60 mV and the carbon wax blank's offset is at -590 mV. The data is promising since it helps explain why these materials were not able to split water using light. As mentioned earlier, from photoreductive water splitting, catalysts with band gaps lower than 2.30 eV may require an electrical bias to split water. The estimated band gaps from DRS analysis (shown in

Chapter 4 Table 4.8) of $FePS_3$ is 1.63 eV, $CoPS_3$ is 1.66 eV, and $NiPS_3$ is 1.36 eV. The NiP_2 sample was analyzed using DRS but it did not have any onset absorption drops across the entire visible spectrum.

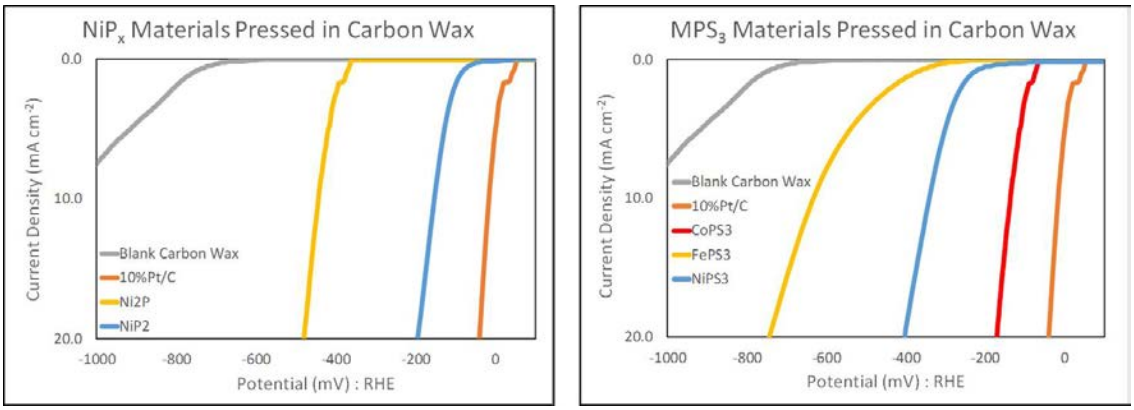

Figure 6.3 Current density vs potential plots for NiP_2 (cubic), Ni_2P, and MPS_3 (M= Fe, Co, Ni).

Our current ongoing research involves synthesizing other MPS_3 materials which involves improving the $MnPS_3$ synthesis and investigating the $CdPS_3$ material. We are also testing the MPS_3 materials and CoP_3, CuP_2 and the Cu_3PS_4 materials for their HER capabilities.

6.5 Concluding Remarks

The research done in this thesis demonstrated the use of SSM and ampoule reactions to synthesize metal oxides, phosphides, sulfides and thiophosphate materials. The use of fluxes in ampoule reactions enabled new synthesis pathways for our group to use for improved morphology of M-P and M-P-S materials. Much more research can be done with the applications of these materials in catalysis. The degradation of organic pollutants is very useful in industry. Quick, cost effective, environmentally friendly and

reusable, heterogeneous catalysts are ideal. Water reduction is a very powerful technique that has been applied in several areas of research by various materials. The next step is how to store the “fuel” safely.

It would be useful to bridge the gap between quick effective solid state synthesis and ideal sample particle size and morphology. This is a difficult and challenging task since several factors on each end oppose one another, but it can be done. There are several variables that can be adjusted which opens up opportunities for continuation in this research. Hopefully, this research has inspired future researchers to discover adaptations and improvements in the field.

REFERENCES

(1) Perera, S.; Zelenski, N.; Gillan, E. G., Synthesis of nanocrystalline TiO2 and reduced titanium oxides via rapid and exothermic metathesis reactions, *Chemistry of Materials* **2006**, *18*, 2381-2388.

(2) Barry, B. M.; Gillan, E. G., A General and Flexible Synthesis of Transition-Metal Polyphosphides via PCl3 Elimination, *Chemistry of Materials* **2009**, *21*, 4454-4461.

(3) Snell, P.-O.; Ödberg, L.; Högfeldt, E.; Norin, T.; Eriksson, G.; Blinc, R.; Paušak, S.; Ehrenberg, L.; Dumanović, J., The Crystal Structure of TiP, *Acta Chemica Scandinavica* **1967**, *21*, 1773-1776.

(4) Jeitschko, W.; Flörke, U.; Scholz, U. D., Ambient pressure synthesis, properties, and structure refinements of VP4 and CoP2, *Journal of Solid State Chemistry* **1984**, *52*, 320-326.

(5) Schlesinger, M. E., The thermodynamic properties of phosphorus and solid binary phosphides, *Chem Rev* **2002**, *102*, 4267-4301.

(6) Jeitschko, W.; Donohue, P. C., The high pressure synthesis, crystal structure, and properties of CrP4 and MoP4, *Acta Crystallographica Section B Structural Crystallography and Crystal Chemistry* **1972**, *28*, 1893-1898.

(7) Jeitschko, W.; Donohue, P. C., High-pressure MnP4, a polyphosphide with Mn–Mn pairs, *Acta Crystallographica Section B* **1975**, *31*, 574-580.

(8) Rundqvist, S.; Sillén, L. G.; Timm, D.; Motzfeldt, K.; Theander, O.; Flood, H., Phosphides of the B31 (MnP) Structure Type, *Acta Chemica Scandinavica* **1962**, *16*, 287-292.

(9) Rundqvist, S.; Yhland, M.; Dahlbom, R.; Sjövall, J.; Theander, O.; Flood, H., X-Ray Investigations of Mn3P, Mn2P, and Ni2P, *Acta Chemica Scandinavica* **1962**, *16*, 992-998.

(10) Olofsson, O.; Hassel, O.; Sillén, L. G.; Gronowitz, S.; Hoffman, R. A.; Westerdahl, A., The Crystal Structures of CuP2 and AgP2 with some Phase Analytical Data of the Cu-P and Ag-P Systems, *Acta Chemica Scandinavica* **1965**, *19*, 229-241.

(11) Riekel, C.; Schollhorn, R., Structure Refinement of Nonstoichiometric Tis2, *Materials Research Bulletin* **1975**, *10*, 629-634.

(12) Furuseth, S.; Kjekshus, A.; Niklasson, R. J. V.; Brunvoll, J.; Hinton, M., On the Properties of alpha-MnS and MnS2, *Acta Chemica Scandinavica* **1965**, *19*, 1405-1410.

(13) Brostigen, G.; Kjekshus, A.; Astrup, E. E.; Nordal, V.; Lindberg, A. A.; Craig, J. C., Redetermined Crystal Structure of FeS2 (Pyrite), *Acta Chemica Scandinavica* **1969**, *23*, 2186-2188.

(14) Craig, J. R.; Vaughan, D. J.; Higgins, J. B., Phase equilibria in the copper-cobalt-sulfur system, *Materials Research Bulletin* **1979**, *14*, 149-154.

(15) Mcwhan, D. B.; Marezio, M.; Remeika, J. P.; Dernier, P. D., Pressure-Temperature Phase-Diagram and Crystal-Structure of Nis, *Physical Review B-Solid State* **1972**, *5*, 2552-&.

(16) Oliveria, M.; Mcmullan, R. K.; Wuensch, B. J., Single-Crystal Neutron-Diffraction Analysis of the Cation Distribution in the High-Temperature Phases Alpha-Cu2-Xs, Alpha-Cu2-Xse, and Alpha-Ag2se, *Solid State Ionics* **1988**, *28*, 1332-1337.

(17) Strehlow, W. H.; Cook, E. L., Compilation of Energy Band Gaps in Elemental and Binary Compound Semiconductors and Insulators, *J. Phys. Chem. Ref. Data* **1973**, *2*, 163-199.

(18) Lewkebandara, T. S.; Proscia, J. W.; Winter, C. H., Precursor for the Low-Temperature Deposition of Titanium Phosphide Films, *Chemistry of Materials* **1995**, *7*, 1053-1054.

(19) Perkins, P.; Marwaha, A.; Stewart, J. P., The band structure and magnetic properties of some transition-metal phosphides. II. V, Cr, and Mn monophosphides, *Theoretica chimica acta* **1981**, *59*, 569-583.

(20) Rout, C. S.; Kim, B.-H.; Xu, X.; Yang, J.; Jeong, H. Y.; Odkhuu, D.; Park, N.; Cho, J.; Shin, H. S., Synthesis and Characterization of Patronite Form of Vanadium Sulfide on Graphitic Layer, *Journal of the American Chemical Society* **2013**, *135*, 8720-8725.

(21) Sharon, M.; Tamizhmani, G., Transition metal phosphide semiconductors for their possible use in photoelectrochemical cells and solar chargeable battery (Saur Viddyut Kosh V), *Journal of Materials Science* **1986**, *21*, 2193-2201.

(22) Zhang, H.; Ji, Z.; Xia, T.; Meng, H.; Low-Kam, C.; Liu, R.; Pokhrel, S.; Lin, S.; Wang, X.; Liao, Y.-P.; Wang, M.; Li, L.; Rallo, R.; Damoiseaux, R.; Telesca, D.; Mädler, L.; Cohen, Y.; Zink, J. I.; Nel, A. E., Use of Metal Oxide Nanoparticle Band Gap To Develop a Predictive Paradigm for Oxidative Stress and Acute Pulmonary Inflammation, *Acs Nano* **2012**, *6*, 4349-4368.

(23) Maneeprakorn, W.; Malik, M. A.; O'Brien, P., The preparation of cobalt phosphide and cobalt chalcogenide (CoX, X = S, Se) nanoparticles from single source precursors, *Journal of Materials Chemistry* **2010**, *20*, 2329-2335.

(24) Mane, S. T.; Kamble, S. S.; Deshmukh, L. P., Cobalt sulphide thin films: Chemical bath deposition, growth and properties, *Materials Letters* **2011**, *65*, 2639-2641.

(25) Cheng, F. Y.; Su, C. H.; Yang, Y. S.; Yeh, C. S.; Tsai, C. Y.; Wu, C. L.; Wu, M. T.; Shieh, D. B., Characterization of aqueous dispersions of Fe(3)O(4) nanoparticles and their biomedical applications, *Biomaterials* **2005**, *26*, 729-738.

(26) Hao, R.; Xing, R.; Xu, Z.; Hou, Y.; Gao, S.; Sun, S., Synthesis, functionalization, and biomedical applications of multifunctional magnetic nanoparticles, *Adv Mater* **2010**, *22*, 2729-2742.

(27) Oelerich, W.; Klassen, T.; Bormann, R., Metal oxides as catalysts for improved hydrogen sorption in nanocrystalline Mg-based materials, *Journal of Alloys and Compounds* **2001**, *315*, 237-242.

(28) Wang, C.; Daimon, H.; Sun, S., Dumbbell-like Pt-Fe3O4 nanoparticles and their enhanced catalysis for oxygen reduction reaction, *Nano Lett* **2009**, *9*, 1493-1496.

(29) Xu, H.; Ouyang, S. X.; Liu, L. Q.; Reunchan, P.; Umezawa, N.; Ye, J. H., Recent advances in TiO2-based photocatalysis, *Journal of Materials Chemistry A* **2014**, *2*, 12642-12661.

(30) Bingham, S.; Daoud, W. A., Recent advances in making nano-sized TiO2 visible-light active through rare-earth metal doping, *Journal of Materials Chemistry* **2011**, *21*, 2041-2050.

(31) Nosaka, Y.; Matsushita, M.; Nishino, J.; Nosaka, A. Y., Nitrogen-doped titanium dioxide photocatalysts for visible response prepared by using organic compounds, *Science and Technology of Advanced Materials* **2005**, *6*, 143-148.

(32) Sato, S.; Nakamura, R.; Abe, S., Visible-light sensitization of TiO2 photocatalysts by wet-method N doping, *Applied Catalysis a-General* **2005**, *284*, 131-137.

(33) Cong, Y.; Zhang, J. L.; Chen, F.; Anpo, M., Synthesis and characterization of nitrogen-doped TiO2 nanophotocatalyst with high visible light activity, *Journal of Physical Chemistry C* **2007**, *111*, 6976-6982.

(34) Irie, H.; Watanabe, Y.; Hashimoto, K., Carbon-doped Anatase TiO₂ Powders as a Visible-light Sensitive Photocatalyst, *Chemistry Letters* **2003**, *32*, 772-773.

(35) Wu, G.; Nishikawa, T.; Ohtani, B.; Chen, A., Synthesis and Characterization of Carbon-Doped TiO2 Nanostructures with Enhanced Visible Light Response, *Chemistry of Materials* **2007**, *19*, 4530-4537.

(36) Ren, W.; Ai, Z.; Jia, F.; Zhang, L.; Fan, X.; Zou, Z., Low temperature preparation and visible light photocatalytic activity of mesoporous carbon-doped crystalline TiO2, *Applied Catalysis B-Environmental* **2007**, *69*, 138-144.

(37) Tang, X.; Li, D., Sulfur-Doped Highly Ordered TiO2 Nanotubular Arrays with Visible Light Response, *The Journal of Physical Chemistry C* **2008**, *112*, 5405-5409.

(38) Dvoranova, D.; Brezova, V.; Mazur, M.; Malati, M. A., Investigations of metal-doped titanium dioxide photocatalysts, *Applied Catalysis B-Environmental* **2002**, *37*, 91-105.

(39) Nagaveni, K.; Hegde, M. S.; Madras, G., Structure and Photocatalytic Activity of Ti1-xMxO2±δ (M = W, V, Ce, Zr, Fe, and Cu) Synthesized by Solution Combustion Method, *The Journal of Physical Chemistry B* **2004**, *108*, 20204-20212.

(40) Manriquez, V.; Hönle, W.; von Schnering, H. G., Zur Chemie und Strukturchemie von Phosphiden und Polyphosphiden. 42. Trilithiumheptaphosphid Li3P7: Darstellung, Struktur und Eigenschaften, *Zeitschrift Fur Anorganische Und Allgemeine Chemie* **1986**, *539*, 95-109.

(41) Von Schnering, H. G.; Hoenle, W., Chemistry and structural chemistry of phosphides and polyphosphides. 48. Bridging chasms with polyphosphides, *Chemical Reviews* **1988**, *88*, 243-273.

(42) Elfström, M.; Rånby, B.; Sjöberg, B.; Mellander, O.; Hinton, M., The Crystal Structure of Ni5P4, *Acta Chemica Scandinavica* **1965**, *19*, 1694-1704.

(43) Snell, P.-O.; Lumme, P.; Karvonen, P.; Virtanen, A. I.; Paasivirta, J., Phase Relationships in the Ti-P System with some Notes on the Crystal Structures of TiP2 and ZrP2, *Acta Chemica Scandinavica* **1968**, *22*, 1942-1952.

(44) Bowker, R. H.; Ilic, B.; Carrillo, B. A.; Reynolds, M. A.; Murray, B. D.; Bussell, M. E., Carbazole hydrodenitrogenation over nickel phosphide and Ni-rich bimetallic phosphide catalysts, *Applied Catalysis a-General* **2014**, *482*, 221-230.

(45) Wang, X. Q.; Clark, P.; Oyama, S. T., Synthesis, characterization, and hydrotreating activity of several iron group transition metal phosphides, *Journal of Catalysis* **2002**, *208*, 321-331.

(46) Oyama, S. T.; Gott, T.; Zhao, H. Y.; Lee, Y. K., Transition metal phosphide hydroprocessing catalysts: A review, *Catalysis Today* **2009**, *143*, 94-107.

(47) Hillerova, E.; Vit, Z.; Zdrazil, M.; Shkuropat, S. A.; Bogdanets, E. N.; Startsev, A. N., Comparison of Carbon and Alumina Supported Nickel-Molybdenum Sulfide Catalysts in Parallel Hydrodenitrogenation and Hydrodesulfurization, *Applied Catalysis* **1991**, *67*, 231-236.

(48) Smit, T. S.; Johnson, K. H., A Unified Theory of Periodic and Promotion Effects in Transition-Metal Sulfide Hydrodesulfurization Catalysts, *Catalysis Letters* **1994**, *28*, 361-372.

(49) Pawelec, B.; Navarro, R. M.; Campos-Martin, J. M.; Agudo, A. L.; Vasudevan, P. T.; Fierro, J. L. G., Silica-alumina-supported transition metal sulphide catalysts for deep hydrodesulphurization, *Catalysis Today* **2003**, *86*, 73-85.

(50) M. Stanley Whittingham, A. J. J. *Intercalation Chemistry*; Academic Press, 1982.

(51) Wu, B.; Guo, C.; Zheng, N.; Xie, Z.; Stucky, G. D., Nonaqueous production of nanostructured anatase with high-energy facets, *J Am Chem Soc* **2008**, *130*, 17563-17567.

(52) Raula, M.; Rashid, M. H.; Paira, T. K.; Dinda, E.; Mandal, T. K., Ascorbate-assisted growth of hierarchical ZnO nanostructures: sphere, spindle, and flower and their catalytic properties, *Langmuir* **2010**, *26*, 8769-8782.

(53) Ambrus, Z.; Balazs, N.; Alapi, T.; Wittmann, G.; Sipos, P.; Dombi, A.; Mogyorosi, K., Synthesis, structure and photocatalytic properties of Fe(III)-doped TiO(2) prepared from TiCl(3), *Applied Catalysis B-Environmental* **2008**, *81*, 27-37.

(54) Wang, C.; Zhao, J. C.; Wang, X. M.; Mai, B. X.; Sheng, G. Y.; Peng, P.; Fu, J. M., Preparation, characterization and photocatalytic activity of nano-sized ZnO/SnO2 coupled photocatalysts, *Applied Catalysis B-Environmental* **2002**, *39*, 269-279.

(55) Bondioli, F.; Corradi, A. B.; Leonelli, C.; Manfredini, T., Nanosized CeO2 powders obtained by flux method, *Materials Research Bulletin* **1999**, *34*, 2159-2166.

(56) Naidu, H. P.; Virkar, A. V., Low-temperature TiO2-SnO2 phase diagram using the molten-salt method, *Journal of the American Ceramic Society* **1998**, *81*, 2176-2180.

(57) Poser, J. D.; Meyer, H. J., An Experimental Study of a Flux Modulated Solid State Metathesis Reaction, *Zeitschrift Fur Anorganische Und Allgemeine Chemie* **2012**, *638*, 1293-1296.

(58) Jana, N. R.; Chen, Y.; Peng, X., Size- and Shape-Controlled Magnetic (Cr, Mn, Fe, Co, Ni) Oxide Nanocrystals via a Simple and General Approach, *Chemistry of Materials* **2004**, *16*, 3931-3935.

(59) Patil, P. S., Versatility of chemical spray pyrolysis technique, *Materials Chemistry and Physics* **1999**, *59*, 185-198.

(60) Gao, Z. H.; Cui, Z. D.; Zhu, S. L.; Liang, Y. Q.; Li, Z. Y.; Yang, X. J., Fabrication, characterization, and photocatalytic properties of anatase TiO2 nanoplates with exposed {001} facets, *Journal of Nanoparticle Research* **2013**, *16*.

(61) Sun, W.; Liu, H.; Hu, J. C.; Li, J., Controllable synthesis and morphology-dependent photocatalytic performance of anatase TiO2 nanoplates, *Rsc Advances* **2015**, *5*, 513-520.

(62) Gong, D.; Grimes, C. A.; Varghese, O. K.; Hu, W. C.; Singh, R. S.; Chen, Z.; Dickey, E. C., Titanium oxide nanotube arrays prepared by anodic oxidation, *Journal of Materials Research* **2001**, *16*, 3331-3334.

(63) Mor, G. K.; Shankar, K.; Paulose, M.; Varghese, O. K.; Grimes, C. A., Use of highly-ordered TiO(2) nanotube arrays in dye-sensitized solar cells, *Nano Lett* **2006**, *6*, 215-218.

(64) Cozzoli, P. D.; Kornowski, A.; Weller, H., Low-temperature synthesis of soluble and processable organic-capped anatase TiO2 nanorods, *J Am Chem Soc* **2003**, *125*, 14539-14548.

(65) Liu, B.; Aydil, E. S., Growth of oriented single-crystalline rutile TiO(2) nanorods on transparent conducting substrates for dye-sensitized solar cells, *J Am Chem Soc* **2009**, *131*, 3985-3990.

(66) Li, H.; Bian, Z.; Zhu, J.; Zhang, D.; Li, G.; Huo, Y.; Li, H.; Lu, Y., Mesoporous titania spheres with tunable chamber stucture and enhanced photocatalytic activity, *J Am Chem Soc* **2007**, *129*, 8406-8407.

(67) Yang, H. G.; Zeng, H. C., Preparation of hollow anatase TiO2 nanospheres via Ostwald ripening, *Journal of Physical Chemistry B* **2004**, *108*, 3492-3495.

(68) Qian, C.; Kim, F.; Ma, L.; Tsui, F.; Yang, P.; Liu, J., Solution-Phase Synthesis of Single-Crystalline Iron Phosphide Nanorods/Nanowires, *Journal of the American Chemical Society* **2004**, *126*, 1195-1198.

(69) Dahl, E.; Hazell, R. G.; Rasmussen, S. E.; Heinegård, D.; Balaban, A. T.; Craig, J. C., Refined Crystal Structures of PtP2 and FeP2, *Acta Chemica Scandinavica* **1969**, *23*, 2677-2684.

(70) Llunell, M.; Alemany, P.; Alvarez, S.; Zhukov, V. P.; Vernes, A., Electronic structure and bonding in skutterudite-type phosphides, *Physical Review B* **1996**, *53*, 10605-10609.

(71) Donohue, P. C.; Bither, T. A.; Young, H. S., High-pressure synthesis of pyrite-type nickel diphosphide and nickel diarsenide, *Inorganic Chemistry* **1968**, *7*, 998-1001.

(72) Møuller, M. H.; Jeitschko, W., Darstellung, Eigenschaften und Kristallstruktur von Cu2P7 und Strukturverfeinerungen von CuP2 und AgP2, *Zeitschrift Fur Anorganische Und Allgemeine Chemie* **1982**, *491*, 225-236.

(73) Andresen, A. F.; Furuseth, S.; Kjekshus, A.; Åkeson, Å.; Theorell, H.; Blinc, R.; Paušak, S.; Ehrenberg, L.; Dumanović, J., On the Ferromagnetism of CoS2, *Acta Chemica Scandinavica* **1967**, *21*, 833-835.

(74) Furuseth, S.; Kjekshus, A.; Andresen, A. F.; Nordal, V.; Lindberg, A. A.; Craig, J. C., On the Magnetic Properties of CoSe2, NiS2, and NiSe2, *Acta Chemica Scandinavica* **1969**, *23*, 2325-2334.

(75) Fjellvag, H.; Gronvold, F.; Stolen, S.; Andresen, A. F.; Mullerkafer, R.; Simon, A., Low-Temperature Structural Distortion in Cus, *Zeitschrift für Kristallographie* **1988**, *184*, 111-121.

(76) Ouvrard, G.; Brec, R.; Rouxel, J., Structural determination of some MPS3 layered phases (M = Mn, Fe, Co, Ni and Cd), *Materials Research Bulletin* **1985**, *20*, 1181-1189.

(77) Taylor, B. E.; Steger, J.; Wold, A., Preparation and properties of some transition metal phosphorus trisulfide compounds, *Journal of Solid State Chemistry* **1973**, *7*, 461-467.

(78) Marzik, J. V.; Hsieh, A. K.; Dwight, K.; Wold, A., Photoelectronic properties of Cu3PS4 and Cu3PS3Se single crystals, *Journal of Solid State Chemistry* **1983**, *49*, 43-50.

(79) Odile, J. P.; Soled, S.; Castro, C. A.; Wold, A., Crystal growth and characterization of the transition-metal phosphides copper diphosphide, nickel diphosphide, and rhodium triphosphide, *Inorganic Chemistry* **1978**, *17*, 283-286.

(80) Rickard, D.; Luther, G. W., 3rd, Chemistry of iron sulfides, *Chem Rev* **2007**, *107*, 514-562.

(81) Parkin, I. P., Solid state metathesis reaction for metal borides, silicides, pnictides and chalcogenides: Ionic or elemental pathways, *Chemical Society Reviews* **1996**, *25*, 199-+.

(82) Bonneau, P. R.; Jarvis, R. F.; Kaner, R. B., RAPID SOLID-STATE SYNTHESIS OF MATERIALS FROM MOLYBDENUM-DISULFIDE TO REFRACTORIES, *Nature* **1991**, *349*, 510-512.

(83) Treece, R. E.; Macala, G. S.; Rao, L.; Franke, D.; Eckert, H.; Kaner, R. B., Synthesis of III-V semiconductors by solid-state metathesis, *Inorganic Chemistry* **1993**, *32*, 2745-2752.

(84) Rao, L.; Gillan, E. G.; Kaner, R. B., Rapid Synthesis of Transition-Metal Borides by Solid-State Metathesis, *Journal of Materials Research* **1995**, *10*, 353-361.

(85) Janes, R. A.; Low, M. A.; Kaner, R. B., Rapid solid-state metathesis routes to aluminum nitride, *Inorg Chem* **2003**, *42*, 2714-2719.

(86) Gillan, E. G.; Kaner, R. B., Rapid Solid-State Synthesis of Refractory Nitrides, *Inorganic Chemistry* **1994**, *33*, 5693-5700.

(87) Anderson, A. J.; Blair, R. G.; Hick, S. M.; Kaner, R. B., Microwave initiated solid-state metathesis routes to Li2SiN2, *Journal of Materials Chemistry* **2006**, *16*, 1318-1322.

(88) Gillan, E. G.; Kaner, R. B., Rapid, energetic metathesis routes to crystalline metastable phases of zirconium and hafnium dioxide, *Journal of Materials Chemistry* **2001**, *11*, 1951-1956.

(89) Wiley, J. B.; Gillan, E. G.; Kaner, R. B., Rapid Solid-State Metathesis Reactions for the Synthesis of Copper-Oxide and Other Metal-Oxides, *Materials Research Bulletin* **1993**, *28*, 893-900.

(90) Gillan, E. G.; Kaner, R. B., Synthesis of refractory ceramics via rapid metathesis reactions between solid-state precursors, *Chemistry of Materials* **1996**, *8*, 333-343.

(91) Nartowski, A. M.; Parkin, I. P.; Craven, A. J.; MacKenzie, M., Rapid, solid-state metathesis routes to metal carbides, *Advanced Materials* **1998**, *10*, 805-808.

(92) Shimizu, N.; Ogino, C.; Dadjour, M. F.; Murata, T., Sonocatalytic degradation of methylene blue with TiO2 pellets in water, *Ultrason Sonochem* **2007**, *14*, 184-190.

(93) Bubacz, K.; Choina, J.; Dolat, D.; Morawski, A. W., Methylene Blue and Phenol Photocatalytic Degradation on Nanoparticles of Anatase TiO2, *Polish Journal of Environmental Studies* **2010**, *19*, 685-691.

(94) Jiang, G.; Lin, Z.; Chen, C.; Zhu, L.; Chang, Q.; Wang, N.; Wei, W.; Tang, H., TiO2 nanoparticles assembled on graphene oxide nanosheets with high photocatalytic activity for removal of pollutants, *Carbon* **2011**, *49*, 2693-2701.

(95) Guillard, C.; Lachheb, H.; Houas, A.; Ksibi, M.; Elaloui, E.; Herrmann, J. M., Influence of chemical structure of dyes, of pH and of inorganic salts on their photocatalytic degradation by TiO2 comparison of the efficiency of powder and supported TiO2, *Journal of Photochemistry and Photobiology a-Chemistry* **2003**, *158*, 27-36.

(96) Karukstis, K. K.; Savin, D. A.; Loftus, C. T.; D'Angelo, N. D., Spectroscopic Studies of the Interaction of Methyl Orange with Cationic Alkyltrimethylammonium Bromide Surfactants, *Journal of Colloid and Interface Science* **1998**, *203*, 157-163.

(97) Asiri, A. M.; Al-Amoudi, M. S.; Al-Talhi, T. A.; Al-Talhi, A. D., Photodegradation of Rhodamine 6G and phenol red by nanosized TiO2 under solar irradiation, *Journal of Saudi Chemical Society* **2011**, *15*, 121-128.

(98) Fu, H.; Pan, C.; Yao, W.; Zhu, Y., Visible-Light-Induced Degradation of Rhodamine B by Nanosized Bi2WO6, *The Journal of Physical Chemistry B* **2005**, *109*, 22432-22439.

(99) Lachheb, H.; Puzenat, E.; Houas, A.; Ksibi, M.; Elaloui, E.; Guillard, C.; Herrmann, J.-M., Photocatalytic degradation of various types of dyes (Alizarin S, Crocein Orange G, Methyl Red, Congo Red, Methylene Blue) in water by UV-irradiated titania, *Applied Catalysis B: Environmental* **2002**, *39*, 75-90.

(100) Fujishima, A.; Honda, K., Electrochemical Photolysis of Water at a Semiconductor Electrode, *Nature* **1972**, *238*, 37-38.

(101) Li, X.; Yu, J.; Low, J.; Fang, Y.; Xiao, J.; Chen, X., Engineering heterogeneous semiconductors for solar water splitting, *Journal of Materials Chemistry A* **2015**, *3*, 2485-2534.

(102) Ni, M.; Leung, M. K. H.; Leung, D. Y. C.; Sumathy, K., A review and recent developments in photocatalytic water-splitting using TiO2 for hydrogen production, *Renewable & Sustainable Energy Reviews* **2007**, *11*, 401-425.

(103) Kudo, A.; Miseki, Y., Heterogeneous photocatalyst materials for water splitting, *Chemical Society Reviews* **2009**, *38*, 253-278.

(104) Jing, D.; Guo, L., A Novel Method for the Preparation of a Highly Stable and Active CdS Photocatalyst with a Special Surface Nanostructure, *The Journal of Physical Chemistry B* **2006**, *110*, 11139-11145.

(105) Puangpetch, T.; Sreethawong, T.; Yoshikawa, S.; Chavadej, S., Hydrogen production from photocatalytic water splitting over mesoporous-assembled SrTiO3 nanocrystal-based photocatalysts, *Journal of Molecular Catalysis A: Chemical* **2009**, *312*, 97-106.

(106) Howard, C. J.; Sabine, T. M.; Dickson, F., Structural and Thermal Parameters for Rutile and Anatase, *Acta Crystallographica Section B-Structural Science* **1991**, *47*, 462-468.

(107) Cromer, D. T.; Herrington, K., The Structures of Anatase and Rutile, *Journal of the American Chemical Society* **1955**, *77*, 4708-4709.

(108) Baur, W. H., Atomabstande Und Bindungswinkel Im Brookit, Tio2, *Acta Crystallographica* **1961**, *14*, 214-&.

(109) Mo, S. D.; Ching, W. Y., Electronic and optical properties of three phases of titanium dioxide: Rutile, anatase, and brookite, *Phys Rev B Condens Matter* **1995**, *51*, 13023-13032.

(110) Hanaor, D. A. H.; Sorrell, C. C., Review of the anatase to rutile phase transformation, *Journal of Materials Science* **2011**, *46*, 855-874.

(111) Zhang, Y.; Wei, S.; Zhang, H.; Liu, S.; Nawaz, F.; Xiao, F.-S., Nanoporous polymer monoliths as adsorptive supports for robust photocatalyst of Degussa P25, *Journal of Colloid and Interface Science* **2009**, *339*, 434-438.

(112) Byrne, H. E.; Kostedt Iv, W. L.; Stokke, J. M.; Mazyck, D. W., Characterization of HF-catalyzed silica gels doped with Degussa P25 titanium dioxide, *Journal of Non-Crystalline Solids* **2009**, *355*, 525-530.

(113) Ohtani, B.; Prieto-Mahaney, O. O.; Li, D.; Abe, R., What is Degussa (Evonik) P25? Crystalline composition analysis, reconstruction from isolated pure particles and photocatalytic activity test, *Journal of Photochemistry and Photobiology A: Chemistry* **2010**, *216*, 179-182.

(114) Bacsa, R. R.; Kiwi, J., Effect of rutile phase on the photocatalytic properties of nanocrystalline titania during the degradation of p-coumaric acid, *Applied Catalysis B: Environmental* **1998**, *16*, 19-29.

(115) Yu, J. G.; Xiong, J. F.; Cheng, B.; Liu, S. W., Fabrication and characterization of Ag-TiO2 multiphase nanocomposite thin films with enhanced photocatalytic activity, *Applied Catalysis B-Environmental* **2005**, *60*, 211-221.

(116) Patsoura, A.; Kondarides, D. I.; Verykios, X. E., Enhancement of photoinduced hydrogen production from irradiated Pt/TiO2 suspensions with simultaneous degradation of azo-dyes, *Applied Catalysis B: Environmental* **2006**, *64*, 171-179.

(117) Galińska, A.; Walendziewski, J., Photocatalytic Water Splitting over Pt−TiO2 in the Presence of Sacrificial Reagents, *Energy & Fuels* **2005**, *19*, 1143-1147.

(118) Subramanian, V.; Wolf, E. E.; Kamat, P. V., Catalysis with TiO2/gold nanocomposites. Effect of metal particle size on the Fermi level equilibration, *J Am Chem Soc* **2004**, *126*, 4943-4950.

(119) Sakthivel, S.; Shankar, M. V.; Palanichamy, M.; Arabindoo, B.; Bahnemann, D. W.; Murugesan, V., Enhancement of photocatalytic activity by metal deposition: characterisation and photonic efficiency of Pt, Au and Pd deposited on TiO2 catalyst, *Water Res* **2004**, *38*, 3001-3008.

(120) Zhang, H.; Liu, X.; Wang, Y.; Liu, P.; Cai, W.; Zhu, G.; Yang, H.; Zhao, H., Rutile TiO2 films with 100% exposed pyramid-shaped (111) surface: photoelectron transport properties under UV and visible light irradiation, *Journal of Materials Chemistry A* **2013**, *1*, 2646-2652.

(121) Ong, W.-J.; Tan, L.-L.; Chai, S.-P.; Yong, S.-T.; Mohamed, A. R., Highly reactive {001} facets of TiO2-based composites: synthesis, formation mechanism and characterization, *Nanoscale* **2014**, *6*, 1946-2008.

(122) Cong, Y.; Zhang, J.; Chen, F.; Anpo, M.; He, D., Preparation, Photocatalytic Activity, and Mechanism of Nano-TiO2 Co-Doped with Nitrogen and Iron (III), *The Journal of Physical Chemistry C* **2007**, *111*, 10618-10623.

(123) Chen, D.; Jiang, Z.; Geng, J.; Wang, Q.; Yang, D., Carbon and Nitrogen Co-doped TiO2 with Enhanced Visible-Light Photocatalytic Activity, *Industrial & Engineering Chemistry Research* **2007**, *46*, 2741-2746.

(124) Akpan, U. G.; Hameed, B. H., The advancements in sol–gel method of doped-TiO2 photocatalysts, *Applied Catalysis A: General* **2010**, *375*, 1-11.

(125) Gomathi Devi, L.; Kavitha, R., Review on modified N-TiO2 for green energy applications under UV/visible light: selected results and reaction mechanisms, *Rsc Advances* **2014**, *4*, 28265-28299.

(126) Tamaki, Y.; Furube, A.; Murai, M.; Hara, K.; Katoh, R.; Tachiya, M., Direct Observation of Reactive Trapped Holes in TiO2 Undergoing Photocatalytic Oxidation of Adsorbed Alcohols: Evaluation of the Reaction Rates and Yields, *Journal of the American Chemical Society* **2006**, *128*, 416-417.

(127) Treece, R. E.; Macala, G. S.; Kaner, R. B., Rapid synthesis of gallium phosphide and gallium arsenide from solid-state precursors, *Chemistry of Materials* **1992**, *4*, 9-11.

(128) Parkin, I. P.; Komarov, A. V.; Fang, Q., Alternative solid state routes to mixed metal oxides (LnCrO3, LnFeO3), *Polyhedron* **1996**, *15*, 3117-3121.

(129) Elwin, G.; Parkin, I. P.; Bui, Q. T.; Barquin, L. F.; Pankhurst, Q. A.; Komarov, A. V.; Morozov, Y. G., Self-propagating high-temperature synthesis of SrFe12O19 from reactions of strontium superoxide, iron metal and iron oxide powders, *Journal of Materials Science Letters* **1997**, *16*, 1237-1239.

(130) Xu, A. W.; Gao, Y.; Liu, H. Q., The preparation, characterization, and their photocatalytic activities of rare-earth-doped TiO2 nanoparticles, *Journal of Catalysis* **2002**, *207*, 151-157.

(131) Perera, S.; Gillan, E. G., A facile solvothermal route to photocatalytically active nanocrystalline anatase TiO2 from peroxide precursors, *Solid State Sciences* **2008**, *10*, 864-872.

(132) Tan, B. J.; Klabunde, K. J.; Sherwood, P. M. A., X-Ray Photoelectron-Spectroscopy Studies of Solvated Metal Atom Dispersed Catalysts - Monometallic Iron and Bimetallic Iron Cobalt Particles on Alumina, *Chemistry of Materials* **1990**, *2*, 186-191.

(133) Agostinelli, E.; Battistoni, C.; Fiorani, D.; Mattogno, G.; Nogues, M., An XPS study of the electronic structure of the ZnxCd1−xCr2(X = S, Se) spinel system, *Journal of Physics and Chemistry of Solids* **1989**, *50*, 269-272.

(134) Allen, G. C.; Curtis, M. T.; Hooper, A. J.; Tucker, P. M., X-Ray Photoelectron Spectroscopy of Chromium-Oxygen Systems, *Journal of the Chemical Society-Dalton Transactions* **1973**, 1675-1683.

(135) Di Castro, V.; Polzonetti, G.; Contini, G.; Cozza, C.; Paponetti, B., XPS study of MnO2 minerals treated by bioleaching, *Surface and Interface Analysis* **1990**, *16*, 571-574.

(136) Tan, B. J.; Klabunde, K. J.; Sherwood, P. M. A., XPS studies of solvated metal atom dispersed (SMAD) catalysts. Evidence for layered cobalt-manganese particles on alumina and silica, *Journal of The American Chemical Society* **1991**, *113*, 855-861.

(137) Umezawa, Y.; Reilley, C. N., Effect of Argon Ion-Bombardment on Metal-Complexes and Oxides Studied by X-Ray Photoelectron-Spectroscopy, *Analytical chemistry* **1978**, *50*, 1290-1295.

(138) Bonnelle, J. P.; Grimblot, J.; D'Huysser, A., Influence de la polarisation des liaisons sur les spectres esca des oxydes de cobalt, *Journal of Electron Spectroscopy and Related Phenomena* **1975**, *7*, 151-162.

(139) Chuang, T. J.; Brundle, C. R.; Rice, D. W., Interpretation of the x-ray photoemission spectra of cobalt oxides and cobalt oxide surfaces, *Surface Science* **1976**, *59*, 413-429.

(140) Khawaja, E. E.; Salim, M. A.; Khan, M. A.; Aladel, F. F.; Khattak, G. D.; Hussain, Z., Xps, Auger, Electrical and Optical Studies of Vanadium Phosphate-Glasses Doped with Nickel-Oxide, *Journal of Non-Crystalline Solids* **1989**, *110*, 33-43.

(141) Nemoshkalenko, V. V.; Didyk, V. V.; Krivitskii, V. P.; Senkevich, A. I., Study of the Charge State of Atoms in Iron, Cobalt and Nickel Phosphides, *Zhurnal Neorganicheskoi Khimii* **1983**, *28*, 2182-2186.

(142) Carver, J. C.; Carlson, T. A.; Schweitz.Gk, Use of X-Ray Photoelectron Spectroscopy to Study Bonding in Cr, Mn, Fe, and Co Compounds, *Journal of Chemical Physics* **1972**, *57*, 973-&.

(143) Li, W.; Li, D.; Lin, Y.; Wang, P.; Chen, W.; Fu, X.; Shao, Y., Evidence for the Active Species Involved in the Photodegradation Process of Methyl Orange on TiO2, *The Journal of Physical Chemistry C* **2012**, *116*, 3552-3560.

(144) Kislov, N.; Lahiri, J.; Verma, H.; Goswami, D. Y.; Stefanakos, E.; Batzill, M., Photocatalytic Degradation of Methyl Orange over Single Crystalline ZnO: Orientation Dependence of Photoactivity and Photostability of ZnO, *Langmuir* **2009**, *25*, 3310-3315.

(145) Kansal, S. K.; Singh, M.; Sud, D., Studies on photodegradation of two commercial dyes in aqueous phase using different photocatalysts, *J Hazard Mater* **2007**, *141*, 581-590.

(146) Kucernak, A. R. J.; Naranammalpuram Sundaram, V. N., Nickel phosphide: the effect of phosphorus content on hydrogen evolution activity and corrosion resistance in acidic medium, *Journal of Materials Chemistry A* **2014**, *2*, 17435-17445.

(147) Maneeprakorn, W.; Nguyen, C. Q.; Malik, M. A.; O'Brien, P.; Raftery, J., Synthesis of the nickel selenophosphinates [Ni(Se2PR2)2] (R = iPr, tBu and Ph) and their use as single source precursors for the deposition of nickel phosphide or nickel selenide nanoparticles, *Dalton Transactions* **2009**, 2103-2108.

(148) Brockway, L.; Van Laer, M.; Kang, Y.; Vaddiraju, S., Large-scale synthesis and in situ functionalization of Zn3P2 and Zn4Sb3 nanowire powders, *Physical Chemistry Chemical Physics* **2013**, *15*, 6260-6267.

(149) Hector, A. L.; Parkin, I. P., Self-propagating routes to transition-metal phosphides, *Journal of Materials Chemistry* **1994**, *4*, 279-283.

(150) Shaw, G. A.; Morrison, D. E.; Parkin, I. P., Solid state synthesis of binary metal chalcogenides, *Journal of the Chemical Society, Dalton Transactions* **2001**, 1872-1875.

(151) Qian, C.; Kim, F.; Ma, L.; Tsui, F.; Yang, P. D.; Liu, J., Solution-phase synthesis of single-crystalline iron phosphide nanorods/nanowires, *Journal of the American Chemical Society* **2004**, *126*, 1195-1198.

(152) Zhang, Z. S.; Yang, J.; Nuli, Y.; Wang, B. F.; Xu, J. Q., CoPx synthesis and lithiation by ball-milling for anode materials of lithium ion cells, *Solid State Ionics* **2005**, *176*, 693-697.

(153) Aso, K.; Hayashi, A.; Tatsumisago, M., Phase-Selective Synthesis of Nickel Phosphide in High-Boiling Solvent for All-Solid-State Lithium Secondary Batteries, *Inorganic Chemistry* **2011**, *50*, 10820-10824.

(154) Song, L.; Zhang, S.; Wei, Q., An approach to preparing porous and hollow metal phosphides with higher hydrodesulfurization activity, *Journal of Solid State Chemistry* **2011**, *184*, 1556-1560.

(155) Sawhill, S. J.; Phillips, D. C.; Bussell, M. E., Thiophene hydrodesulfurization over supported nickel phosphide catalysts, *Journal of Catalysis* **2003**, *215*, 208-219.

(156) Hayes, J. R.; Bowker, R. H.; Gaudette, A. F.; Smith, M. C.; Moak, C. E.; Nam, C. Y.; Pratum, T. K.; Bussell, M. E., Hydrodesulfurization properties of rhodium phosphide Comparison with rhodium metal and sulfide catalysts, *Journal of Catalysis* **2010**, *276*, 249-258.

(157) Oyama, S. T., Novel catalysts for advanced hydroprocessing: transition metal phosphides, *Journal of Catalysis* **2003**, *216*, 343-352.

(158) Xie, Y.; Su, H. L.; Qian, X. F.; Liu, X. M.; Qian, Y. T., A Mild One-Step Solvothermal Route to Metal Phosphides (Metal=Co, Ni, Cu), *Journal of Solid State Chemistry* **2000**, *149*, 88-91.

(159) Liu, J.; Chen, X.; Shao, M.; An, C.; Yu, W.; Qian, Y., Surfactant-aided solvothermal synthesis of dinickel phosphide nanocrystallites using red phosphorus as starting materials, *Journal of Crystal Growth* **2003**, *252*, 297-301.

(160) Donohue, P. C.; Bither, T. A.; Young, H. S., High-Pressure Synthesis of Pyrite-Type Nickel Diphosphide and Nickel Diarsenide, *Inorganic Chemistry* **1968**, *7*, 998-&.

(161) Itthibenchapong, V.; Kokenyesi, R. S.; Ritenour, A. J.; Zakharov, L. N.; Boettcher, S. W.; Wager, J. F.; Keszler, D. A., Earth-abundant Cu-based chalcogenide semiconductors as photovoltaic absorbers, *Journal of Materials Chemistry C* **2013**, *1*, 657-662.

(162) Takano, Y.; Arai, A.; Takahashi, Y.; Takase, K.; Sekizawa, K., Magnetic properties and specific heat of new spin glass Mn0.5Fe0.5PS3, *Journal of Applied Physics* **2003**, *93*, 8197-8199.

(163) Clement, R.; Girerd, J. J.; Morgensternbadarau, I., DRAMATIC MODIFICATION OF THE MAGNETIC-PROPERTIES OF LAMELLAR MNPS3 UPON INTERCALATION, *Inorganic Chemistry* **1980**, *19*, 2852-2854.

(164) Aruchamy, A.; Berger, H.; Levy, F., Photoelectronic properties of the p-type layered trichalcogenophosphates FePS3 and FePSe3, *Journal of Solid State Chemistry* **1988**, *72*, 316-323.

(165) Ichimura, K.; Sano, M., ELECTRICAL-CONDUCTIVITY OF LAYERED TRANSITION-METAL PHOSPHORUS TRISULFIDE CRYSTALS, *Synthetic Metals* **1991**, *45*, 203-211.

(166) Boda, G.; Stenström, B.; Sagredo, V.; Beckman, O.; Carlsson, B.; Rundqvist, S., Magnetic and Electric Properties of FeP 2 Single Crystals, *Physica Scripta* **1971**, *4*, 132.

(167) Ackermann, J.; Wold, A., The preparation and characterization of the cobalt skutterudites CoP3, CoAs3 and CoSb3, *Journal of Physics and Chemistry of Solids* **1977**, *38*, 1013-1016.

(168) Brec, R., REVIEW ON STRUCTURAL AND CHEMICAL-PROPERTIES OF TRANSITION-METAL PHOSPHORUS TRISULFIDES MPS3, *Solid State Ionics* **1986**, *22*, 3-30.

(169) Ismail, N.; Madian, M.; El-Meligi, A. A., Synthesis of NiPS3 and CoPS and its hydrogen storage capacity, *Journal of Alloys and Compounds* **2014**, *588*, 573-577.

(170) Brec, R.; Schleich, D. M.; Ouvrard, G.; Louisy, A.; Rouxel, J., Physical properties of lithium intercalation compounds of the layered transition-metal chalcogenophosphites, *Inorganic Chemistry* **1979**, *18*, 1814-1818.

(171) Brec, R.; Ouvrard, G.; Louisy, A.; Rouxel, J.; Le Mehaute, A., The influence, on lithium electrochemical intercalation, of bond ionicity in layered chalcogenophosphates of transition metals, *Solid State Ionics* **1982**, *6*, 185-190.

(172) Fuentealba, P.; Cortes, C.; Audebrand, N.; Le Fur, E.; Paredes-Garcia, V.; Venegas-Yazigi, D.; Manzur, J.; Spodine, E., First copper(ii) phase MMnPS.0.25HO and analogous M' = Co, Ni and Zn materials obtained by microwave assisted synthesis, *Dalton Trans* **2015**.

(173) Jeitschko, W.; Foecker, A. J.; Paschke, D.; Dewalsky, M. V.; Evers, C. B. H.; Künnen, B.; Lang, A.; Kotzyba, G.; Rodewald, U. C.; Möller, M. H., Crystal Structure and Properties of Some Filled and Unfilled Skutterudites: GdFe4P12, SmFe4P12, NdFe4As12, Eu0.54Co4Sb12, Fe0.5Ni0.5P3, CoP3, and NiP3, *Zeitschrift Fur Anorganische Und Allgemeine Chemie* **2000**, *626*, 1112-1120.

(174) Sangster, J.; Pelton, A. D., Phase Diagrams and Thermodynamic Properties of the 70 Binary Alkali Halide Systems Having Common Ions, *Journal of Physical and Chemical Reference Data* **1987**, *16*, 509-561.

(175) Lange, S.; Bawohl, M.; Weihrich, R.; Nilges, T., Mineralization routes to polyphosphides: Cu2P20 and Cu5InP16, *Angewandte Chemie-International Edition* **2008**, *47*, 5654-5657.

(176) Nahigian, H.; Steger, J.; Arnott, R. J.; Wold, A., Preparation and properties of the system CoPxS2−x, *Journal of Physics and Chemistry of Solids* **1974**, *35*, 1349-1354.

(177) Maeda, K.; Takata, T.; Hara, M.; Saito, N.; Inoue, Y.; Kobayashi, H.; Domen, K., GaN:ZnO solid solution as a photocatalyst for visible-light-driven overall water splitting, *J Am Chem Soc* **2005**, *127*, 8286-8287.

(178) Ohno, T.; Bai, L.; Hisatomi, T.; Maeda, K.; Domen, K., Photocatalytic water splitting using modified GaN:ZnO solid solution under visible light: long-time operation and regeneration of activity, *J Am Chem Soc* **2012**, *134*, 8254-8259.

(179) Xing, Z. C.; Liu, Q.; Asiri, A. M.; Sun, X. P., High-Efficiency Electrochemical Hydrogen Evolution Catalyzed by Tungsten Phosphide Submicroparticles, *ACS Catalysis* **2015**, *5*, 145-149.

(180) Zhou, H. Q.; Su, X.; Zhang, X. A.; Chen, X. G.; Yang, C. L.; Qin, J. G.; Inokuchi, M., Intercalation of amino acids into layered MnPS3: Synthesis, characterization and magnetic properties, *Materials Research Bulletin* **2006**, *41*, 2161-2167.

(181) Cleary, D. A.; Francis, A. H., Electron spin resonance spectra of cobaltocene intercalated cadmium phosphorus sulfide (CdPS3) layered host lattices, *The Journal of Physical Chemistry* **1985**, *89*, 97-100.

(182) Clement, R., Ion-Exchange Intercalation into the Mps(3) Layered Compounds - Design of Nanocomposites with Unusual Magnetic, Electrical, and Nonlinear-Optical Properties, *Hybrid Organic-Inorganic Composites* **1995**, *585*, 29-42.

(183) Kerrache, I.; Julien, C.; Sourisseau, C., Raman scattering studies of lithium-intercalated NiPS3, *Solid State Ionics* **1996**, *92*, 37-43.

(184) Lagadic, I.; Lacroix, P. G.; Clement, R., Layered MPS3 (M = Mn, Cd) thin films as host matrixes for nonlinear optical material processing, *Chemistry of Materials* **1997**, *9*, 2004-2012.

(185) Doeuff, M.; Cartier, C.; Clement, R., Phosphorus vacancies and intercalation in lamellar NiPS3, *Journal of the Chemical Society, Chemical Communications* **1988**, 629-630.

(186) Zhang, X.; Chen, X. G.; Su, X.; Yang, C. L.; Qin, J. G.; Inokuchi, M., The intercalation reaction of 2,2 '-bipyridine with layered compound MnPS3, *Journal of Solid State Chemistry* **2004**, *177*, 2014-2022.

(187) Miyazaki, T.; Ichimura, K.; Matsuzaki, S.; Sano, M., PYRIDINE-INTERCALATED MNPS3 SINGLE-CRYSTALS, *Journal of Physics and Chemistry of Solids* **1993**, *54*, 1023-1026.

(188) Joy, P. A.; Vasudevan, S., The Intercalation Reaction of Pyridine with Manganese Thiophosphate, Mnps3, *Journal of the American Chemical Society* **1992**, *114*, 7792-7801.

(189) Osterloh, F. E., Inorganic materials as catalysts for photochemical splitting of water, *Chemistry of Materials* **2008**, *20*, 35-54.